DROPLET DYNAMICS ON NON-POROUS AND POROUS MEDIA: IMPACT, SPREADING AND ABSORPTION

A thesis submitted to attain the degree of

DOCTOR OF SCIENCES of ETH ZURICH

(Dr. sc. ETH Zurich)

presented by

JAE BONG LEE

Master of Science in Mechanical Engineering

Chung-Ang University

born 26 May 1981

citizen of Republic of Korea

accepted on the recommendation of

Prof. Dr. Jan Carmeliet, examiner

Prof. Dr. Daniel Bonn, co-examiner

Prof. Dr. Ali Dolatabadi, co-examiner

Prof. Dr. Dimos Poulikakos, co-examiner

Dr. Dominique Derome, co-examiner

2015

Look deep into nature,
and then you will understand everything better.

– Albert Einstein

ABSTRACT

Wetting by impinging drops on a porous material is an ubiquitous phenomenon, with numerous engineering applications, e.g. rain drops falling on leaf or building facade, a drop of coffee on a napkin, printing on paper. Wind-driven rain (WDR), referring to rain droplets carried by the wind and impacting on building façade, is one of the main moisture sources with potentially negative effects on hygrothermal performance and durability of building facades. Understanding drop impact phenomena can lead to a better estimation of WDR intensity on buildings within urban environments.

In this thesis, drop physics on porous media, namely droplet impact, spreading, absorption and evaporation, in the general framework of wind-driven rain in the built environment, is studied experimentally, theoretically and numerically. Starting with experimental work on impermeable surfaces which excludes the influence of absorption, theoretical and numerical models are developed for the estimation of maximum spreading considering the influence of liquid properties, wetting behavior and roughness. Spreading on porous media is presented by focusing on the influence of the media wetting behavior, the morphology of porous surfaces and the effects of permeability and porosity. The developed theoretical model for maximum spreading on impermeable surface is applied to drop impact on porous media, and could be extended for any complex surface. Water droplet mass transfer into porous media is captured experimentally and numerically. The absence of inertia driven penetration and capillary absorption during spreading is demonstrated. Droplets impacting on porous media are pinned at maximum spreading. These findings allow to estimate the water mass transport accurately from rain droplet to building façade, and they provide a better insight into drop impact on natural porous substrate.

ZUSAMMENFASSUNG

Das Benetzen von porösen Materialien durch aufprallende Tropfen ist ein allgegenwärtiges Phänomen, welches für viele Ingenieuranwendungen, wie zum Beispiel das Auftreffen von Regentropfen auf Blätter von Pflanzen oder Gebäudefassaden, ein Kaffeetropfen auf einer Serviette oder das Bedrucken von Papier, wichtig ist. Schlagregen (WDR: wind driven rain), bezeichnet einen Regen, bei welchem die Regentropfen vom Wind getragen werden und auf Gebäudefassaden aufprallen, was eine der Hauptfeuchtequellen von Gebäudefassaden ist und potenziell einen negativen Effekt auf dessen hygrothermisches Verhalten und deren Dauerhaftigkeit haben kann. Das Verständnis von Tropfenaufprallphänomenen kann zu einer besseren Abschätzung von WDR Intensitäten auf Gebäuden in urbanen Gebieten führen. In dieser Doktorarbeit wird die Aufprallphysik von Tropfen auf porösen Materialien, im Detail der Aufprall, die Ausbreitung, die Absorption und die Evaporation, im Zusammenhang von WDR in der bebauten Umgebung experimentell, theoretisch und numerisch untersucht. Beginnend mit einer experimentellen Arbeit über wasserundurchlässige Oberflächen, wo keine Absorption vorkommt werden theoretische und numerische Modelle entwickelt, mit welchen die maximale Ausbreitung unter Berücksichtigung von den Eigenschaften der Flüssigkeit, des Benetzungsverhaltens und der Rauigkeit bestimmt werden kann. Die Ausbreitung auf porösen Materialien wird mit dem Fokus auf dem Einfluss dessen Benetzungsverhaltens, der Morphologie der porösen Oberflächen und der Effekte von der Wasserdurchlässigkeit und der Porosität präsentiert. Das entwickelte, theoretische Modell für die maximale Ausbreitung auf wasserundurchlässigen Oberflächen wird für den Aufprall von Tropfen auf poröse Materialien angewendet und kann für alle komplexen Oberflächen erweitert werden. Der Massetransport von Wassertropfen in poröse Materialien hinein wird experimentell und numerisch erfasst. Das Nichtvorhandensein des durch Massenträgheit herbeigeführten Eindringens und der Kapilarabsorption während der Ausbreitung wird demonstriert. Tropfen, welche auf porösen Materialien auftreffen, haften mit der maximalen Ausbreitung fest. Diese Erkenntnisse erlauben den Wassertransport vom Regentropfen zur Gebäudefassade

exakt abzuschätzen und sie geben einen besseren Einblick in die Physik des Tropfenaufpralls auf natürlichen, porösen Substraten.

ACKNOWLEDGMENTS

My PhD project during last three years and eight months would not have been possible without the support and help of many colleagues and friends. Therefore, I appreciate deeply all people who participated directly and indirectly for the success of my thesis.

Prof. Jan Carmeliet. Thank you very much for offering me the opportunity to continue the journey of droplet at ETH Zurich. I greatly respect your scientific desire regarding the specific discussion and suggestion. Based on your essential questions and advices, I could develop my thesis.

Dr. Dominique Derome. Thank you for your supervising during last 3.8 years. I really thank you for your encouragement when my work was not going well.

Prof. Dimos Poulikakos. I would like to thank you for accepting to be a member of the examination board and for your constructive remarks and suggestions. Moreover, thank you for your supervising at the beginning of my PhD. I also thank Prof. Manish, Carlo and Tanmoy.

Prof. Daniel Bonn and Noushine Shahidzadeh. I want to thank for all the discussions on droplet during last 3 years and for your support. I also thank Nick, Georgios and Karla for their help.

Prof. Ali Dolatabadi. I very much appreciate your efforts of being my co-examiner of my PhD thesis. Moreover, thank you for the discussion and help for numerical works.

Prof. Robert Guyer. I would like to thank for fruitful discussions and suggestions.

Prof. Seong Hyuk Lee. I very much appreciate your support during my master and PhD.

I want to thank all colleagues at EMPA. Martina, Stefan, Guylaine, Roger and Beat thanks for their excellent support. Karol, Sreeyuth and Aytac for creating a nice working environment. I want to express my gratitude to all former and present colleagues, Peter, Hannelore, Alessandra, Enrico, Michela, Saeed, Ahmad, Behrooz, Thijs, Jonas, Andrea, Mark, Marcel, Marcelo, Laure, Lento, Chi, Omid, Mingyang Soyoun.

I want to thank my family and friends for their big support and warm consideration. A special thanks to my parents Kyungwon Lee and

CONTENTS

1

INTRODUCTION

1.1 MOTIVATION

Wetting by Wind-Driven Rain (WDR) refers to rain droplets carried by the wind and impacting on the building façade. The droplet impact leads to a rich pallet of surface and contact phenomena, such as (1) dynamic spreading, splashing or bouncing of the droplet depending on impact velocity, incident angle and surface characteristics such as wetting behavior and roughness, (2) droplet deposition, (3) absorption of the droplet into the porous substrate, (4) evaporation from the droplet surface and wetted surface and (5) film forming and run-off. WDR water is a main agent of deterioration of building materials, which becomes an important issue when, for example, retrofitting old or historical buildings by adding insulation, in order to make our cities more energy efficient. Not only for durability assessment, but also for the assessment of soiling of façades and leaching of harmful biocides and nanoparticles from our buildings, the amount of WDR and the duration of its presence/contact on different façade parts has to be determined accurately. In addition to WDR on building façade and in the built environment, drop impact on surfaces is an everyday and ubiquitous phenomenon with important applications in natural, agricultural and industry processes such as coating, printing, spraying technology, microchip production, microfluids applications, analysis of DNA microarrays and even within bloodstain pattern analysis where one requires the velocity of a blood drop for crime scene reconstruction. Because of the importance on these many aspects, drop impact has been studied extensively experimentally, theoretically and numerically for many materials and many situations.

Despite the large number of fundamental and applied studies, the study of drops impacting porous media has received little attention compared to similar studies on impermeable surfaces, although such event is more commonplace and often plays an important role in several processes. A comprehensive explanation of drop physics on porous media is intricate, due to the complex structure of porous media in terms of surface roughness and absorption by capillary force. The typical process

of spreading and penetration occurs in micro or milliseconds over micro or millimeter length. The currently available experimental methods do not allow yet to examine all the aspects of droplet physics on porous media with sufficient spatial and temporal resolution and information inside porous media. With the novel experimental approaches, and in conjunction with theoretical analysis and numerical methods, further work to grasp the missing knowledge should be attempted. There is indeed a great need for experimental, theoretical and numerical study that will capture the hydrodynamics of impacting droplet on complex porous surface and the water mass migration inside porous media as well as the subsequent phenomena, e.g. evaporation. The answers that still await a comprehensive explanation are how the impinging droplet spreads over the porous media, how the water is absorbed into porous media from impacting droplet, and what are the mechanisms of water distribution inside porous media.

Therefore, the motivation of this thesis is to enable novel technologies and solutions for long-standing problems on fluidics by improving our understanding of droplet impact on porous media. Due to the complexity on porous media, this research is the first of its kind for drop impact on natural porous stone using experimental methods (high-speed camera and neutron radiography) and simulation and therefore can enrich the current state of the art. The results of this work are important for a wide range of applications for which the control of droplet deposition is of prominent importance.

1.2 SCOPE AND OBJECTIVES

The aim of this study is to understand the drop physics on porous media that accompany droplet impact, spreading, absorption and evaporation, in the general framework of wind-driven rain in the built environment. The specific objectives of this work are:

- To develop an experimental and modeling framework for the study of the fate of droplets impacting porous media.

- To understand and model the dynamics of impacting liquid droplets considering different liquids and surfaces, when absorption is excluded.

- To understand and model the fate of liquid droplets impacting porous stones, including absorption.

This thesis addresses the following three points to picture the full fate of drop impact on porous media: (1) Drop impact phenomena on impermeable surface: to understand the hydrodynamics of droplet excluding the influence of absorption, the drop impact on impermeable surface will be investigated to figure out the influence of liquid properties (surface tension, viscosity), wetting behavior (equilibrium contact angle, dynamic contact angle) and roughness, experimentally, theoretically and numerically. (2) Drop impact phenomena on porous media focusing on the droplet hydrodynamics on the surface: based on the knowledge of drop impact on impermeable surface, the dynamics of drop impact on porous media will be investigated more specifically focusing on the influence of their wetting behavior, the morphology of porous surface and the effects of permeability and porosity. (3) Mass transfer from impinging droplet to porous media: towards understanding drop hydrodynamics on porous media, the water droplet mass transfer into porous media will be pictured experimentally and numerically in terms of inertia driven penetration and capillary absorption in order to draw the full fate of droplet impacting on porous media.

1.3 OUTLINE OF THE DISSERTATION

The thesis is composed of thirteen chapters. Chapter 2 presents the state of the art in terms of understanding the fate of liquid droplets impacting impervious and porous surfaces in the spreading and receding phases, but not venturing in the splashing domain. Experimental approaches and previous work are synthesized. Different analytical and numerical studies are reviewed. The actual theoretical models are detailed in chapter 3, specially for the prediction of the maximum spreading based on the energy balance approach. Chapter 3 also described the Computational Fluid Dynamics (CFD) and Volume-of-Fluid (VOF) methods with dynamic contact angle model used for simulating drop impact.

The experimental materials and methods are presented in the next two chapters. In chapter 4, the properties of the liquids and the substrates used to study the dynamics of drop impact are characterized and listed. In chapter 5, the experimental methods used for visualization and quantification of the drop impact and absorption are described in

detail. A shadowgraphy setup and a high-speed camera captures either the few milliseconds of the spreading of the impacting droplet or the few seconds of absorption of droplets on porous media. Neutron radiography documents moisture content distribution within the stones.

Then follows a series of four chapters studying droplets impacting impervious surfaces. In chapter 6, droplet spreading with various liquids on various smooth and rough surfaces is studied, with special attention on the dynamic wetting behavior at low impact velocity. Chapter 7 looks at the influence of the air layer between the droplet and the surface by looking at drop impact on smooth and rough glass surfaces. In chapter 8, the role of parameters, such as surface tension, viscosity, wettability and surface roughness, on the maximum spreading ratio is presented and taken into account in the development of an updated model for the maximum spreading ratio, based on the energy balance approach. To close this series, in chapter 9, the role of liquid properties on drop impact is studied numerically with CFD-VOF simulations. Special attention is given to the appropriate determination of the boundary conditions, namely on the dynamic contact angle at maximum spreading. The simulations aim at providing complementary information, not available with experiments, such as energy dissipation.

In the last part of the thesis, droplet fate on porous media is studied using three isotropic porous natural stones. Chapter 10 looks at spreading on the stones in comparison with the behavior on impervious surface. Maximum spreading and dynamic contact angle at low impact velocity are also particularly studied. In chapter 11, the full absorption process of impinging droplets on natural porous stones is documented by combining high-speed imaging, neutron radiography and numerical simulation. Chapter 12 further explores droplet spreading and penetration in porous stones by taking benefit of neutron radiography. A string of droplets dropped on top of the same position, two series of droplets dropped side by side and a drop impact on oblique surface are documented.

Chapter 13 summarizes the main conclusions of this thesis and presents the perspectives.

STATE OF THE ART
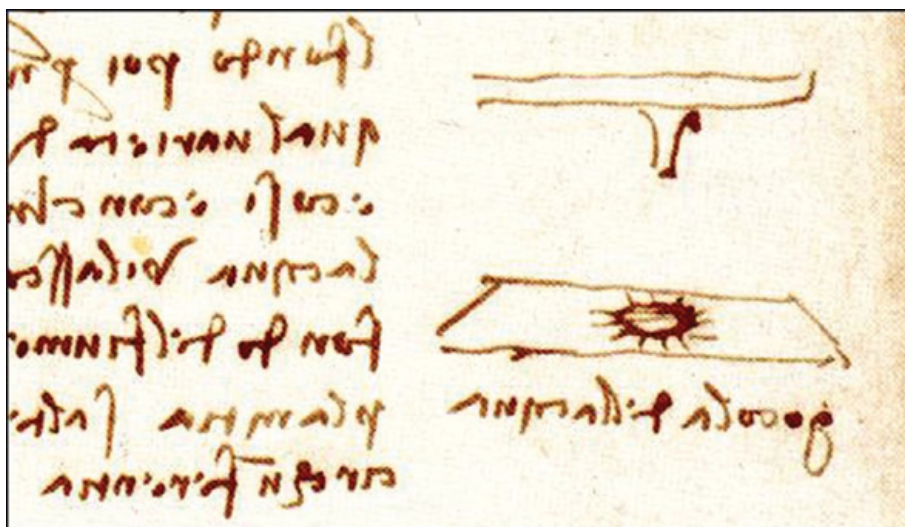
Figure 2.1: Axisymmetric imprint of drop impact with fingering shape at the rim drawn by Leonardo da Vinci in 1508 in the margin of folio 33r of Codex Leicester (Villermaux and Bossa, 2009)

Drop impacts on solid surface are ubiquitously encountered in nature, life and technical applications. Drop impact phenomena have fascinated scientists for centuries. Leonardo da Vinci drew the imprint of a drop impacted on a sheet of paper in his Codex Leicester as shown in Figure 2.1 (Villermaux and Bossa, 2009). The study of the drop impact benefitted greatly from the development of imaging technologies. In the first systematic investigation on drop impact, Worthington (1876) captured the impact of milk or mercury droplets on a glass surface by using a spark illumination in a dark room and with his naked eye as the recorder (Figure 2.2). As Worthington predicted (Thoroddsen et al., 2008), the development of fast photography led to numerous studies of drop impact for a multitude applications. Despite more than 100 years of imaged-based research, the phenomenon is still far from being fully
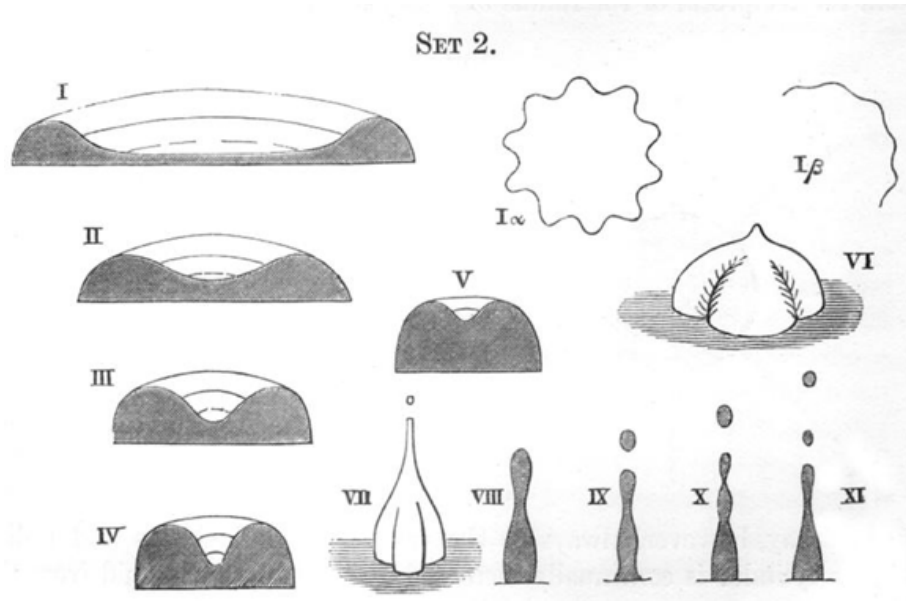
Figure 2.2: Worthington's illustrations of milk drop impact on glass surface (Worthington, 1876). I: spreading phase with wavy edge (Iα top view of spreading phase); II-VI: receding phase; VII: small detached drop moving upwards; VIII-XI: consecutive split phases.

understood and continues to attract the attention of physicists, engineers and mathematicians (Yarin, 2006).

Drops impacting solid walls may undergo very different outcomes such as deposition, spreading, splashing, receding or rebound, Figure 2.3 (Marengo et al., 2011). The outcome of drop impact depends on impact conditions (impact velocity, drop size, angle of impact, cross air flow, liquid and air temperature, etc.), properties of the liquid (density, viscosity, surface tension) and properties and geometry of the surface (wettability, roughness) (Yarin, 2006). Given the wealth of combinations of parameters in studying droplet impact, this field is constantly evolving. One of the aspects of drop impact dynamics that is frequently studied is the spreading behavior. The understanding of spreading is crucial towards the determination of the outcome of droplet impact and of its deposition on surfaces. Such knowledge is directly related with many applications, either for industrial processes or water transport in natural phenomena. This topic underwent recently a tremendous increase of

experimental, theoretical and numerical investigations (Marengo et al., 2011). A comprehensive review can be found in Yarin (2006) and Marengo et al. (2011) for experimental and Malgarinos et al. (2014) for numerical studies.

This chapter presents first drop impact on impermeable horizontal surfaces. The spreading behavior of the impacting droplet has been analyzed experimentally, theoretically and numerically in terms of maximum spreading. Then, the drop impact on porous media is reviewed in terms of spreading and absorption behavior. Finally, the needs for further research are pointed out.

2.1 DROP SPREADING ON IMPERMEABLE SURFACES

Maximum spreading has been studied experimentally, theoretically and numerically. In fact, the experimental work of drop impact has led to the development of theoretical models to analyze the spreading behavior and to predict the outcome of the drop impact. The process of drop spreading can be considered to be a balance of the kinetic ($E_k = \rho D_0^3 V_i^2$), capillary ($E_\gamma = \gamma D_0^2$) and viscous ($E_\mu = \rho V_i D_0^2$) energies, where ρ is the liquid droplet density, γ the liquid-vapor surface tension, μ the viscosity, D0 the initial drop diameter and V_i the impact velocity. Most of the existing models use two dimensionless numbers: Weber number ($We = \rho V_i^2 D_0/\gamma$), the ratio between the inertial and capillary forces (kinetic and capillary energies, E_k/E_γ), and Reynolds number ($Re = \rho V_i D_0/\mu$), the ratio between the inertial and viscous forces (kinetic and viscous energies, E_k/E_μ). The maximum spreading diameter is often reported as the maximum spreading ratio $\beta_{max} = D_{max}/D_0$ where D_{max} is the maximum spreading diameter.

As most of experimental results document only the exterior geometry of the drop during spreading, numerical studies are used to identify flow and pressure fields within the drop during impact.

2.1.1 *Experimental work*

Maximum spreading depends on several parameters, impact velocity, drop size, the properties of liquid, surface roughness and wettability, and is analyzed with Weber and Reynolds numbers. Maximum spreading can be controlled by the liquid properties of viscosity and surface tension. The
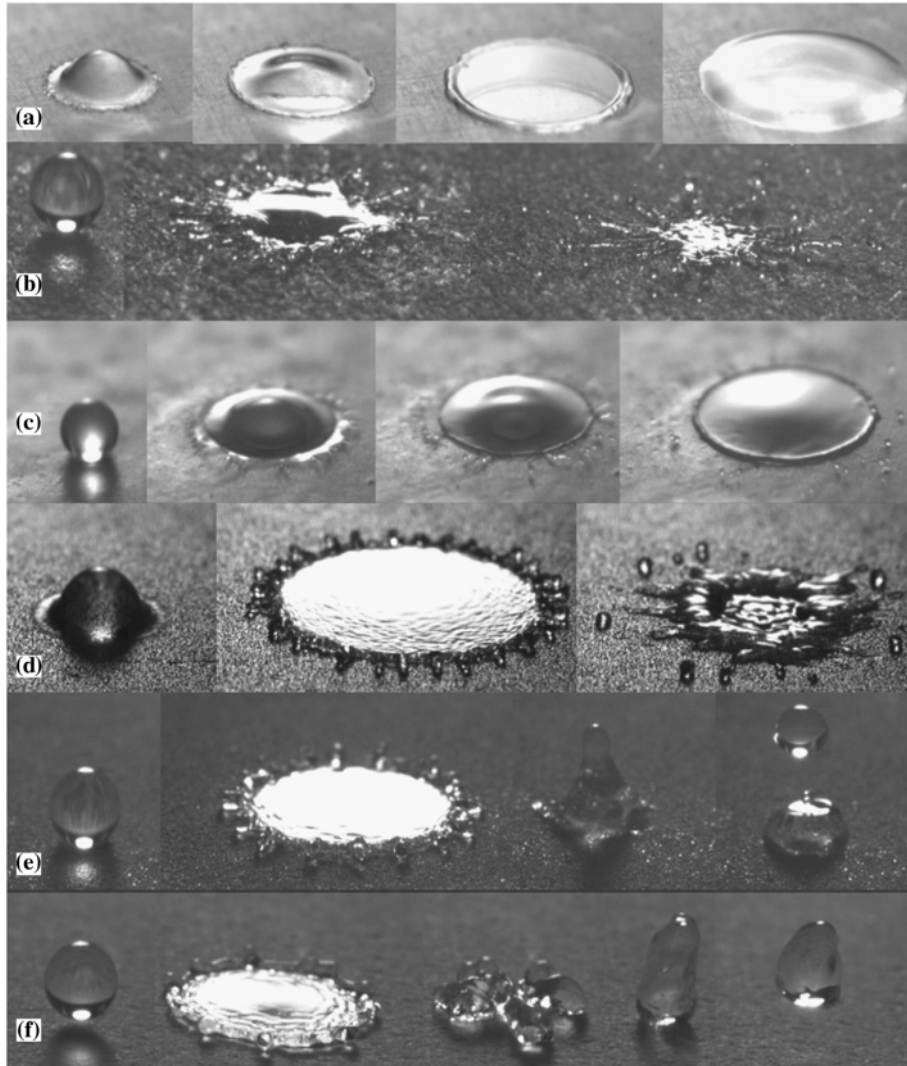
Figure 2.3: Outcomes of drop impact: (a) deposition (isopropanol on rough glass), (b) prompt splash (water on rough PE), (c) corona splash (isopropanol on rough ceramic), (d) receding breakup (water on porous stainless steel), (e) partial rebound (water on porous bronze) and (f) rebound (water on porous PTFE) (Marengo et al., 2011).

effect of viscosity has often been studied using water-glycerol mixtures. Scheller and Bousfield (1995), studying the effect of viscosity with different glycerol-water mixtures (μ from 1.0 to 300 mPa·s) on drop spreading on glass and polystyrene surfaces, found good agreement between measured maximum spreading and their semi-empirical model that considered viscosity by scaling with Reynolds and Ohnesorge numbers. Šikalo et al. (2002) investigated the effects of viscosity by using glycerol droplets and found no significant difference on the initial spreading phase but a decreased maximum spreading due to the effect of viscosity. Rioboo et al. (2002) looked at the time evolution of drop spreading for different liquids (water, silicone oil and glycerol) to understand the influence of wettability and roughness of surface and found that the influence of viscosity on spreading diameter increases with time. The maximum diameter is smaller and is reached earlier as viscosity increases. Bartolo et al. (2005) used glycerol-water mixtures on parafilm to demonstrate the existence of a transition between the capillary-inertial regime to the capillary-viscous regime of drop spreading. This transition is characterized by Ohnesorge number (Oh = 0.05) based on experiments and simple hydrodynamic models. They proposed a phase diagram delimiting four regions for spreading and retraction dynamics. Vadillo et al. (2009) studied the maximum droplet spreading of two glycerol-water mixtures compared with water and proposed to use the averaged dynamic contact angle to consider the influence of viscosity and surface tension on contact line during the spreading phase. For non-Newtonian blood, Laan et al. (2014) showed that the maximum spreading of a droplet of water-glycerol mixture, a surrogate of blood, on various surfaces is limited by high shear rate viscosity. Although it is known that increasing viscosity leads to slower spreading and small expansion due to high shear rate, the influence of viscous forces is not fully understood when also taking into account capillary forces in the evolution of spreading.

To understand the effect of surface tension, several studies used silicone oil (Kim and Chun, 2001; Rioboo et al., 2001; Rioboo et al., 2002), isopropanol (Šikalo et al., 2002), ethanol (Rioboo et al., 2001; Bayer and Megaridis, 2006) and surfactants (Crooks et al., 2001; Aytouna et al., 2009; Zhang and Basaran, 1997). Kim and Chun (2001) investigated the maximum spreading of different liquid droplets (water, ink and silicone oil) and proposed a modified analytical method to account for wetting and viscous effects. Rioboo et al. (2001) and Rioboo et al. (2002) studied the outcomes of drop impact and drop spreading with silicone oil droplets

to figure out the surface tension effects. Šikalo et al. (2002) showed that a droplet with low surface tension (isopropanol) splashes at small Reynolds and Weber number and spreads more than water with increasing impact velocity. Bayer and Megaridis (2006) used various liquids for a wide variation of contact angles and found that maximum spreading is insensitive to surface wettability defined by the equilibrium contact angle. Zhang and Basaran (1997) measured the maximum spreading of droplets of different concentrations of surfactant solution on a glass surface. They demonstrated that maximum spreading could be increased by the addition of surfactant to the droplet liquid at low impact velocity. Aytouna et al. (2009) also showed that maximum spreading increases for various surfactant solutions, which have lower surface tension. However, surfactant additives, commonly used in applications, are seen often to change the drop size distribution of sprays in an undesirable manner (Bartolo et al., 2007). In general, the effect of surface tension has been characterized with the contact angle of the deposited droplet. For instance, lower surface tension, which leads to smaller contact angle, makes that the surface is considered as hydrophilic. However, the surface energy due to surface tension is not fully known during spreading due to the complexity of the surface shape of a droplet. Although many studies have investigated the role of viscosity and surface tension on maximum spreading with various liquids, prediction models of maximum spreading considering evolution of spreading with viscosity and surface tension are still to be developed.

Several studies have investigated the effect of surface wettability on maximum spreading by varying the surfaces. In general, surface wettability is characterized by contact angle, resulting from intermolecular interactions and the balance of adhesive and cohesive forces. Collings et al. (1990) documented liquid metal spreading on copper, alumina and fused quartz surfaces and formulated a theoretical model taking into account the liquid/surface interaction. Pasandideh-Fard et al. (1996) measured drop impact on glass (equilibrium contact angle, $\theta_{eq} = 27°$) and beeswax ($\theta_{eq} = 111°$) surfaces. They showed good agreement on maximum spreading between experiments and numerical simulation, taking the measured dynamic contact angle into account. Also they proposed a theoretical model for maximum spreading applying the measured advancing contact angle as surface wettability. Mao et al. (1997) investigated the maximum spreading of water drop impact on paraffin wax ($\theta_{eq} = 97°$), stainless steel ($\theta_{eq} = 67°$) and glass ($\theta_{eq} = 37°$). They found that impact velocity

and liquid viscosity play an important role on maximum spreading, while viscosity and static contact angle play a dominant role in determining the tendency of a droplet to rebound. Ukiwe and Kwok (2004) studied drop impact on three different polymer surfaces of different solid-vapor surface tension. They reported that the drop impact dynamics is influenced by the impact energy of the drop and solid-vapor surface tension, which they measured. German and Bertola (2009) measured drop impact on parafilm and glass surface and reported that surface wettability does not appear to significantly influence the spreading phase. Vadillo et al. (2009) used nine different surfaces, treated to be hydrophilic to hydrophobic ($\theta_{eq} = 5°$ to 111°) with organic siloxanes molecules grafting, for drop impact tests. They introduced the averaged dynamic contact angle to estimate surface energy during spreading and showed good agreement between their measurements and a theoretical model taking account into surface wettability. Recently, Antonini et al. (2012) investigated maximum spreading on nine surfaces with different wettability. They used the advancing contact angle to characterize the wettability for spreading, and showed the increase of maximum spreading with respect to increasing advancing contact angle at lower Weber number. Although many studies have investigated the influence of surface wettability on drop impact, the role of wettability during spreading is still the object of discussion.

Early studies on the role of surface roughness on drop impact were conducted to describe the relationship of roughness with drop splashing (Engel, 1955; Stow and Hadfield, 1981; Mundo et al., 1995). Roughness, determined by arithmetic average roughness, R_a, was indeed found to promote drop splashing. Bussmann et al. (2000) investigated water drop impacting three different rough stainless steel surfaces, characterized by $R_a = 0.065, 0.16$ and 0.22 μm. The only effect noticed on drop impact was a gradual decrease of the number of fingers with increasing roughness at the beginning of spreading. Šikalo et al. (2002) compared maximum spreading on smooth ($R_a = 0.003$ μm) and rough ($R_a = 3.6$ μm) glass surfaces of impinging droplets. The smaller maximum spreading is found to be an effect of the larger advancing contact angle experienced on rough surface than the one on smooth surface. Kannan and Sivakumar (2008) investigated drop impact on rough surfaces using microgroove textured surfaces ($R_a = 0.2 - 0.37$ μm). They reported smaller maximum spreading on microgroove textures since the grooves offer more resistance to the spreading liquid. Vaikuntanathan et al. (2010) studied drop impact at the junction of a hydrophobic microgroove texture and a hydrophilic
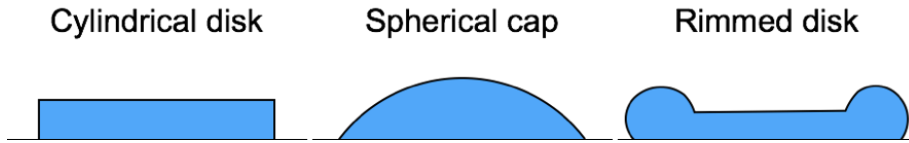
Figure 2.4: Models used in literature for the free surface shape of impacting drop at maximum spreading.

smooth surface. They showed that the spreading in the early phase is not affected on the texture of the substrates. However, no quantitative description of the role of surface roughness on spreading exists due to the difficulty of defining roughness and the lack of understanding of the contact line movement on complex rough surfaces.

2.1.2 *Theoretical models*

Many experimental studies propose and use theoretical models to support the physical understanding of the problem and to predict the drop impact characteristics, at asymptotic conditions, which cannot be achieved in experiments. Models, used in combination with experiments, can provide insights in the details of the flow field within the droplet, as such information is not attainable with measurements. Since Engel (1955) proposed an energy balance approach to predict the spreading diameter of drop impact taking kinetic, capillary and dissipation energies into account, many studies on the prediction for maximum spreading based on the energy balance approach followed. To do so, different shapes of the droplet during spreading have been assumed as shown in Figure 2.4.

Using a simplified cylindrical disk shape, Chandra and Avedisian (1991) formulated an energy balance equation for maximum spreading on hot flat surfaces. Pasandideh-Fard et al. (1996) suggested a prediction model for maximum spreading on a cool surface, taking into account the advancing contact angle and viscous boundary layer. Mao et al. (1997) and Ukiwe and Kwok (2004) proposed some modifications to the model of Pasandideh-Fard et al. (1996) by taking into account the lateral area of the cylinder disk. Mao et al. (1997) also proposed an empirical equation using the energy balance approach and a large amount of literature experimental data covering large domains for the We and Re numbers. Although good agreement was found between experiments in a wide range of impact parameter and the energy balance approach

(Roisman, 2009), this energy balance model had two problematic terms: (1) a viscous dissipation term integrated until the time of maximum spreading and (2) a surface energy term estimated by the contact angle as per Young's equation. Pasandideh-Fard et al. (1996) derived the time at maximum spreading $t_{\max} = (8/3) \cdot D_0 / V_i$ based on simple geometric assumptions. Vadillo et al. (2009) found disagreements between measured times at maximum spreading and times derived with the model of Pasandideh-Fard et al. (1996). Regarding the surface energy term, different contact angles have been considered such as the equilibrium contact angle (Bennett and Poulikakos, 1993; Mao et al., 1997), the contact angle at maximum spreading (Pasandideh-Fard et al., 1996; Lee and Lee, 2011), the advancing contact angle (Ukiwe and Kwok, 2004), the averaged advancing contact angle (Vadillo et al., 2009) and finally, in non-wetting conditions $\theta = 180°$ (Visser et al., 2012). Even though all these different contact angle approaches allow to quantify maximum spreading for some experiment cases, not one unified approach is applicable for various liquids and surfaces due to the difficulty of defining properly wettability during spreading.

Assuming a spherical cap, Bechtel et al. (1993) proposed the first energy balance approach based on such a shape. Starting from this work, Kim and Chun (2001) added a simple differential equation to describe the evolution of frictional dissipation in the truncated sphere shape. Finally, assuming a rimmed cylinder shape, Attané et al. (2007) proposed an additional dissipation mode due to the rolling motion in the rim. Although none of the models based on the energy balance approach can capture the various aspects of drop impact, the advantage of this approach is that the main physics of drop impact can be captured with a simple analytical or differential equation.

2.1.3 *Numerical simulations*

Numerous studies explored the possibilities offered by CFD simulations to look at drop impact. Several interface tracking approaches have been used: VOF (Sikalo et al., 2005; Strotos et al., 2011; Nikolopoulos et al., 2007) method, Solution Algorithm for Transient Fluid Flow with Multiple Free Boundaries (SOLA-VOF) (Pasandideh-Fard et al., 1996; Pasandideh-Fard et al., 1998; Pasandideh-Fard et al., 2001), Coupled Level Set/Volume-of-Fluid (CLSVOF) (Yokoi et al., 2009), level set (Caviezel et al., 2008; Griebel and Klitz, 2014). A comprehensive review

can be found in Malgarinos et al. (2014). One of the most challenging tasks in CFD simulation for drop impact is the correct prediction of the liquid-vapor interface at the line of contact with the surface. Thus, the implementation the contact angle as a boundary condition has been the main object of attention in CFD simulation of drop impact. Fukai et al. (1995) were the first to simulate drop impact with the contact angle as a boundary condition. Assuming that dynamic contact angle is independent of velocity, the measured advancing and receding contact angles were applied for spreading and receding phase, respectively. Pasandideh-Fard et al. (1996) compared the use of the constant equilibrium contact angle and the dynamic contact angle determined from experiment, and reported that the use of dynamic contact angle results in accurate prediction of drop spreading. Bussmann et al. (1999) determined the dynamic contact angle with stiched linear functions for advancing, equilibrium and receding contact angle in relation to velocity. Šikalo et al. (2005) used the Kistler model (Kistler, 1993) to describe the dynamic contact angle as function of contact line velocity, simulating the drop impact of water and glycerol droplets onto hydrophilic and hydrophobic surfaces. They showed that, with the Kistler model for dynamic contact angle, the droplet behavior during spreading and receding phases is better predicted than when using a fixed dynamic contact angle, either advancing or receding. Roisman et al. (2008) applied the dynamic contact angle as predicted by the Kistler model for simulating water drop impact on stainless steel. They used in the Kistler model, the advancing and receding contact angles instead of the equilibrium contact angle to consider the effect of contact angle hysteresis. Farhangi et al. (2012) used the approach of Roisman et al. (2008) to simulate the coalescence of droplets on superhydrophobic surfaces. In all these studies, the dynamic contact angle is an input to the CFD simulation as boundary condition at the contact line and the spreading is predicted and compared to the experiments. It is still not clear how this dynamic contact should be modelled and, more especially, it is not yet totally clear which contact angle has to be used as input to the dynamic contact model of Kistler.

2.2 DROP IMPACT ON POROUS MEDIA

Drop impact on porous media is expected to differ from the behavior observed on impermeable surfaces due to the surface roughness and the potential for liquid to penetrate or to be absorbed into the porous
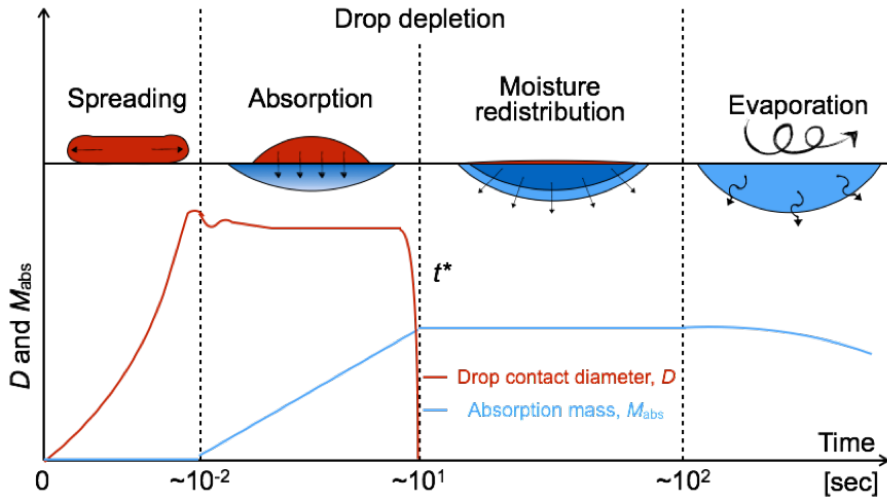
Figure 2.5: Schematic of fate of impinging droplet on porous media. Red line indicates drop spreading diameter D. Blue line is absorption mass M_{abs} in porous media.

media (Reis Jr. et al., 2008). After drop impact on a porous medium, the liquid droplet spreads over the porous surface and is absorbed into porous media by capillarity. The spreading of the impacting drop over the porous surface is governed by the same factors, i.e. impact condition (impact velocity, drop size), the properties of liquid (density, viscosity, surface tension), surface wettability and roughness as mentioned above, plus obviously absorption (Alam et al., 2007). Absorption of droplet on porous media is dependent on the properties of the liquid and the porous medium, such as porosity, pore size and connectivity and wettability in the pore (Hapgood et al., 2002). The absorption is also observed during droplet spreading over porous surface as summarized in the review of Gambaryan-Roisman (2014). Once the inertia of drop impact is dissipated, the capillary absorption of the deposited droplet into the porous medium continues until the liquid is depleted from surface. The absorbed liquid is further redistributed and also evaporates through the surface of the medium (Reis et al., 2003). Figure 2.5 illustrates the fate of a droplet at different time scales. In this section, first drop spreading on porous media is reviewed and then its absorption is discussed.

2.2.1 *Drop spreading on porous media*

The study of impacting drops spreading over porous media has received little attention compared to similar studies on impermeable surfaces, although such event is more commonplace and often plays an important role in several processes (Clarke et al., 2002). One of the first studies for drop impact on permeable surface was performed by Wallace and Yoshida (1978). They investigated the spread factor defined as the ratio between the initial drop diameter and the diameter of a stain on paper as function of the impact energy for pesticide spray application. Chandra and Avedisian (1992) compared drop impact on impermeable stainless steel surfaces and porous ceramic surfaces. They used the difference of volume before and after impact to estimate the volume absorbed into the ceramic substrate. Although such difference was measured to be between 12 to 15%, considering the time scale of maximum spreading (under 5 ms), the absorbed volume was finally neglected in their maximum spreading prediction. Previous work focused mainly on the depletion of the droplet from surface and the influence of governing parameters such as the properties of porous media (porosity, pore size) and liquid. However, there is little information about liquid (re)distribution inside the porous media.

In terms of computational work, Yu et al. (2008) and Reis Jr. et al. (2008) performed numerical simulations of drop impact on porous media with VOF method. Yu et al. (2008) compared the experimental results of the drop impact on heated porous media with simulation results. They investigated drop impact on porous media, without absorption into substrate due to the presence of a vapor layer on the porous substrate. Reis Jr. et al. (2004) and Reis Jr. et al. (2008) developed a numerical model to resolve the shape of the impacting drop on the surface and the liquid content distribution in the porous medium and performed a parametric study for impact condition, permeability, porosity, pore size and wettability. The simulated shape of droplet on surface agrees with what is seen in experiment. The simulated liquid content in the porous medium is compared with Magnetic Resonance Imaging (MRI) after full absorption and a good agreement is found with a shape similar to a half-spheroid whose aspect ratio depends on the porous media and liquid droplet characteristics (Reis Jr. et al., 2004). More recently, drop impact on granular media has been quite studied. Marston et al. (2010) studied the maximum droplet spreading diameter on packed glass beads

for different liquids, i.e. 50% ethanol-water mixture, ethanol, water and acetone droplet experimentally and reported that the maximum spreading scales with $\text{We}^{1/5}$. Katsuragi (2010) studied the size of craters in granular layers resulting from water drop impact. He assumed that the crater size is determined by the maximum spreading diameter of droplet and reported that the crater size scales with $\text{We}^{1/4}$, the same scaling proposed for smooth impermeable (no deformable) substrate by Clanet et al. (2004). Delon et al. (2011) also reported a $D_{\max}/D_0 \sim \text{We}^{1/4}$ scaling when studying water drop impact on sand substrates of different grain sizes. Nefzaoui and Skurtys (2012) reported that maximum droplet spreading on dry glass beads substrate scales with $\text{We}^{1/5}$ for water droplet and with We1/4 for liquids with higher surface tension. Zhao et al. (2015a) showed that crater size scales with impact energy on substrates of different grain sizes. Recently, Zhao et al. (2015b) measured the maximum crater depth and showed that maximum spreading for water drops impacting dry glass beads granular media scales with the effective Weber number defined by the maximum crater depth. Although several studies have investigated drop impact on porous media, the influence of porous media on spreading is still unknown due to the presence of simultaneous phenomena occuring, especially spreading and absorption, and due to the lack of knowledge of the contact line behavior on porous and rough surfaces. There is a clear need to properly quantify droplet spreading on porous media.

2.2.2 *Absorption into porous media*

The absorption of deposited droplets has been studied theoretically, experimentally and numerically. Davis and Hocking (1999) and Davis and Hocking (2000) studied spreading and imbibition of deposited droplets on porous media theoretically. To predict the depletion time of deposited droplets, they elaborated an analytical model that considered the contact line slip on the surface using the lubrication approximation. Clarke et al. (2002) showed the absorption of deposited droplet into microporous filter membranes by measuring the volume of deposited droplet remaining on the surface and proposed an analytical model using Lucas-Washburn equation derived from Darcy's law. Lucas-Washburn equation is used when saturated flow is assumed (Hapgood et al., 2002; Clarke et al., 2002; Alleborn and Raszillier, 2004). Hapgood et al. (2002) investigated experimentally absorption on various powder bed substrates to measure the depletion time of deposited droplets, and compared the experimental

results with an analytical model from Denesuk et al. (1993) by taking the measured pore size and wetting properties of the powder bed substrates into account. However, several studies showed evidence of unsaturated flow in porous media experimentally (Reis et al., 2003; George W Wagner et al., 2004; D'Onofrio et al., 2010; Ben Jazia et al., 2011; Jung et al., 2012) and numerically (Reis Jr. et al., 2004; Markicevic et al., 2009; Navaz et al., 2008; Willis et al., 2011). Ben Jazia et al. (2011) showed the deviations from the expected square root time-dependence characterizing the imbibition in the Darcy's regime with experiments of drop absorption into hydrophilic nanoporous media formed by polystyrene microbeads assemblies. They calculated the absorption volume from the drop volume remaining on the surface with the spherical cap approximation. Markicevic and Navaz (2010) showed numerically the transition between fully and partially saturated moisture content during droplet absorption. These previous works have focused on absorption mass and depletion time to understand absorption behavior as they had no information on liquid transport inside porous media.

For a better understanding of the absorption process inside porous media, the direct observation of the liquid content redistribution in the porous medium is required. Absorption in porous media has been studied with non-destructive techniques (X-ray, neutron and gamma-ray radiography, MRI, and Nuclear Magnetic Resonance (NMR)) and destructive techniques. Reis Jr. et al. (2006) used a MRI measurement (temporal resolution 3.2 min, spatial resolution 78 μm) to investigate the evaporation of the droplets in glass beads substrates. They showed that the general shape of liquid redistributed within the porous media resembles a half spheroid and compared with the CFD numerical simulation. Jung et al. (2012) observed the absorption of impinging droplet with X-ray radiography (temporal resolution 6.4 s, spatial resolution 9 μm). They documented the migration of the moisture front inside packed sand sample and distinguished two water migration regions: a region influenced by inertia and a region where inertia does not play a role, based on velocity of the moisture front. D'Onofrio et al. (2010) measured the penetration depth of a nerve warfare agent (VX) sessile droplet into sand using a container of varying depth with detector paper on its bottom to measure the time when liquid reaches the bottom. They showed a good agreement between numerical simulation using continuum model and their experiments. However, these previous NMR or X-ray studies have

low temporal and spatial resolutions to capture the absorption process of a droplet in a porous medium in sufficient detail.

2.3 NEEDS FOR FURTHER RESEARCH

This state of the art identifies clear gaps in the understanding of drop impact on impermeable surfaces and on porous media. Although numerous experimental data are already available in the literature, full characterization of the effect of the liquid properties (surface tension, viscosity), surface properties (wettability, roughness) on drop impact and evolution, especially at lower impact velocities, is still to be achieved. Theoretical modeling of maximum spreading for drop impact on impermeable surface has attained a certain level of reliability, although there is still no complete agreement on the estimation of viscous dissipation and boundary layer height in the droplet, the time at maximum spreading and the dynamic wetting behavior as characterized by the dynamic contact angle during spreading. Moreover, scaling approaches for maximum spreading diameter have to be enhanced considering dynamic wettability and roughness for especially low impact velocity where surface properties play a more dominant role. In numerical simulation of drop impact, especially using the VOF method, the use of dynamic contact angle is found to be very important so that the temporal evolution of phenomena can be captured more accurately.

In the literature, there is a dearth of experimental data for drop impact on porous media. Most of previous studies have investigated drop impact on isotropic porous structure, although in general porous media have an anisotropic porous structure. In absorption studies, the experimental techniques used imposed serious limits on the amount of information obtained concerning the behavior inside the porous media. It is extremely challenging to experimentally resolve the full process of absorption. The intension of this thesis is to capture the full process of drop impact and absorption on natural porous stones by comparing with the drop impact behavior on impermeable surfaces and porous media, the mechanism of drop spreading on porous media will be analyzed. In addition, the wetting process by impacting of several droplets on porous media along with absorption will be presented. The absorption process inside porous media will be captured by different experimental techniques. This thesis aims at providing a fully integrated experimental dataset for drop impact on impermeable surfaces and porous media, which is

then used to tackle some remaining problems on theoretical modeling and numerical simulations, with a special focus on the process of drop spreading and absorption into porous media.

GOVERNING EQUATIONS AND COMPUTATIONAL DETAILS

In this chapter, state-of-the-art models for the prediction of the maximum spreading based on the energy balance approach are described. The method is based on energy terms involved in drop impact and adequate equations to describe these terms are introduced. Based on these equations, different models for maximum spreading developed are presented. The first part of this chapter is devoted to the overview of these energy balance approaches. In a second part of this chapter, the computational methods used in this thesis to simulate drop impact on a solid surface are shortly described: Computational Fluid Dynamics (CFD) and Volume-of-Fluid (VOF).

3.1 ENERGY BALANCE APPROACH FOR MAXIMUM SPREADING
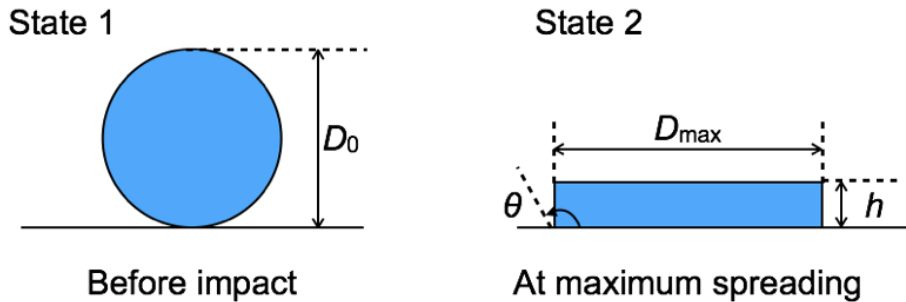
Figure 3.1: Schematics of a liquid droplet before impact (State 1) and the shape at maximum spreading (State 2).

The maximum spreading ratio $\beta_{\max} = D_{\max}/D_0$ can be obtained from an energy balance before impact and at maximum spreading. Before impact (see Figure 3.1), the kinetic energy (KE_1) and surface energy (SE_1) of the spherical droplet are given by:

$$\mathrm{KE}_1 = \frac{1}{2}mV_{\mathrm{i}}^2 = \frac{1}{2}\left(\frac{4}{3}\pi\left(\frac{D_0}{2}\right)^3\right)\rho V_{\mathrm{i}}^2 = \frac{\pi}{12}D_0^3\rho V_{\mathrm{i}}^2 \qquad (3.1)$$

$$\text{SE}_1 = \pi D_0^2 \gamma_{\text{LV}} \tag{3.2}$$

where m is the droplet mass, V_i is the impact velocity, is the liquid density and γ_{LV} is interfacial tension between the liquid and vapor phases. After impact, when the droplet is at its maximum spreading diameter D_{max} (State 2 in Figure 3.1), the kinetic energy (KE_2) is assumed to have decreased to zero and the surface energy (SE_2) is given by:

$$\text{SE}_2 = S_{\text{LV}} \cdot \gamma_{\text{LV}} + S_{\text{SL}} \cdot (\gamma_{\text{SL}} - \gamma_{\text{SV}}) \tag{3.3}$$

where S_{LV} and S_{SL} are interfacial surface areas between liquid-vapor and solid-liquid, respectively. If we assume that the shape of maximum spreading drop is a cylindrical disk, e.g. similar to a pancake, SE_2 is:

$$\text{SE}_2 = \left(\frac{\pi}{4} D_{\text{max}}^2 + \pi D_{\text{max}} h \right) \cdot \gamma_{\text{LV}} + \frac{\pi}{4} D_{\text{max}}^2 \cdot (\gamma_{\text{SL}} - \gamma_{\text{SV}}) \tag{3.4}$$

where $h = (2/3) \cdot (D_0^3 / D_{\text{max}}^2)$ is the height of the pancake as derived from mass conservation between spherical drop and pancake. The interfacial tension for solid-liquid and solid-vapor is estimated by Young's equation ($\gamma_{\text{SV}} = \gamma_{\text{SL}} + \gamma_{\text{LV}} \cos \theta$). SE_2 then becomes:

$$\text{SE}_2 = \frac{\pi}{4} D_{\text{max}}^2 \cdot \gamma_{\text{LV}} (1 - \cos \theta) + \pi D_{\text{max}} h \gamma_{\text{LV}} \tag{3.5}$$

or

$$\text{SE}_2 = \frac{\pi}{4} D_{\text{max}}^2 \cdot \Gamma + \frac{2\pi}{3} \left(\frac{D_0^3}{D_{\text{max}}} \right) \cdot \gamma_{\text{LV}} \tag{3.6}$$

with

$$\Gamma = \gamma_{\text{LV}} (1 - \cos \theta) \tag{3.7}$$

where Γ is referred to as the effective surface energy. The energy lost due to viscosity in deforming the droplet is:

$$\text{W} = \int_0^{t_{\text{max}}} \int_{\Omega} \phi d\Omega dt \approx \phi \Omega t_{\text{max}} \tag{3.8}$$

where Ω is the volume where viscous dissipation occurs and t_{max} is the time at maximum spreading (state 2). The dissipation function is given by (Pasandideh-Fard et al., 1996):

$$\phi = \mu \left(\frac{\partial \mathbf{U}_x}{\partial y} + \frac{\partial \mathbf{U}_y}{\partial x} \right) \frac{\partial \mathbf{U}_x}{\partial y} \approx \mu \left(\frac{V_i}{L} \right)^2 \tag{3.9}$$

where μ is the liquid viscosity and L is a characteristic length.

The energy balance in droplet between two states is:

$$\mathrm{KE}_1 + \mathrm{SE}_1 = \mathrm{SE}_2 + \mathrm{W} \tag{3.10}$$

To solve this equation, different assumptions have been proposed in the literature concerning:

A. Interfacial area at state 2, S_{LV}

   1. Neglecting lateral sides of the pancake (Chandra and Avedisian, 1992; Pasandideh-Fard et al., 1996)

   2. Including lateral sides of the pancake (Mao et al., 1997; Ukiwe and Kwok, 2004)

B. Characteristic length L equal to:

   1. The height of pancake h (Chandra and Avedisian, 1992)

   2. The boundary layer thickness δ (Pasandideh-Fard et al., 1996; Mao et al., 1997; Ukiwe and Kwok, 2004)

C. Time at maximum spreading $t_{\max}$

   1. $t_{\max} = D_{\max}/V_i$ Chandra and Avedisian, 1992

   2. Geometical flow assumption $t_{\max} = (8/3) \cdot (D_0/V_i)$ (Pasandideh-Fard et al., 1996; Mao et al., 1997; Ukiwe and Kwok, 2004)

D. Contact angle θ:

   1. Equilibrium contact angle (Bennett and Poulikakos, 1993; Mao et al., 1997)

   2. Advancing contact angle (Ukiwe and Kwok, 2004)

   3. Contact angle at maximum spreading (Lee and Lee, 2011)

   4. Averaged spreading contact angle (Vadillo et al., 2009)

   5. Non-wetting contact angle $\theta = 180°$ (Visser et al., 2012)

In case where capillary forces can be neglected (e.g. low surface tension), the energy balance can be formulated solely with kinetic energy (KE_1) and viscous dissipation (W) as:

$$KE_1 = W \tag{3.11}$$

If the characteristic length L in Eq. 3.9 is assumed to be the height of pancake h, and the time at maximum spreading is approximated by $t_{max} \approx D_{max}/V_i$, the scaling for maximum spreading is given by (Chandra and Avedisian, 1992; Clanet et al., 2004):

$$\beta_{max} \sim Re^{1/5} \tag{3.12}$$

In case where capillary forces play an important role during spreading, the kinetic energy can be equated to the surface energy at maximum spreading neglecting viscous dissipation (W) and initial surface energy (SE_1) (Collings et al., 1990). The energy balance is then given by:

$$KE_1 = SE_2 \tag{3.13}$$

The maximum spreading ratio then scales as:

$$\beta_{max} \sim We^{1/2} \tag{3.14}$$

On the other hand, based on momentum conservation approach (Clanet et al., 2004) the maximum spreading ratio can then be scaled as:

$$\beta_{max} \sim We^{1/4} \tag{3.15}$$

Asymptotic scaling approaches can be also derived from an energy balance where the boundary layer height equals the depth to which momentum can diffuse on the time scale of drop motion:

$$\delta = \sqrt{cD_\mu \cdot t_{max}} \tag{3.16}$$

where $D_\mu = \mu/\rho$ is the transverse momentum diffusion constant and c is a constant. The viscous dissipation then becomes:

$$W = \frac{\pi}{4}\rho V_{max}^2 D_0 D_{max}^2 \cdot \frac{\Delta}{c} \tag{3.17}$$

with the non-dimensional boundary thickness Δ given by:

$$\Delta = \delta/D_0 \tag{3.18}$$

24

Using Eqs. 3.1, 3.2, 3.6 in the energy balance equation (Eq. 3.10) and multiplying with $12/(\pi D_0^2)$ gives:

$$\rho V_i^2 D_0 + 12\gamma_{LV} = 3\Gamma\beta_{max}^2 + 8\gamma_{LV}\frac{1}{\beta_{max}} + \frac{12}{\pi D_0^2}W \tag{3.19}$$

Mao et al. (1997) and Ukiwe and Kwok (2004) assumed that the characteristic length equals the boundary layer thickness $\delta = 2D_0/\sqrt{Re}$, as originally proposed by Pasandideh-Fard et al. (1996). They also assumed the time at maximum spreading t_{max} to be equal to $t_{max} = (8/3)\cdot(D_0/V_i)$ based on the assumption that the spherical drop spreads into a cylindrical disk. Note that when using Eq. 3.16 with $c = 3/2$, the boundary layer thickness is:

$$\delta = \sqrt{\frac{3}{2}\frac{\mu}{\rho}\frac{8}{3}\frac{D_0}{V_i}} = 2\frac{D_0}{\sqrt{Re}} \tag{3.20}$$

as proposed by Pasandideh-Fard et al. (1996), or

$$\Delta = \frac{2}{\sqrt{Re}} \tag{3.21}$$

Then, the balance equation (Eq. 3.19) becomes:

$$\rho V_i^2 D_0 + 12\gamma_{LV} = 3\Gamma\beta_{max}^2 + 8\gamma_{LV}\frac{1}{\beta_{max}} + 2\rho V_i^2 D_0\beta_{max}^2\Delta \tag{3.22}$$

or

$$\beta_{max}^2 = \frac{12\gamma_{LV} + \rho V_i^2 D_0}{3\Gamma + 2\rho V_i^2 D_0\Delta} - \frac{8\gamma_{LV}}{3\Gamma + 2\rho V_i^2 D_0\Delta}\cdot\frac{1}{\beta_{max}} \tag{3.23}$$

From Eq. 3.23 at the limit $V_i = 0$:

$$\beta_{max}^2 = \frac{4\gamma_{LV}}{\Gamma}\left(1 - \frac{2}{3\beta_{max}}\right) \tag{3.24}$$

From Eq. 3.23 at large V_i ($V_i \to$ inf.), the equation is:

$$\beta_{max}^2 = \frac{1}{2\Delta} = \frac{\sqrt{Re}}{4} \tag{3.25}$$

or

$$\beta_{max} \sim Re^{1/4} \tag{3.26}$$

Pasandideh-Fard et al. (1996) proposed a model similar to Eq. 3.26 in viscous regime.

The derivation of Eq. 3.23 is based on the assumption that the substrate is non-porous or $\Phi = 0$. Assuming however that the droplet is in the Cassie-Baxter state on a porous substrate, the surface tension energy at maximum spreading reads $SE_2 = S_1 \cdot \gamma_{LV} + S_2 \cdot (\gamma_{SL} - \gamma_{SV})(1 - \Phi) + S_2 \cdot \gamma_{LV}\Phi$, where S_1 is the surface between droplet and surrounding air and S_2 is the contact area droplet–substrate. If we once more assume that the shape of maximum spreading drop is a cylindrical disk on the porous medium, SE_2 becomes:

$$SE_2 = \frac{\pi}{4}D_{max}^2\gamma_{LV} + \frac{\pi}{4}D_{max}^2(\gamma_{SL} - \gamma_{SV})(1 - \Phi)$$
$$+ \frac{\pi}{4}D_{max}^2 \cdot \Phi + \pi D_{max}h\gamma_{LV} \tag{3.27}$$

and the Eq. 3.22 becomes:

$$\beta_{max}^2 = \frac{12\gamma_{LV} + \rho V_i^2 D_0}{3\Psi + 2\rho V_i^2 D_0 \Delta} - \frac{8\gamma_{LV}}{3\Psi + 2\rho V_i^2 D_0 \Delta} \cdot \frac{1}{\beta_{max}} \tag{3.28}$$

with

$$\Psi = \gamma_{LV}((1 + \Phi) - (1 - \Phi)\cos\theta) \tag{3.29}$$

This leads to a modification of Eq. 3.24 at the limit $V_i = 0$:

$$\beta_{max}^2 = \frac{4\gamma_{LV}}{\Psi}\left(1 - \frac{2}{3\beta_{max}}\right) \tag{3.30}$$

3.1.1 *New model developed in this thesis*

In this thesis, the equations of the energy balance approach are carefully validated using own measured data measured and results of detailed CFD-VOF simulations. Based on this comparison, some modifications to the Pansandideh-Fard model are proposed. The major improvement lies in the current modelling of the time at maximum spreading, $t_{max} = (8/3) \cdot (D_0/V_i)$, which is found to depend also on the surface tension of the fluid. Therefore, it is logical to assume that the time at maximum spreading equals:

$$t_{max} = b\frac{D_{max}}{V_i} \tag{3.31}$$

where b is a constant. The boundary layer thickness then becomes according to Eq. 3.16:

$$\delta = \sqrt{c\frac{\mu}{\rho}b\frac{D_{\max}}{V_{\mathrm{i}}}} = \sqrt{cb}\frac{\sqrt{D_0}}{\sqrt{\mathrm{Re}}}\sqrt{D_{\max}} \tag{3.32}$$

or

$$\Delta = \sqrt{cb}\frac{1}{\sqrt{\mathrm{Re}}}\sqrt{\beta_{\max}} \tag{3.33}$$

The balance equation (Eq. 3.19) then becomes:

$$\begin{aligned}
\rho V_{\mathrm{i}}^2 D_0 + 12\gamma_{\mathrm{LV}} \quad = \quad & 3\Gamma\beta_{\max}^2 + 8\gamma_{\mathrm{LV}}\frac{1}{\beta_{\max}} \\
& + 3\rho V_{\mathrm{i}}^2 D_0 \beta_{\max}^{5/2}\frac{1}{\sqrt{\mathrm{Re}}}\sqrt{\frac{b}{c}}
\end{aligned} \tag{3.34}$$

From Eq. 3.34 at the limit $V_{\mathrm{i}} = 0$:

$$\beta_{\max}^2 = \frac{4\gamma_{\mathrm{LV}}}{\Gamma}\left(1 - \frac{2}{3\beta_{\max}}\right) \tag{3.35}$$

which is equivalent to Eq. 3.24.
From Eq. 3.30 at large V_{i} ($V_{\mathrm{i}} \to \inf.$):

$$\beta_{\max}^{5/2} = \sqrt{\frac{c}{9b}}\sqrt{\mathrm{Re}} \tag{3.36}$$

or

$$\beta_{\max} \sim \mathrm{Re}^{1/5} \tag{3.37}$$

Finally, other works which use a scaling based on the energy balance approach are mentioned for completeness. In the capillary (low impact velocity) limit, where kinetic energy is totally transformed into capillary energy, the maximum spreading ratio scales as $\beta_{\max} \sim \mathrm{We}^{1/2}$ (Madejski, 1976; Collings et al., 1990; Bennett and Poulikakos, 1993). In the viscous limit, the kinetic energy is totally transformed into viscous energy and the maximum spreading ratio scales as $\beta_{\max} \sim \mathrm{Re}^{1/4}$ or $\mathrm{Re}^{1/5}$ (Madejski, 1976; Chandra and Avedisian, 1992).

3.2 CFD SIMULATION FOR DROP IMPACT

3.2.1 *VOF method for two-phase flow*

The numerical simulation of the droplet impact is performed using the Volume-of-Fluid (VOF) method for Newtonian and incompressible two-phase flow with free surface. The governing equations include the mixture, continuity and momentum equations:

$$\nabla \cdot \mathbf{U} = 0 \tag{3.38}$$

$$\frac{\partial f}{\partial t} + \nabla \cdot (\mathbf{U}f) = 0 \tag{3.39}$$

$$
\begin{aligned}
\frac{\partial(\rho\mathbf{U})}{\partial t} + \nabla \cdot (\rho\mathbf{U}\mathbf{U}) = \\
- \nabla p^* + \nabla \cdot (\mu \cdot \nabla \mathbf{U}) + (\nabla \mathbf{U}) \cdot \nabla\mu \\
- g \cdot \mathbf{x}\nabla\rho + \gamma\kappa\nabla f
\end{aligned}
\tag{3.40}
$$

where f is the indicator function for the phase fraction, $\mathbf{U}$ the velocity vector, t the time, $\mathbf{x}$ the coordinate vector, $p^* = p - \rho g \cdot \mathbf{x}$ the modified pressure, γ the surface tension, κ the curvature of the interface. The indicator function f represents the volume fraction of each phase and is defined as:

$$
f = \begin{cases}
0, & \text{for points belonging to gas phase} \\
0 < f < 1 & \text{for points at the phase interface} \\
1 & \text{for points belonging to liquid phase}
\end{cases}
\tag{3.41}
$$

The two immiscible fluids are considered as one effective fluid with physical properties of the mixture calculated as weighted averages:

$$
\begin{aligned}
\rho &= f\rho_l + (1 - f)\rho_g \\
\mu &= f\mu_l + (1 - f)\mu_g
\end{aligned}
\tag{3.42}
$$

A critical aspect in numerical simulation using VOF is the treatment of the sharp interface between the two phases. In this study, the compression term in Eq. 3.39 is discretized for the volume fraction equation with a

bounded compression scheme, which facilitates the simulation of a sharp interface:

$$\frac{\partial f}{\partial t} + (\mathbf{U} \cdot \nabla)f + \nabla \cdot (\mathbf{U}_c f(1 - f)) = 0 \tag{3.43}$$

where $\mathbf{U}_c = \mathbf{U}_l - \mathbf{U}_g$ is the liquid-gas relative velocity vector given by:

$$\mathbf{U}_c = k_c n \max \frac{|n \cdot \mathbf{U}|}{|\mathbf{S}|^2} \tag{3.44}$$

where k_c is a coefficient used to adjust the amount of compression and $\mathbf{S}$ is the vector normal to the surface. In the computational model, $k_c = 1.5$ is used which was shown by Farhangi et al. (2012) to provide sharp interfaces for drop impact. The unit normal flux at cell faces in the interface region n is computed taking the gradient of phase fraction at the cell faces:

$$n = \frac{(\nabla f)_{\mathrm{f}}}{|\nabla f|_{\mathrm{f}} + \delta} \tag{3.45}$$

where δ is a small number in order to stabilize the calculation in regions outside the transition region where . In this study, $\delta = 10^{-8}$ is used. The artificial compressive term is active only near the interface due to the term $f(1 - f)$. The Continuum Surface Force (CSF) method is used to implement the surface tension force as a body force in the flow model.

The equations are solved using the numerical code OpenFOAM. Every new calculation step, the time step is adjusted to meet the specified maximum courant number (Co = 0.2) and the phase fraction equation is solved. The fluid properties are updated from the pressures, using the PISO algorithm (Pressure Implicit with Splitting of Operators) for momentum-pressure coupling. The momentum equation is solved and volumetric fluxes are obtained from the first approximation of the velocities. Using these fluxes, the pressure equation is solved. This step is followed by correcting the fluxes and explicitly reconstructing the velocities, based on the obtained pressure.

Figure 3.2 shows the axisymmetric wedge computational domain, discretized as a 2D-mesh with one cell in azimuthal direction (wedge angle = 2°). The dimensions of the computational domain are 7 mm × 5 mm (width, x and height, y). The mesh is fixed in space (total cell number is less than 670 000) and the smallest cell length is about 5 µm. The numerical grid used in this study is confirmed with the grid dependence
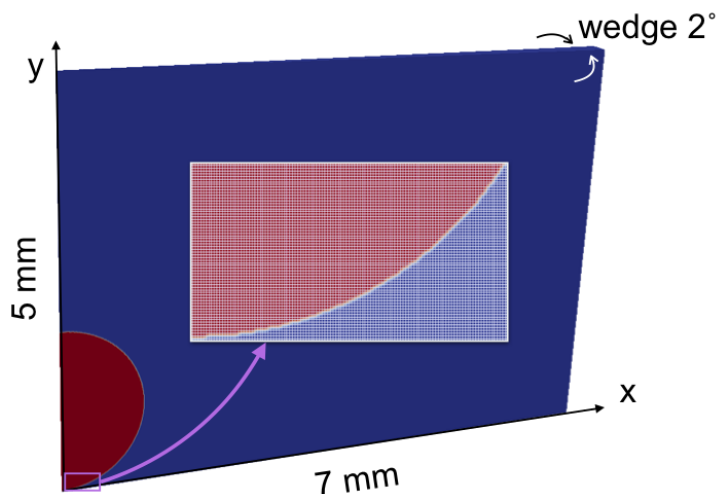
Figure 3.2: Numerical grid used for the computations, showing initial configuration and the wedge domain for axi-symmetric.

test (the finest grid used had 2 668 920 cells with a minimum size of 2.5 μm), it is found to be sufficiently fine for parametric studies of drop impact to capture the spreading diameter, yielding an estimated error smaller than 1%.

At the symmetry line in the axisymmetric model, a free-slip and no-penetration boundary condition is applied. The boundary conditions at top and the right side are formulated using combined inlet-outlet boundary conditions for velocity and a prescribed total pressure. The bottom boundary is set as a no-slip condition.

3.2.2 *Dynamic contact angle model*

In the numerical simulation, the dynamic contact angle is assumed to be a function of the contact line velocity using the relation proposed by Kistler (1993). To avoid confusion with the experimental dynamic contact angle, the subscript sim is used for this contact angle, $\theta_{D,sim}$. The dynamic contact angle is calculated for each time step as following:

$$\theta_{D,sim} = f_H \left(Ca + f_H^{-1}(\theta_k) \right) \qquad (3.46)$$

where f_H is the Hoffman's function:

$$f_{\mathrm{H}}(x) = \arccos\left\{1 - 2\tanh\left[5.16\left(\frac{1}{1 + 1.31 x^{0.99}}\right)\right]^{0.706}\right\} \tag{3.47}$$

and Ca is the capillary number

$$\mathrm{Ca} = \frac{\mu V_{\mathrm{CL}}}{\gamma} \tag{3.48}$$

where V_{CL} is the contact line velocity which is approximated using the velocity at the interface in the first computational point above the wall. The input contact angle in the original Kistler model θ_k in Eq. 3.46 equals the equilibrium contact angle for a smooth surface. In this study, the input contact angle θ_k in Eq. 3.46 is proposed to equal the dynamic contact angle during spreading phase ($V_{\mathrm{CL}} > 0$), as measured experimentally at maximum spreading $\theta_{\mathrm{D}}(t_{\mathrm{max}})$, in order to consider dynamic effects during spreading. The dynamic contact angle $\theta_{\mathrm{D,sim}}$, for the receding phase ($V_{\mathrm{CL}} < 0$) is estimated using the measured receding contact angle in Eq. 3.46. When the droplet is in equilibrium state and the contact line does not move ($V_{\mathrm{CL}} = 0$), the dynamic contact angle $\theta_{\mathrm{D,sim}}$ equals the measured equilibrium contact angle.

3.2.3 *Kinetic energy and viscous dissipation*

In the CFD-VOF studies, the change of initial surface energy, kinetic energy and transformation in viscous dissipation energy can be determined and analyzed. These terms are calculated as follows: The kinetic energy per unit volume in droplet is given by:

$$\mathrm{KE} = \frac{1}{2}\rho \cdot |\mathbf{U}|^2 \tag{3.49}$$

The viscous dissipation function is defined as (Qian et al., 2006):

$$\phi = \frac{\mu}{2}\left(\frac{\partial \mathbf{U}_y}{\partial x} + \frac{\partial \mathbf{U}_x}{\partial y}\right)^2 \tag{3.50}$$

The energy by viscous dissipation during spreading that occurs within an impacting drop is(Chandra and Avedisian, 1991):

$$\mathrm{W}_{\mathrm{vis}} = \int_0^t \int_\Omega \phi \, d\Omega \, dt \tag{3.51}$$

where Ω is the volume where viscous dissipation occurs and t is the time from impact. The surface energy at a time t is calculated as the difference between the initial energy before impact E_1 at $t = 0$ and the kinetic energy $KE(t)$ plus viscous dissipation energy $W_{vis}(t)$ at time t, or $SE(t) = E_1 - (KE(t) + W_{vis}(t))$. The initial energy E_1 equals the sum of initial kinetic energy and surface energy just before impact.

3.3 CONCLUSION

In this chapter, different models for the prediction of the maximum spreading ratio based on the energy balance approach are formulated. These models compare the kinetic energy and surface tension energy before impact, and the surface tension energy and cumulative viscous dissipation at maximum spreading. The models allow to formulate different scaling laws for the maximum spreading ratio at low and high impact velocity. These scaling laws and predictions by energy balance models will be validated in this thesis based on an extensive database of drop impact measurements. Also, in this thesis, a new energy balance model is proposed which major improvement lies in the accurate modelling of the time at maximum spreading. In the second part of the chapter, the computational approach using CFD-VOF is documented including geometry, boundary conditions, mesh and solution method. Special attention is given to the prediction of the dynamic contact angle, which is based on the Kistler model.

4

PROPERTIES OF DROPLET AND SUBSTRATES

This chapter describes the properties of the liquids and substrates used in the drop impact experiments. Liquids of different surface tension and viscosity are selected in order to document the spreading behavior in both the capillary and viscous regimes. The impermeable and permeable substrates are studied to further understand the influence of substrates on the dynamics of drop impact and, more specifically, the influence of their wetting behavior, the morphology of their surface, and, for the porous substrates, the effects of porosity and capillary uptake characteristics.

4.1 LIQUID DROPLET CHARACTERISTICS

The five liquids selected have surface tension and viscosity properties different from the ones of deionized water, used as reference, as listed in Table 4.1. For low surface tension, pure ethanol (absolute $\geq 99.8\%$, SIGMA-ALDRICH) is used. To vary viscosity, glycerol-water mixtures, with glycerol ($\geq 99\%$, SIGMA-ALDRICH) and water are used to produce glycerol 6, 10 and 51 mPa·s. The density ρ, surface tension γ and viscosity μ of glycerol-water mixture are determined with an empirical formula (Cheng, 2008). Liquid droplets are generated by means of the pendant method. The liquid is dispensed with an injection system which consists of a flat-tipped metal hub needle (Gauge 33 for water and glycerol, 27

Table 4.1: Properties of liquid at 25°C

	Density (kg/m^3)	Surface tension (mN/m)	Viscosity $(mPa \cdot s)$
Ethanol	789	23.2	1.2
Water	998	72.8	1.0
Glycerol 6 mPa·s	1124	66.3	6.6
Glycerol 10 mPa·s	1158	68.2	10.0
Glycerol 51 mPa·s	1204	65.2	51.0

for ethanol, HAMILTON) and a syringe pump (NE-1000, NewEra). The syringe pump pushed the liquid at the rate of 20 μl/min though the needle until a droplet detaches. The drop generation occurs when the droplet mass exceeds the capillary force that holds it at the end of the needle (Tate's law) (Gennes et al., 2004). The capillary force is equal to $\pi D_{NI} \gamma$, where D_{NI} is the inner diameter of the needle. At detachment from the needle, the droplet stretches, a neck forms and gets distended, so that, in the end, only a fraction, α, of the original volume breaks off (α is typically about 60%). Empirically, the droplet diameter can be found from balancing capillary force and the droplet mass:

$$D_0 = \left(\frac{6}{\alpha} \kappa^{-2} D_{NI} \right)^{1/3} \tag{4.1}$$

where $\kappa^{-1} = \gamma / \rho g$ is the capillary length. The inner diameters of the gauge 33 and 27 needles are 0.11 and 0.21 mm, respectively. The initial diameter D_0 of the generated droplet is measured with high-speed camera imaging and the mass of the droplet with high precision microbalance (ML304T, METTLER TOLEDO) as reported in Table 4.2. The initial drop size is measured for every drop impact test. The error of D_0 reported in Table 4.2 is the standard deviation over several thousands of drop impact tests. The mass of the droplet is measured 10 times for each liquid and needle size. The droplet generation in this study is remarkably reproducible.

The generated droplet is accelerated by gravity reaching an impact velocity, V_i. By varying the release height, H, from 3 to 820 mm, the impact velocity ranges between 0.2 and 3.7 m/s. The impact velocity is determined with high-speed camera images as shown in Figure 4.1a. The center position of droplets is determined on 10 images (different color

Table 4.2: Initial drop size

	Gauge	Initial drop diameter D_0 (mm)	Weight of droplet (mg)
Ethanol	27	1.84 ± 0.02	2.6 ± 0.1
	26	1.99 ± 0.02	3.2 ± 0.1
Water	33	2.01 ± 0.02	4.3 ± 0.1
Glycerol 10 mPa·s	33	1.86 ± 0.03	4.0 ± 0.1

circles represent the position of droplet over time) before impact. The circles are fitted using a custom-made image analysis MATLAB code. The time derivative of the calculated center position is fitted with a linear line which slope gives the velocity at the moment of impact (Figure 4.1b). Each liquid/needle/height combination is tested more than 10 times (for $H = 13, 51, 204$ and 460 mm corresponding to impact velocity $V_i = 0.5$, $1.0, 2.0$ and 3.0 m/s). The relative error of impact velocity measurements is within 2%, based on the standard deviation of all measurements.

(a) Detection of impinging droplet over one millisecond by fitting a circle

(b) Time derivative of droplet center displacement just before impact
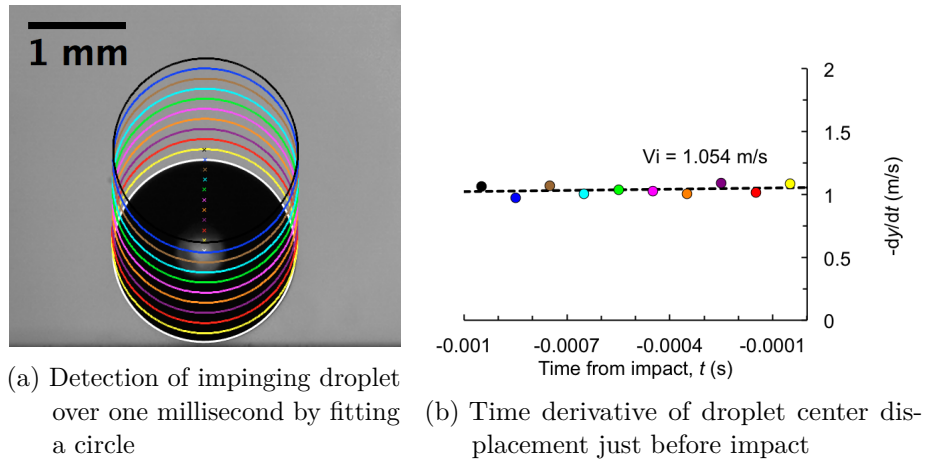
Figure 4.1: Determination of impact velocity with high-speed camera images.

4.2 IMPERMEABLE SUBSTRATES CHARACTERISTICS

Four different substrates are chosen in order to study the influence of wettability on the dynamics of droplet impact: glass, stainless steel, aluminum and parafilm. The glass substrate used is coverslip glass (Wash-N-Dry^{TM}, SIMGA-ALDRICH), stainless steel substrate is polished by means of electropolishing and the aluminum substrate is prepared with lapping process. The parafilm substrate is prepared on the slide glass with a plastic paraffin film (PARAFILM M, SIGMA-ALDRICH).

The influence of roughness is studied with different rough aluminum substrates and different grit size sandpapers (Silicon Carbide Paper, BUEHLER). The different roughnesses of the aluminum substrates are created on the lapped surface ($R_a \sim 0.2$) by polishing with P240 and

P600 sandpapers, to R_a values 0.4 and 0.7 μm, respectively (Table 4.3). The properties of surface morphology of sandpapers are reported in Table 4.6. The roughness of sandpaper varies from 3 to 20 μm of which is at least a 10 times larger roughness value than for the smooth surface used in this work.

Before testing, each surface is carefully cleaned in two steps: (i) washing with 1:1 deionized water and isopropanol mixture and drying in compressed dry clean air flow; (ii) careful rinsing in deionized water and drying in compressed dry clean air flow. The parafilm substrate is cleaned with step (ii) only to prevent reactions between isopropanol and paraffin.

The wettability of the substrates is characterized by Equilibrium Contact Angle (ECA), Advancing Contact Angle (ACA) and Receding Contact Angle (RCA). The measurement method of contact angle is described in section 5.1.1. The measured contact angles are reported in Table 4.3 for water, Table 4.4 for ethanol, and Table 4.5 for glycerol 10 mPa·s. Roughness is measured by a contact profilometer (Surftest-211, Mitutoyo) equipped with a 5 μm radius diamond-tipped stylus. Each specimen was traced in ten arbitrary locations near the location of droplet impact over a 0.8 mm sampling length. The roughness value R_a is the arithmetic average of absolute measured values. In addition, the roughness of smooth glass is measured using atomic force microscopy (AFM) to capture features smaller than the resolution of stylus profilometer. The results of AFM measurement are presented in chapter 7.

Table 4.3: Contact angles of water on the selected substrates

	Roughness R_a (μm)	Water		
		ECA θ_{eq} (°)	ACA θ_{adv} (°)	RCA θ_{rec} (°)
Glass(smooth)	<0.01	22.8 ± 4.3	28.6 ± 3.4	∼0
Glass(rough)	0.2	25.6 ± 2.8	28.4 ± 1.1	∼0
Steel	0.4	60.9 ± 1.3	61.5 ± 3.3	6.8 ± 1.0
Aluminum	0.2	62.8 ± 5.6	73.2 ± 1.4	16.2 ± 4.1
	0.4	87.6 ± 7.1	94.0 ± 2.8	∼0
	0.7	92.9 ± 10.2	99.4 ± 2.8	∼0
Parafilm	0.5	109.6 ± 2.6	115.0 ± 6.3	∼0

Table 4.4: Contact angles of ethanol on the selected substrates

| | Ethanol | | | |
| | Roughness | ECA | ACA | RCA |
	R_a (μm)	θ_{eq} (°)	θ_{adv} (°)	θ_{rec} (°)
Glass	0.2	~0	~0	~0
Steel	0.4	~0	~0	~0
Aluminum	0.2	11.2 ± 1.6	~0	~0
	0.4	~0	~0	~0
	0.7	~0	~0	~0
Parafilm	0.5	21.3 ± 1.9	22.5 ± 1.4	~0

Table 4.5: Contact angles of glycerol on the selected substrates

| | Glycerol (10 mPa·s) | | | |
| | Roughness | ECA | ACA | RCA |
	R_a (μm)	θ_{eq} (°)	θ_{adv} (°)	θ_{rec} (°)
Glass	0.2	21.8 ± 1.2	24.5 ± 4.8	~0
Steel	0.4	52.4 ± 3.7	48.5 ± 4.3	~0
Aluminum	0.2	60.1 ± 1.8	65.2 ± 4.2	~0
	0.4	59.8 ± 2.6	59.4 ± 1.4	~0
	0.7	53.5 ± 1.7	51.8 ± 1.5	~0
Parafilm	0.5	94.4 ± 3.4	105.4 ± 4.5	71.3 ± 2.0

The contact angles of water on the different surfaces vary (ECA 23° to 110°). On smooth surface ($R_a < 0.5$), ECA denotes an hydrophilic behavior on glass, steel and aluminum surfaces, while ECA on parafilm indicates an hydrophobic behavior (Table 4.3). It is found that ECA increases with roughness on aluminum surfaces.

Ethanol shows in most case a zero contact angle (Table 4.4), indicating that ethanol is totally wetting the surface in quasi-static conditions. Only on aluminum and on parafilm does ethanol show an equilibrium contact angle higher than zero degree, i.e. 11° and 22°. Glycerol shows a wetting behavior on glass, steel and aluminum (of all three roughness) with an ECA between 22° and 60°. Glycerol is found to be non-wetting on the parafilm substrate. In general, it is found that the ACA is quite similar to the equilibrium contact angle (differences less than 16%). The RCA is

Table 4.6: Properties of sandpaper

ISO Grit designation	Average particle diameter (μm)	Roughness R_a (μm)	ECA with water θ_{eq} (°)
P120	125.0	20.8	69.5 ± 3.8
P240	58.5	12.1	74.3 ± 3.1
P600	25.8	6.2	83.5 ± 2.4
P2500	8.4	2.7	81.0 ± 1.7

much lower than the ECA and, in several cases, could not be measured since the droplet remained pinned. Water shows a wetting behavior on sandpaper with an ECA between 70° and 84°, see Table 4.6. ACA and RCA were not measured on sandpapers. The sandpaper becomes more hydrophilic , showing the significant influence of increasing surface roughness on the equilibrium contact angle. As mentioned by Gennes et al. (2004), it is observed with increasing roughness, a hydrophilic substrate becomes even more hydrophilic, while an initially hydrophobic becomes more hydrophobic (Figure 4.2).
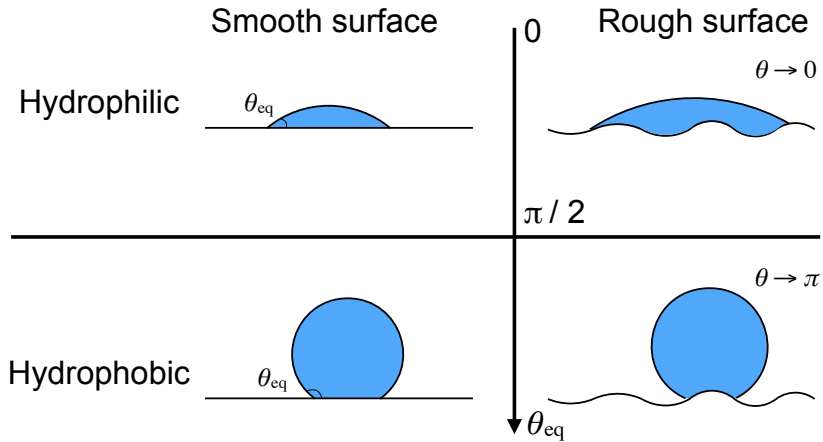

Figure 4.2: Schematic representation showing control of wettability by substrate roughness, based on Gennes et al. (2004)

4.3 POROUS SUBSTRATES

Three natural stones are selected to study droplet impact on porous media: Savonnières, Meule and Pietra Serena. The stones are selected mainly in terms of open porosity. Savonnières is highly porous (26.9%), a quasi-pure calcitic stone (99.8% CaCO3 (Fronteau, 2000)) and is used as a building material on facades of historical buildings (a famous example if the railway station Gare de l'Est in Paris), as a stone for sculptures (e.g. sculptures of the facade of the cathedrals of Aachen and Cologne), and is still often used for restoration purposes (Dreesen and Dusar, 2004; Derluyn, 2012). The grès de Meules (Meule), the middle case here in terms of porosity (16.6%) is composed of quartz grain (74%), contains clay and other secondary mineralization and is used as a building material (e.g. the tower of the Cathedral of Strasbourg) (Moonen, 2009). Pietra Serena is a fine-grained compact sandstone, of very low porosity 5.1%, used widely as a building material for columns, cornices and arches and as a stone for sculptures (e.g. the Pazzi Chapel and the Medici Chapel in Florence). Figure 4.3 shows microscope images of surface of the three porous stones, saw cut and unpolished.

(a) Savonnières   (b) Meule   (c) Pietra serena
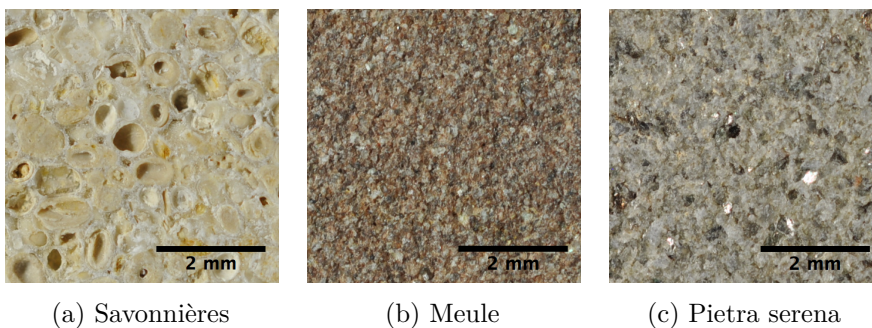
Figure 4.3: Microscope images of the surfaces of the porous stones

The porous stones are cut into cubes of $20 \times 20 \times 20$ mm^3 to be used for the drop impact tests. The bulk density ρbulk, open porosity Φ and saturated water content w_{sat} of the cubes are measured. The bulk density ρ_{bulk} is defined as the ratio of the dry mass of a sample to its total volume, including the total pore space:

$$\rho_{\mathrm{bulk}} = \frac{m_{\mathrm{dry}}}{V} \tag{4.2}$$

where m_{dry} is dry stone mass and V is volume of stone, measured by caliper. The open porosity Φ is defined as the ratio of the volume of open pores to the total volume of the stone:

$$\Phi = \frac{m_{\mathrm{sat}} - m_{\mathrm{dry}}}{\rho_{water} V} \tag{4.3}$$

where m_{sat} is saturated stone mass, determined after water imbibition under vacuum. Thus saturated water content w_{sat} is total mass of water that fills the open pore space:

$$w_{\mathrm{sat}} = \Phi \cdot \rho_{water} \tag{4.4}$$

Table 4.7 summarizes the measured properties of the three stones. Further details on pore structure, and moisture and mechanical properties of Savonnières and Meule can be found in **bouwfysica:IF/jFDfn**; Derluyn (2012) and Moonen (2009). The instrument used for roughness determination provides the roughness of the stones, except the large features (approx. pore radius 100 µm) of Savonnières. The equivalent pore radius R_{eq} is determined from pore size distribution measurement using mercury intrusion porosimetry (MIP) (Derluyn, 2012; Moonen, 2009) and scanning electron microscope (SEM) image (**bouwfysica:IF/jFDfn**).

Table 4.7: Properties of porous stones

	Savonnières	Meule	Pietra Serena
ρ_{bulk} (kg/m^3)	1974.5 ± 38.7	2253.2 ± 14.3	2558.7 ± 21.9
Φ (%)	26.9 ± 1.4	16.6 ± 0.3	5.1 ± 0.6
w_{sat} (kg/m^3)	268.2 ± 13.6	165.7 ± 4.0	50.9 ± 6.0
w_{cap} (kg/m^3)	151.1 ± 6.4	119.8 ± 4.0	41.6 ± 2.5
A_{cap} (kg/m^{2}s$^{1/2}$)	0.089 ± 0.012	0.028 ± 0.003	0.004 ± 0.001
R_a (µm)	10.3 ± 3.5	9.1 ± 1.5	4.4 ± 1.5
R_{eq} (µm)	100	10	0.04

The capillary water content w_{cap} and the water absorption coefficient A_{cap} are determined from capillary water uptake experiments. Six samples, the same that are used for droplet impact tests, are tested with flow direction perpendicular to the bedding direction. The lateral sides of the samples are sealed with aluminum foil tape (Aluminum Foil, 3M$^{\mathrm{TM}}$)

and paraffin wax (Paraffin wax, SIGMA-ALDRICH) to prevent water absorption and evaporation from the lateral sides. The sample is placed in a water basin and, at fixed moments, is weighed on a balance to monitor mass change in function of time.

Figure 4.4 presents the uptake experiments in terms of absorbed moisture mass per area taking up water as a function of square root of time. The uptake process shows two stages (represented as blue and red dashed lines in Figure 4.4). In the first stage, the water uptake is driven by capillary forces and the water front reaches the upper surface. After the water front reaches the top surface, in the second stage, the water uptake continues slowly by dissolution of entrapped air through the liquid phase. The capillary absorption coefficient A_{cap} is the slope of the first stage and the capillary water content w_{cap} is the moisture content related to the transition between two stages.
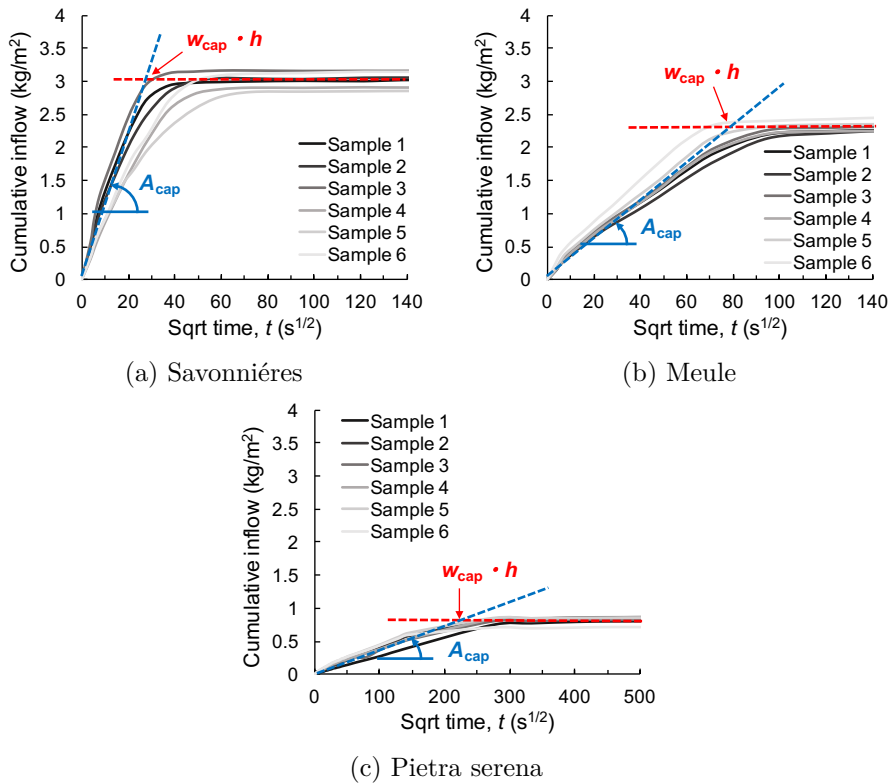

(a) Savonniéres

(b) Meule

(c) Pietra serena

Figure 4.4: Capillary water uptake in sample of $20 \times 20 \times 20$ mm^3. Flow is perpendicular to the bedding direction.

The capillary water content w_{cap} and the capillary absorption coefficient A_{cap} are reported in Table 4.7. Savonnières shows a faster water absorption and a higher capillary water content than the other two stones. The capillary water content is, as expected, less than the saturated water content due to air entrapment. Pietra Serena shows the lowest water uptake coefficient and capillary water content. The pore space of the stones, i.e. Savonnières, Meule and Pietra Serena, is filled at 56%, 72% and 80% with water, respectively, after capillary uptake. The measured capillary water content and the capillary absorption coefficient for Savonnières are similar to the ones measured by Derluyn (2012).

4.4 CONCLUSION

This chapter presents the properties of the liquids impermeable and porous substrates. The values are needed as input for theoretical and numerical modeling of impact, spreading and absorption dynamics. The density, surface tension and viscosity of the liquids are obtained from literature. The roughness and wettability of impermeable substrates are experimentally determined on the samples used in the experiments reported in Chapters 6, 7 and 8. The moisture properties of porous stones are experimentally determined on the specific cube samples used for the drop impact test and the drop absorption test as reported in Chapters 10, 11 and 12.

5

EXPERIMENTAL METHODS

In this chapter, the experimental methods used for visualization and quantification of the drop impact and its absorption are described in detail. Backlight imaging (shadowgraphy) is used to capture impacting droplet with high contrast and sharp outline. The dynamic behavior of impacting droplets is visualized at different time scales with high-speed imaging method, i.e. at the scale of a few milliseconds for the dynamic spreading or at the scale of a few seconds for absorption of droplets deposited on porous media. Moisture transport within the stones is visualized by neutron radiography which allows quantifying at high resolution the moisture content distribution. All digitized imaging data is analyzed with custom-made computational imaging analysis codes to determine with consistency the required values.

5.1 HIGH-SPEED IMAGING SETUP

The human eye is obviously limited to observe fast motion. Particularly, capturing impacting drop movements has been challenging and benefitted from high-speed camera development (see reviewed by Thoroddsen et al. (2008)). In this study, the high-speed imaging setup is used to capture the static and dynamic behavior of droplets. Figure 5.1 shows the configuration of the high-speed imaging setup for shadowgraphy and the droplet generation setup (see section 4.1 for the detailed configuration of the injection system). This optical system consists of an illuminator, zoom lens and high-speed camera. The high intensity homogeneous backlighting (45W LED, flux $\sim$ 550 lm, white light within 6 000K) is achieved with a LED illuminator (LLS3, SCHOTT) and a translucid polyethylene diffuser. The zoom lens (12$\times$ zoom lens, Navitar) combined with 1.0$\times$ extension tube is used for higher magnification and long working distance (2 cm) to allow visualizing the sample and droplet size within the field of view. The high-speed camera (NX7-S2) is used to capture digital images, at high frame rate (up to 65 000 fps for a field of view of 112 pixel $\times$ 64 pixel, 7.24 $\times$ 7.24 μm for pixel size) with high light sensitivity (10 bit mono pixel depth).
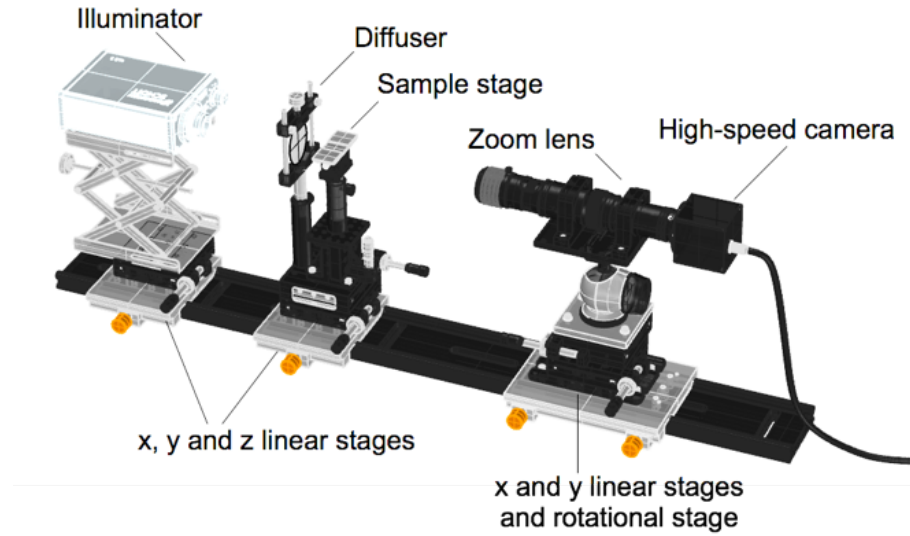
(a) High-speed imaging setup for shadowgraphy
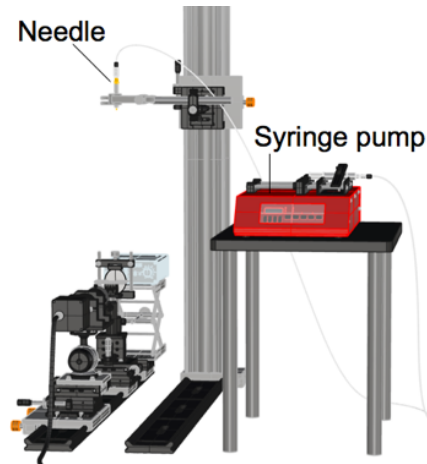
(b) Drop injection system

Figure 5.1: Illustrations of the configuration of (a) high-speed imaging setup for shadowgraphy and (b) drop injection system.
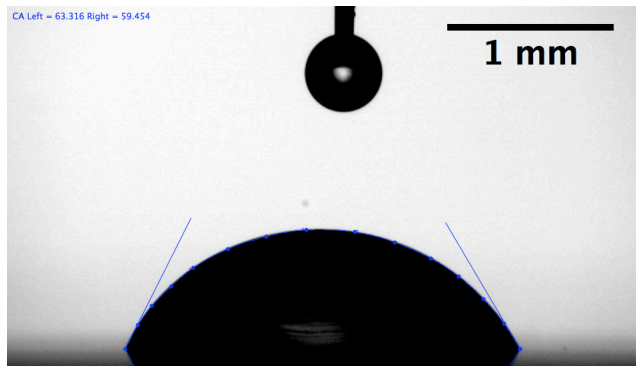
Figure 5.2: Shadowgraphy for a measurement of equilibrium contact angle using B-spline snake method (Stalder et al., 2006). Blue outline indicates the segmentation result of the active contours on the image and the tangential slope determines the contact angle.

The optical setup is optimized to achieve the best quality images for the different experiments, i.e. imaging the static, quasi-static and dynamic behavior of the droplets. The required frame rate is majorly affected by the optical magnification of the imaging. For instance, a velocity of 1 m/s of a moving object corresponds to a velocity of 1 µm/ µs in microscale. Thus, the frame rate, exposure time and magnification need to be optimized in order to capture the dynamic behavior of droplets at microscale and at the different time scales involved. The optimized setups to characterize contact angle of static and quasi-static droplets and to observe spreading and absorption for dynamics of drop impact are detailed below in the section on image analysis method.

5.1.1 *Contact angle*

The contact angle is defined as the angle made by the intersection of the liquid-solid interface and the liquid-vapor interface. On partial wetting surfaces, the equilibrium contact angle, θ_{eq}, is measured as the drop forms a spherical cap on the surface after gentle deposition. There are several methods to measure the equilibrium contact angle: (i) side view photograph of drop profile combined with goniometer method, (ii) divergence angle of laser beam, (iii) interference contrast microscopy in reflection and (iv) distortion of the grid image (Gennes et al., 2004).
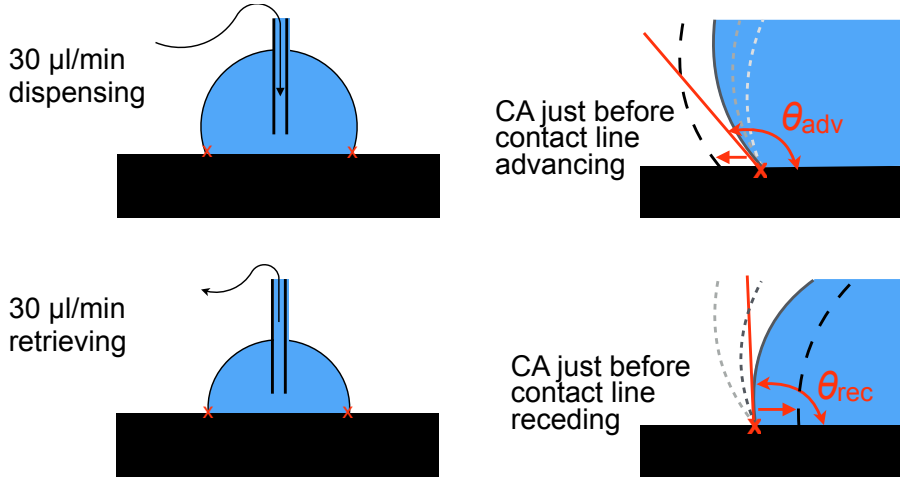
Figure 5.3: Determination of advancing and receding contact angles.

In this study, the goniometer method is used to measure the contact angle. For θ_{eq} measurement, a 3.0 µl droplet is very gently deposited on the surface using the z-axis linear stage. The deposited droplet is imaged with the high-speed camera setup with a pixel resolution of 7.38 µm and frame rate of 100 fps. The contact angle is determined at 1 second after the drop touches the surface using an imaging trigger system linked to the high-speed camera to minimize the influence of evaporation. Figure 5.2 shows the shadowgraphy of a deposited droplet in equilibrium state. The contact angle is obtained by taking the tangent to the piecewise polynomial fit of the segmented droplet using MATLAB (MathWorks Inc.), where the polynomial fit is formed by active (B-spline snake) segments using the ImageJ plugin (Stalder et al., 2006).

The equilibrium contact angle can be used in Young's equation when the surface is clean, planar and solid. On a non-ideal surface, the equilibrium contact angle is not unique, but shows an advancing and receding contact angle. Figure 5.3 shows the determination of advancing and receding contact angles, θ_{adv} and θ_{rec}, measured by quasi-statically expanding or contracting the deposited sessile droplet, respectively. The contact angle θ can exceed θ_{eq} without the line of contact moving at all. Eventually, θ reaches a threshold value θ_{adv} beyond which the line of contact moves. Likewise, when the liquid is sucked out of the deposited droplet, θ can decrease down to a limiting value θ_{rec}. The increasing and decreasing volume rate of the sessile drop is controlled by a syringe pump and

equal to 30 μl/min. The θ_{adv} and θ_{rec} are captured with the high-speed camera setup (7.38 μm spatial resolution, 1000 fps and 30 μs exposure time) and analyzed using the same method used for equilibrium contact angle determination. In this study, all contact angle measurements are repeated 10 times for each sample to verify reproducibility. The results of contact angle measurements are reported in Section 4.2 for impermeable substrates.

5.1.2 *Drop impact*

The drop impacting the substrate is observed with the high-speed camera setup. The configuration of the optical system is optimized for the droplet impact conditions (Table 5.1). Simple models for maximum spreading (Clanet et al., 2004) and time at maximum spreading (Pasandideh-Fard et al., 1996) are used to estimate the field of view (FOV) and the frame rate. The 14 mm × 4 mm (width × height) FOV is set for all impact conditions, based on the estimated maximum spreading diameter at highest Weber number, $D_{\text{max}} = D_0 \cdot \text{We}^{1/4} \approx 9.4$ mm. Considering the estimated time at maximum spreading $t_{\text{max}} = (8/3) \cdot (D_0/V_{\text{i}}) \approx 1.4$ ms, a frame rate of 10 000 fps is selected. The exposure time is fixed at 5 μs due to the limit of light intensity of the illuminator and light sensitivity of the camera. Although 1.8 μs of exposure time would have been sufficient to capture an object moving at 4 m/s with a 7.38 μm pixel, 5 μs of exposure time is chosen for a better brightness of the image. There is a risk of image blurring due to motion over 1 or 2 pixels for high impact velocities.

Table 5.1: Droplet impact conditions

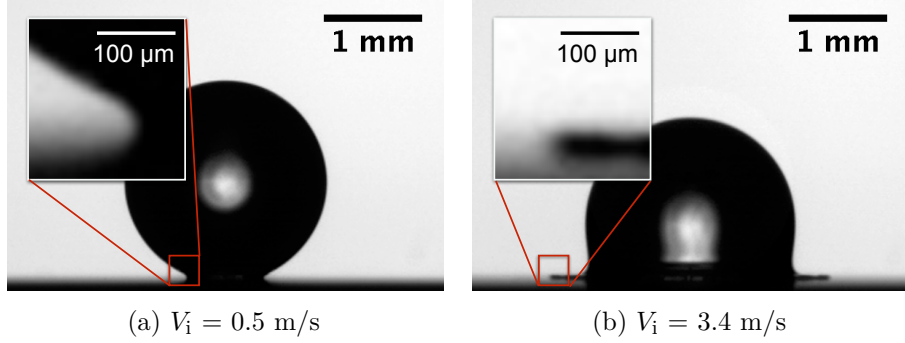|	D_0 (mm)	V_{i} (m/s)	Weber Number	Reynolds number
Ethanol	1.8 - 2.0	0.2 - 2.7	2 - 500	250 - 3 500
Water	2.0	0.2 - 3.6	1 - 360	450 - 7 000
Glycerol 10 mPa·s	1.8	0.2 - 3.7	1 - 430	40 - 800

(a) $V_i = 0.5$ m/s   (b) $V_i = 3.4$ m/s

Figure 5.4: Snapshots of drop impacts with high-speed camera setup (7.38 μm spatial resolution, 10 000 fps and 5 μs exposure time) at $t = 0.1$ ms after impact: (a) $V_i = 0.5$ m/s and (b) V_i = 3.4 m/s. Insets: magnified images on the front of contact line showing the motion blur on the right.

However, such motion blur is seen only for the first two frames after impact, since the speed of the droplet base decreases exponentially after impact. Figure 5.4 shows the images captured at $t = 0.1$ ms for low (V_i = 0.5 m/s) and high impact velocity ($V_i = 3.4$ m/s) on steel substrate with high-speed camera setup. The magnified image of the lamella front of the high impact velocity droplet (Figure 5.4b) shows the motion blur in a few pixels from the visible outline of the lamella.

Drop impact is characterized with the spreading diameter $D(t)$, the dynamic contact angle $\theta_D(t)$, the maximum spreading diameter D_{max}, the time at maximum spreading t_{max} and the dynamic contact angle at maximum spreading $\theta_D(t_{max})$ as shown in Figure 5.5.
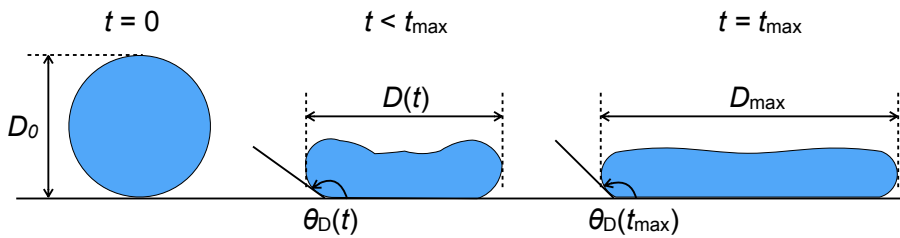

Figure 5.5: Schematic representation of the spreading droplet and its characteristic dimensions.

The high-speed images are analyzed in MATLAB (MathWorks Inc.) using an own developed code. The procedure of image analysis is as follows:

1. Calculate the averaged background images of 10 images without droplet

2. Determine the moment of contact of drop with surface

3. Divide drop images by the averaged background image

4. Segment the outline of droplet with the threshold method

5. Fill the segmented area to remove bright reflection regions

6. Register the outline in Cartesian coordinates

7. Calculate $D(t)$ and $\theta_D(t)$

8. Determine t_{max} from the profile of $D(t)$

9. Determine $D_{max} = D(t_{max})$ and $\theta_D(t_{max})$ at t_{max}

Figures 5.6a-b show the results of image analysis using the code in terms of spreading ratio $\beta = D(t)/D_0$ and dynamic contact angle $\theta_D(t)$. Figure 5.6c illustrates droplet segmentation. Figure 5.6d shows three liquid-vapor interfaces near the surface line and the schematic of the goniometric mask used for determining the dynamic contact angle (Biolè and Bertola, 2015). The $D(t)$ is the longest horizontal line in the segmented droplet outline. The contact line diameter $D_{CL}(t)$ measured during the absorption process is the horizontal length at the surface. When no rim is formed at the edges of the lamella (see green line on Figure 5.6c), $D(t)$ is equal to $D_{CL}(t)$.

The dynamic contact angle is obtained from the image by applying a goniometric mask on a region of 100 μm vertically above the surface line (Biolè and Bertola, 2015). This method allows to measure small angles and large curvatures of the interface accurately and at a low computational cost. As shown in Figure 5.6d, the Cartesian coordinate system is applied with an equilateral triangle mask at the triple point where three phases meet. In general, the tangent method determines $\theta_D = \tan^{-1} m$ where m is determined from the straight tangent line $y = mx$. In this mask method, the same angle θ_D is defined using line

(a) Spreading ratio versus time

(b) Dynamic contact angle versus time

(c) Segmented outlines of spreading droplets

(d) Contact line profiles from surface to 10 pixels height and schematic of goniometric mask for dynamic contact angle measurement.
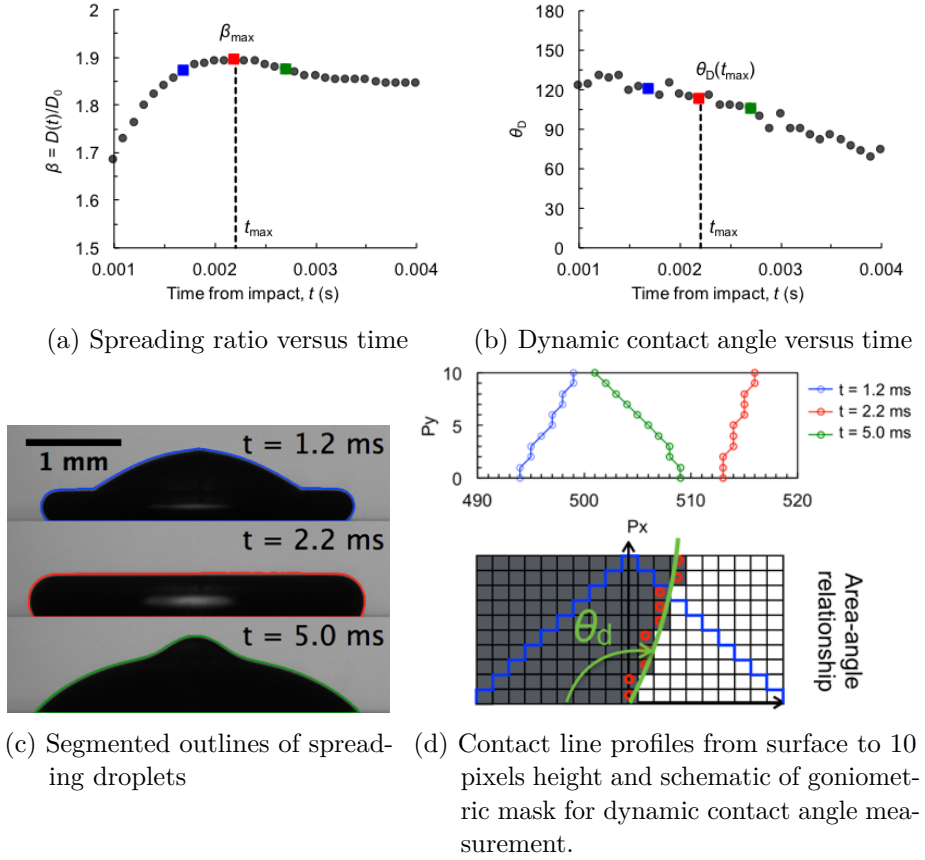
Figure 5.6: Image analysis of spreading droplet.

$y = mx$, intersecting with a triangle of arbitrary height R and with the two sides defined by $y = R - x$, $y = R + x$.

Figures 5.7a and b illustrate the triangle cut by the tangent and thus creating two polygons corresponding to positive and negative values of the angular coefficient m. The intercept, B_λ, of the line $y = mx$ with either $y = R - x$ or $y = R + x$ is defined as:

$$B_\lambda : \begin{cases} y = \lambda |m| x \\ R - \lambda x \end{cases} \tag{5.1}$$

where $\lambda = sgn(m)$ and the coordinates are:

$$B_\lambda : \left\{ \frac{\lambda R}{|m| + 1}; \frac{|m| R}{|m| + 1} \right\} \tag{5.2}$$
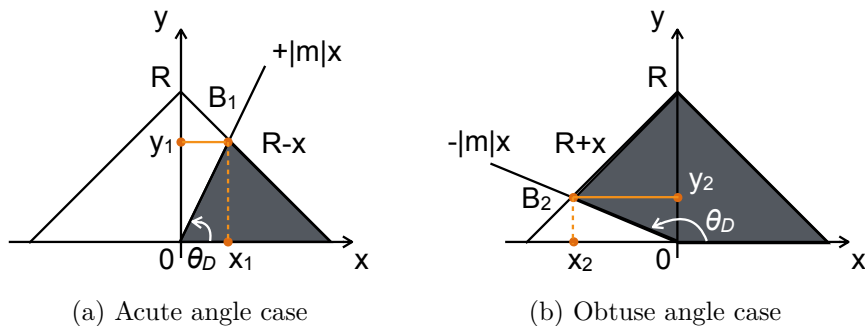
(a) Acute angle case (b) Obtuse angle case

Figure 5.7: Geometric construction for the derivation of the area-angle formula. The figures is redrawn based on Biolè and Bertola (2015).

The polygon area (filled area in the Figure 5.7) can be written as:

$$A_\lambda = \frac{R^2 \left(|m| + (1 - \lambda)\right)}{2 \quad |m| + 1} \tag{5.3}$$

The contact angle θ_D can be expressed as a function of the polygon area and of the sign parameter λ:

$$\tan \theta_D = \lambda |m| = \lambda \frac{R^2(1 - \lambda) - 2A_\lambda}{2A_\lambda - R^2} \tag{5.4}$$

$$\theta_D = \frac{\pi}{2}(1 - \lambda) + \tan^{-1}\left(\lambda \frac{R^2(1 - \lambda) - 2A_\lambda}{2A_\lambda - R^2}\right) \tag{5.5}$$

To assess the accuracy of the method, an ideal sphere model and a falling droplet are imaged and analyzed by the code. A 3 mm diameter plastic ball is imaged with the high-speed camera setup. The diameter of plastic ball is measured by the image analysis code and compared with the actually diameter. The error of the diameter measurement is found to be less than 1% (maximum 4 pixels difference). In addition, the code is validated with a falling droplet ($D_0 = 2.0$ mm and $V_i = 1.0$ and 3.0 m/s) captured with the high-speed camera setup (7.38 µm spatial resolution, 10 000 fps and 5 µs exposure time). The measured diameter by the code is compared with the diameter derived from the mass of the droplet and shows about 3% deviation which includes the error of weighing with the microbalance. The goniometric mask method is compared with the polynomial fitting method and a maximal difference of 5% between the two methods is observed for the spreading droplet.

5.1.3 *Change of droplet volume during absorption*

In order to measure the mass transfer rate into the porous medium by capillary action, the volume of drop resting on surface is determined using the high-speed camera setup. To capture the life time of a droplet during the absorption process into the porous medium, the frame rate is optimized with as limiting factor the memory of the high-speed camera. Thus the absorption is imaged at 1 000 fps and 30 μs exposure time, resulting in a spatial resolution of 7.38 μm. The drop volume on the surface is calculated from the side view with the image analysis code with two methods as described below: (i) spherical cap method and (ii) pixelwise volume calculation.
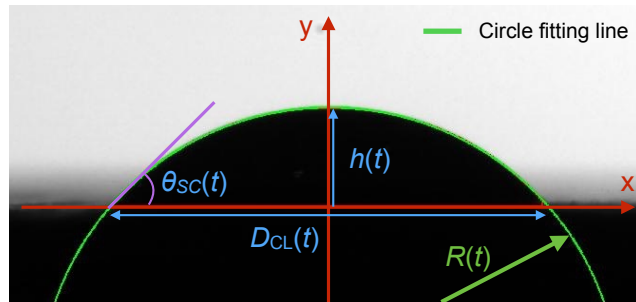
(a) Profile of the spherical cap description for a deposited droplet on porous media
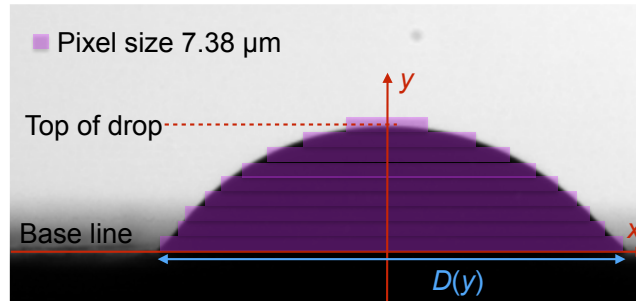
(b) Schematic for the pixelwise volume calculation with axisymmetric assumption

Figure 5.8: Methods for drop volume calculation

Figure 5.8 illustrates the two methods for drop volume calculation. In figure 5.10a, the drop is assumed to have the shape of a spherical cap. The height of the drop apex, $h(t)$, the width of the droplet base, $D_{\mathrm{CL}}(t)$, and the radius of the circle fitting the spherical cap, $R(t)$, are obtained

from image analysis using the developed code. The drop volume on surface and the contact angle $\theta_{\text{sc}}(t)$. Once $h(t)$ and $D_{\text{CL}}(t)$ are known, then determining the volume and the contact angle of a spherical cap is straightforward:

$$V_{\text{drop}} = \frac{\pi h(t)}{6} \left(3 \left(\frac{D_{\text{CL}}(t)}{2} \right)^2 + h(t)^2 \right) \tag{5.6}$$

$$\theta_{\text{sc}} = \arccos \frac{D_{\text{CL}}/2}{R(t) - h(t)} \tag{5.7}$$

Figure 5.10c shows the drop volume calculation with pixelwise volume. The Cartesian coordinate is located on the intersection of the circle fitting the outline of deposited droplet and the surface line. Then the volume is considered as a pile of circular disks of one pixel height and diameter $D(y)$. The volume can thus be written as:

$$V_{\text{drop}} = \sum_{y=0}^{y=\text{top}} \frac{\pi}{4} D(y)^2 \cdot \text{pixel size} \tag{5.8}$$

The two methods are validated with a 4.3 mg of water droplet deposited on impermeable steel surface and show less than 3% deviation from the target volume, which includes 1% of the error on drop generation. However, when a droplet becomes a very thin layer, e.g. due to volume loss by absorption into the substrate, both methods fail to measure the volume because of the lack of information on a drop height due to the reflection from the liquid puddle and bubble eruption. In this study, the two methods are used for the measurement of drop volume on porous media and the results are analyzed. The difference between two methods is less than 5% which is attributed to the problem of correct segmentation at the contact line due to slight deviations from the axi-symmetry of the drop. In what follows, the data on remaining volume on substrate are obtained using the spherical cap method.

5.2 NEUTRON RADIOGRAPHY

Visualization of water migration inside porous media is a main challenge when studying unsaturated flow in opaque porous media. Recently, non-invasive imaging techniques (gamma radiation, Magnetic Resonance Imaging (MRI), X-ray and neutron radiography) have been used to capture water transport in porous media (Jung et al., 2012). In this
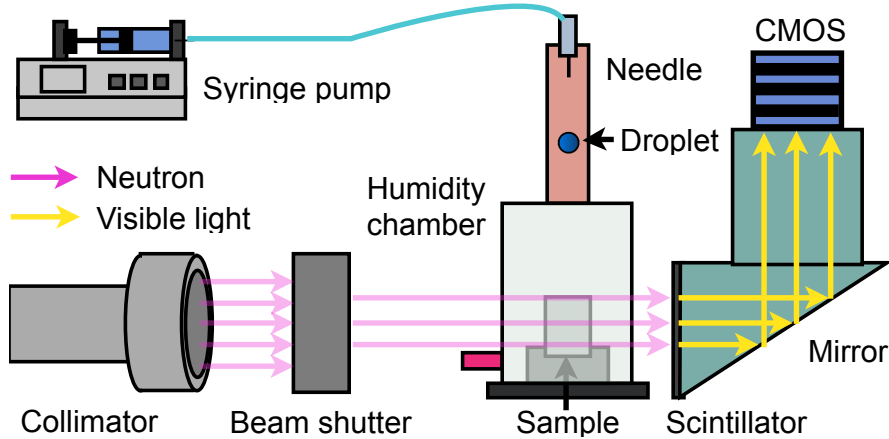
Figure 5.9: Schematic of NEUTRA beam line configuration.

study, the absorption into the porous medium from a drop impacting on a porous stone is captured by neutron radiography. Contrary to X-ray, neutrons are highly attenuated by the hydrogen in water, but not by the elements composing our porous stone.

The experiment for the absorption of drop impact is performed at the NEUtron Transmission RAdiography (NEUTRA) beamline of the Paul Scherrer Institute, Villigen, Switzerland. This beamline is fed by the Swiss Neutron Spallation Source (SINQ) and is operated with neutrons within a thermal spectrum characterized by a Maxwell-like probability density function, with a most probable energy level of about 25 MeV (Lehmann, 2008). Figure 5.9 shows a schematic overview of the neutron beamline and the experimental setup for drop impact. The steady state neutron source, driven by a 590 MeV proton beam from a ring cyclotron with a power in the MW range produces 25 meV neutrons through the collimator. The transmitted neutrons through the sample is converted into visible light photons by the scintillator, a plane slab of ZnS crystal, doped with ^{6}Li as neutron absorbing agent (200 μm thick). The photons are then led via a mirror onto a CMOS camera (1024 x 1024 pixels, Andor Neo). The necessary exposure time for each image is 3 seconds, the field of view is 31 x 60 mm^2 and the spatial resolution of the neutron radiography is 45.5 μm/pixel. This configuration and settings are used for all experiments.
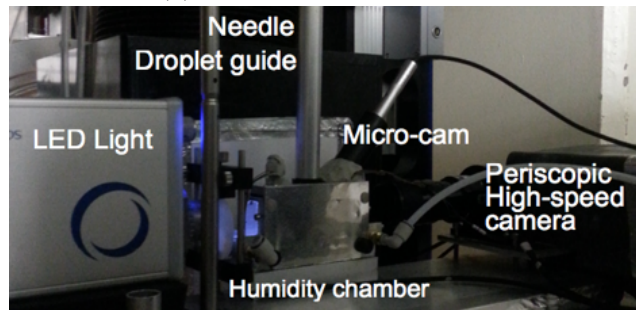
5.2.1 *Drop impact setup*

As shown in Figure 5.9, the experimental set-up for the droplet test is placed in the beamline aligned with the neutron beam direction. To visualize the drop impact with higher temporal resolution, the NEUTRA beamline was synchronized with the droplet test setup. Figure 5.10 shows the configuration of the droplet test setup equipped with: droplet generator, angleview camera to generate the trigger signal to NEUTRA and humidity controller. Blocks of boronated polyethylene, a material opaque to neutron radiation, shield any sensitive equipment, such as the camera, against neutron radiation. Once the sample is installed in the field of view, a reference radiograph of the sample at the initial state (dry or moist) is obtained right after the sample is placed on the sample holder. Measurements on moist samples were soon discontinued because the required high RH ambient conditions could not be achieved. 4.3 mg of de-ionized water droplet is generated at heights of 13.5 and 46.0 mm from the top of sample and falls through the shielding guide tube impacting the top of the sample. After drop impact on the sample, the moisture distribution is recorded by neutron radiography at regular interval, of typically 3 seconds, over a period of 10 minutes depending on the uptake rate of the different samples. As control, the mass of the specimens before and after the droplet test is taken.

The experiments were performed over a total of 3 beamtimes (November 23rd to 26th, 2012, June 18th to 22nd, 2013 and August 27th to 31st, 2015) at NEUTRA in PSI. The objectives of the beamtime experiments are to capture the absorption process of single and multiple droplets on horizontal and oblique porous stones. Three beamtimes are conducted with same configuration of NEUTRA setup as explained above and the conditions of temperature and relative humidity are $24.8 \pm 0.5°$C and $12.5 \pm 1.8\%$ RH for first beamtime, $28.1 \pm 3.5°$C and $10.5 \pm 2.1\%$ RH for the second and $30.2 \pm 2.5°$C and $54.5 \pm 7.8\%$ RH for the third. For the first and second beamtimes, these are the conditions inside the controlled environmental chamber, for the third, the conditions are measured in the beam hutch.
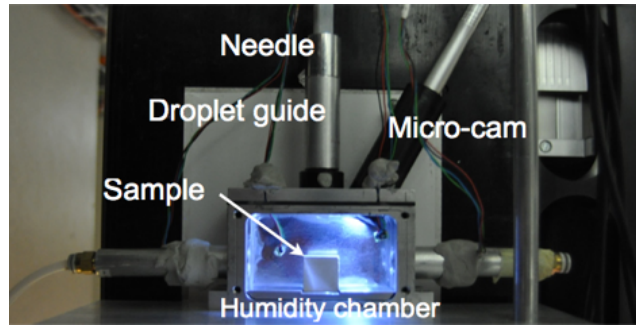
(a) Single drop impact setup

(b) Multiple drop impact setup
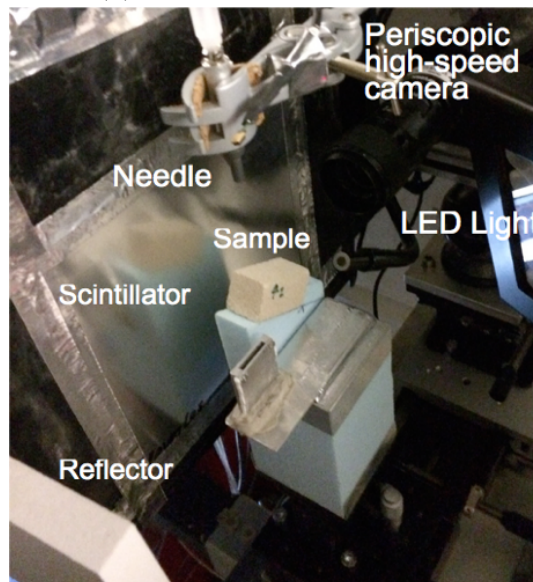
(c) Drop impact on oblique surface

Figure 5.10: Experimental set-up for drop impact test inside the NEU-TRA beamline: (a) a single drop impact setup (first beamtime); (b) multiple drop impact setup (second beamtime) and (c) setup for drop impact on oblique surface (third beamtime).

5.2.2 *Moisture content quantification with neutron radiography*

Neutron radiography is based on intensity measurements of a neutron beam transmitted through an object. The intensity of the transmitted beam I, can be described with the Beer-Lambert law:

$$I = I_0 \exp -\Sigma \cdot d(t) \tag{5.9}$$

where I_0 is the intensity of the incident neutron beam, $d(t)$ is the total thickness of the object along the beam direction and Σ is the macroscopic linear attenuation coefficient. Note that the use of Σ is a convention in neutron radiography although it may lead to confusion with the summation sign Σ. Σ is a measure of the degree to which a material of one pure element interacts with and attenuates the neutron beam:

$$\Sigma = \sigma \cdot N \tag{5.10}$$

where σ is the neutron total microscopic attenuation coefficient representing the interaction probability with the incident radiation, and N is the elemental density, which is equal to the product of m, the material density, with N_A, the Avogadro constant, divided by A the elemental molar mass. For a compound material like a stone or water, the microscopic attenuation coefficients σ of the individual elements (hydrogen, oxygen, carbon, silicon or calcium) can be summed to define the macroscopic total attenuation coefficient Σ:

$$\Sigma = \sum_{i=1}^{n} \Sigma_i = \sum_{i=1}^{n} (\sigma_i, N_i) \tag{5.11}$$

where the index i identifies the ith elemental component and n is total number of them. In this work, the variable of interest is the water drop mass in each pixel at any time step. The water drop mass distribution in porous stone can be calculated from subtractions of the transmission value of dry stone from the transmission value of water drop and wet stone. From Eq. 5.9, the change of the transmission T based on time t is given by:

$$T(t) = \frac{I}{I_0} = \exp\left(-\Sigma \cdot d(t)\right) \tag{5.12}$$

The transmission at the initial dry state of a stone sample T_{dry} is

$$T_{\text{dry}} = \exp\left(-\Sigma_{\text{stone}} \cdot d_{\text{stone}}\right) \tag{5.13}$$

where Σ_{stone} is macroscopic attenuation coefficient for sample and d_{stone} is the thickness of the sample along the beam direction. The transmission value after drop impact T_{drop} can be described as:

$$T_{\text{drop}} = \exp\left(-\Sigma_{\text{stone}} \cdot d_{\text{stone}} - \Sigma_{\text{water}} \cdot d_{\text{water}}\right) \tag{5.14}$$

where Σ_{water} is macroscopic attenuation coefficient for water and d_{water} is the equivalent water thickness in the stone along the beam direction at time t. Therefore, water drop mass $M(t)$ in each pixel at time t is:

$$M(t) = \frac{\rho_{\text{water}} \cdot \text{pixelsize}^2}{\Sigma_{\text{water}}} \ln\left(\frac{T_{\text{dry}}}{T_{\text{drop}}(t)}\right) \tag{5.15}$$

where ρ_{water} is density of water. The water attenuation coefficient of NEUTRA setup used in this work is $\Sigma_{\text{water}} = 3.63$ (1/cm). In order to correct for some of the artifacts produced by the experimental configuration, each raw neutron radiography requires to be pre-processed before used for quantitative analysis. The images are corrected with following corrections:

1. Dark field correction

2. Flat field correction

3. Intensity correction

The dark field correction compensates for the background noise of the CMOS camera. The flat field correction allows to eliminate inhomogeneities of the beam and detector by compensating for different gains and dark currents. The intensity correction scales the measured radiograph, so that the same neutron source flux is assumed for all radiographs of a series. Figure 5.11 shows the neutron radiography and the corrected image.

For the correction, the dark current (DC) which is an image without neutron beam and flat-field (FF) which is a neutron radiograph without sample are taken for each drop impact experiments. The neutron radiography is corrected as:

$$T_{\text{corr}} = \frac{(\text{Img} - \text{DC}) \cdot \text{dose}}{\text{FF} - \text{DC}} \tag{5.16}$$
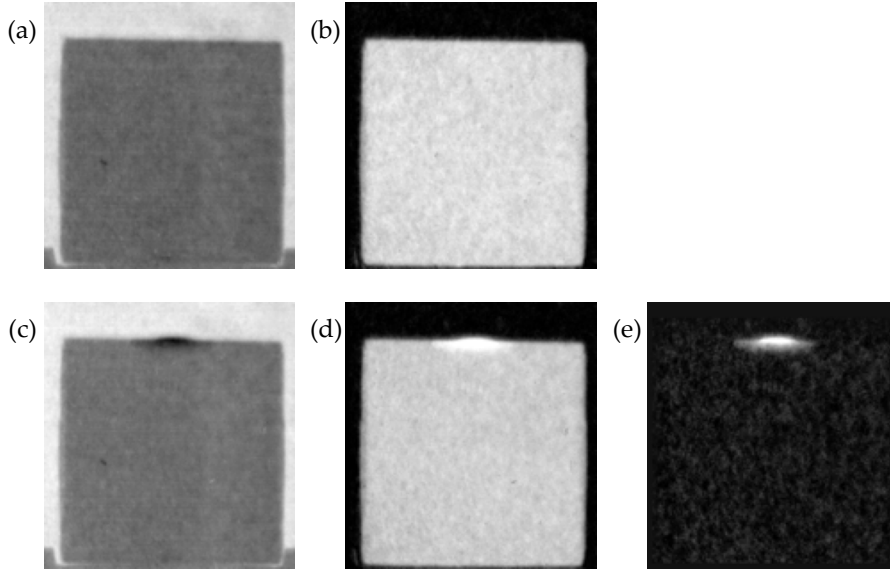
Figure 5.11: Images of neutron radiography and corrected one: (a) neutron radiography of dry porous stone, (b) image after flat-field and dose corrections, (c) neutron radiography of drop on porous stone, (d) corrected and (e) subtraction image between (b) and (d).

$$\text{dose} = \frac{\text{mean}(\text{FF}_{\text{ROI}})}{\text{mean}(\text{Img}_{\text{ROI}})} \tag{5.17}$$

where T_{corr} is the corrected transmission value for neutron radiography, Img is the original image to be corrected and the subscript ROI is the selected region for intensity correction. The neutron radiographs of the drop impact experiments are quantified using a custom made MATLAB code.

The quality of neutron radiograph is evaluated in this study with an aluminum stair sample filled with water which is a well-known test to evaluate the beam quality and to calibrate for water attenuation. Figure 5.12 illustrates the actual geometry of the aluminum stair and the neutron radiography of the aluminum stair filled with water. Figure 5.13 shows the comparison between the evaluated water thickness and the actual water thickness inside the aluminum stairs. The total deviation between two thicknesses is less than 5%. In addition, the drop impact experiment by neutron radiography is verified by comparing between the mass of the
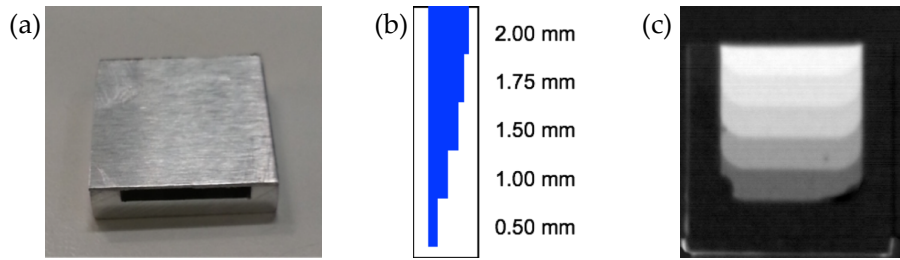
Figure 5.12: (a) Aluminum stair specimen, (b) schematic of water thickness inside the specimen and (c) neutron radiography of the aluminum stairs filled with water.
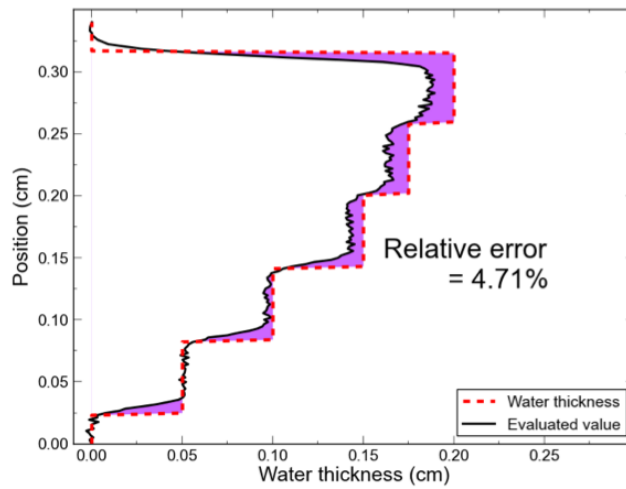
Figure 5.13: Water thickness of the aluminum stairs: actual water thickness inside the aluminum stairs (red dash line) and estimated water thickness from corrected neutron radiography (black line).

drop produced by the injection system and the total water mass at 3 s after drop impact as quantified by neutron radiography. The deviation is less than 6.5% for all experiments in this work.

5.3 CONCLUSION

In this chapter, two different imaging techniques, high-speed imaging and neutron radiography are described for drop impact and absorption quantification. The images are analyzed with custom-made imaging analysis codes. The image analysis methods are evaluated and the error of the experimental setup and the analysis methods is discussed. Appendices A and B provide the details of the codes.

MAXIMUM SPREADING OF LIQUID DROP IMPACTING ON IMPERVIOUS SURFACES

This chapter is based on the paper Lee JB, Laan N, de Bruin KG, Skantzaris G, Shahidzedeh N, Derome D, Carmeliet J, Bonn D. "Universal rescaling of drop impact on smooth and rough surfaces" Journal of Fluid Mechanics, 786, R4 (Lee et al., 2016c).
Experiments for high viscous droplets (Glycerol 6 and 51 mPa·s) have been done in collaboration with the group of Prof. Daniel Bonn of University of Amsterdam.

6.1 INTRODUCTION

Understanding maximum spreading of drop impact is key to control the drop dynamics in several applications (Rioboo et al., 2001; Yarin, 2006). For example, in the case rain drop impact on soil or building, the wetted area for liquid transport into the substrate is directly related to the maximum spreading (Blocken and Carmeliet, 2015; Erkal et al., 2012). Different models have been proposed for the maximum spreading ratio. Studies distinguish two main domains: the capillary regime at low impact velocity and the viscous regime at high impact velocity (Clanet et al., 2004). For the viscous regime, based on energy conservation between kinetic and viscous dissipation energy, a scaling of $\beta_{\max}$ with $\mathrm{Re}^{1/5}$ is found (Madejski, 1976; Roisman et al., 2002). Based on an energy approach for a cylindrical disk-shaped droplet at maximum spreading, including kinetic and surface energy before impact and surface energy and viscous dissipation at maximum spreading, a scaling with $\mathrm{Re}^{1/4}$ is found (Pasandideh-Fard et al., 1996). Clanet et al. (2004) proposed, based on momentum conservation, a scaling of $\beta_{\max}$ with $\mathrm{We}^{1/4}$. Laan et al. (2014) showed that, even though the scaling with $\mathrm{We}^{1/4}$ seems consistent for some liquids, such as water, it is not for other liquids, like blood. Based on energy conservation between kinetic and surface energy, a scaling of $\beta_{\max}$ with $\mathrm{We}^{1/2}$ is found (Collings et al., 1990; Bennett and Poulikakos, 1993). However, Laan et al. (2014) showed that none of their data scaled with the dependencies reported in literature ($\mathrm{Re}^{1/4}$, $\mathrm{Re}^{1/5}$,

$We^{1/4}$ and $We^{1/2}$). Therefore, they proposed a solution that introduces a broad crossover regime between the low and high impact velocities by interpolating between $We^{1/2}$ and $Re^{1/5}$. The interpolation between the two scaling laws showed a good agreement with experimental data. This method thus demonstrated clearly that droplet spreading could not be predicted simply by equating kinetic energy either to capillary energy or viscous dissipation, since, in most cases of practical interest, all three energies are important. However, Laan's approach implies that at zero impact velocity the spreading ratio equals zero, which is physically impossible. This means that the liquid wettability on the surface will play a role, determining the spreading ratio at low impact velocity.

This work examines how the wettability of a liquid on a surface influences the maximum spreading at low impact velocity. Therefore, the drop impact experiments are conducted with various liquids on smooth surface with varying wettability. In addition, the experiments are repeated for rough surfaces, whereas it is shown that no additional parameter is required for these kinds of surfaces. More specifically, the aim of this study is to extend the approach of Laan et al. (2014) in order to include the dynamic wettability.

6.2 DROP IMPACT EXPERIMENTS

To analyze the influence of surface tension and viscosity of liquid, five liquids are used: pure ethanol (ethanol), deionized water (water), 1:1 glycerol-water mixture (glycerol 6 mPa·s), 1:1.3 glycerol-water mixture (glycerol 10 mPa·s) and 1:3 glycerol-water mixture (glycerol 51 mPa·s). The liquid density ρ, viscosity μ and surface tension γ are reported in Table 4.1.

Three smooth surfaces are selected with an arithmetic average roughness $R_a < 0.5$ μm: glass, steel and parafilm. The rough surfaces are sandpaper (Silicon Carbide Paper, BUEHLER) with different grit sizes (P120, P240, P600 and P2500), a mono-layer of glass beads sintered to a glass surface (GB) and a sandblasted glass slide (SB). The roughness Ra for the different surfaces is given in Table 6.1.

The wettability in equilibrium conditions is characterized by the droplet contact angle (Table 6.2). At equilibrium conditions, glass and steel are wetting surfaces for all liquids, while parafilm is wetting for ethanol and non-wetting for water and glycerol. The impact conditions are given in Table 6.3.

Table 6.1: Roughness and particle size of surfaces

	Smooth surface		
Parameter	Glass	Steel	Parafilm
R_a (μm)	0.2	0.4	0.5
Averaged particle dia. (μm)	-	-	-

	Rough surface					
	P120	P240	P600	P2500	GB	SB
R_a (μm)	20.8	12.1	6.2	2.7	9.5	4.7
Averaged particle dia. (μm)	125.0	58.5	25.8	8.4	30~50	-

Table 6.2: Equilibrium and dynamic contact angles for different surfaces and liquids

	Glass		Steel		Parafilm	
	θ_{eq} (°)	θ_D (°)	θ_{eq} (°)	θ_D (°)	θ_{eq} (°)	θ_D (°)
Ethanol	~0	52	~0	44	21	63
Water	23	94	61	103	110	108
Glycerol 10 mPa·s	22	123	52	121	94	116

Table 6.3: Drop impact conditions

	D_0 (mm)	V_i (m/s)	We	Re
Ethanol	1.8	0.2 - 2.7	2 - 500	250 - 3 500
Water	1.8 - 3.6	0.2 - 5.0	1 - 1 300	450 - 18 000
Glycerol 6 mPa·s	2.0 - 3.3	0.2 - 5.0	1 - 1 500	60 - 3 200
Glycerol 10 mPa·s	1.8	0.2 - 3.7	1 - 430	40 - 800
Glycerol 51 mPa·s	2.0 - 3.2	1.0 - 5.0	35 - 1 500	45 - 400

Figure 6.1 shows the typical time evolution of the spreading ratio $\beta(t) = D(t)/D_0$, the dynamic contact angle $\theta_D(t)$, as well as the maximum spreading ratio β_{max} and the dynamic contact angle at maximum spreading $\theta_D(t_{max})$ for three liquids on a steel surface with $V_i \sim 1.0$ m/s.

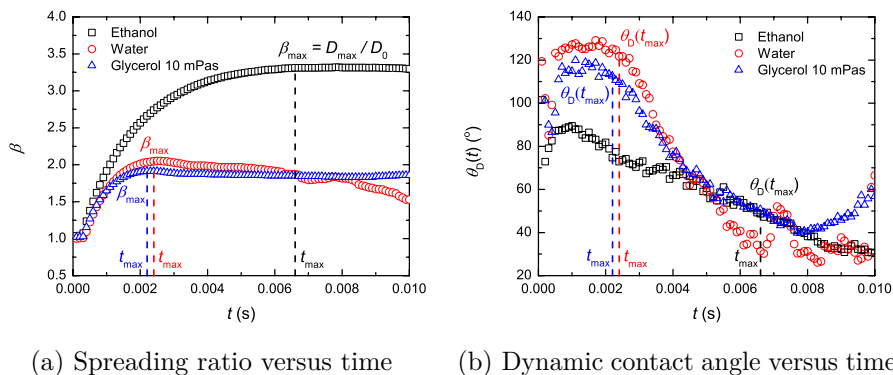(a) Spreading ratio versus time   (b) Dynamic contact angle versus time

Figure 6.1: Time evolution of: (a) spreading ratio; (b) dynamic contact angle for different liquids. Vertical lines indicate the time at maximal spreading.

Figure 6.2 shows snapshots of ethanol, water and glycerol 10 mPa·s impacting on a smooth steel surface at maximum spreading for different impact velocities ($V_i = 0.2$ - 1.8 m/s). The maximum spreading ratio β_{max} increases with impact velocity for all three liquids. Ethanol spreads further and reaches its maximum spreading later in time than water and glycerol. The dynamic contact angle at maximum spreading, also indicated in the figure, is approximately constant over the impact velocity range. We report the average values of dynamic contact angle at maximum spreading in Table 6.2. The dynamic contact angle of ethanol lies in the range of 44° to 63°, which is higher than the equilibrium contact angle (21°). Water and glycerol show also a higher dynamic contact angle (94° to 123°) than the equilibrium contact angle (22° to 61°) for glass and steel, while for parafilm the equilibrium and dynamic contact angles are equal (approx. 110°). For completeness, the time at maximum spreading t_{max} is indicated in the images, which decreases with impact velocity.

There is a clear distinction in the maximum spreading ratio β_{max} between the different liquids on the smooth surfaces (glass, steel and parafilm) as a function of the impact velocity (Figure 6.3). Given a specific liquid, the maximum spreading ratio is almost identical for all
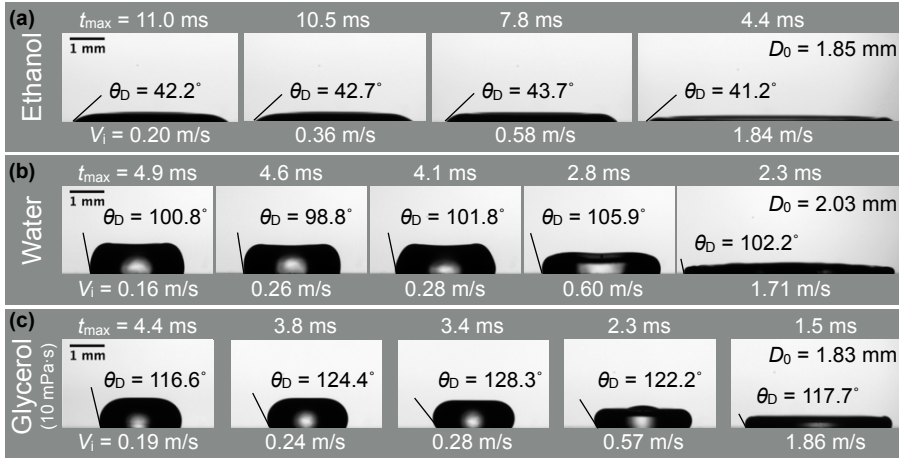
(a) Ethanol

t_{max} = 11.0 ms	10.5 ms	7.8 ms	4.4 ms
1 mm			D_0 = 1.85 mm
θ_D = 42.2°	θ_D = 42.7°	θ_D = 43.7°	θ_D = 41.2°
V_i = 0.20 m/s	0.36 m/s	0.58 m/s	1.84 m/s

(b) Water

t_{max} = 4.9 ms	4.6 ms	4.1 ms	2.8 ms	2.3 ms
1 mm				D_0 = 2.03 mm
θ_D = 100.8°	θ_D = 98.8°	θ_D = 101.8°	θ_D = 105.9°	θ_D = 102.2°
V_i = 0.16 m/s	0.26 m/s	0.28 m/s	0.60 m/s	1.71 m/s

(c) Glycerol (10 mPa·s)

t_{max} = 4.4 ms	3.8 ms	3.4 ms	2.3 ms	1.5 ms
1 mm				D_0 = 1.83 mm
θ_D = 116.6°	θ_D = 124.4°	θ_D = 128.3°	θ_D = 122.2°	θ_D = 117.7°
V_i = 0.19 m/s	0.24 m/s	0.28 m/s	0.57 m/s	1.86 m/s

Figure 6.2: Snapshots of droplets impacting on a steel surface at maximal spreading as a function of impact velocity (V_i = 0.2 - 1.8 m/s): (a) Ethanol, (b) Water, (c) Glycerol 10 mPa·s.

the smooth surfaces. Accordingly, it is found that the liquid, not the substrate, plays the most important role. Ethanol shows the highest maximum spreading, while glycerol shows the lowest maximum spreading. The maximum spreading of water shows a transition between the glycerol at low impact velocity and ethanol at high impact velocity. At low impact velocity, spreading is similar for water and glycerol as their values of surface tension are similar. This shows that the nature of the substrate has only a small influence on the spreading.

Figure 6.4 shows the maximum spreading ratio for liquids of increasing viscosity: water and water-glycerol mixtures 6, 10 and 51 mPa·s, respectively. The liquid viscosity limits the spreading at high velocity, but does not influence the spreading at low velocity, where all curves tend to acquire similar values.

Figure 6.5 shows the maximum spreading ratio for water on rough surfaces: 4 sandpapers of different roughnesses, mono-layered sintered glass beads (GB) and sandblasted glass (SB). Although the surfaces have different roughness and equilibrium wetting characteristics, the maximum spreading ratio is almost identical for all and is equal to the spreading ratio on a smooth surface. It therefore can be concluded that the roughness of each substrate has a rather small influence on the spreading.
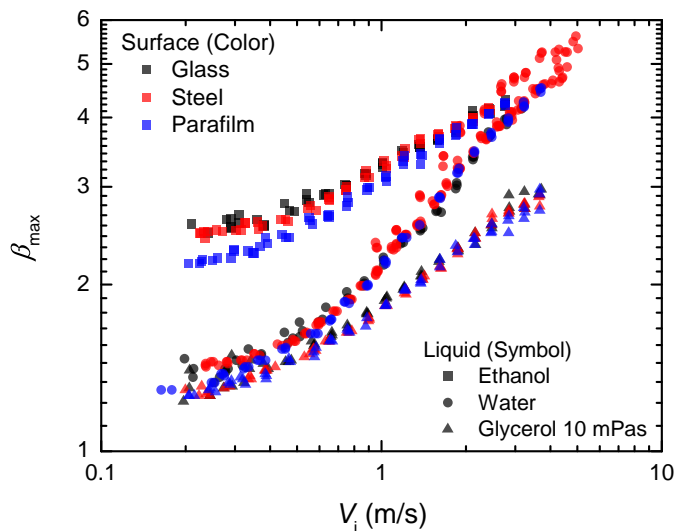
Figure 6.3: Maximum spreading ratio as a function of impact velocity in log-log plot for different liquids on different smooth surfaces.

6.3 SCALING FOR THE MAXIMUM SPREADING DIAMETER

Considering the energy balance of a droplet impacting on a solid substrate, the kinetic energy, the capillary energy and the viscous dissipation have to be taken into account. During impact, the spreading droplet deforms until its maximum diameter $D_{\max}$ within a few milliseconds. The capillary energy can then be written as $E_\gamma \sim \gamma D_{\max}^2$ and the energy dissipated by viscous forces as $E_\mu \sim \mu V_i D_{\max}^5 / D_0^3$ (Collings et al., 1990; Madejski, 1976). In the capillary limit, we can assume that kinetic energy is transformed into capillary energy $E_k \sim E_\gamma$. In this regime, the maximum spreading ratio scales as $\beta_{\max} \sim \mathrm{We}^{1/2}$ (Bennett and Poulikakos, 1993; Eggers et al., 2010). In the viscous limit, the kinetic energy is totally transformed into viscous energy $E_k \sim E_\mu$. Then the maximum spreading ratio scales as $\beta_{\max} \sim \mathrm{Re}^{1/5}$ (Madejski, 1976; Chandra and Avedisian, 1991). The scaling of $\beta_{\max} \sim \mathrm{We}^{1/2}$ implies that, at zero impact velocity, the spreading ratio equals zero, which is physically impossible ($\beta_{\max} \geq 1$). At low impact velocity, the spreading ratio does not tend to zero, but levels off to a limiting value, which is referred to in the following as $\beta_{V_i=0}$ (Figure 6.6).
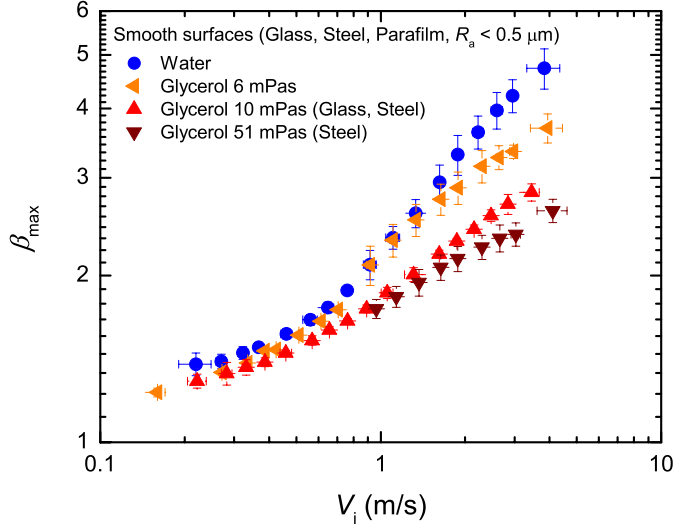
Figure 6.4: Influence of viscosity on maximum spreading ratio for smooth surfaces.

The spreading ratio $\beta_{V_i=0}$ is determined by approximating the measured data by the function:

$$\beta_{\max} = \beta_{V_i=0} + A \cdot \frac{V_i^C}{B + V_i^C} \tag{6.1}$$

where A, B, C and $\beta_{V_i=0}$ are fitting parameters. Figure 6.5 shows that Eq. 6.1 describes the measured data for liquid droplets on a steel surface satisfactorily. Table 6.4 gives the values for $\beta_{V_i=0}$ on different substrates and for different liquids.

Assuming the spreading droplet attains the form of a spherical cap while it keeps a constant volume (Berthier and Beebe, 2007), the spreading ratio $\beta_{V_i=0}$ can be related to a contact angle $\theta_{V_i=0}$. It is necessary to discern between the case for a hydrophilic surface ($\theta_{V_i=0} < 90°$) and hydrophobic surface ($\theta_{V_i=0} > 90°$). The spreading ratio is given by:

$$\beta_{V_i=0} = \begin{cases} \left(\dfrac{4\sin^3\theta_{V_i=0}}{2-3\cos\theta_{V_i=0}+\cos^3\theta_{V_i=0}}\right)^{1/3} & \text{if } \theta_{V_i=0} < 90° \\[2ex] \left(\dfrac{1}{(2+\cos\theta_{V_i=0})\sin^4(\theta_{V_i=0}/2)}\right)^{1/3} & \text{if } \theta_{V_i=0} > 90° \end{cases} \tag{6.2}$$
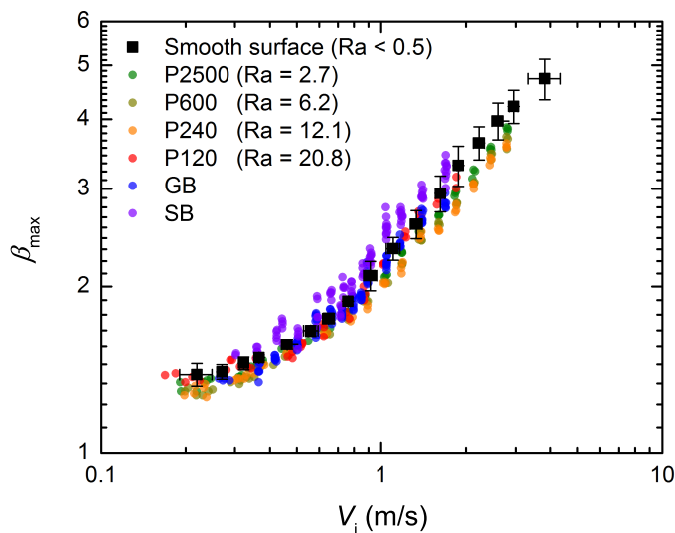
69

Figure 6.5: Influence of roughness on maximum spreading ratio for water droplet.

This equation allows determining a contact angle $\theta_{V_i=0}$ given a value of $\beta_{V_i=0}$. Figure 6.7 compares the dynamic contact angle $\theta_D(t_{max})$, determined from experiments, and the contact angle $\theta_{V_i=0}$, determined from $\beta_{V_i=0}$ using eqn. 6.2. Regardless of a constant offset, the contact angle $\theta_{V_i=0}$ predicts fairly well the measured contact angles during dynamic wetting $\theta_D(t_{max})$. The offset is attributed to an empty volume in the spherical cap model (see figure 6.8), since the real droplet shape does not totally resembles a spherical cap but rather acquires the form of pancake. The missing volume leads to an underprediction of the contact angle by the spherical cap model.

The aim of this analysis is to demonstrate that dynamic wetting plays an important role in the spreading at low velocities, and that the dynamic wetting as characterized by the dynamic contact angle θ_D has to be taken into account for predicting the maximum spreading. The analysis above shows that the capillary energy related to $\theta_{V_i \to 0}$ or to $\beta_{V_i \to 0}$ has to be incorporated in the maximum spreading model.

To do so, capillary energy is added in the low velocity limit, $E_{\gamma 0} \sim \gamma D_{V_i=0}^2$ in the low velocity limit, where $D_{V_i=0} = \beta_{V_i=0} \cdot D_0$. Then the energy balance reads:
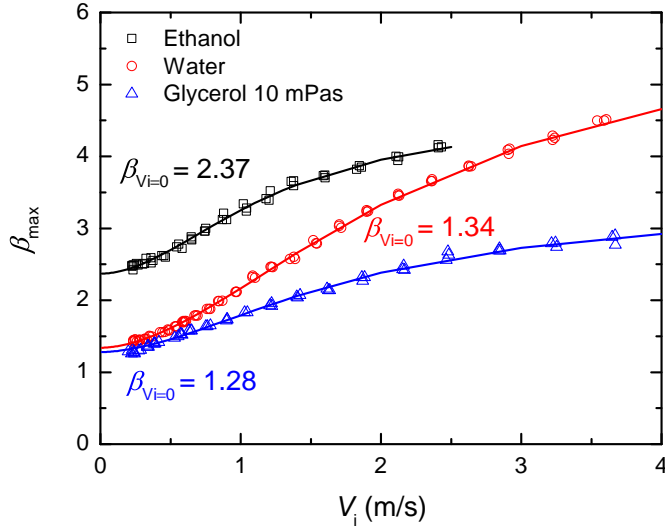
Figure 6.6: Example of the determination of the maximum spreading ratio at zero impact velocity $\beta_{V_i=0}$ by fitting Eq. 6.1 to the measured data.

$$E_k + E_{\gamma 0} \sim E_\gamma$$

$$\text{or} \tag{6.3}$$

$$\rho D_0^3 V_i^2 + \gamma D_{V_i=0}^2 = \gamma D_{\max}^2$$

which leads to

$$\sqrt{\beta_{\max}^2 - \beta_{V_i=0}^2} = \text{We}^{1/2} \tag{6.4}$$

Equation 6.4 shows that we can still assume a scaling with $\text{We}^{1/2}$ after a correction for dynamic wetting using the maximum spreading ratio at zero velocity $\beta_{V_i=0}$ as from Eq. 6.1. After correction, the maximum spreading should still scale with $\text{We}^{1/2}$ and $\text{Re}^{1/5}$ at low and high velocities respectively. Similar to Laan et al. (2014), the interpolation between the low and high impact velocity regimes can be written as:

$$\left(\beta_{\max}^2 - \beta_{V_i=0}^2\right)^{1/2} \propto \text{Re}^{1/5} f(\text{We}) \tag{6.5}$$

Table 6.4: Spreading ratio $\beta_{V_i=0}$ at zero impact velocity

	Ethanol	Water	Glycerol		
			6 mPa·s	10 mPa·s	51 mPa·s
Glass	2.45	1.30	-	1.29	-
Steel	2.37	1.34	1.24	1.28	1.24
Parafilm	2.09	1.25	-	1.24	-
P2500	-	1.24	-	-	-
P600	-	1.21	-	-	-
P240	-	1.23	-	-	-
P120	-	1.29	-	-	-
GB	-	1.20	-	-	-
SB	-	1.30	-	-	-

The function f allows a smooth crossover between the two limits where only one fitting parameter is required to successfully describe the data and is based on the first order Padé approximation (Laan et al., 2014):

$$\left(\beta_{\max}^2 - \beta_{V_i=0}^2\right)^{1/2} \cdot \mathrm{Re}^{-1/5} = \mathrm{We}^{1/2}/(A + \mathrm{We}^{1/2}) \qquad (6.6)$$

Figure **??** shows the rescaled measured data $(\beta_{\max}^2 - \beta_{V_i=0}^2)^{1/2}$ versus the Weber number. It is clear shown that all rescaled data, for all liquids and all substrates (roughness, nature) collapse onto a single curve. In addition, using this approach shows that for low impact velocities the maximum spreading ratio approaches $\beta_{V_i=0}$ and for high impact velocities, the $\mathrm{Re}^{1/5}$ scaling is again present. Moreover, the transition from low impact velocity towards high impact velocity is a function of $\mathrm{We}^{1/2}$. The curve as predicted by Eq. 6.6 ($A = 7.6$) describes the data very well. The larger error bars at low velocity are due to the logarithmic scaling.

This result shows that the proposed approach universally rescales the maximum spreading ratio for different liquids and substrates into a single description, when the dynamic wettability is taken accurately into account. A hypothesis is that the origin of this successful rescaling can be attributed to the presence of a thin air layer between droplet membrane and the surface during spreading, which leads to a similar physical behavior for all surfaces and liquids. The contact angle of the
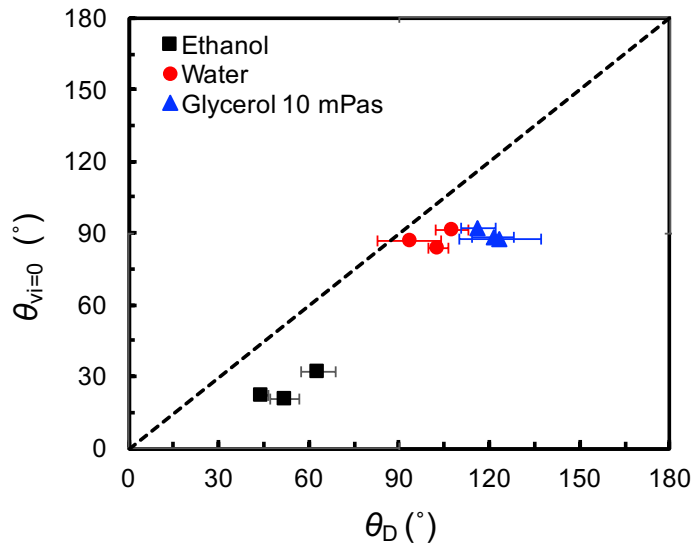
Figure 6.7: Comparison of the dynamic contact angle $\theta_D(t_{max})$ (from experiments) and the contact angle $\theta_{V_i=0}$ determined from $\beta_{V_i=0}$ using eqn. 6.2.

droplet with this air film on the substrate depends primarily on the surface tension of the liquid, and to a lesser extent on the nature and roughness of the substrate.

6.4 CONCLUSIONS

This chapter shows that a universal scaling can be used to describe the maximum spreading of liquid droplets impacting on smooth and rough surfaces from low to high impact velocity. At low impact velocity, the droplet spreading follows a scaling with $We^{1/2}$ after correcting for dynamic wetting behavior. The dynamic wetting is described by the maximum spreading at zero velocity, which can be related to a corresponding contact angle using the spherical cap model. Although the spherical cap model shows some limitation in describing the droplet shape at maximum spreading, it is demonstrated that the contact angle describing the wetting behavior at low impact velocity correlates with the dynamic contact angle at maximum spreading, as determined in our measurements. The influence of the liquid as well as the nature and roughness of the
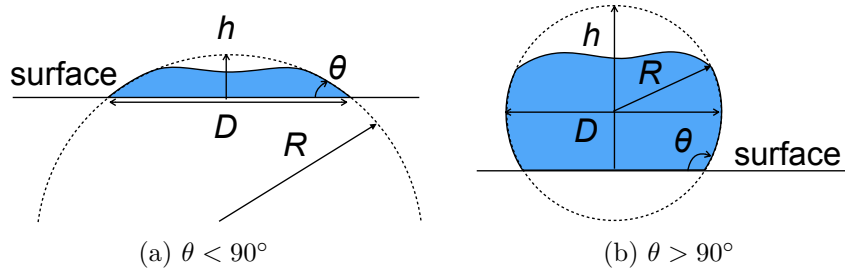
(a) $\theta < 90°$ (b) $\theta > 90°$

Figure 6.8: Spherical cap representation of a droplet with height h, radius R, maximum droplet diameter D and corresponding contact angle θ.

surface is properly taken into account by the rescaling. It is shown that all data for different liquids and substrates collapse onto a single curve by taking into account the dynamic wetting behavior at low impact velocity.

DROP IMPACT ON SMOOTH AND ROUGH GLASS: WETTING TRANSITION BY AIR LAYER

7.1 INTRODUCTION

This work examines the transition from non-wetting to wetting behavior during spreading seen in drop impact experiments conducted on smooth and rough glass surfaces with varying impact velocity. The spreading is seen to abruptly change from non-wetting to wetting and an explanation for this observation is explored in the presence of an air layer between droplet and surface. In addition, the maximum spreading ratio for smooth and rough glass surfaces is analyzed with the universal scaling approach in order to characterize the dynamic wetting behavior of these two surfaces.

7.2 DROP IMPACT EXPERIMENT

To compare the influence of surface tension and viscosity of liquid, three liquids are used: pure ethanol (ethanol), deionized water (water) and 1:1.3 glycerol-water mixture (glycerol 10 mPa·s). The liquid density ρ, viscosity μ and surface tension γ are reported in Table 7.1.

The smooth glass surface used is coverslip glass (Wash-N-Dry™, SIMGA-ALDRICH). A rough glass surface is obtained by sandpaper polishing (P600, made of 25.8 μm size silicon carbide (SiC) particles, BUEHLER) on smooth glass surface. The wettability in equilibrium conditions is characterized by the droplet contact angle (Table 7.2). Also, the quasi-static advancing and receding contact angles for water droplet are reported in Table 7.2. The equilibrium contact is around 23° for smooth and 26° rough glass. The advancing contact angle is for both surfaces around 28°, while the receding contact angle is ~0°.

Roughness is measured by a contact profilometer (Surftest-211, Mitutoyo) equipped with a diamond-tipped stylus. Each specimen is traced in 15 arbitrary locations near the location of droplet impact over a 0.8 mm sampling length. The roughness value is the arithmetic average of

Table 7.1: Properties of liquids and drop impact conditions

	Liquid properties at 25°C		
	ρ (kg/m^3)	μ (mPa·s)	γ (mN/m)
Ethanol	789	1.2	23.2
Water	998	1.0	72.8
Glycerol 10 mPa·s	1158	10.0	68.3
	Impact conditions			
	D_0 (mm)	V_i (m/s)	We	Re
Ethanol	1.8	0.2 - 2.7	2 - 500	250 - 3 500
Water	1.8 - 2.0	0.2 - 4.5	1 - 1 300	450 - 18 000
Glycerol 10 mPa·s	1.8	0.2 - 3.7	1 - 430	40 - 800

Table 7.2: Contact angles and roughness parameter R_a for smooth and rough glass surfaces

	Smooth	Rough
θ_{eq} (°)	22.8 ± 4.3	25.6 ± 2.8
θ_{adv} (°)	28.6 ± 3.4	28.4 ± 1.1
θ_{rec} (°)	22.8 ± ~0 ± ~0	
R_a (μm)	by stylus < 0.05	sample 1 0.15 ± 0.03
	by AFM < 0.005	sample 2 0.29 - 1.3

absolute measured values. The roughness R_a for smooth glass is 0.05 μm, and for rough glass 0.15 μm. A second sample, sent to another type of scanner at University of Amsterdam, was scanned 5 times with R_a = 0.292, 0.407, 0.460, 0.716 and 1.301 μm. The roughness R_a for the smooth and rough glass surfaces is given in Table 7.2. The roughness of rough glass surface is around one order of magnitude larger than the one of smooth glass.

In addition, the roughness of smooth glass is measured using atomic force microscopy (AFM) to capture features smaller than the resolution of stylus profilometer (Figure 7.1a and b), by the group of Prof. Daniel Bonn of University of Amsterdam. The local roughness reaches 6 nm on these small surfaces. Although, at nanoscale, the smooth glass surface is somewhat wavy in nanometer scale due to the manufacturing method of
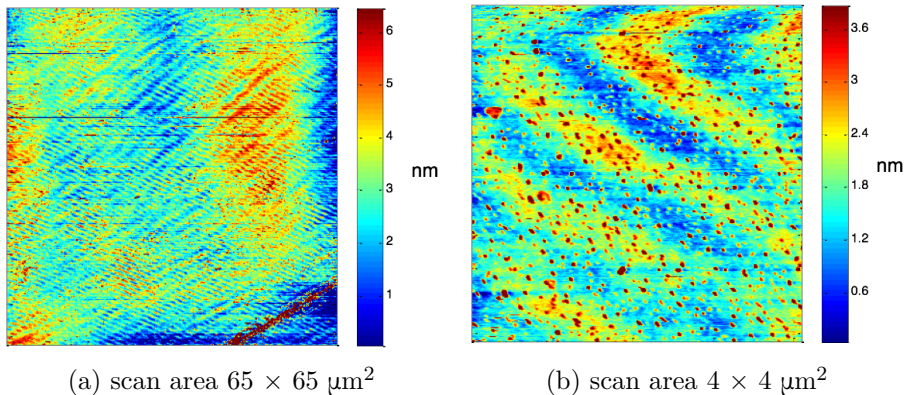
(a) scan area 65 × 65 μm²

(b) scan area 4 × 4 μm²

Figure 7.1: AFM for smooth glass surface showing roughness.

glass plate, it is an almost ideal flat surface compared to the rough glass surface.

7.3 RESULTS

The spreading behavior is illustrated with high-speed images for the smooth (Figure 7.2a) and rough (Figure 7.2b) glass surfaces. Initial contact of the droplet with the smooth surface shows a hydrophobic contact angle. Then, the drop shows a sudden transition from hydrophobic ($\theta_D > 90°$) to hydrophilic ($\theta_D < 90°$) behavior at $t = 1.2$ ms, seen on the right side of the droplet. The transition produces a capillary wave propagating on the surface of the droplet. The capillary wave seems to induce the transition also to occur on left side. After this transition to hydrophilic contact angles, further spreading follows a hydrophilic behavior, where spreading is not only driven by inertia but also by capillary forces. On the other hand, the spreading on rough glass surface does not show this transition until it reaches maximum spreading. The water droplet on the rough glass surface shows a hydrophobic behavior during the whole spreading process and the droplet spreads mainly by inertia driven flow. After maximum spreading, the dynamic contact angle becomes less than 90° after reaching maximum spreading. It is further analyzed this wetting transition and its impact on spreading ratio.

Figure 7.3 shows the time evolution of the spreading ratio $\beta(t) = D(t)/D_0$ and the dynamic contact angle $\theta_D(t)$ at three impact velocities. At $V_i \sim 0.3$ m/s, the water droplet spreads more on the smooth surface
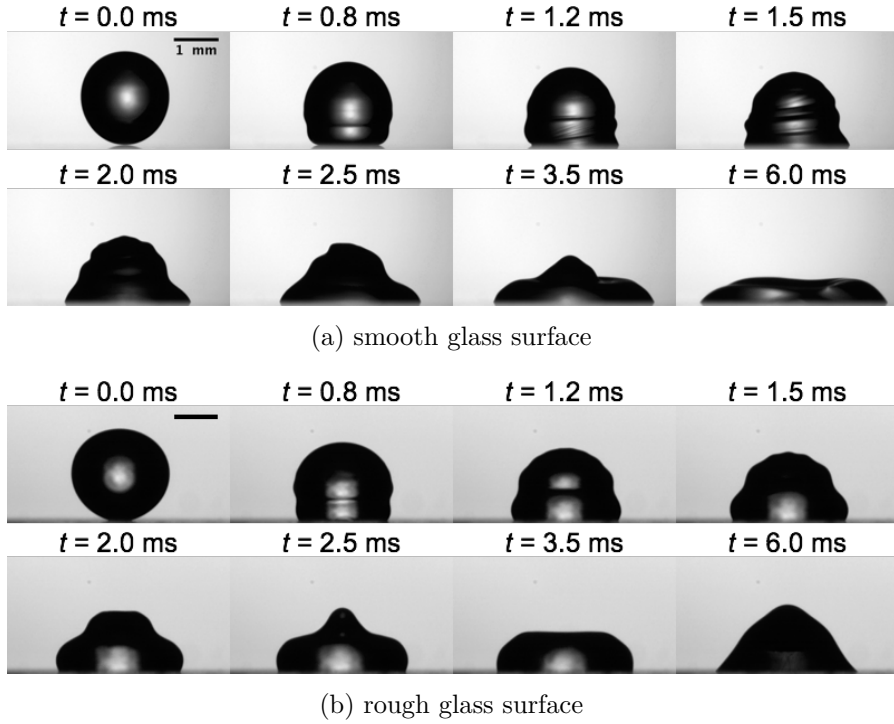
(a) smooth glass surface


(b) rough glass surface

Figure 7.2: Snapshots of drop impact ($V_i \sim 0.3$ m/s) on (a) smooth glass and (b) rough glass surfaces showing wetting transition occurring on smooth glass.

than on rough surface, and the spreading continues almost until $t \sim 9$ ms. The dynamic contact angle on the smooth surface shows a remarkable sharp transition at $t \sim 1$ ms from $138°$ to $85°$ (Figure 7.3b black and gray circles), while the dynamic contact angle on the rough surface shows a smooth transition from $118°$ to $87°$. For an impact velocity of $V_i \sim 1.3$ m/s and 2.1 m/s, a different behavior is observed. The rough and smooth surfaces show a same tendency, attaining a clear maximum spreading ratio followed by a slow decrease of the spreading ratio. The spreading ratio on smooth surface is somewhat larger than the one on rough surface. The dynamic contact angles on smooth and rough surfaces are quite similar. At the higher impact velocities, the smooth surface does not show a wetting transition in contrast to the case of low impact.

A closer look is taken at this wetting transition during spreading analyzing the high-speed snapshots of water drop impact on smooth
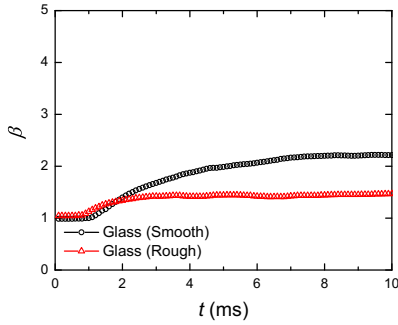
(a) spreading ratio ($V_i \sim 0.3$ m/s)
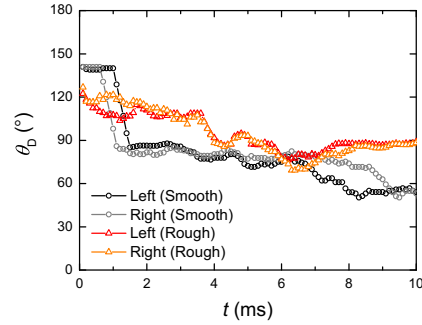
(b) dynamic contact angle
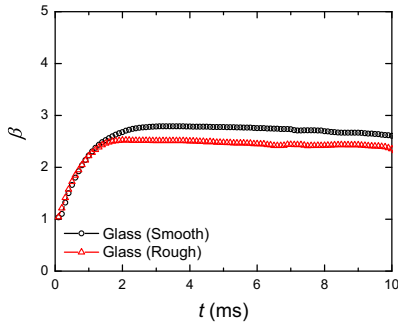
(c) spreading ratio ($V_i \sim 1.3$ m/s)
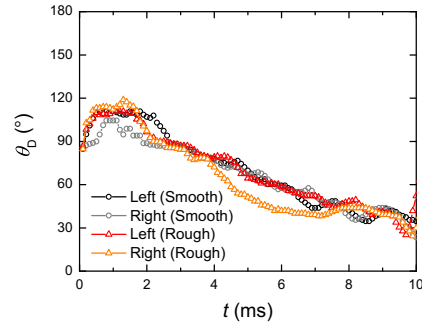
(d) dynamic contact angle
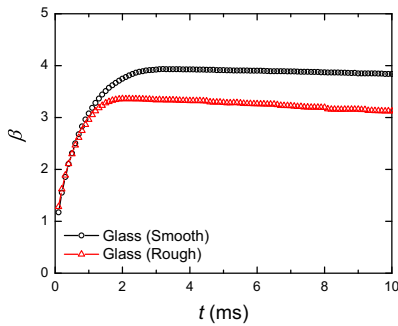
(e) spreading ratio ($V_i \sim 2.1$ m/s)
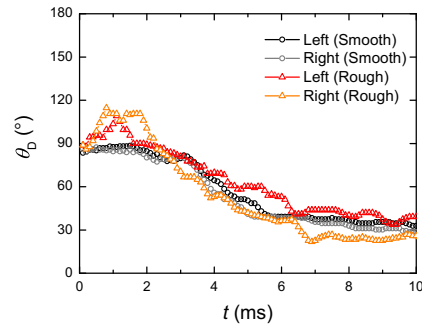
(f) dynamic contact angle

Figure 7.3: Time evolution of (a, c, e) spreading ratio and (b, d, f) dynamic contact angle on smooth and rough surfaces, for impact velocity (a, b) $V_i \sim 0.3$ m/s, (c, d) $V_i \sim 1.3$ m/s, (e, f) $V_i \sim 2.1$ m/s.

glass at low impact velocities ($V_i = 0.2 - 0.9$ m/s) . After impact, the droplet is deformed by inertia and does not wet the smooth surface, as seen in the non-wetting images (left column Figure 7.4). It is observed that this non-wetting behavior changes to wetting behavior, when the droplet contact angle suddenly changes, which is marked in the images as wetting transition (second column). This is transition in contact angle is explained by the fact that the water at this transition "touches" the smooth surface. By touching the surface, a capillary wave is generated, soon followed by the establishment of wetting conditions on the all sides of the droplet. After the wetting transition, the droplet shows a hydrophilic behavior on the smooth surface. The time when wetting transition occurs decreases with increasing impact velocity. At $V_i = 0.2$, 0.4 and 0.6 m/s, the wetting transition occurs at $t = 2.2$, 0.8, 0.4 ms, respectively.

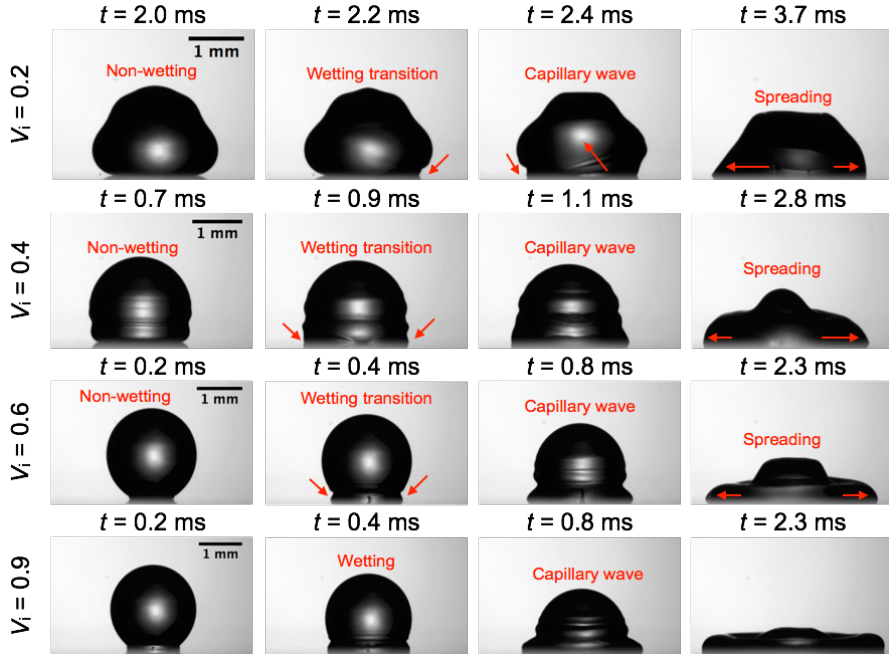Figure 7.4: Sequence of snapshots for wetting transition on smooth glass at different impact velocities ($V_i = 0.2 - 0.9$ m/s).

The maximum spreading ratio β_{max} as a function of impact velocity for water droplets on smooth and rough glass is given in Figure 7.5. The results include also the spreading ratio for ethanol and glycerol on the smooth glass surface. In general, the maximum spreading ratio β_{max}

increases with impact velocity for all liquids and surface. There is a clear distinction in maximum spreading ratio $\beta_{\max}$ between the different liquids for the smooth glass surface. Ethanol shows a higher maximum spreading ratio due to its lower surface tension, and a wetting transition does occur since the spreading droplet is already in dynamic wetting behavior. Glycerol shows a lower maximum spreading ratio due to its higher viscosity, showing dynamic non-wetting behavior and no wetting transition occurs due to the high viscosity. The spreading of water on rough glass shows a transition from the glycerol curve at low impact velocity to the curve of ethanol at high impact velocity. The maximum spreading ratio curve on smooth glass forms a scattered curve, but in general the maximum spreading ratio is higher for smooth glass than for rough glass. The higher spreading ratio for smooth glass is attributed to the wetting transition and the appearance of capillary forces. At high impact velocity, where no wetting transition is observed, the maximum spreading on smooth and rough surface almost coincide.

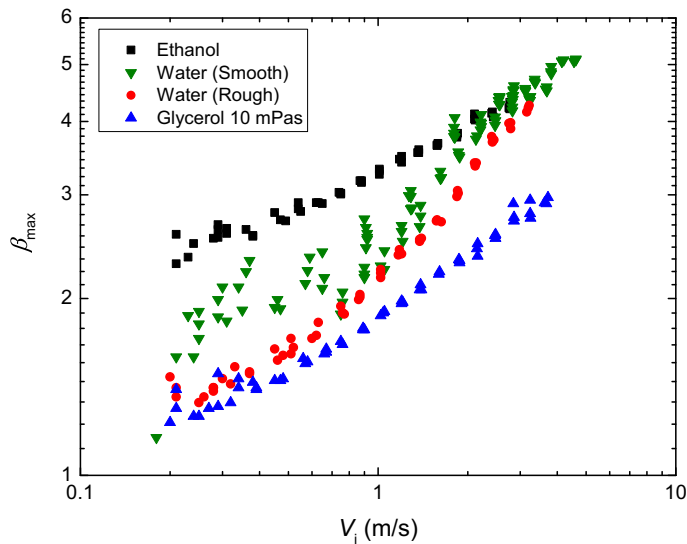Figure 7.5: Maximum spreading ratio as a function of impact velocity in log-log plot for different liquids on different smooth surfaces.

The explanation for the observation of a wetting transition for smooth glass at low impact velocity, while this transition does not occur for rough glass and for high impact velocity on smooth glass is based on the hypothesis of the existence of an air layer between the impinging droplet

and the glass surface. It is noted that the air layer between droplet and surface was not observed directly, and the explanation needs more direct demonstration. However, the abrupt change in wetting behavior and the observation of capillary waves point to the breaking of surface layer of the droplet when touching the roughness of the smooth glass surface. This 'touching' behavior is explained by the not sufficient protection by the air layer between the impinging droplet and the glass surface. The existence of such as layer has been demonstrated by several investigations (Mani et al., 2010; Ruiter et al., 2015). The air layer on a rough surface is assumed to be built up by compressed air pockets in the roughness of the surface as well as an air layer above this roughness layer (Figure 7.6). This air layer makes the droplet to behave as a balloon, which explains the non-wetting. This behavior occurs on rough surfaces, but also on smooth surfaces at high impact velocity. However, the air layer is assumed to be thinner on a smooth surface and breakage of the water balloon is more likely to occur. In figure 7.5 it was found the maximum spreading on smooth glass at low impact velocity to be essentially stochastic. This random behavior is explained by the fact that the breakage of the water balloon depends on the probability that the droplet hits an irregularity on the smooth surface higher than the thin air film thickness (Figure 7.6).
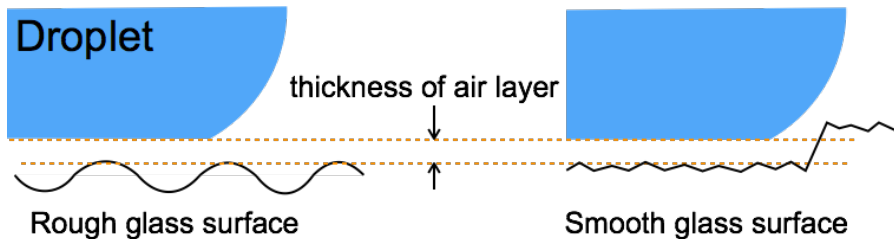
Figure 7.6: Schematic of drop spreading on rough and smooth glass surfaces showing an air layer on the rough surface supported by air pockets in roughness and irregularity on smooth surface.

7.4 SCALING FOR THE MAXIMUM SPREADING DIAMETER

Based on the universal scaling proposed in chapter 6, the maximum spreading can be rescaled taking into account the dynamic wetting behavior at low impact velocity. The maximum spreading ratio at zero

impact velocity $\beta_{V_i=0}$ is estimated using Eq. 6.1 (Figure 7.7). The estimated $\beta_{V_i=0}$ values are reported in the inset table in Figure 7.7.
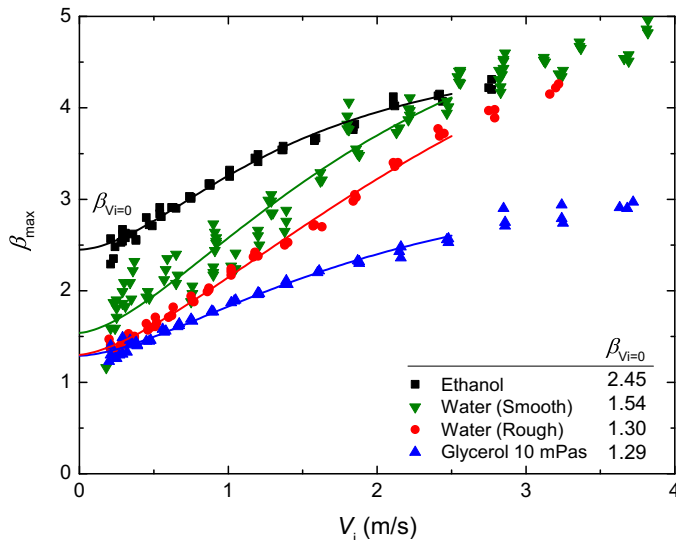
Figure 7.7: Maximum spreading ratio at zero impact velocity $\beta_{V_i=0}$ determined by fitting Eq. 6.1 to the measured data. The inset table gives the estimated $\beta_{V_i=0}$ values for different liquids on smooth glass surface and water on rough glass surface.

Figure 7.8 shows the rescaled measured data $(\beta_{max}^2 - \beta_{V_i=0}^2)^{1/2}$ versus the Weber number. The curve shown is predicted using Eq. 6.6 with $A = 7.6$. It is clear that all rescaled data, including different liquids on the smooth glass surface and water on rough and smooth glass surface collapse onto a single curve. This result shows that the proposed approach universally rescales the maximum spreading ratio including the effect of wetting transition into a single curve when the dynamic wetting behavior is taken accurately into account.

This result shows that the proposed approach universally rescales the maximum spreading ratio including the effect of wetting transition into a single curve when the dynamic wettability is taken accurately into account. The underlying hypothesis, although hard to demonstrate experimentally, is that a thin air layer between droplet membrane and the surface during spreading exists leading to a dynamic hydrophobic behavior. Even though a wetting transition may happen due to a breakage of the air film, the proposed rescaling with the $(\beta_{max}^2 - \beta_{V_i=0}^2)^{1/2}$, where
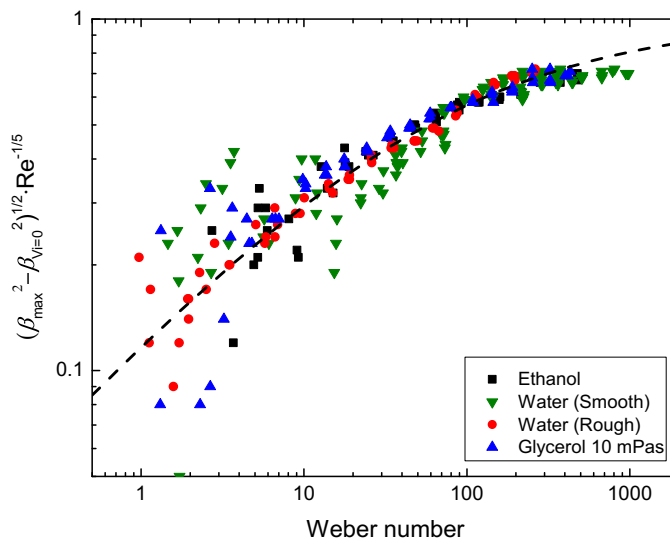
Figure 7.8: Rescaled maximum spreading ratio as a function of Weber number in log-log plot for all liquids and smooth and rough glass surfaces. The dashed line represents the first order Padé approximation (Eq. 6.6) with $A = 7.6$.

$\beta_{V_i=0}$ is the maximum spreading ratio at zero impact velocity, is able to predict the maximum spreading by taking into account the dynamic wetting behavior of the surface.

7.5 CONCLUSION

In this chapter, the maximum spreading on smooth and rough glass surfaces is studied for different liquids and impact velocities. An anomalous behavior was observed for smooth glass at low impact velocity, where a wetting transition was found to occur from non-wetting conditions, accompanied by capillary waves in the droplet, leading to an increase of the maximum spreading ratio. This wetting transition does not occur on a smooth glass surface at high impact velocity and for a rough glass surface over the whole impact velocity range. Wetting transition is explained by the breaking the droplet balloon hitting a small roughness on the surface. This rather random hitting event leads to a touching of the droplet balloon to the substrate, breakage of the surface layer and a change from dynamic non-wetting to dynamic wetting conditions on the

hydrophilic porous surface. All data including impacts measurements of different liquids on smooth and rough surfaces are successfully rescaled introducing a correction for the maximum spreading ratio at zero impact velocity. It is shown that the proposed approach universally rescales the maximum spreading ratio into a single curve, taking into account correctly the influence of liquid characteristics and the phenomenon of wetting transition during spreading.

ENERGY BALANCE APPROACH FOR MAXIMUM SPREADING DIAMETER

This chapter is based on the paper Lee JB, Derome D, Guyer R, Carmeliet J. "Modeling the maximum spreading of liquid droplets impacting on wetting and nonwetting surfaces" Langmuir, 32 (5), pp 1299–1308 (Lee et al., 2016b).

8.1 INTRODUCTION

A common interest in drop impact dynamics is the analysis and prediction of the maximum spreading ratio $\beta_{\max} = D_{\max}/D_0$ where $D_{\max}$ is the maximum spreading diameter and D_0 the initial drop diameter prior to impact. Controlling or predicting maximum spreading is essential for many problems involving the deposition of an impacting drop. A large number of parameters, such as drop size, impact velocity, liquid properties (density, viscosity and surface tension), surface roughness and wettability, plays a role in the maximal spreading achieved by a droplet. Spreading is governed by the balance of the inertial, capillary and viscous forces. The energies associated with these forces in spreading are kinetic ($E_k = \rho D_0^3 V_i^2$), capillary ($E_\gamma = \gamma_{\mathrm{LV}} D_0^2$) and viscous ($E_\mu = \mu V_i D_0^2$) energy. Most of the existing models are formulated based on two dimensionless parameters: Weber number ($\mathrm{We} = \rho V_i^2 D_0/\gamma_{\mathrm{LV}}$), the ratio between the inertial and capillary forces (kinetic and capillary energies, E_k/E_γ), and Reynolds number ($\mathrm{Re} = \rho V_i D_0/\mu$), the ratio between the inertial and viscous forces (kinetic and viscous energies, E_k/E_μ), where ρ is the liquid droplet density, γ_{LV} the surface tension, μ the viscosity, D_0 the initial drop diameter and V_i the impact velocity. In this chapter, the role of parameters, such as surface tension, viscosity, wettability and surface roughness, on the maximal spreading ratio $\beta_{\max}$ is investigated experimentally and a new updated model for the maximum spreading ratio is proposed using the energy balance approach. In contrast to most of the earlier studies, the spreading behavior is studied from the capillary to the viscous regime and the asymptotic condition is explained using the

Table 8.1: Mean and standard deviation of surface roughness R_a for five substrates

	Al sm	Aluminum	Al ro	Steel	Parafilm
R_a (μm)	0.05	0.41	0.69	0.42	0.45
standard deviation	0.00	0.06	0.08	0.05	0.06

Al sm: smooth; Aluminum: reference; Al ro: rough

energy balance approach. Three different liquids with different surface tension and viscosity, three different surfaces with different wettability, and three surface roughnesses are used to achieve a comprehensive picture from capillary to viscous regime, in order to analyze the quality of the prediction model for the maximum spreading diameter.

8.2 DROP IMPACT EXPERIMENT

8.2.1 *Material and methods*

Influence of the liquid-gas surface tension and the liquid viscosity was investigated on the spreading of a droplet using three different liquids: ethanol, water (deizonized) and a 55% glycerol-water mixture (referred to as glycerol). The properties of the liquids are given in Table 8.1. Taking water as the reference liquid, ethanol shows a three times smaller surface tension than water, while the viscosity is quite similar. Glycerol shows a 10 times larger viscosity than water, while the surface tension is quite similar to water. Three substrates are considered: steel, aluminum and a paraffin/thermoplastic film (trademark Parafilm). For aluminum, the original smooth surface is roughened by sand paper, attaining three roughness values, referred to as Al sm (smooth), aluminum (reference) and Al ro (rough), given in Table 8.1. The arithmetic average roughness (average height irregularities) R_a ranges between 0.41 to 0.69 μm for the rough surfaces and is less than 0.05 μm for smooth aluminum.

The wettability of the substrate is characterized by the equilibrium (θ_{eq}), advancing (θ_{adv}) and receding (θ_{rec}) contact angle. The results are presented in Figure 8.1. Ethanol shows in most cases a zero contact angle, indicating that ethanol is totally wetting the surface in quasi-static conditions. Ethanol shows on smooth aluminum and parafilm an

(a) equilibrium contact angle

(b) advancing contact angle

(c) receding contact angle

(d) dynamic at maximum spreading
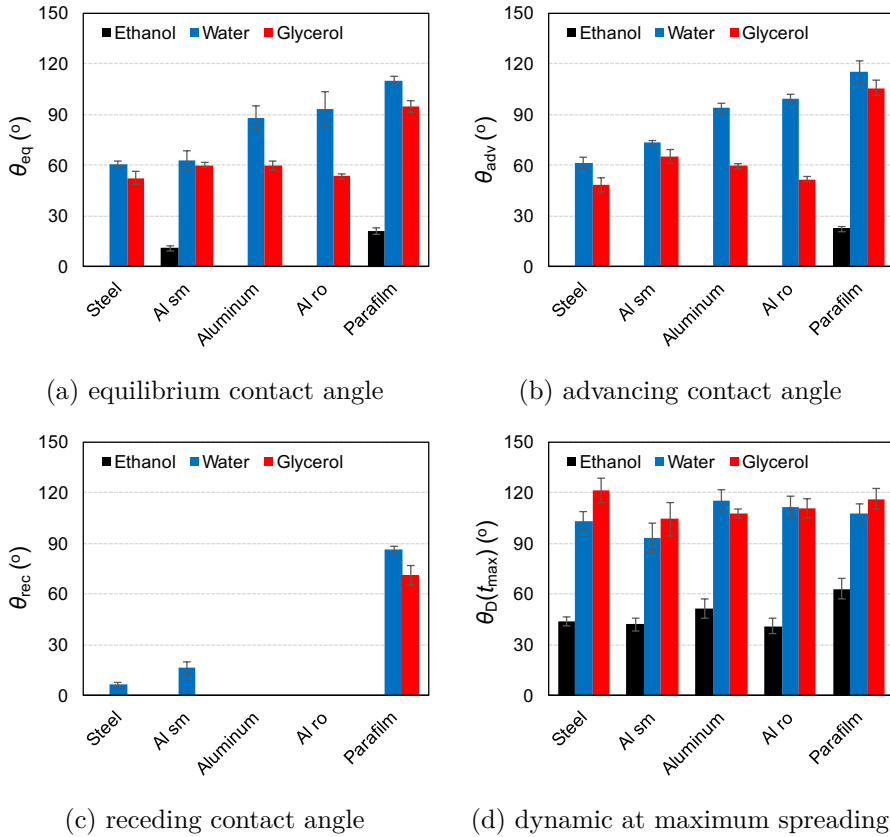
Figure 8.1: Wettability characterized by the contact angle for ethanol, water and glycerol on steel, smooth, reference and rough aluminum and parafilm.

equilibrium contact angle higher than zero, i.e. $11°$ and $22°$. Glycerol shows a wetting behavior on steel and aluminum (from smooth to rough) with an equilibrium contact angle between $52°$ and $60°$, while it is non-wetting on parafilm. Water shows the highest equilibrium contact angles, and is wetting on steel and aluminum, while it is non-wetting on rough aluminum and parafilm. In general, it was found that the advancing contact angle is quite similar to the equilibrium contact angle (differences less than 16%). The receding contact angle is much lower than the equilibrium contact angle and, in several cases, cannot be measured, since the droplet remained pinned. In the following, the equilibrium

contact angle will be compared to the dynamic contact angle during droplet spreading.

For the impact measurements, as the release height varies from 3 to 820 mm, the impact velocity ranges between 0.2 and 3.7 m/s (see Table 8.2) with a relative error of 2%.

Table 8.2: Properties of the three liquids and drop impact conditions

	Liquid properties at 25°C		
	ρ (kg/m^3)	μ (mPa·s)	γ (mN/m)
Ethanol	789	1.2	23.2
Water	998	1.0	72.8
Glycerol 10 mPa·s	1158	10.0	68.3

	Impact conditions		
	D_0 (mm)	V_i (m/s)	We	Re
Ethanol	1.8, 2.0	0.2 - 2.4	2 - 315	260 - 2 900
Water	2.0	0.2 - 3.2	1 - 290	350 - 6 300
Glycerol 10 mPa·s	1.8	0.2 - 3.7	1 - 414	40 - 750

8.2.2 *Experimental results*

Figure 8.2 shows that the ethanol droplet spreads more than the water droplet on all three surfaces at low impact velocity ($V_i = 0.5$ m/s). Ethanol reaches its maximum diameter later in time than water, indicated by the vertical lines in Figure 8.3a. Until maximum spreading, the droplet diameter evolution is rather similar for all three surfaces. The dynamic contact angle at maximum spreading for ethanol is around 60° showing a dynamic wetting behavior (Figure 8.2b). The dynamic contact angle for water is higher than for ethanol and reaches a value of around 105° at maximum spreading, showing a dynamic non-wetting behavior for all surfaces during spreading.

Figures 8.3a and 8.3b show images of the droplets at different times for ethanol and water respectively. At maximum spreading, ($t_{max} = 2.7$ ms) the water droplet shows a pancake form with a contact angle higher than 90°, showing a dynamic non-wetting behavior. At the same time, the ethanol droplet shows a spreading lamella at the droplet contact line. At maximum spreading (7.8 ms), ethanol forms a flat liquid layer with
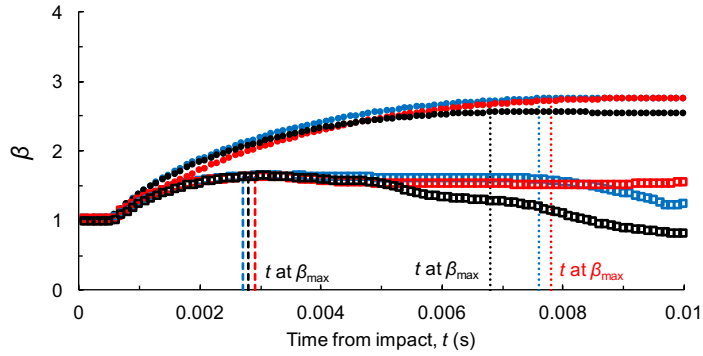
(a) spreading diameter ratio
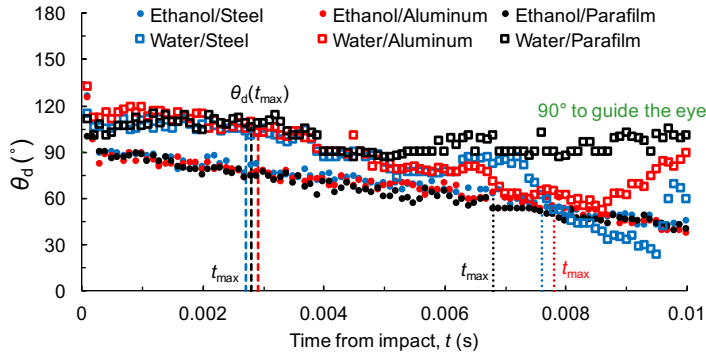
(b) dynamic contact angle

Figure 8.2: Time evolution of (a) spreading diameter ratio β and (b) dynamic contact angle θ_D at low impact velocity ($V_i = 0.5$ m/s) for ethanol and water droplet on three substrates: steel (blue), aluminum (red), and parafilm (black).

a dynamic contact angle lower than 60°, showing a dynamic wetting behavior.

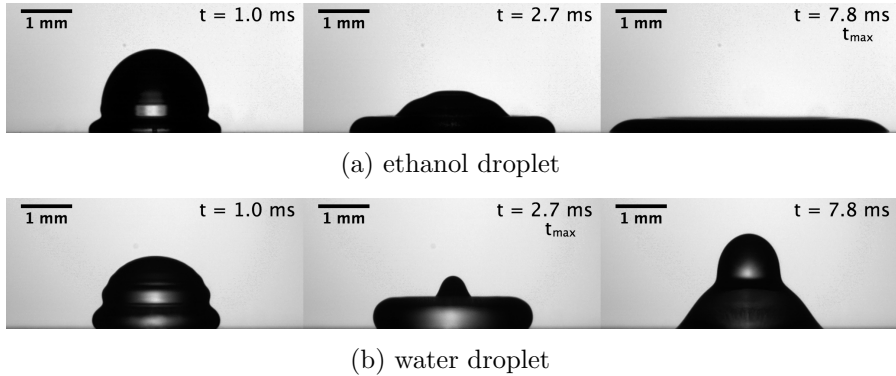(a) ethanol droplet

(b) water droplet

Figure 8.3: Snapshots of drop impact on aluminum surface for (a) ethanol and (b) water droplets at $V_i = 0.5$ m/s.

In Figure 8.4a and 8.4b the results for two liquids, water and glycerol, at high impact velocity ($V_i = 2.1$ m/s) are represented. Glycerol spreads less than water, reaching its maximum diameter earlier in time, which is attributed to its higher viscosity, causing that the kinetic energy is dissipated faster. Figure 8.4b shows that the dynamic contact angle during spreading and at maximum spreading is quite similar for water and glycerol ranging from 107° to 123°, showing a dynamic non-wetting behavior.

Figure 8.5a shows that the water droplet displays a spreading lamella at short impact time. Visual observation from above indicates that the lamella evolves to a fingering shape at longer time. In Figure 8.5b, glycerol also shows initially a lamella, but later a pancake form appears.

Figure 8.6 shows that the maximum spreading ratio β_{max} for three substrates with same roughness (steel, aluminum, parafilm), given a specific liquid, is almost identical for all the surfaces. Ethanol shows the highest maximum spreading, glycerol the lowest spreading, while water shows a transition behavior between both. At low impact velocity, spreading is similar for water and glycerol as the values for surface tension of these liquids are similar. At low impact velocity, the data level off to a constant spreading ratio, which will be denoted further by $\beta_{V_i=0}$. The data for ethanol and glycerol at high impact velocity tend to an asymptotic behavior with constant slope. It should be noted that water does not attain this asymptotic behavior, since splashing occurs before.
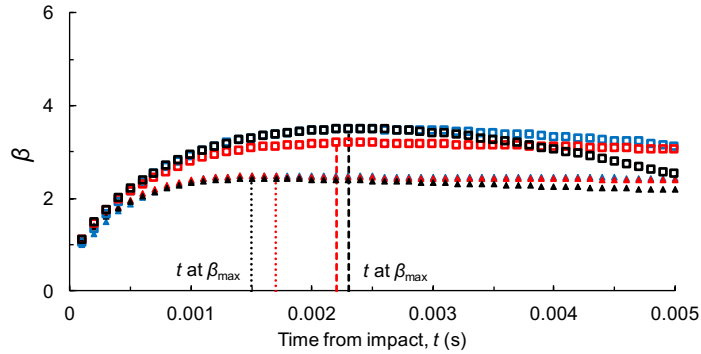
(a) spreading diameter ratio
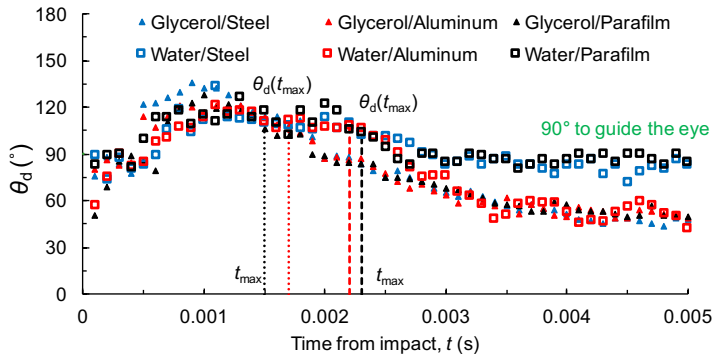
(b) dynamic contact angle

Figure 8.4: Time evolution of (a) spreading diameter ratio β and (b) dynamic contact angle θ_D at low impact velocity ($V_i = 2.1$ m/s) for water and glycerol droplet on three substrates: steel (blue), aluminum (red), and parafilm (black).

(a) water droplet (b) glycerol droplet

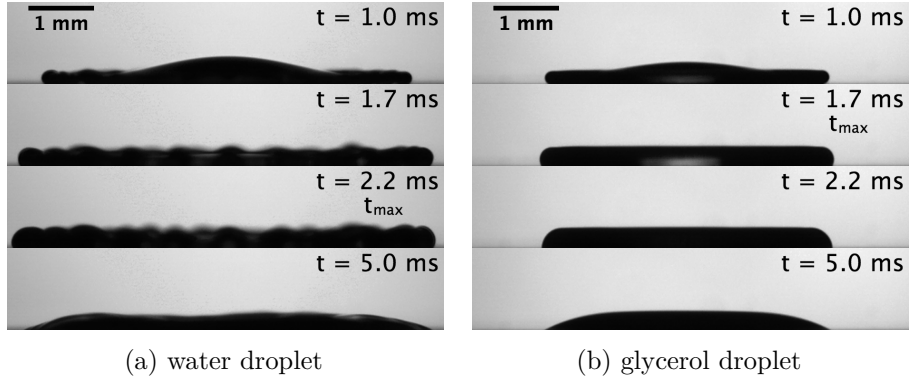Figure 8.5: Snapshots of drop impact on aluminum surface for (a) water and (b) glycerol droplets at $V_i = 2.1$ m/s.

Figure 8.7 shows the maximum spreading ratio for the aluminum surface with increasing roughness. The maximum spreading ratio data per liquid almost coincide, showing that roughness plays a less important influence on maximum spreading. It is likely that the nature, not of the substrate, but of the liquid plays the most important role in the maximum spreading of a droplet on a solid surface.

Figure 8.8 shows, as an example, the dynamic contact angle at maximum spreading $\theta_D(t_{max})$ in function of impact velocity for the different liquids on the steel substrate. The dynamic contact angle $\theta_D(t_{max})$ is quite constant over the impact velocity range, and depends mainly on the nature of the fluid. It is noted that, in supplementary experiments, the dynamic contact angle for the other substrates follows the same observations. The average values of the dynamic contact angle at maximum spreading are reported in Table 8.3. Ethanol shows a dynamic contact angle between 41° and 63° and is dynamically wetting all substrates. Water and glycerol show a contact angle ranging from 93° to 121°, and are dynamically non-wetting. Comparing the dynamic and equilibrium contact angles (Figure 8.1), the dynamic contact angle is higher than the equilibrium contact angle, except for water on parafilm where the two contact angles are quite similar. It is observed that the dynamic contact angle depends less on the nature and roughness of the surface than the equilibrium contact angle does.

In Figures 8.9a-d, the time at maximum spreading is shown. Figure 8.9a shows that the time at maximum spreading decreases with impact velocity. Ethanol shows a higher spreading time than water and glycerol, which is
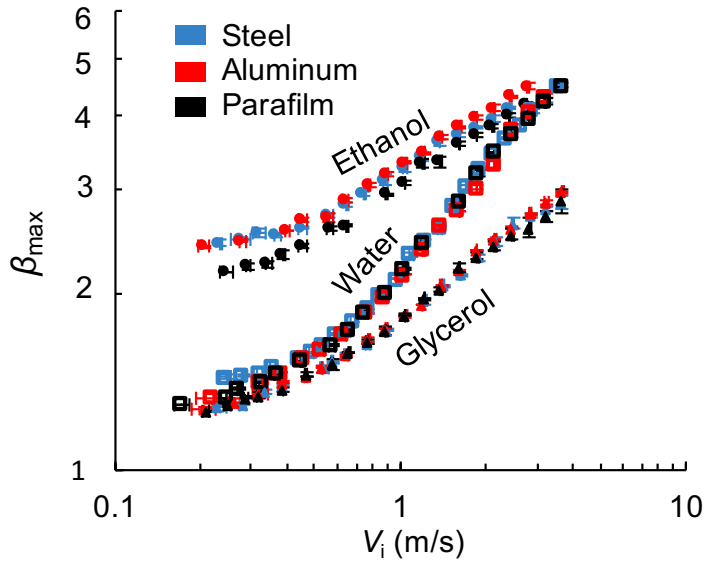
Figure 8.6: Maximum spreading ratio β_{max} versus impact velocity V_{i} for different liquids on smooth surface (Steel, Aluminum, Parafilm).
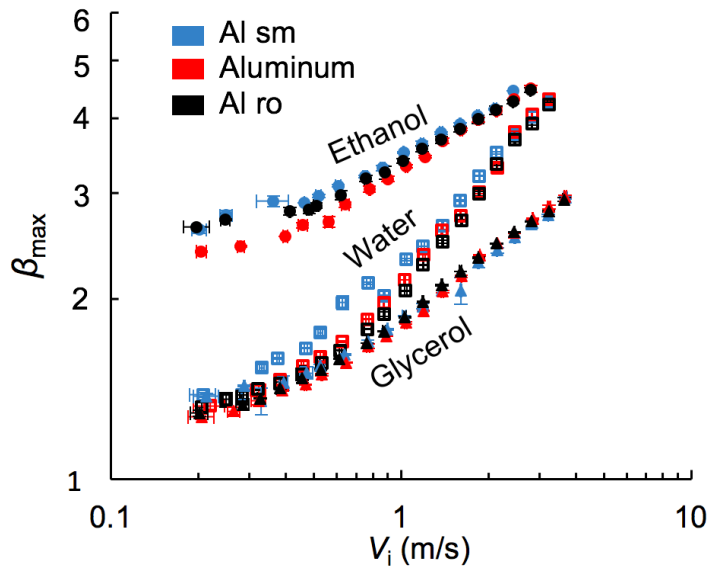
Figure 8.7: Maximum spreading ratio β_{max} versus impact velocity V_{i} for different liquids on aluminum with different roughness.
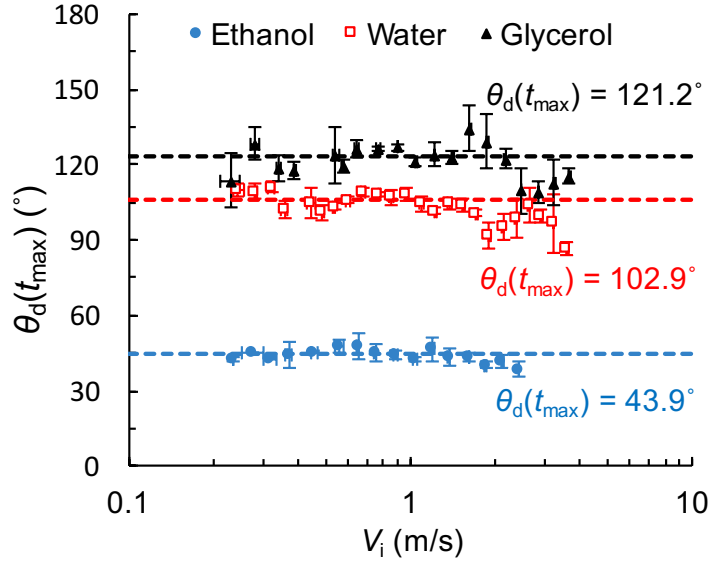
Figure 8.8: Dynamic contact angle at maximum spreading $\theta_D(t_{max})$ as a function of the impact velocity V_i on steel substrate.

Table 8.3: Dynamic contact angle at maximum spreading

$\theta_D(t_{max})$	Al sm	Aluminum	Al ro	Steel	Parafilm
Ethanol	42.2	51.4	41.2	43.9	63.0
standard deviation	3.8	5.8	4.8	2.5	5.9
Water	93.1	115.5	111.1	102.9	107.6
standard deviation	8.8	5.8	6.9	3.2	5.6
Glycerol	104.2	107.6	110.7	121.2	116.2
standard deviation	9.8	2.9	5.6	6.9	5.9

(a) measured data

(b) rescaled data

(c) comparison of measured data with Eq. **??**

(d) comparison of measured data with Eq. 8.5
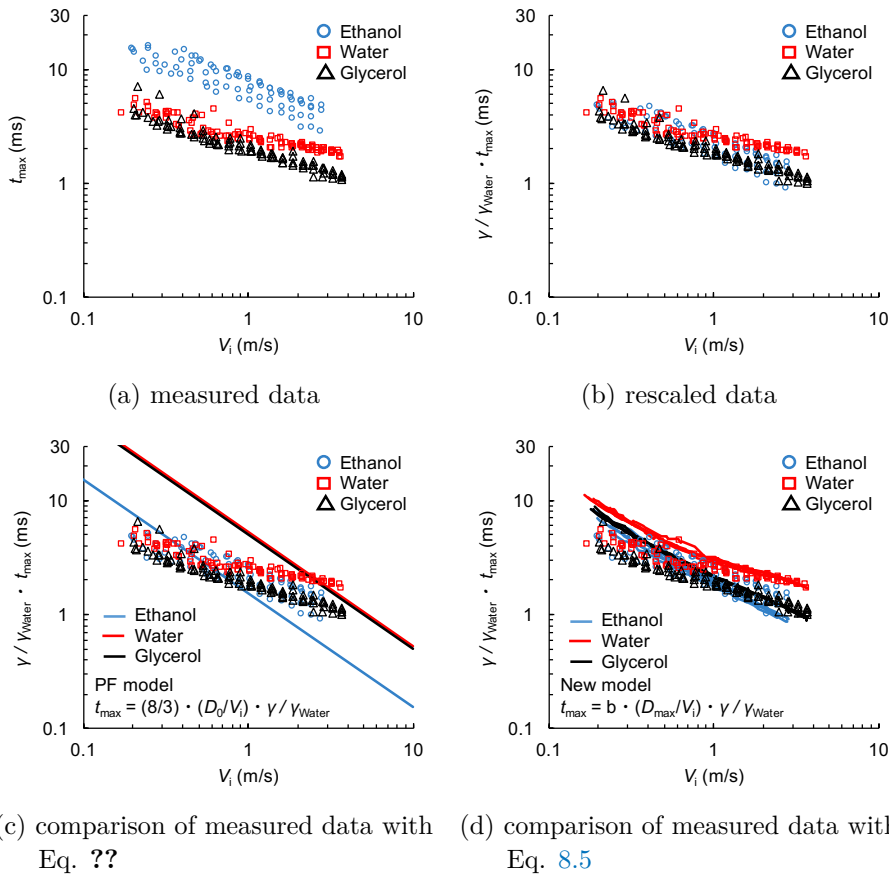
Figure 8.9: Time at maximum spreading t_{max} versus impact velocity.

attributed to its lower surface tension. The time at maximum spreading is similar for water and glycerol as their values for surface tension are similar. This observation suggests that the time at maximum spreading scales with the surface tension. Figure 8.9b shows that, after scaling the time at maximum spreading with the surface tension, $t_{max} \cdot \gamma_l / \gamma_{water}$, all data collapse onto a single curve.

8.3 MODELING

The energy balance of a droplet impacting on a solid surface consists in kinetic energy, capillary or surface tension energy and energy loss due to viscous dissipation. The kinetic energy before impact is $KE_1 =$

$(\pi/12) \cdot D_0^3 \rho V_i^2$ and the surface tension energy before impact equals $SE_1 = \pi D_0^2 \gamma_{LV}$. The surface tension energy at maximum spreading is $SE_2 = S_{LV} \cdot \gamma_{LV} + S_{SL} \cdot (\gamma_{SL} - \gamma_{SV})$, where S_{LV} is the droplet surface contacting the vapor phase, while S_{SL} is the droplet surface contacting the solid surface. The loss of energy due viscous dissipation during spreading is (Pasandideh-Fard et al., 1996):

$$W = \int_0^{t_{max}} \int_\Omega \tau d\Omega dt \approx \tau \Omega t_{max} \tag{8.1}$$

where τ is the mean value of the viscous dissipation energy per unit time and volume (Huh and Scriven, 1971) and $\tau \approx \mu(V_i/\delta)^2$. Ω in Eq. 8.1 is the volume where viscous dissipation occurs $\Omega = (\pi/4 D_{ma}^2) \cdot \delta$, where δ is the boundary layer thickness. The boundary layer thickness is the depth to which momentum can diffuse on the time scale of the drop motion, or $\delta = \sqrt{cD_\mu \cdot t_{max}}$, where c is a constant equal to 2 for one-dimensional diffusion perpendicular to the surface. The transverse momentum diffusion constant equals $D_\mu = \mu/\rho$. The energy balance equation between state 1 (before impact) and 2 (at maximum spreading) is $KE_1 + SE_1 = SE_2 + W$. Different models have been proposed (Chandra and Avedisian, 1992; Mao et al., 1997; Pasandideh-Fard et al., 1996; Ukiwe and Kwok, 2004), which differ in the choice of terms included in this energy balance, as wells as the geometry of the droplet during spreading and the specific description of the terms SE_2 and W.

8.3.1 *Low impact velocity (capillary regime)*

At very low impact velocity, the dissipation energy W can be neglected and the balance equation becomes $KE_1 = SE_2$. Assuming the spherical droplet being deformed into a pancake-like droplet, and $SE_2 = \pi/4\gamma_{LV} \cdot D_{max}^2$, it can be shown that β_{max} scales with $We^{1/2}$. This scaling is regularly assumed in literature (Collings et al., 1990; Eggers et al., 2010; Laan et al., 2014). On the other hand, Clanet et al. (2004) developed a model based on momentum and mass conservation, and found a scaling of β_{max} with $We^{1/4}$. Our measuring results of the maximum spreading ratio versus We number in Figure 8.10 indicate that the data do not scale with $We^{1/4}$ nor with $We^{1/2}$. While a $We^{1/4}$ scaling could be consistent for water, it is not for ethanol and glycerol. The scaling of $\beta_{max} \sim We^\alpha$ implies that at zero impact velocity the maximum spreading ratio equals zero, which is physically not possible ($\beta_{max} \geq 1$). Our results in Figures
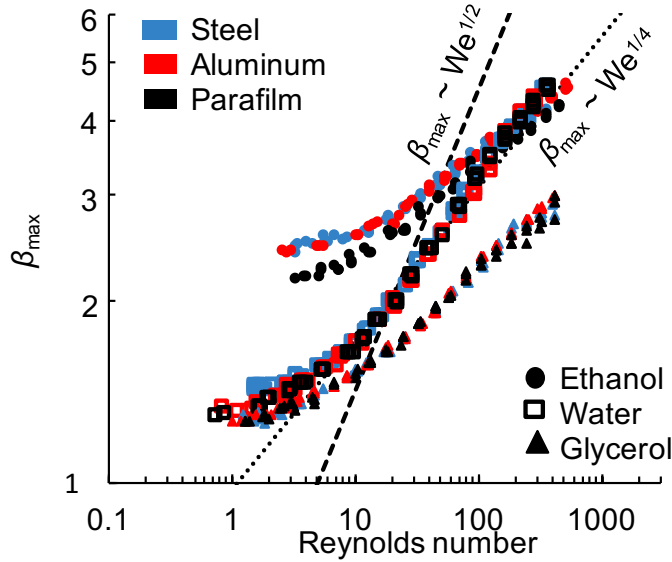
Figure 8.10: Maximum spreading ratio as function of We number, and scaling with $We^{1/2}$ (dashed line) and $We^{1/4}$ (dotted line).

8.7 and 8.8 show that at low impact velocity, the data do not tend to zero, but level off to a constant maximum spreading ratio, which is denoted by $\beta_{V_i=0}$.

To account for the dynamic wetting behavior correctly, the surface tension energy before impact SE_1 and at maximum spreading SE_2 has to be included in the energy balance. Assuming the spherical droplet being deformed into a pancake-like droplet with height h, and using Young's equation $\gamma_{SV} = \gamma_{SL} + \gamma_{LV} \cos\theta$, the surface tension energy at maximum spreading equals $SE_2 = \pi/4 D_{max}^2 \gamma_{LV}(1 - \cos\theta) + \pi D_{max} h \gamma_{LV}$ (Madejski, 1976; Ukiwe and Kwok, 2004). For determining the dissipation energy W, the time from impact to maximum spread t_{max} is derived assuming the spherical drop spreads into a cylindrical disk (Pasandideh-Fard et al., 1996):

$$t_{max} = \frac{8}{3} \frac{D_0}{V_i} \tag{8.2}$$

The boundary layer thickness then equals $\delta = \sqrt{cD_\mu \cdot t_{max}}$, where $c = 3/2$ (Pasandideh-Fard et al., 1996; Roisman, 2009; Visser et al., 2015). Remark that the coefficient c in this model does not equal the theoretical

value 2 as reported before. Solving the energy balance for the maximum spreading ratio, it is therefore

$$\beta_{\max}^2 = \frac{12\gamma_{\mathrm{LV}} + \rho V_{\mathrm{i}}^2 D_0}{3\Gamma + 2\rho V_{\max}^2 D_0 \Delta} - \frac{8\gamma_{\max}}{3\Gamma + 2\rho V_{\max}^2 D_0 \Delta} \cdot \frac{1}{\beta_{\max}} \tag{8.3}$$

with $\Delta = \delta/D_0$ the dimensionless boundary layer height and $\Gamma = \gamma_{\mathrm{LV}}(1 - \cos\theta)$, the effective surface tension. This equation is commonly referred to as the impact-spreading model of Pasandideh-Fard et al. (1996) (referred to as the PF model in this thesis). At the limit of zero impact velocity ($V_{\mathrm{i}} = 0$), maximum spreading becomes:

$$\beta_{V_{\mathrm{i}}=0}^2 = \frac{4}{1 - \cos\theta_{V_{\mathrm{i}}=0}}\left(1 - \frac{2}{3\beta_{V_{\mathrm{i}}=0}}\right) \tag{8.4}$$

This equation shows that the limit of maximum spreading ratio at zero impact only depends on the contact angle, which is denoted as $\theta_{V_{\mathrm{i}}=0}$. The value of $V_{\mathrm{i}} = 0$ is determined from the experimental data by fitting Eq. 8.3 to the data. As an example Figure 8.11a shows that Eq. 8.3 describes the measured data for liquid droplets impacting on the steel surface satisfactorily, allowing to determine the contact angle $\theta_{V_{\mathrm{i}}=0}$. Figure 8.11b compares the dynamic contact angle $\theta_{\mathrm{D}}(t_{\max})$ directly determined in the experiments and the contact angle $\theta_{V_{\mathrm{i}}=0}$ as determined by fitting Eq. 8.3 to the data. The contact angle $\theta_{V_{\mathrm{i}}=0}$ predicts fairly well the measured contact angle during at maximum spreading $\theta_{\mathrm{D}}(t_{\max})$.

The PF model is based on the assumption that the time at maximum spreading is properly described by Eq. 8.2, indicating $t_{\max}$ is only dependent on the impact velocity given the initial drop diameter, and not on the surface tension. In Figures 8.9a-b our data showed that $t_{\max}$ is also dependent on the surface tension and can be rescaled by the ratio of liquid surface tension. Figure 8.9c shows that Eq. 8.2 for predicting $t_{\max}$ is not in good agreement with the experimental data. It is more reasonable to assume that the time at maximum spreading scales with $D_{\max}/V_{\mathrm{i}}$ instead of with D_0/V_{i}. It is therefore analyzed how are measured data of $D_{\max}$ as function of the impact velocity V_{i} predict the time at maximum spreading. Figure 8.9d confirms that the equation

$$t_{\max} = b D_{\max}/V_{\mathrm{i}} \tag{8.5}$$

with b counting for the scaling with surface tension is in much better agreement with our measurements. Assuming $t_{\max} = b D_{\max}/V_{\mathrm{i}}$, the boundary layer thickness equals $\delta = \sqrt{c D_\mu \cdot t_{\max}} = \sqrt{bc/\mathrm{Re}}\sqrt{D_0 D_{\max}}$,
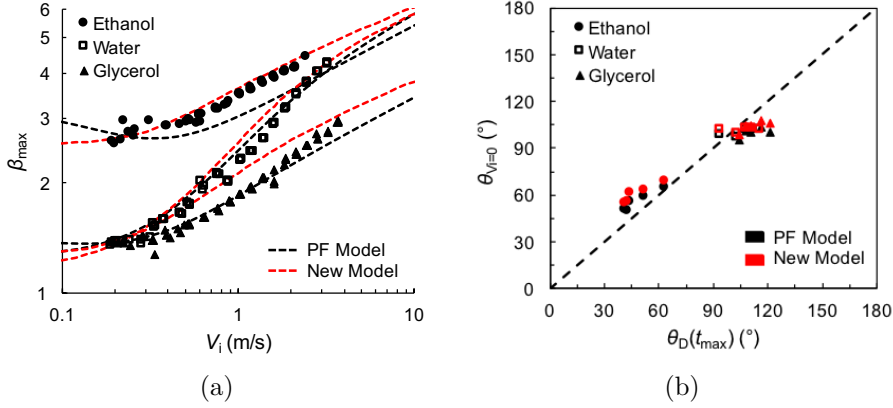
Figure 8.11: (a) Comparison of measured data for maximum spreading ratio versus impact velocity and predictions by two models: PF model (black dash) and new model (red dash) for droplet impact on smooth aluminum. (b) Comparison of contact angle $\theta_{V_i=0}$ with measured the dynamic contact angle at maximum spreading, $\theta_D(t_{max})$: PF model (black symbol) and new model (red symbol).

where the constant $c = 2$. Solving the energy balance for the maximum spreading ratio, this expression expands to

$$\rho V_i^2 D_0 + 12\gamma_{LV} = 3\Gamma\beta_{max}^2 + 8\gamma_{LV}\frac{1}{\beta_{max}} + 3\sqrt{b/c}\rho V_i^2 D_0\beta_{max}^{5/2}\frac{1}{\sqrt{Re}} \quad (8.6)$$

This model is referred to as 'new' model. This model cannot be solved directly for β_{max} and is solved numerically. At zero impact velocity ($V_i = 0$ in Eq. 8.6), Eq. 8.4 is recovered, showing that both models have the same limit at low impact velocity. In the same manner as above, the value of $V_i = 0$ was determined from the experimental data by fitting Eq. 8.6 to the data. Figure 8.11a gives an example. Figure 8.11b shows the agreement between the experimental dynamic contact angle $\theta_D(t_{max})$ and the contact angle $\theta_{V_i=0}$ determined by this new model. It was observed that the PF model (Eq. 8.3) and the new model both perform reasonable well in predicting the maximum spreading ratio. Also both models results suggest that the appropriate contact angle to be used in these models is the dynamic contact angle during spreading, indicating that the influence of dynamic wetting on maximum spreading is properly described by the dynamic contact angle at maximum spreading.

8.3.2 *Limit at high impact velocity (viscous regime)*

At high impact velocity (viscous regime), the surface tension energies SE_1 and SE_2 can be neglected, and $KE_1 = W$. It is assumed further the volume of the droplet at maximum spreading to be a cylinder with diameter D_{max} and height h, the boundary layer height $\delta = h$ and the time at maximum spreading given by $t_{max} = D_{max}/V_i$. The maximum spreading ratio β_{max} scales then with $\text{Re}^{1/5}$. Further, considering the asymptotic solution of Eq. 8.3 of the PF model at large impact velocity $(V_i \to \infty)$:

$$\beta_{max}^2 = \text{Re}^{1/2} \to \beta_{max} \sim \text{Re}^{1/4} \tag{8.7}$$

The asymptotic solution for Eq. 8.6 of the new model at large impact velocity $(V_i \to \infty)$ is

$$\beta_{max}^{5/2} = \sqrt{c/9b}\sqrt{\text{Re}} \to \beta_{max} \sim \text{Re}^{1/5} \tag{8.8}$$

Equations 8.7 and 8.8 show that the maximum spreading ratio should scale at high impact velocity with $\text{Re}^{1/4}$ or $\text{Re}^{1/5}$. Figure ?? shows the measured data for β_{max} together with the scaling $\text{Re}^{1/4}$ and $\text{Re}^{1/5}$. It is challenging to be conclusive on the correct scaling exponent. A main reason for this uncertainty is that two orders of magnitude on both axes are needed to determine a scaling exponent accurately. This is not the case for our measurements due to the occurrence of splashing at higher impact velocity. However, an estimate of the exponent α can be obtained using the following procedure. The scaling exponent is determined using the n last data points. Then the exponent is plotted for different numbers of last data points. Figure 8.12 plots as an example the scaling exponent α as function of n for ethanol on different substrates. By linearly extrapolating the results to n is 0, an estimate of the scaling exponent is obtained. The scaling exponent varies between 0.22 (steel), 0.26 (aluminum) and 0.27 (parafilm). No conclusive statement can be formulated about the exact scaling at high velocity, but the exponent varies between 0.2 and 0.3.

8.4 CONCLUSIONS

Droplet impact has been imaged on different rigid, smooth and rough substrates for three liquids with different viscosity and surface tension,
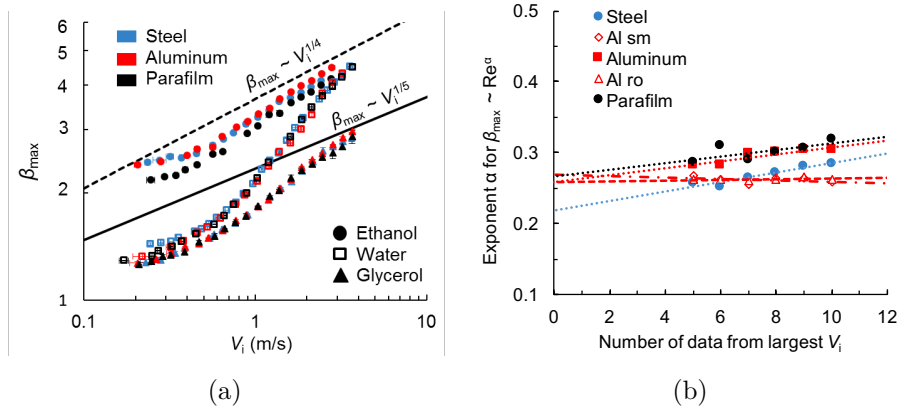
Figure 8.12: (a) Comparison of the measurements with scaling to 0.2 and 0.25. (b) Determination of the scaling exponent α in Re for ethanol. The number n on the x-axis represents the number of data points used to determine the scaling exponent. The dotted lines represent the linear fitting and extension to $n = 0$.

with special attention to the lower impact velocity range. The maximum spreading ratio as a function of impact velocity clearly shows the main role of surface tension and viscosity. The dynamic contact angle at maximum spreading has been identified to characterize properly this dynamic wetting process, especially important at low velocity.

Experiments show that the time at maximum spreading decreases with impact velocity depending on the surface tension of the liquid, and a new scaling of the time at maximum spreading with maximum spreading diameter and surface tension is proposed. Based on this finding, an adapted energy balance model for maximum spreading ratio is proposed based on a correct modeling of the time at maximum spreading, which is an input to the model for predicting the viscous energy dissipation at maximum spreading. The model uses the dynamic contact angle at maximum spreading to describe the dynamic wetting process at low impact velocity. This new model shows good agreement compared to experiments for the maximum spreading ratio versus impact velocity for different liquids.

The dynamic contact angle is found to be in general higher than the equilibrium contact angle, showing that statically wetting surfaces can become less wetting or even non-wetting under dynamic droplet impact.

Surface roughness and type of surface (steel, aluminum and parafilm) slightly affect the dynamic wettability and maximum spreading at low impact velocity, while the type of liquid is found to play a major role.

Scaling according to $We^{1/2}$ is found invalid for low velocities, since the curves levels off to higher maximum spreading ratios due to a dynamic wetting process. At high impact velocity, where viscosity governs the spreading of liquid droplet due to viscous dissipation, $Re^{1/4}$ and $Re^{1/5}$ is scaled with the data, and an uncertainty remains in the determination of the asymptote at high impact velocity is compared. The determination of the scaling exponent is hindered by limited scale range, and a new method is proposed to determine scaling exponent when only a limited amount of data is available.

NUMERICAL SIMULATIONS FOR DROP IMPACT

This chapter is based on the paper Lee JB, Derome D, Dolatabadi A, Carmeliet J. "Energy budget of liquid drop impact at maximum spreading: numerical simulations and experiments" Langmuir, 32 (5), pp 1279–1288 (Lee et al., 2016a).

9.1 INTRODUCTION

In this chapter, the role of liquid properties, such as surface tension and viscosity, on drop impact is investigated experimentally and numerically by CFD-VOF. Droplet spreading is measured under various conditions from low to high impact velocities for three different liquids. It is proposed to use the dynamic contact angle determined experimentally at maximum spreading in the Kistler model. This assumption is validated by comparing experimental and numerical results. Using CFD-VOF, the energy balance evolution during spreading is analyzed and the results are evaluated with respect to the analytical models commonly used for predicting maximum spreading.

9.2 EXPERIMENTAL AND NUMERICAL CASES

The influence of the surface tension and viscosity of the liquid on droplet spreading is investigated using three liquids: pure ethanol (ethanol), deionized water (water) and 1:1.3 glycerol-water mixture (glycerol). The liquid density ρ, viscosity μ and surface tension γ are reported in Table 9.1. Steel surface is used as substrate for the drop impact tests. The arithmetic average roughness R_a of the steel surface is 0.42 μm. The wettability of steel surface is characterized with equilibrium, advancing and receding contact angles by sessile drop method (Table 9.1). Ethanol shows a total wetting on steel surface and spreads completely due to its lower surface energy ($\theta_{eq} \sim 0°$). Water and glycerol show a wetting behavior on the steel surface with an equilibrium contact angle between $52°$ to $61°$. The advancing contact angle of water and glycerol on the

Table 9.1: Properties of liquids and contact angles on steel surface

| | Liquid properties at 25°C | | |
	ρ (kg/m^3)	μ (mPa·s)	γ (mN/m)
Ethanol	789	1.2	23.2
Water	998	1.0	72.8
Glycerol	1 158	10.0	68.3
	Contact angle on steel		
	θ_{eq} (°)	θ_{adv} (°)	θ_{rec} (°)
Ethanol	~ 0	~ 0	~ 0
Water	60.9 ± 1.3	61.5 ± 3.3	6.8 ± 1.0
Glycerol	52.4 ± 3.7	48.5 ± 4.3	~ 0

steel surface is quite similar to the equilibrium contact angle (difference less than 7%). Only water shows a receding contact angle higher than zero degree ($\theta_{\text{rec}} \sim 7°$).

The impact conditions, drop size and impact velocity for the experiments and simulations are reported in Table 9.2. The drop impact from low to high impact velocity (0.2 to 3.2 m/s) is investigated experimentally to capture the maximum spreading of the impinging droplets. The experimental results are used to validate the CFD simulations. CFD is presented in section 3.2. The input contact angle θ_k in Eq. 3.46 equals the dynamic contact angle during spreading phase ($V_{\text{CL}} > 0$), as measured experimentally at maximum spreading $\theta_{\text{D}}(t_{\text{max}})$, in order to consider dynamic effects during spreading. Figure 9.1 shows the plot of dynamic contact angle $\theta_{\text{D, sim}}$, as predicted by the Kistler model using Eq. 3.46, as function of contact line velocity for different liquids. The dynamic contact angle $\theta_{\text{D, sim}}$, for the receding phase ($V_{\text{CL}} < 0$) is estimated using the measured receding contact angle in Eq. 3.46. When the droplet is in equilibrium state and the contact line does not move ($V_{\text{CL}} = 0$), the dynamic contact angle $\theta_{\text{D, sim}}$ equals the measured equilibrium contact angle.

Figure 9.2 shows the comparison of the simulation results for water drop impact on the steel surface ($V_{\text{i}} = 1.0$) considering two cases. In the first case, the dynamic contact angle at maximum spreading is used as input to the Kistler model for the spreading phase, while in the second case the advancing contact angle is used as input value in Eq. 3.46. It is
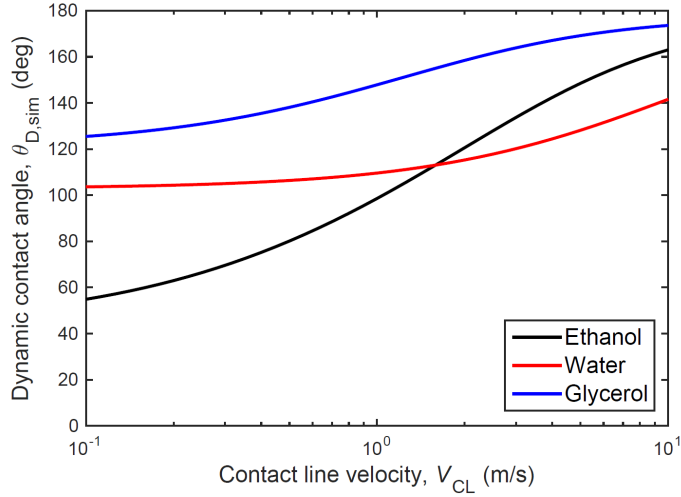
Figure 9.1: Kistler's correlation of the dynamic contact angle $\theta_{D,\,sim}$ with as input $\theta_k = \theta_{D,\,sim}$ for different liquids: ethanol $\theta_D(t_{max}) = 43.9°$, water $\theta_D(t_{max}) = 102.9°$ and glycerol $\theta_D(t_{max}) = 121.2°$.

observed that results with the Kistler model using the advancing contact angle shows an overprediction for spreading ratio and an underprediction for dynamic contact angle during spreading compared to when it is used the dynamic contact angle at maximum spreading, which gives good agreement with the experiments.

9.3 SPREADING DYNAMICS

After impact, the liquid droplet spreading as predicted by the numerical method is compared with the one from the experimental results. The spreading diameter ratio $\beta = D(t)/D_0$ and the apparent dynamic contact angle $\theta_D(t)$ for different liquids are shown in Figure 9.3a-b. Figure 9.3a shows β for different liquid droplets with an impact velocity of ~ 1.0 m/s on steel surface. Ethanol spreads further than the other liquids, while glycerol spreads less than water. A good agreement between experiments and simulations is obtained during the spreading phase. The maximum spreading is defined as the largest spreading diameter ratio (indicated by the vertical line in Figure 9.3a: experiment (dash) and simulation

(a) spreading ratio

(b) dynamic contact angle
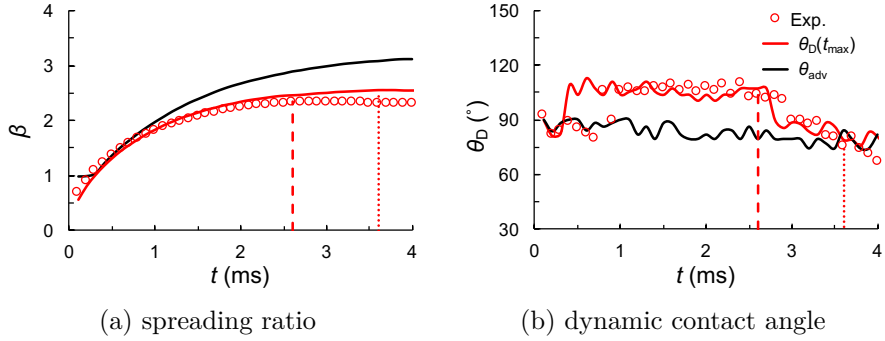
Figure 9.2: Comparison of the predictions using the measured dynamic contact angle at maximum spreading and advancing contact angle as input in the Kistler model during spreading phase: (a) spreading ratio β and (b) dynamic contact angle θ_D for water drop impact on steel surface with $V_i = 1.0$ m/s.

Table 9.2: Impact conditions and dynamic wettability for experiments and simulations

	Liquid	D_0 (mm)	V_i (m/s)	We	Re	$\theta_D(t_{max})$ (°)
Exp. E	Ethanol	1.8 ± 0.04	0.2 - 2.4	2.5 - 370	270 - 3 000	43.9 ± 2.5
Sim. E	Ethanol	1.8	0.2 - 2.4	2.5 - 367	247 - 2 969	
Exp. W	Water	2.0 ± 0.01	0.2 - 3.6	1.1 - 360	450 - 7 000	102.9 ± 3.2
Sim. W	Water	2.0	0.2 - 3.2	1.1 - 289	389 - 6 292	
Exp. G	Glycerol	1.8 ± 0.01	0.2 - 3.7	1.2 - 410	42 - 760	121.2 ± 6.9
Sim. G	Glycerol	1.8	0.2 - 3.2	1.2 - 330	42 - 686	

(dotted)). Ethanol reaches its maximum spreading later in time, while glycerol reaches its maximum spreading earlier in time. The simulated time at maximum spreading agrees well with the experimental time for ethanol and glycerol. The simulated maximum spreading ratio for water is higher than the measured results, leading also to an overprediction of the time at maximum spreading in the simulation. Figure 9.3b shows that the simulations of the dynamic contact angle agree well with the experiment during spreading phase. Less agreement is obtained for glycerol in the receding phase, where the simulation overpredicts 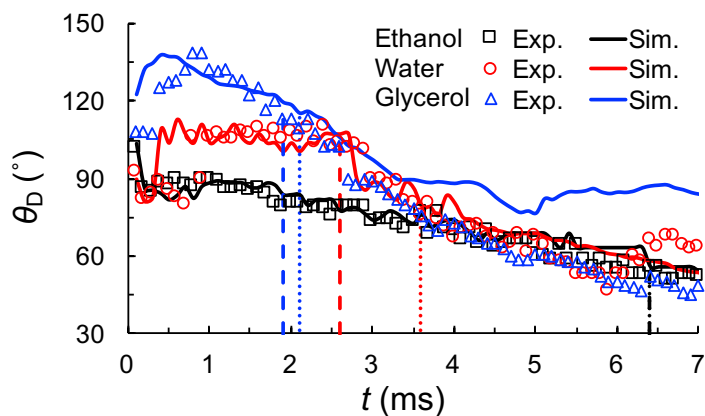the dynamic contact angle. The CFD simulations are able to model the change of the dynamic contact angle from non-wetting to wetting behavior as shown in Figure 9.3b, which play an important role in the spreading process of the drop. As a note, the dynamic contact angle is determined in a similar way in the experiments and in the simulations.

Figure 9.4 compares the outlines of impacting droplets for the experiments and simulations at different times during spreading. The color map indicates the kinetic energy per volume (left side) and viscous energy dissipation per volume (right side) determined in the simulations. Note that the outline of impact droplet from the experiments (red line) shows the silhouette of the droplet determined experimentally by shadowgraphy, while the outline from the simulation (white line) is from the middle plane of the droplet showing also the detailed shape of the rim. Good agreement between the experiments and the numerical model is found for different liquid droplets. It was found that the numerical model is sensitive to the input contact angle θ_k used in the Kistler equation (Eq. 3.46). Considering the uncertainty on the measured dynamic contact angle at maximum spreading (up to 6% standard deviation), the numerical simulation are found to agree quite well with the experimental results.

The color maps display the variations in kinetic energy and in viscous energy dissipation. The initial kinetic energy is the main driving energy for drop spreading on the surface, and is converted into surface energy and dissipated by viscosity effects. At earlier time, as shown in Figure 9.4 on the left side of the color maps, the kinetic energy primary promotes the spreading at the rim. Simultaneously, energy is dissipated by viscosity near the surface and at the free surface of the liquid droplet where high shear stresses occur. The liquid droplet spreads further due to kinetic energy until an equilibrium state is reached between inertia and surface tension at maximum spreading. Ethanol, water and glycerol droplets reach their maximum spreading at 6.3, 2.6 and 1.9 ms, respectively. At
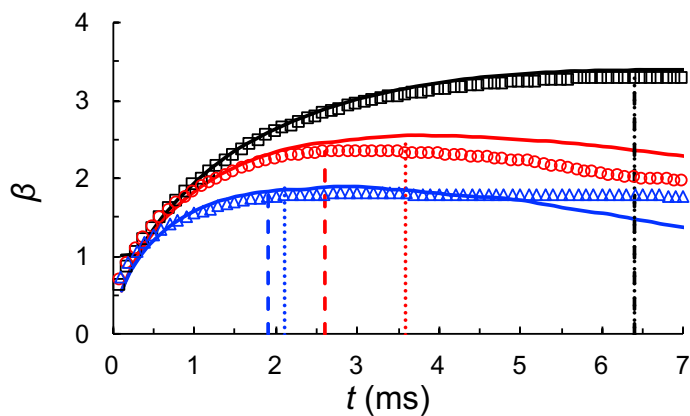
(a) spreading ratio

(b) dynamic contact angle

Figure 9.3: Comparison of the experiment and simulation results for (a) spreading ratio $\beta = D(t)/D_0$ and (b) dynamic contact angle θ_D versus time for drop impact with $V_\mathrm{i} = 1.0$ m/s. Symbols show experimental results on the steel surface. Lines shows simulation results. The vertical lines indicate the time at maximum spreading for experiments (dash) and simulations (dotted).
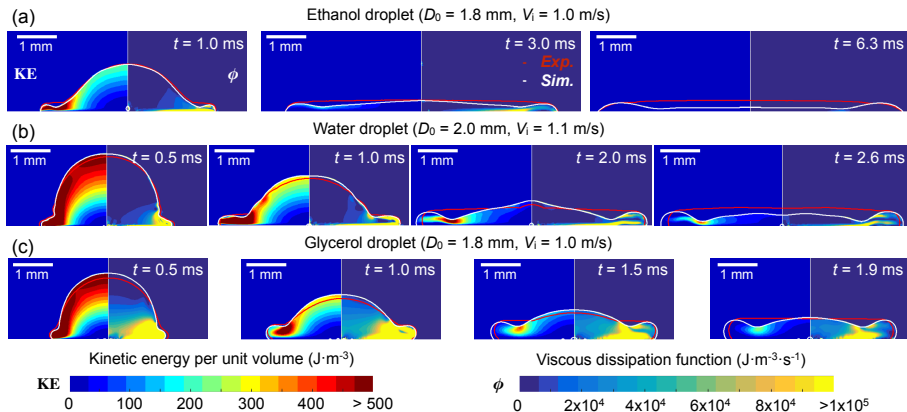
Figure 9.4: Time evolution of drop impact for ethanol, water and glycerol on steel surface ($V_i = 1.0$ m/s). The lines show the liquid-vapor interfaces from experimental images (red) and numerical results (blue). The contour map on left side depicts kinetic energy per unit volume KE and right side shows viscous energy dissipation function.

maximum spreading some kinetic energy remains in the system, but further spreading of liquid droplet is hindered by surface tension forces. At the beginning of impact, surface tension forces limits the spreading for ethanol on steel surface, since the dynamic contact angle shows a hydrophobic behavior at $V_{CL} \sim 1.0$ m/s (See Figure 9.1). However, when the kinetic energy is converted into surface energy later in the spreading process, the surface tension force promotes further spreading due to the hydrophilic dynamic contact angle of ethanol on steel surface.

Figure 9.5 shows the time evolution of the energy terms after drop impact for different liquids. Before drop impact (referred to using subscript 1), the total energy in the droplet is the sum of kinetic energy KE_1 and surface energy SE_1. After impact, kinetic energy $KE(t)$ decreases with time and is converted into surface energy $SE(t)$ and viscous dissipation W_{vis}. The surface energy increases with time due to increase of surface area during the spreading phase. Simultaneously, the cumulative viscous dissipation energy W_{vis} increases. At maximum spreading, the remaining kinetic energy in the droplet is less than 5% compared to total energy (ethanol 0.2%, water 3.0% and glycerol 4.2% for V_i 1.0 m/s). Ethanol shows a smaller initial energy than water and glycerol before drop impact ($KE_1+SE_1 = 1.6 \times 10^{-6}$ for ethanol and 3.4×10^{-6} J for water), but at
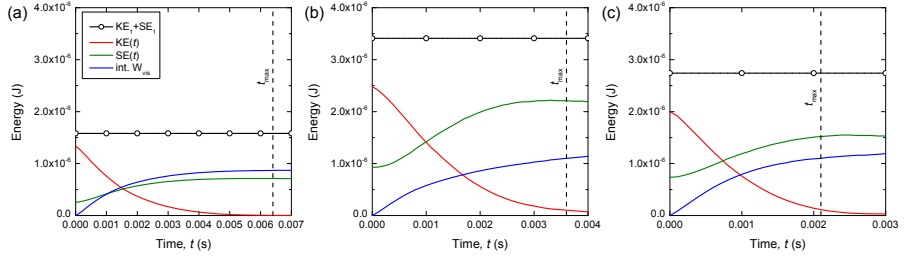
Figure 9.5: Time evolution of energy terms during spreading of drop with ~ 1.0 m/s impact velocity: (a) ethanol, (b) water and (c) glycerol.

maximum spreading, the cumulative viscous dissipation is quite similar for all liquids ($W_{\text{vis}} = 0.9 \times 10^{-6}$ J for ethanol and 1.1×10^{-6} J for water and glycerol), even though glycerol has a 10 times higher viscosity than water. This similar result can be explained by the fact that the maximum spreading time for glycerol (1.9 s) is shorter than the one of water (2.6 s). It is noted that the accurate prediction of the cumulative viscous dissipation at maximum spreading $W_{\text{vis}}(t_{\text{max}})$ is crucial as this term is one of the inputs of energy balance models used to predict the maximum spreading.

9.4 MAXIMUM SPREADING

Figure 9.6 shows snapshots of maximum spreading for different impact velocities comparing experiments and simulation results. The boundary layer development at the surface is represented by the vector plot of the horizontal velocity $\mathbf{U}_x$. The outline of the droplets at maximum spreading shows good agreement between simulation and experiment. Recall that the outline of impact droplet from the experiments (red line) shows the silhouette and the outline from the simulation (white line) is from the cutting plane in the middle of the droplet.

The local boundary layer thickness δ is defined as the height where 99% of the maximal horizontal velocity is reached. To obtain a single value for the boundary layer thickness value for each instant in time, the boundary layer thickness is spatially averaged as (Visser et al., 2015):

$$\bar{\delta}(t) = \frac{4 \int_0^{2\pi} \int_0^{D(t)/2} \delta(x,t)x\,dx\,d\alpha}{\pi D(t)^2} \tag{9.1}$$
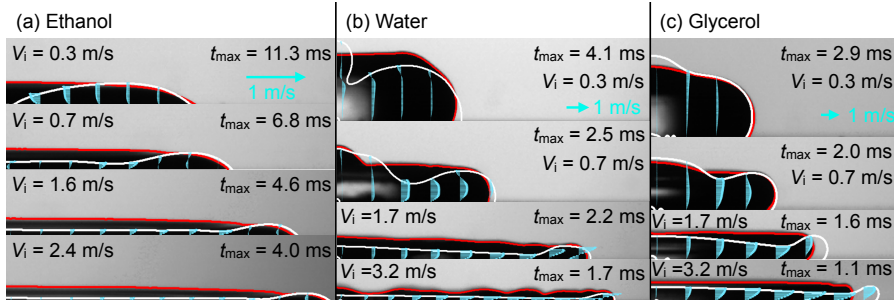
Figure 9.6: Snapshots of the maximum spreading as function of the impact velocity. The white line shows liquid-vapor interface of simulation. The boundary layer development at the surface is represented by the blue vector plot of the horizontal velocity $\mathbf{U}_x$.

where α is the angular coordinate.

Figure 9.7a shows the non-dimensional boundary layer thickness $\bar{\delta} \cdot \sqrt{\mathrm{Re}}/D_0$ as a function of non-dimensional time t/τ where τ is D_0/V_i in log-log plotting for three different impact velocities ($V_i = 0.5$, 1.0, 1.7 m/s) and three different liquids. The results are compared the prediction by Roisman et al. (2009) (dashed line with 0.5 slope). We observe that at $t/\tau < 1$, where the inertia driven flow is dominant in the droplet, the different curves collapse for different impact velocity and liquids showing a scaling with the Reynolds number. For $t/\tau > 1$, the curves start to deviate from the scaling slope, especially for ethanol. For glycerol and water at low impact velocity, the boundary layer thickness mainly increases until maximum spreading is reached. On the contrary for ethanol the boundary layer thickness reduces before reaching its maximum spreading, showing that the viscous dissipation becomes less important close to maximum spreading. This is explained by the fact that the ethanol droplet will still spread due to capillary forces even after inertia flow is dissipated.

This time dependent boundary layer thickness may be further averaged over time to obtain a single value for the boundary layer thickness for the total spreading process. An analytical expression for this average boundary layer thickness can be attained assuming that the liquid motion in the droplet can be represented by an axisymmetric stagnation point flow(Pasandideh-Fard et al., 1996):
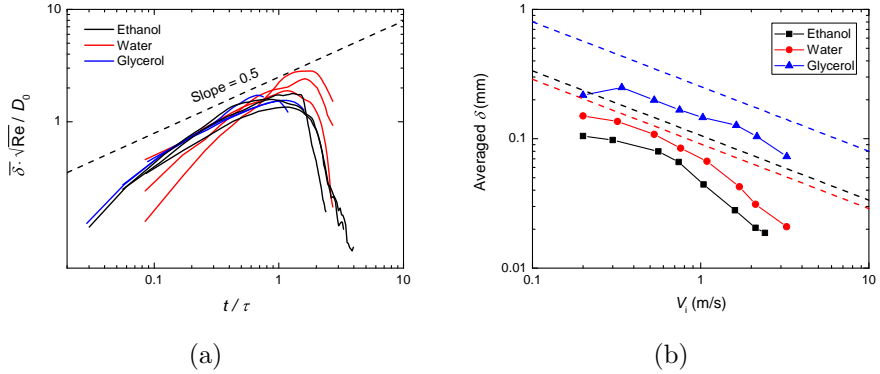
(a)   (b)

Figure 9.7: (a) Non-dimensional boundary thickness averaged over space as function of the non-dimensional time obtained by CFD simulations. (b) Time-averaged boundary layer thickness during spreading phase as a function of impact velocity determined from CFD simulation. Dashed line is the theoretical model of Pasandideh-Fard et al. (1996) for ethanol (black), water (red) and glycerol (blue).

$$\delta = 2 \frac{D_0}{\sqrt{\text{Re}}} \qquad (9.2)$$

Considering Figure 9.7a showing that the boundary layer thickness varies highly over time, this averaging over time to obtain one single value of the boundary thickness may be questioned. However, such a single value as given in Eq. 9.2 is commonly used in energy balance model because of its simplicity for predicting the cumulative viscous dissipation at maximum spreading, allowing the prediction of the maximum spreading. In Figure 9.7b, the time averaged boundary layer thickness obtained by our CFD simulations is compared to the analytical prediction by Eq. 9.2 (dashed line) for different liquids. In general, the analytical model overpredicts the average boundary layer thickness. However, the slope of the simulated boundary layer thickness as a function of impact velocity agrees quite well with the analytical model. At higher impact velocity, the simulated boundary layer thickness decreases more than the one predicted by the analytical model, since, in the simulation, the boundary layer spreads over the total thickness and is therefore limited by the droplet height.
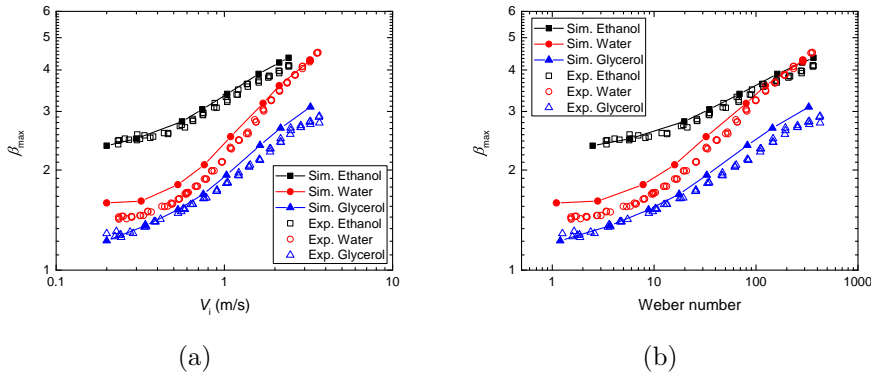
Figure 9.8: Maximum spreading ratio of droplets of the three liquids versus impact velocity (a) and versus Weber number (b). Experimental results empty symbols, simulation results in line and full symbols.

Figure 9.8a shows the maximum spreading ratio $\beta_{\max}$ as a function of impact velocity V_i for the experiments and simulations. Overall, the numerical method captures the maximum spreading for different liquids very well, when using, for the boundary condition, the experimental dynamic contact angle measured at maximum spreading as input in Eq. 3.46. Ethanol shows the highest maximum spreading, while glycerol shows the lowest maximum spreading. Water shows a transition curve from the lowest spreading at lower impact velocity like glycerol to the highest spreading at higher impact velocity like ethanol. These results clearly show the roles of surface tension and viscosity of liquid on the maximum spreading. The CFD approach, using the measured dynamic contact angle at maximum spreading in the Kistler model to define the boundary condition, captures correctly the experiments over the total range of impact velocities. In most publications, the maximum spreading ratio is plotted versus the Weber number to scale for the effect of the surface tension of liquid as shown in Figure 9.8b. At high impact velocity, the curve for ethanol starts to collapses with the curve of water, but general trends do not change. At lower impact velocity, the different curves still diverge and the Weber number does not scale the data properly due to the fact that, at low impact velocity, dynamic wetting plays also a role. For this reason, in this thesis, the results are generally plotted versus impact velocity and not versus We number.
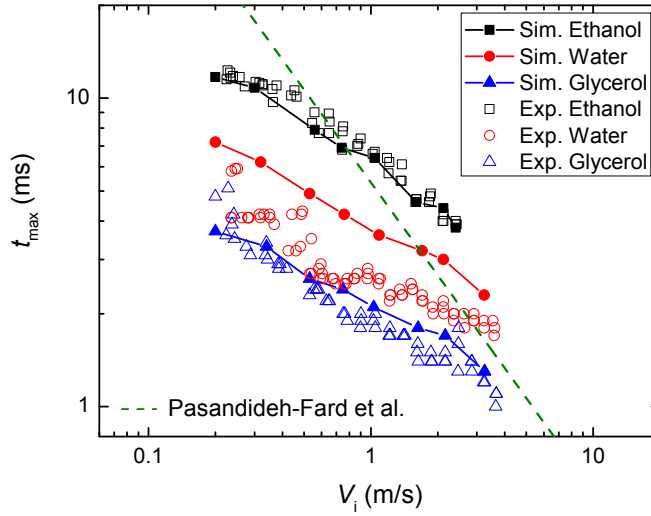
Figure 9.9: Time at maximum spreading determined experimentally and with simulation, and comparison with model by Pasandideh-Fard et al. (1996) (green dash line).

The experimental and numerical results of time at maximum spreading are shown in Figure 9.9 for the different liquids and impact velocities. Good agreement is achieved for ethanol and glycerol. A slight over-prediction in maximum spreading, as seen in Figure 9.3a, results in an overprediction of the time at maximum spreading. The simple analytical model $t_{max} = 8D_0/3V_i$, where Pasandideh-Fard et al. (1996) assumed the drop spreading into a cylindrical disk, is also shown on Figure 9.9. This simple model clearly does not predict the slope of the time at maximum spreading versus impact velocity correctly, and also does not predict the dependence of the time at maximum spreading on surface tension.

In Figure 9.10, the measured and simulated dynamic contact angles at maximum spreading $\theta_D(t_{max})$ as a function of impact velocity V_i are compared. The dynamic contact angle at maximum spreading is found to be quite constant, independent of impact velocity and average values are reported in Table 9.2.

The dynamic contact angles at maximum spreading determined by simulation and compared with the experimental ones show a good agreement for ethanol and glycerol, but less agreement for water. The reason for this poor agreement is obviously that the time at maximum spreading
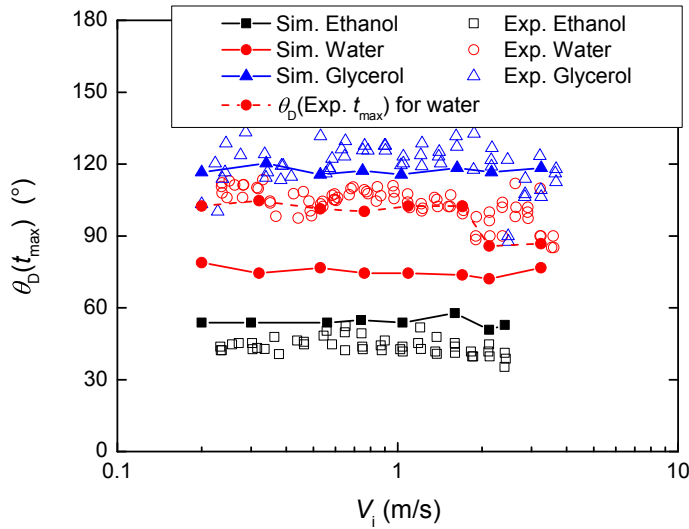
Figure 9.10: Dynamic contact angle at maximum spreading determined experimentally and with simulation versus impact velocity.

for water is overpredicted, as explained above in Figure 9.3a. Since the dynamic contact angle is decreasing during the spreading phase, an overprediction of the time at maximum spreading results in an underprediction of the dynamic contact angle at maximum spreading. To test this explanation, the simulated dynamic contact angle at the experimental time of maximum spreading is determined. These results are represented in Figure 9.10 by the dashed red line and, as can be seen, these results coincide very well with the measured data. This means that the underestimation of the dynamic contact angle at maximum spreading can be attributed to the overestimation of the time at maximum spreading for water.

In Figures ??a-c the energy budget and the partition of energy at maximum spreading is shown as a function of the impact velocity. Figure 9.11d shows the relative proportion of the different energy terms. From Figure 9.11d it is clear that the remaining kinetic energy at maximum spreading is almost zero (maximal 4% of total energy). The surface energy and viscous dissipation energy increase with impact velocity, which can be directly related to the increase in initial kinetic energy, resulting in an increase in maximum spreading. Interestingly, the relative proportion of the viscous dissipation in the total energy budget increases with impact

(a) ethanol

(b) water

(c) glycerol

(d)
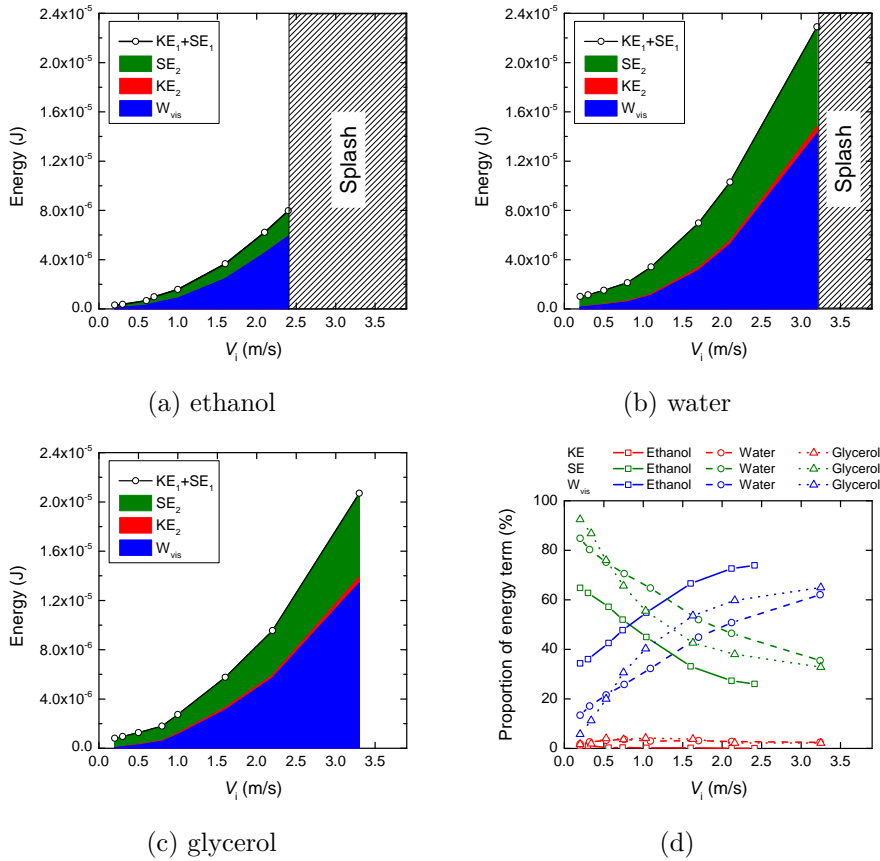
Figure 9.11: Amount (a-c) and proportion (d) of energy terms at maximum spreading as a function of impact velocity for different liquids.

velocity with respect to surface energy. This would justify the assumption that, in the limit of high impact velocity, surface energy does not play a role, and spreading is only governed by viscous dissipation. However, the analysis in this work shows that the contribution of surface energy only decreases very slowly, and that just before splashing, the drop impact is still in the regime where both surface energy and viscous dissipation have to be taken into account. On the other side, the results show also that, at low velocity, viscous dissipation can still play an important role, especially for ethanol.

9.5 CONCLUSIONS

Drop impact has been experimentally studied by high-speed imaging and by CFD-VOF simulation for three liquids with different viscosity and surface tension on steel surface. The spreading of drop impact is analyzed from low to high impact velocity, thereby focusing on the spreading diameter, dynamic contact angle and time at maximum spreading.

The CFD simulations are validated against experiments for ethanol, water and glycerol in all range of impact velocity. It is concluded that the dynamic contact angle at maximum spreading is a suitable choice for the input contact angle of the Kistler model for the spreading phase providing good agreement between simulations and experiments. This dynamic contact angle is found to give better agreement than the quasi-static advancing contact angle, since the former captures better the dynamic wetting behavior during spreading. Deviations between experiments and measurements are attributed mainly to the sensitivity of the CFD model on the contact angle input to the Kistler mode used as boundary condition at the contact line.

Comparison of CFD results with analytical model predictions allowed us to validate the adequacy of analytical equations for average boundary layer thickness and time at maximum spreading, as commonly used in energy balance models for predicting maximum spreading. The analytical model for the time averaged boundary layer thickness is found to predict a similar dependence on impact velocity compared to the CFD simulations, but the value of boundary thickness is overpredicted by the analytical solution. Experiments showed that the time at maximum spreading decreases with impact velocity depending on the surface tension of the liquid. The CFD results adequately predict these experimental dependencies, while the commonly used analytical model does not predict the dependence on impact velocity correctly and does not include a dependence on surface tension. It is remarked that these analytical expressions are commonly used in energy balance models, meaning the validity of the energy balance models has to be reconsidered and updated. The energy budget of drop impact is documented as a function of impact velocity, i.e. the partition between kinetic energy, surface tension energy and cumulative viscous dissipation at maximum spreading versus impact velocity. At low impact velocity, viscous dissipation contributes to a substantial part to the energy budget and cannot be neglected in the prediction of maximum spreading. At high impact velocity, it was

demonstrated that, just before splashing, the spreading regime is both dependent on surface energy and viscous dissipation.

0000

DYNAMICS OF DROP IMPACT ON POROUS MEDIA

This chapter is based on the paper Lee JB, Derome D, Carmeliet J. "Drop impact on natural porous stones" accepted for publication in Journal of Colloid and Interface Science.

10.1 INTRODUCTION

The phenomenon of drop impacting on porous media is still insufficiently understood due to the presence of simultaneous behaviors, spreading and absorption, and due to the lack of knowledge of the contact line behavior on porous and rough surfaces. In this chapter, drop impact and spreading on three natural porous stones is experimentally determined using high-speed imaging and compared with spreading over an impermeable steel surface. Especially, maximum spreading at low impact velocity in view of the dynamic wetting behavior is studied in terms of the dynamic contact angle. A method to scale all data into a single curve taking into account the dynamic contact angle is here also investigated.

10.2 METHODS AND MATERIAL

Three natural stones are selected for droplet impact experiments on porous media: Savonnières, Meule and Pietra Serena. Savonnières is highly porous and a quasi-pure calcitic stone (99.8% CaCO3), and is used as a building material on facades of historical buildings (e.g. railway station Gare de l'Est in Paris), as a stone for sculptures (e.g. the sculptures on the facade of the cathedrals in Aachen and Cologne), and is applied for restoration purposes (Derluyn, 2012; Dreesen and Dusar, 2004). The sandstone Meule (grès à meules) is composed of quartz grain (74%), with clay and other secondary mineralization, and is used as a building material (e.g. tower of the cathedral of Strasbourg) (Moonen, 2009). Pietra Serena is a fine-grained and compact sandstone, and is used widely as a building material for columns, cornices and arches and as a stone for sculptures (e.g. Pazzi and Medici chapels in Florence). Figure

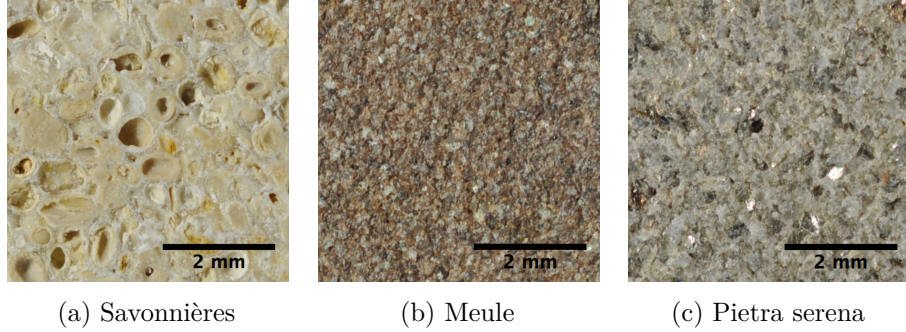(a) Savonnières   (b) Meule   (c) Pietra serena

Figure 10.1: Microscope images of porous stones.

10.1 shows microscope images of the porous stones. The porous stone samples are prepared by cutting cubes ($20 \times 20 \times 20$ mm^3). The bulk density ρ_{bulk} defined as the ratio of the dry mass to the total volume, the open porosity Φ defined as the ratio of the volume of open pores to the total volume and the saturated water content w_{sat} defined as the mass of water filling the open pores per total volume are measured. The water absorption coefficient A_{cap} is determined by measuring the absorption mass rate per unit surface in a free water uptake experiment. The capillary water content w_{cap} equals the water content when the water front reaches the top of the sample during capillary absorption. The impervious surface is steel, with an arithmetic average roughness of 0.42 µm and an equilibrium contact angle of $\theta_{\mathrm{eq}} = 61°$.

In Table 10.1, the measured properties of the three stones are summarized. The stones are selected mainly for their range of open porosity in order to understand the influence of surface pore structure on the dynamics of droplet spreading. Elaborate studies on the pore structure, moisture and mechanical properties of Savonnières and Meule can be found in Refs. (Roels, 2000; Moonen, 2009; Derluyn, 2012). Savonnières shows the highest porosity, a faster water absorption rate and the largest capillary water content compared to the other stones. The capillary water content is smaller than the saturated water content due to air entrapment during imbibition from a free water surface. Pietra serena shows the lowest porosity, water uptake coefficient and capillary water content. The portion of the pore space filled by water at capillary moisture content in Savonnières, Meule and Pietra serena is respectively 56%, 72% and 80%.

The arithmetic average roughness R_a for Savonnières, Meule and Pietra serena is respectively 10, 9 and 4 µm, showing the porous materials

Table 10.1: Properties of porous stones

	Savonnières	Meule	Pietra serena
ρ_{bulk} (kg/m^3)	$1\,974.5 \pm 38.7$	$2\,253.2 \pm 14.3$	$2\,558.7 \pm 21.9$
Φ (%)	26.9 ± 1.4	16.6 ± 0.3	5.1 ± 0.6
w_{sat} (kg/m^3)	268.2 ± 13.6	165.7 ± 4.0	50.9 ± 6.0
w_{cap} (kg/m^3)	151.1 ± 6.4	119.8 ± 4.0	41.6 ± 2.5
A_{cap} (kg/m^{2}s$^{1/2}$)	0.089 ± 0.012	0.028 ± 0.003	0.004 ± 0.001
R_a (µm)	10.3 ± 3.5	9.1 ± 1.5	4.4 ± 1.5
R_{eq} (µm)	100	10	0.04

are quite rough due to the sawing process, compared to the smooth steel surface. The equivalent pore radius R_{eq}, defined from pore size distribution measurement using mercury intrusion porosimetry (MIP) (Moonen, 2009; Derluyn, 2012) and scanning electron microscope (SEM) image (Roels, 2000), for Savonnières, Meule and Pietra serena equals respectively 100, 10 and 0.04 µm. It was not possible to measure the equilibrium contact angle on stones due to immediate spreading of the droplet due capillary uptake by the substrate, so no equilibrium could be found. The main components of the stones display very low contact angles (calcite 0° and quartz 11° to 19°) showing they are almost perfectly wetting (Ardebrant and Pugh, 1991; Okayama et al., 1997; Rodriguez-Valverde et al., 2002).

Water drop impact on porous stone is recorded in shadowgraphy using a high-speed camera (10 000 frame per second, 7.38 µm spatial resolution and 5 µs exposure time). The properties of water and the impact conditions are given in Table 10.2. The drop impact test is repeated more than 10 times with 3 different samples at arbitrary surface locations for each measuring condition in order to obtain sufficient reproducibility. Experimental results are reported by their average value (symbol) and standard deviation (error bar). Drop impact on porous stones is compared with the drop impact on impermeable steel surface. Images captured from high-speed camera are analyzed with a custom made image analysis MATLAB code for determination of: the initial droplet diameter D_0, the impact velocity V_{i}, the spreading diameter at the rim $D(t)$, the spreading diameter at the contact line $D_{\text{CL}}(t)$, the dynamic contact angle θ_{D}, the

Table 10.2: Properties of water droplet and impact conditions for drop test

	Properties at 25°C		
	ρ (kg/m^3)	μ (mPa·s)	γ (mN/m)
Water	998	1.0	72.8
	Impact conditions		
	D_0 (mm)	V_i (m/s)	We	Re
Water	2.0	0.2 - 4.0	1 - 440	400 - 8 000

maximum spreading ratio $\beta_{\max} = D_{\max}/D_0$ and the time at maximum spreading $t_{\max}$. The inset in Figure 10.2 shows the difference between D and D_{CL} during the evolution of spreading. The dynamic contact angle is obtained from the image by applying a goniometric mask (Biolè and Bertola, 2015) on a region of 100 μm vertically above the surface line.

As a reminder, the procedure to determine the mass of water in the porous stone M_{abs} is repeated here. The drop volume remaining on the surface is estimated assuming the shape of a cap method and subtracted from the initial mass of the droplet M_0. The volume V_{drop} of a drop on a surface having a spherical cap is given by:

$$V_{\mathrm{drop}}(t) = \frac{\pi h(t)}{6} \left(3 \left(\frac{D_{\mathrm{CL}}(t)}{2} \right)^2 + h(t)^2 \right) \qquad (10.1)$$

where h is the height of the spherical cap. It is found that the evaporation of a drop deposited on a nonporous surface is negligible during the time of investigation ($\Delta t \sim 0.01$ s), as the volume loss in 10 seconds is less than 3%. The accuracy of the spherical cap approach for determining the remaining volume V_{drop} by depositing a droplet on an impermeable surface was also evaluated. The global systematic error was found to be less than 3%. The mass in the stone M_{abs} is then given by:

$$M_{\mathrm{abs}} = M_0 - \rho \cdot V_{\mathrm{drop}} \qquad (10.2)$$

10.3 SPREADING AND DEPOSITION

The time evolution of the spreading diameters at rim $D(t)$ and at contact line $D_{\mathrm{CL}}(t)$ after impact for drop impacting on Savonnières is presented
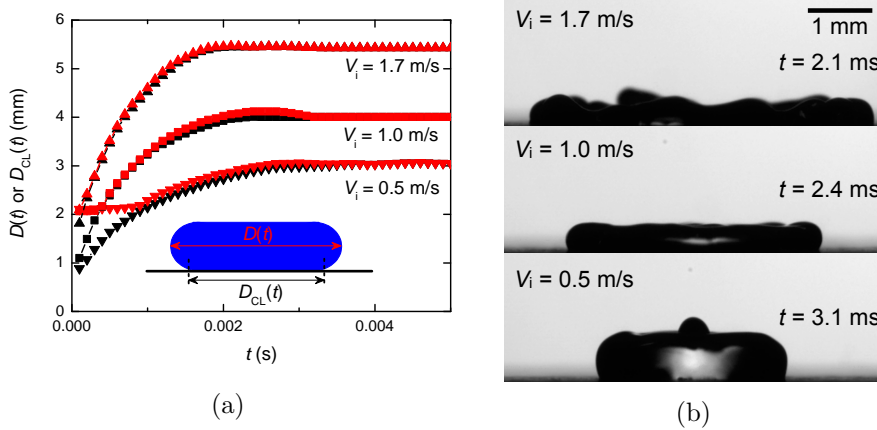
Figure 10.2: (a) Time evolution of spreading diameter at rim D (red) and at contact line D_{CL} (black) and (b) snapshots at maximum spreading for different impact velocities on Savonnières limestone.

in Figure 10.2a. Figure 10.2b shows snapshots at maximum spreading for the different impact velocities. The spreading diameter at rim and the contact line increase with impact velocity due to higher initial kinetic energy of the drop. The difference between spreading diameter at rim and contact line is rather small, especially at maximum spreading. In the following, the contact line diameter to characterize the spreading of the drop during impact on the porous substrate is used.

The impact velocity at $V_{\mathrm{i}} = 1.0$ m/s is selected to compare the spreading on the same porous stone and an impermeable steel surface in Figure 10.3. In Figure 10.3a, the contact line diameter for both cases first increases until reaching its maximum spreading. During this spreading phase, the dynamic contact angle is higher than $90°$, showing a dynamic non-wetting behavior. For the steel surface after reaching the maximum spreading diameter, the contact line diameter reduces during the receding phase (Figure 10.3a), characterized by a reduction of the contact angle below $90°$ until reaching the equilibrium contact angle indicated by the horizontal red dashed line in Figure 10.3b. The contact angle shows some oscillations, when reaching this equilibrium. In contrast, the contact line diameter of Savonnières remains constant indicating the droplet is pinned. While the contact line diameter remains constant, the contact angle decreases showing some oscillations. The inset figures show the

(a) spreading diameter at contact line D_{CL}
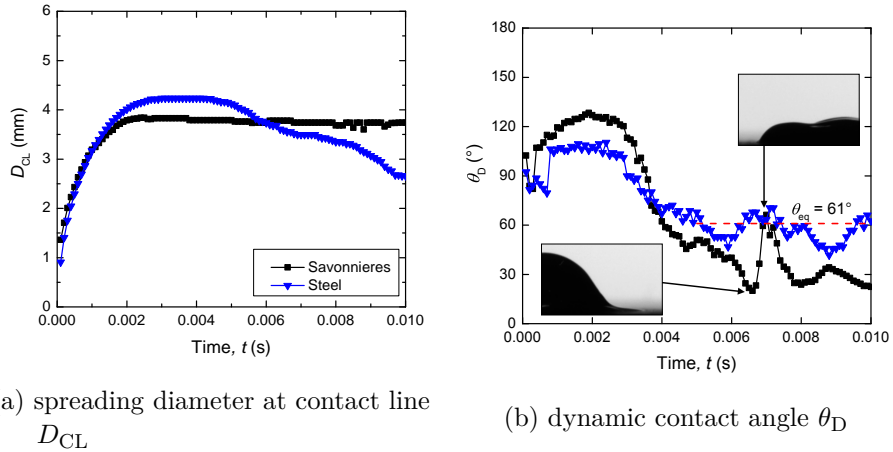
(b) dynamic contact angle θ_{D}

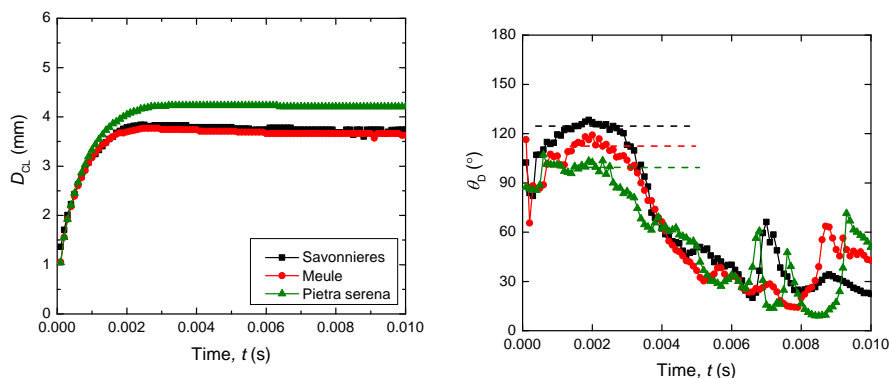Figure 10.3: Comparison of drop impact on porous Savonnières and impermeable steel.

drop shape at two moments around an important change of contact angle, while the drop stays pinned.

Figure 10.4 shows the comparison of drop impact behavior for the three different porous stones. For all porous stones, the contact line diameter remains constant after reaching its maximum, showing that droplets on all porous surfaces are pinned (Figure 10.4a). Droplets on Savonnières and Meule show quite similar evolution of the contact line diameter, while, on Pietra serena, the droplet spreads more compared with droplets on Savonnières and Meule stones. The dynamic contact angle on the different porous stones shows similar behavior (Figure 10.4b): it reaches a maximum during the spreading phase, followed by a decrease of contact angle while staying pinned, followed by some oscillations when reaching its equilibrium value. It was thus observed at short time scale a Constant Contact Radius (CCR) mode. The maximum dynamic contact is different for the three porous materials: Savonnières shows the highest contact angle $\theta_{\mathrm{D}} \sim 123°$, Meule reaches a contact angle of $\theta_{\mathrm{D}} \sim 108°$ and Pietra Serena shows the lowest contact angle $\theta_{\mathrm{D}} \sim 101°$. The maximum dynamic contact angle decreases with decreasing volumetric porosity of the porous material: Savonnières $\Phi = 27\%$, Meule $\Phi = 17\%$ and Pietra serena $\Phi = 5\%$. Assuming the porous media to have a random structure, the areal or surface porosity and volumetric porosity are equal (Dullien, 2012). For Savonnières, an oolithic material with complex pore structure, the ratio between areal and volumetric porosities was found to be 0.87

126

(Roels, 2000). This means that a direct relation between dynamic contact angle and surface porosity is identified.

The dynamic contact angle during spreading shows a dynamic non-wetting or hydrophobic behavior ($\theta_D > 90°$), although the porous stones in quasi-static conditions are clearly hydrophilic as indicated by their capillary active behavior. Figure 10.4c shows a time sequence of snapshots for drop impact on porous stones and steel surface. The droplets on porous stones are pinned at maximum spreading as indicated by the vertical dotted lines. In contrast, the spreading diameter on steel surface reduces until reaching its equilibrium state, showing no pinning occurs on steel. From the dynamic hydrophobic behavior during spreading and the hydrophilicity seen in equilibrium conditions, it is inferred that, at the interface during spreading, air is entrapped in the surface pore structure forming a thin air layer between the liquid and the solid material (Figure 10.5a). The air layer promotes the non-wetting behavior and a dynamic contact angle $> 90°$ during spreading.

The pinning on porous stones and no-pinning behavior on steel could be attributed to the difference in roughness between porous stones (R_a from 10 to 4 μm,) and steel (R_a 0.4 μm). Drop impact measurements on rough sandpaper were also performed (Silicon Carbide Paper, BUEHLER) with different grit size (P120, P240, P600 and P2500), showing a roughness R_a varying between 21 and 3 μm, to study the influence of roughness on pinning behavior (Lee et al., 2016c). In all these experiments on sandpaper, no pinning behavior is observed, but a receding of the droplet occurs after maximum spreading. The conclusion is that the open capillary active pore structure plays an essential role in the pinning and not the roughness. Figure 10.5b shows a schematic of the pinning process due to capillary absorption at the contact line of the droplet at maximum spreading. Since the contact line velocity decreases when reaching maximum spreading, the air layer between droplet and surface can be broken, leading to capillary contact between droplet and porous substrate. This capillary contact induces capillary forces on the droplet by the small pores showing high capillary suction. The droplet remains pinned at the contact line at maximum spreading due to these high capillary forces in the fines pores at the droplet edge leading also to a wetting behavior and a contact angle $< 90°$. Inwards of the pinned contact line, air remains entrapped under the droplet. The presence of this air layer has been observed by high-speed camera for Savonnières,

(a) spreading diameter at contact line D_{CL}

(b) dynamic contact angle θ_D
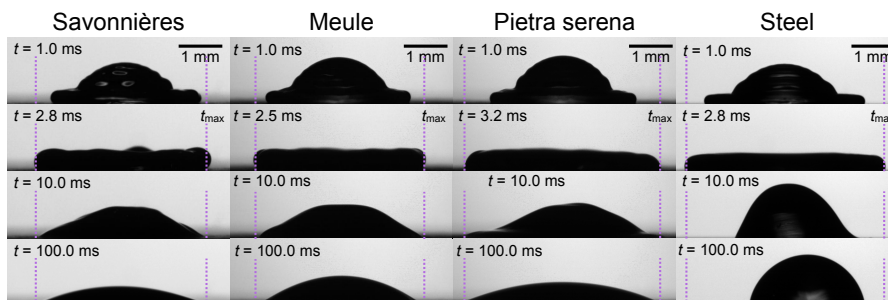
(c) snapshots of drop impact

Figure 10.4: Comparison of drop impacts for $D_0 = 2.0$ mm and $V_i \sim$ 1.0 m/s on different porous stones, (black) Savonnières, (red) Meule and (green) Pietra serena. (a) Time evolution of spreading diameter at contact line D_{CL}. (b) Dynamic contact angle θ_D (c) Snapshots of drop impact on porous materials and steel surface. Vertical line indicates contact line diameter at maximum spreading.
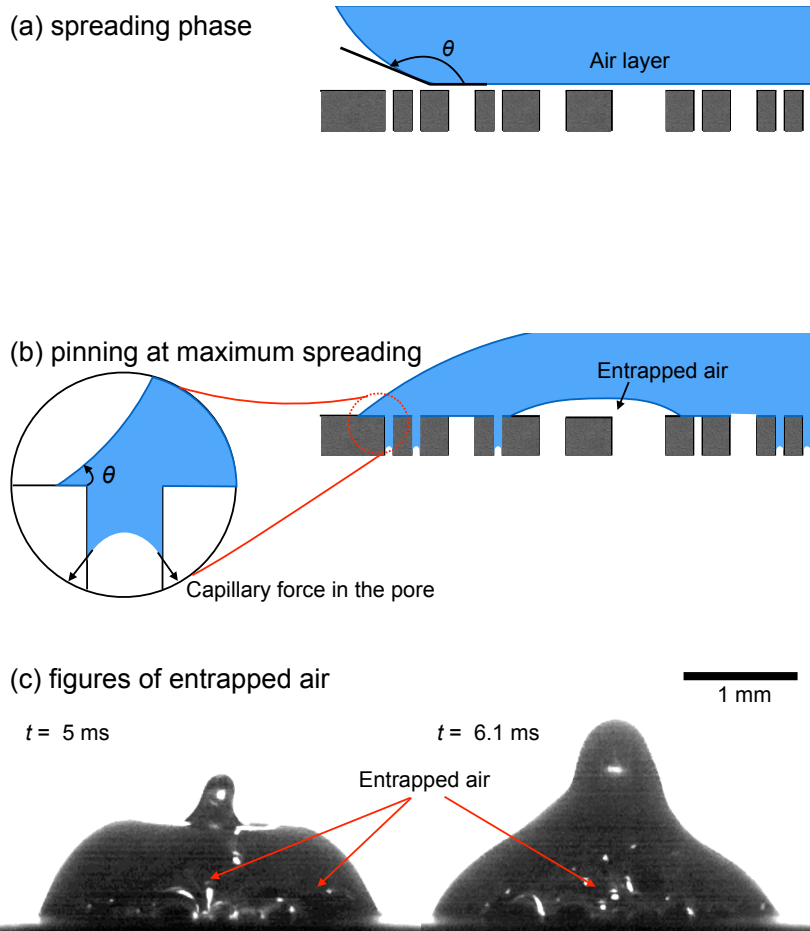
Figure 10.5: Schematic of dynamic spreading and pinning at maximum spreading. (a) Presence of an air layer between droplet and porous substrate leads to a non-wetting dynamic spreading characterized by a contact angle $> 90°$. (b) The droplet is pinned at the contact line at maximum spreading due to capillary forces in fines pores at the droplet edge leading to a wetting behavior and a contact angle $< 90°$. (c) Air remains entrapped under the pinned droplet as shown in receding phase at $t = 6.1$ ms for Savonnières.

demonstrating the adequacy of the assumption on the presence of an air layer (Figure 10.5c).

10.4   MAXIMUM SPREADING

The maximum spreading is characterized by the maximum spreading ratio $\beta_{\mathrm{max}} = D_{\mathrm{max}}/D_0$. Figure 10.6 compares the maximum spreading ratio as a function of impact velocity for the three porous stones and impermeable steel surface. The maximum spreading ratio is quite similar for all substrates at high impact velocity. In this region, viscous effects are dominant and the maximum spreading is mainly determined by the viscosity of the fluid (water). However, at low impact velocity, the curves start to diverge more and more and finally tend to level off to a different maximum spreading ratio at zero velocity, which will be referred to as $\beta_{V_i=0}$. The value for $\beta_{V_i=0}$ is different for the different substrates and its determination will be discussed below. The maximum spreading ratio at low impact velocity is smaller for Savonnières and Meule compared to the one of impermeable steel surface, while the maximum spreading ratio on Pietra serena is higher. The lower maximum spreading on a porous medium compared to a solid surface can be explained by the following phenomena: (1) a part of the drop volume penetrates into the porous stone, resulting in less volume available for spreading and a decrease of the spreading; (2) the dynamic wetting behavior influences the maximum spreading and depends on the nature of the porous material and the presence of an air layer between droplet and this porous surface.

First the first explanation is analyzed in more detail. Droplet spreading is a quite fast phenomenon reaching its maximum spreading in 1E-3 to 1E-2 s. Liquid penetration into the pore structure can be attributed to two phenomena: (1) at early time part of the volume of the droplet penetrates into the pore structure due to inertial effects at impact; (2) at later time, water is uptaken from the droplet due to capillary absorption by the substrate.

To study the inertial effect, the penetration depth z and the time τ over which penetration occurs into the porous substrate were estimated. Consider a cylindrical volume of water that has entered a cylindrical pore to a depth z, $\pi r R^2 z$, with R the radius. The momentum in this liquid is given by:

$$P_{\mathrm{L}} = \pi r R^2 z \rho V_{\mathrm{i}} \qquad (10.3)$$
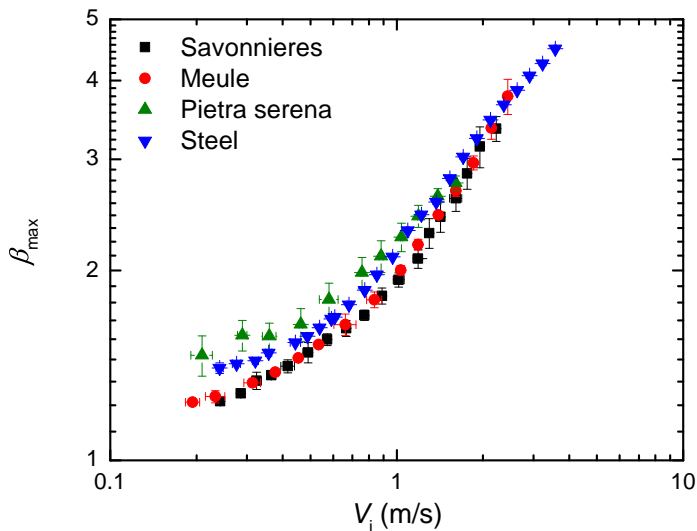
Figure 10.6: Maximum spreading ratio as a function of impact velocity for drop impact on porous stones and steel in log-log plot.

The penetrated liquid is acted upon by a frictional force due to viscous drag, which tries to bring the liquid to a halt. The viscous force per unit area is:

$$f_\mathrm{F} = \mu \frac{V_\mathrm{i}}{R} \tag{10.4}$$

This force works on area $A = 2\pi R z$ for time $\tau \approx z/V_\mathrm{i}$ producing the change in momentum as:

$$P_\mathrm{F} = 2\pi R z f_\mathrm{F} \tau \approx 2\pi R z \mu \frac{V_\mathrm{i}}{R} \frac{z}{V_\mathrm{i}} \approx 2\pi z^2 \mu \tag{10.5}$$

Neglecting capillary penetration at this time scale, the penetration depth z can then be found from equating P_L and P_F (respectively Eqs. 10.3 and 10.5):

$$z \approx V_\mathrm{i} \frac{\rho R^2}{\mu} \tag{10.6}$$

Considering an equivalent pore radius of $R_\mathrm{eq} = 1\mathrm{E}\text{-}5$ m for e.g. Meule (Moonen, 2009), an impact velocity $V_\mathrm{i} = 2$ m/s and initial droplet diameter $D_0 = 2.0$ mm, the penetration depth equals $z \approx 0.2$ mm and time $\tau \approx 1\mathrm{E}\text{-}4$ s. The time where penetration would occur is much

(a) Savonnières   (b) Meule

Figure 10.7: Normalized penetration mass into the pore versus time: (a) Savonnières and (b) Meule for different impact velocities V_i = 0.5, 1.0 and 2.0 m/s.

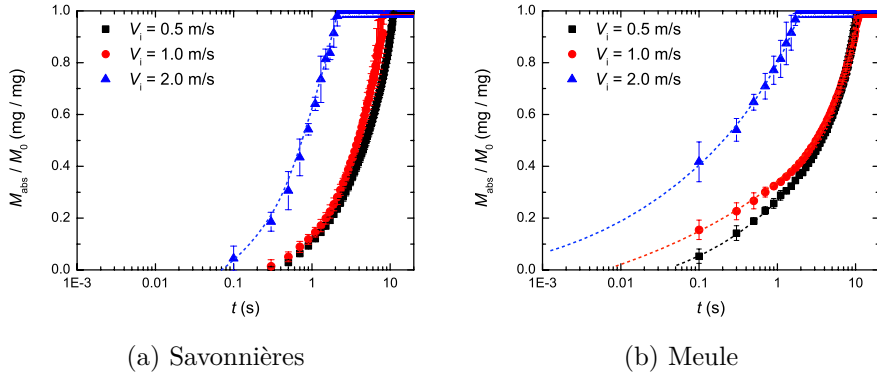shorter $\tau \approx$ 1E-4 s than the time it takes to reach maximum spreading $t \approx$ 1E-2 s. The mass in the porous media is now analyzed at these time scales. Figure 10.7 shows the mass in the porous stone M_{abs} versus time in semi-log plot. The mass in the stone is determined using Eq. 10.2. The remaining drop volume could only be measured accurately once the inertia forces are dissipated ($t > 0.1$s). Figures 10.7a-b show that the main uptake process attributed to capillary absorption occurs for times $t > 0.1$ s, thus after maximum spreading of the droplet. At early time ($t < 0.01$ s), the liquid mass in the stone is negligible for Savonnières and Meule at impact velocities < 1 m/s. Extrapolating the curve for the Savonnières to the time at maximum spreading ($t \sim 0.01$ s) for the impact velocity of 2 m/s shows also that liquid penetration is negligible. When extrapolating the curve to 1E-4s, the estimated time of penetration due to inertia at impact for Meule, at $V_i = 2$ m/s, also leads to the conclusion that no penetration due to inertial effects occurs. Figure 10.6 shows that the maximum spreading ratio at 2 m/s for Meule equals the maximum spreading of the impermeable steel surface, indicating once more that no penetration occurred at maximum spreading.

It is concluded that, for the porous stones studied, the volume loss of the droplet by liquid penetration into the porous substrates due to inertial effects at impact can be neglected and that mass uptake by the substrate due to capillary absorption only starts after maximum spreading of the droplet. Such behavior is explained by the existence of above mentioned air layer, which is entrained between the droplet and

the porous substrate during the spreading process preventing penetration either due to inertial effects or capillary absorption.

To analyze assumption (2) on the influence of dynamic wetting, the maximum spreading ratio on porous and impermeable surfaces is studied in more detail using the energy balance approach. Maximum spreading is governed by the balance between kinetic energy, capillary or surface tension energy before impact and at maximum spreading in surplus of the viscous dissipation during spreading. Energy balance models are commonly formulated using two dimensionless parameters: the Weber number ($We = \rho D_0 V_i^2 / \gamma$) describing the ratio between the kinetic and capillary energy and the Reynolds number ($Re = \rho D_0 V_i / \mu$) describing the ratio between the kinetic and viscous energy. Based on energy balance at low and high impact velocity, two common limit regimes have been introduced: the capillary regime at low impact velocity and the viscous regime at high impact velocity (Clanet et al., 2004). Clanet et al. (2004) proposed, based on momentum conservation, a scaling of $beta_{\max} \sim We^{1/4}$. Based on energy conservation between kinetic and surface energy, a scaling of $beta_{\max} \sim We^{1/2}$ is found (Collings et al., 1990; Bennett and Poulikakos, 1993). Figure 10.8a compares the measured maximum spreading ratio and the two scaling models. No agreement with the scaling of $beta_{\max} \sim We^{1/2}$ is observed, especially at low impact velocity. While the scaling with $We^{1/4}$ could be consistent for the impermeable steel surface, it is clearly less consistent for Savonnières and Meule at low impact velocity. To analyze the scaling of $beta_{\max}$ with $We^{1/4}$ in more detail, additional drop impact experiments were performed on Savonnières with two other liquids: 1:1.3 glycerol-water mixture (glycerol 10 mPa·s) and pure ethanol. Glycerol has a ten times lower viscosity (1.2E-3 Pa·s) than water, while ethanol has a three times lower surface tension (2.3E-2 N/m). Figure 10.8b clearly shows that the $We^{1/4}$ scaling does not apply to current data. In general, the scaling of $beta_{\max} \sim We^{\alpha}$ implies that, at zero impact velocity, $beta_{\max}$ the maximum spreading ratio equals zero, which is physically impossible ($beta_{\max} \geq 1$). Figure 10.8a reveals that, at low impact velocity, the spreading ratio does not tend to zero, but levels off to a constant maximum spreading ratio.

In the viscous regime at high impact velocity, based on energy conservation between kinetic and viscous dissipation energy, a scaling of $\beta_{\max}$ with $Re^{1/5}$ is found (Madejski, 1976; Roisman et al., 2002; Madejski, 1976). Figure 10.8c compares the measured maximum spreading ratio

and scaling of β_{max} with $\mathrm{Re}^{1/5}$. The data for impact on impermeable and porous materials converge to a single curve, although it would be challenging to conclude that the data tend to a slope of $1/5$. Current data do not cover sufficiently high impact velocity to evaluate properly the scaling in the viscous regime, since splashing occurs at such higher impact velocity.

An universal scaling of the maximum spreading with broad cross over from capillary to viscous regime has been proposed by Laan et al. (2014) for impermeable surfaces by interpolating between two scaling models, i.e. $\mathrm{We}^{1/2}$ and $\mathrm{Re}^{1/5}$. Figure **??** shows the rescaling as function of the impact number ($P = \mathrm{We} \cdot \mathrm{Re}^{-2/5}$) for all substrates. At high P, one may conclude that a convergence of the curves as predicted by the model of Laan et al. (2014) is observed. As P becomes smaller, the data deviate from the predicted curve and, even at very low P, the data start to increase again. These observations show that the existing scaling laws do not predict current data correctly. It will be further shown that, when taking into account the dynamic wetting behavior correctly, all data to collapse into a single curve can be rescaled.

To account for the dynamic wetting behavior, a term is added to the energy balance between kinetic energy before impact E_k and capillary energy at maximum spreading E_γ, by taking into account the capillary or surface tension energy at the low impact velocity limit $\mathrm{E}_{\gamma 0}$. The energy balance then reads:

$$\mathrm{E}_k + \mathrm{E}_{\gamma 0} \sim \mathrm{E}_\gamma \tag{10.7}$$

or

$$\rho D_0 V_{\mathrm{i}}^2 + \gamma D_{V_{\mathrm{i}}=0}^2 = \gamma D_{\mathrm{max}}^2 \tag{10.8}$$

which leads to

$$\sqrt{\beta_{\mathrm{max}}^2 - \beta_{V_{\mathrm{i}}=0}^2} = \mathrm{We}^{1/2} \tag{10.9}$$

where $D_{V_{\mathrm{i}}=0} = \beta_{V_{\mathrm{i}}=0} \cdot D_0$. Equation 10.9 shows that the data after correction for $\beta_{V_{\mathrm{i}}=0}$ should scale with $\mathrm{We}^{1/2}$.

To determine the spreading ratio $\beta_{V_{\mathrm{i}}=0}$ the measured data are approximated by the following function:

$$\beta_{\mathrm{max}} = \beta_{V_{\mathrm{i}}=0} + A \cdot \frac{V_{\mathrm{max}}^C}{B + V_{\mathrm{i}}^C} \tag{10.10}$$
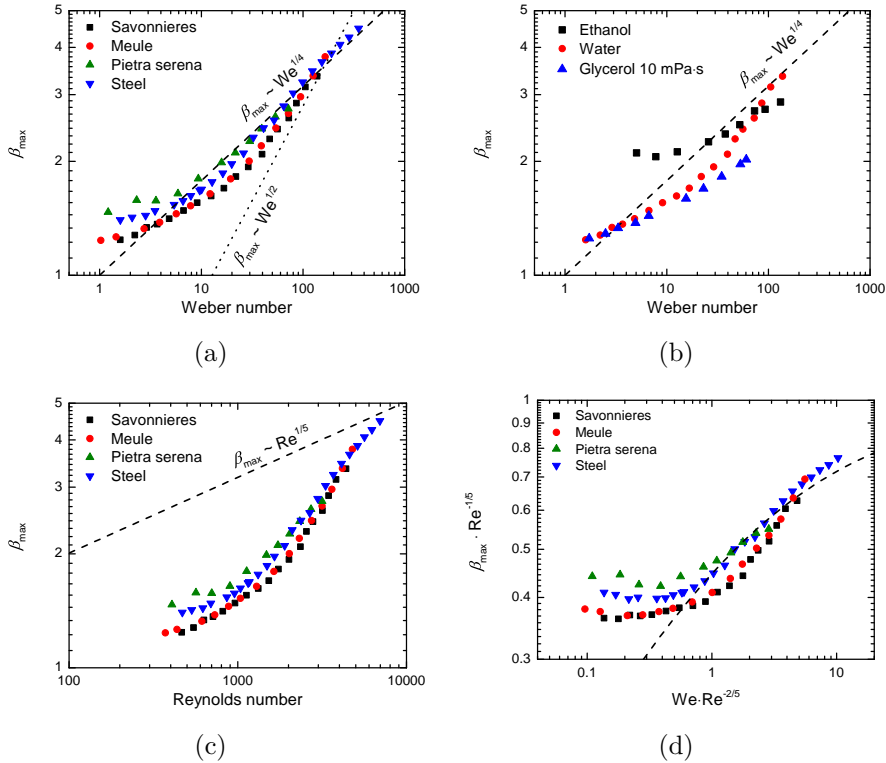
Figure 10.8: Maximum spreading ratio as function of Weber number with scaling laws $\beta_{\max} \sim \text{We}^{1/4}$ and $\beta_{\max} \sim \text{We}^{1/2}$ (a) for water on different substrates; (b) for glycerol, water and ethanol on Savonnières. (c) Maximum spreading ratio as function of Reynolds number and scaling with $\text{Re}^{1/5}$. (d) Rescaled spreading ratio as function of the impact number $P = \text{We} \cdot \text{Re}^{-2/5}$ for water impact on different substrates.
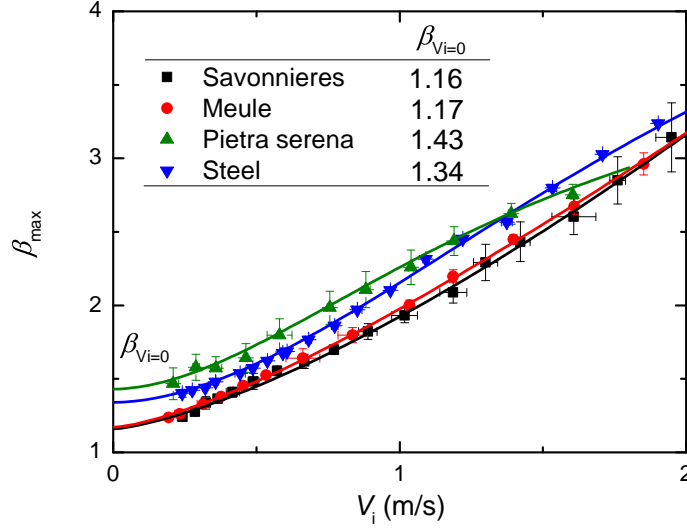
Figure 10.9: Determination of the maximum spreading ratio at zero impact velocity by fitting Eq. 10.4 to the measured data.

where A, B, C and $\beta_{V_i=0}$ are obtained by fitting the curve to current data. Figure 10.9 shows that Eq. 10.10 fits the data satisfactorily allowing to determine the spreading ratio $\beta_{V_i=0}$. The values for $\beta_{V_i=0}$ are given in the inset of the figure. It was observed that the spreading ratios $\beta_{V_i=0}$ for Savonnières and Meule, showing a higher surface porosity, are lower than for the impermeable substrate, while the $\beta_{V_i=0}$ for Pietra serena is higher. This observation is consistent with the porosity values, but the higher $\beta_{V_i=0}$ for Pietra serena compared to the non-porous steel surface has still to be explained further.

According to Eq. 10.9, the corrected maximum spreading $(\beta_{max}^2 - \beta_{V_i=0}^2)^{1/2}$ should scale with $We^{1/2}$. Therefore the approach of Laan et al. (2014) for the corrected maximum spreading ratio can be applied, where a smooth transition between the capillary and viscous regimes is described as:

$$(\beta_{max}^2 - \beta_{V_i=0}^2)^{1/2} \cdot Re^{-1/5} = \frac{We^{1/2}}{(A + We^{1/2})} \qquad (10.11)$$

which is based on the first order Padé approximation. Figure 10.10 shows the corrected measured data as a function of Weber number for drop impact on porous stones and steel surface. The curve as predicted
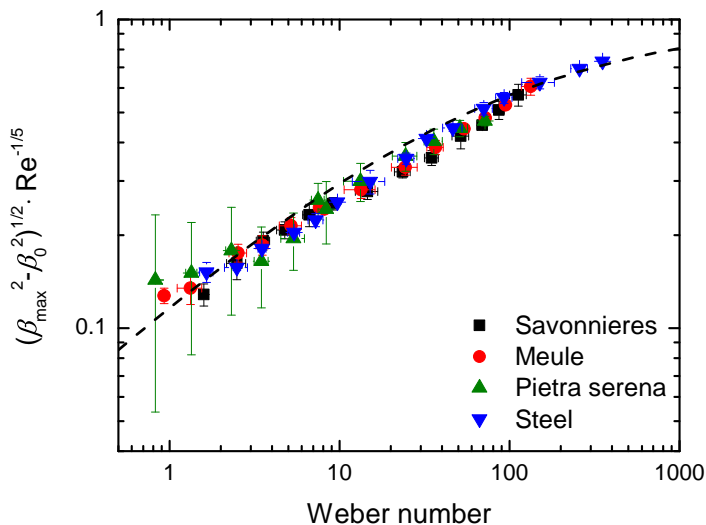
Figure 10.10: Rescaled maximum spreading ratio as a function of Weber number in log-log plot for porous stones. The dotted line is the first order Padé approximation (Eq. 10.9).

by Eq. 10.11, with $A = 7.6$, shows a good agreement with the rescaled data for maximum spreading. The larger error bars at low velocity are due to the logarithmic scaling. This result shows that the maximum spreading ratio for different porous media and for impermeable substrate can be rescaled into a single description, when the data are corrected for the limiting spreading ratio at zero velocity $\beta_{V_i=0}$.

Finally, the physical meaning of the limiting spreading ratio at zero velocity $\beta_{V_i=0}$ is tried to unravel. For this, the energy balance for a pancake-shaped droplet is explored at maximum spreading, including kinetic and surface energy before impact, and surface energy and viscous dissipation at maximum spreading (Mao et al., 1997), given by:

$$\left(\text{We} + 12\right) \beta_{\max} = 8 + \beta_{\max}^3 \left[3(1 - \cos\theta) + \frac{4\text{We}}{\sqrt{\text{Re}}}\right] \tag{10.12}$$

To find an expression for $\beta_{V_i=0}$, the limit for $V_i \to 0$ is taken in Eq. 10.12:

$$\beta_{V_i=0}^2 = \frac{4}{(1 - \cos\theta_{V_i=0})} \left(1 - \frac{2}{3\beta_{V_i=0}}\right) \tag{10.13}$$

This equation shows that the limiting spreading ratio depends on a contact angle, which is denoted as $\theta_{V_i=0}$, and that its value can be obtained

137

directly from $\beta_{V_i=0}$ using Eq. 10.13. The dynamic wetting behavior at maximum spreading is characterized by the dynamic contact angle $\theta_D(t_{max})$ imaged and measured at maximum spreading time t_{max}. Figure 10.11a compares the contact angle $\theta_{V_i=0}$ determined from $\beta_{V_i=0}$ using Eq. 10.13 and the dynamic contact angle $\theta_D(t_{max})$ at maximum spreading, showing a reasonable agreement. This means that the limiting spreading ratio $\beta_{V_i=0}$ describes the dynamic wetting behavior during wetting and is characterized by the dynamic contact angle $\theta_{max}(t_{max})$. The derivation of this equation is based on the assumption that the substrate is non-porous or Φ is zero. Assuming however that the droplet is in the Cassie-Baxter state on a porous substrate, the surface tension energy at maximum spreading reads $SE_2 = S_1 \cdot \gamma_{LV} + S_2 \cdot (\gamma_{SL} - \gamma_{SV})(1 - \Phi) + S_2 \cdot \gamma_{LV}\Phi$, where S_1 is the surface between droplet and surrounding air and S_2 is the contact area droplet–substrate. This leads to a modification of Eq. 10.13 for $\beta_{V_i=0}$:

$$\beta_{max}^2 = \frac{4}{(1 + \Phi) - (1 - \Phi)\cos\theta}\left(1 - \frac{2}{3\beta_{max}}\right) \tag{10.14}$$

The comparison of the contact angles obtained from this relation with current data of dynamic contact at maximum spreading does not give a better agreement (Figure 10.11b). This may indicate that a direct relation between (surface) porosity and dynamic contact does not apply, and other aspects have to be considered.

Maximum spreading can be rescaled properly for porous and impermeable surfaces by taking the capillary energy at zero impact velocity into account. It is hypothesized that the origin of this successful rescaling for porous stone can be attributed to the presence of a thin air layer between droplet and the porous stone during spreading, which leads to a similar spreading behavior on Savonnières and Meule. The different behavior of Pietra serena, showing a lower dynamic contact at low impact velocity and a higher spreading ratio $\beta_{V_i=0}$ than an impermeable surface, is possibly caused by the (partially) breaking of this air layer, leading to a dynamic contact angle $< 90°$ causing capillary forces to enhance the dynamic wetting of the surface.

This analysis demonstrates that dynamic wetting plays an important role in the spreading at low velocity and that the dynamic wetting as characterized by the dynamic contact angle θ_D has to be taken into account for predicting the maximum spreading. The analysis above shows that the capillary or surface tension energy related to $\theta_{V_i=0}$ or to
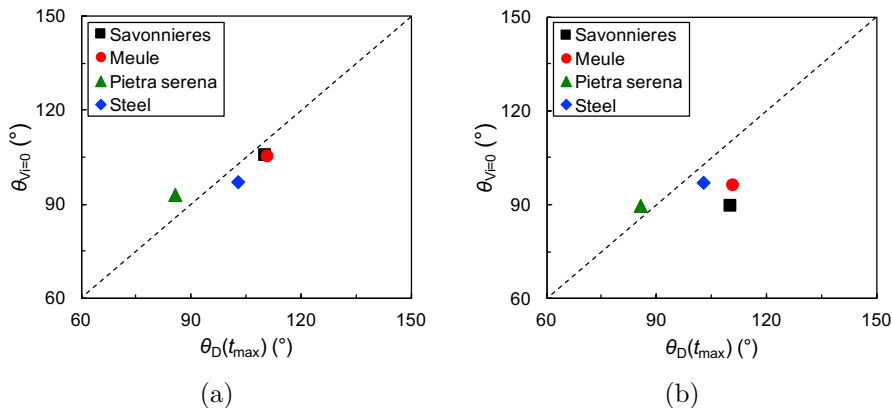
Figure 10.11: (a) Comparison of the dynamic contact angle $\theta_D(t_{max})$ (from experiments) and the contact angle $\theta_{V_i=0}$ determined from $\beta_{V_i=0}$ using Eq. 10.13 assuming no porosity. (b) Comparison of the dynamic contact angle $\theta_D(t_{max})$ (from experiments) and the contact angle $\theta_{V_i=0}$ determined from $\beta_{V_i=0}$ using Eq. 10.13 assuming surface porosity.

$\beta_{V_i=0}$ has to be incorporated in the prediction of the maximum spreading. The relation between the dynamic contact angle at maximum spreading, the dynamic contact angle $\theta_{V_i=0}$ and maximum spreading ratio $\beta_{V_i=0}$ at zero velocity, and its connection to surface properties such as surface porosity and roughness remains however still unclear.

10.5 CONCLUSION

Drop impact on porous stones has been experimentally investigated by high-speed imaging and compared to the drop impact on impermeable surface. For the porous stones studied, no liquid penetrated into the porous substrate due to inertial effects at impact, and the liquid into the porous substrate is only due to capillary absorption by the porous substrate starting after maximum spreading of the droplet. At maximum spreading the contact line on porous substrates pins and the area at maximum spreading determines the contact area between fluid and porous stones for capillary uptake. The dynamic non-wetting behavior during spreading and hydrophobic contact angle $> 90°$ is attributed to the presence of an air layer between droplet and porous substrate. The maximum dynamic contact angle is found to increase for porous stones

with higher porosity. The droplet undergoes pinning when the air layer is broken at the contact line and capillary forces develop in fines pores at the droplet edge pinning the droplet. This pinning due to capillary absorption at the droplet edge leads to a change from dynamic non-wetting to a wetting behavior with a contact angle $< 90°$. Air remains entrapped under the pinned droplet.

Maximum spreading on porous stones increases with impact velocity but does not scale with Weber number at low impact velocity. Dynamic wetting plays an important role in the spreading at low velocity and dynamic wetting as characterized by the dynamic contact angle θ_D has to be taken into account for predicting the maximum spreading. The analysis above shows that the capillary or surface tension energy related to $\theta_{V_\mathrm{i}=0}$ or to $\beta_{V_\mathrm{i}=0}$ has to be incorporated in the prediction of the maximum spreading. Correcting the maximum spreading ratio for the dynamic wetting behavior, it is clearly demonstrated that all data for porous stones and non-porous substrates collapse onto a single curve.

11

ABSORPTION OF IMPINGING DROPLET ON POROUS STONES

This chapter is based on the paper Lee JB, Radu AI, Vontobel P, Derome D, Carmeliet J. "Absorption of impinging droplet on porous stones" submitted to Journal of Colloid and Interface Science.

11.1 INTRODUCTION

This chapter presents an experimental investigation and numerical analysis of the absorption of liquid droplets impacting porous stones. High speed imaging and neutron radiography are used to capture the full absorption process of an impinging droplet in three natural stones of varying porosity. The main experimental challenge for visualizing the absorption process inside porous stones is the limited temporal resolution of the non-destructive technique used. To overcome that, high-speed camera measurements are used to compensate for the time gap in neutron radiography as such images allow the estimation of absorption mass from the remaining volume on the surface. In addition, absorption is studied with a finite element model to evaluate the moisture content inside the porous stone. In contrast to previous studies, the full absorption process of an impinging droplet is characterized in one continuous track, from spreading to evaporation, in terms of absorption mass, depletion time and moisture content distribution.

11.2 EXPERIMENTAL RESULTS AND DISCUSSION

The three stones described in chapter 10 are used. The stones are mainly selected by their open porosity in order to understand the influence of surface pore structure on the dynamics of droplet spreading and absorption.

The drop impact on the porous surface is monitored with high-speed camera setup (1 000 fps, 7.38 μm spatial resolution and 30 μs exposure time) in order to measure the depletion of the droplet and the mass

Table 11.1: Properties of water droplet and impact conditions for drop test

		Properties at 25°C		
		ρ (kg/m^3)	μ (mPa·s)	γ (mN/m)
Water		998	1.0	72.8
		Impact conditions		
	D_0 (mm)	V_i (m/s)	We	Re
Water	2.0	0.5, 1.0, 3.0	7, 27, 247	998, 1 996, 5 988

taken up by the porous medium. In addition, the absorption process into the porous stone is captured by neutron radiography. Neutrons are attenuated by water (hydrogen), but penetrate the porous stone. The detail description for high-speed camera and neutron radiography measurements can be found in chapter 5. Table 11.1 shows the properties of water and the impact conditions of the droplet impact tests.

11.2.1 *Drop impact on porous stones*

Figure 11.1 shows high-speed camera snapshots of drop impact on Savonnières at different velocities. At impact velocities $V_i = 0.5$ (Figure 11.1a) and $V_i = 1.0$ m/s (Figure 11.1b), the liquid droplet spreads over the porous surface until it reaches its maximum spreading diameter ($t \approx 0.003$ s). After maximum spreading, the droplet shows some dynamic behavior, but remains pinned ($t \approx 0.01$ s). Once the kinetic energy of drop impact is dissipated, the droplet forms a spherical cap shape on the surface ($t \approx 0.1$ s). The droplet does not attain an equilibrium state since capillary absorption into the substrate occurs. At high impact velocity at $V_i = 3.0$ m/s (Figure 11.1c), the drop splashes and different droplet fragments are spread over the contact area, forming themselves satellite spherical cap droplets, from where absorption takes place.

11.2.2 *Contact area of drop impact*

In the droplet impact on a porous substrate, three periods are distinguished: (1) spreading at short time after impact; (2) capillary absorption, which ends when the droplet is depleted; (3) evaporation from the wetted

(a) $V_i = 0.5$ m/s

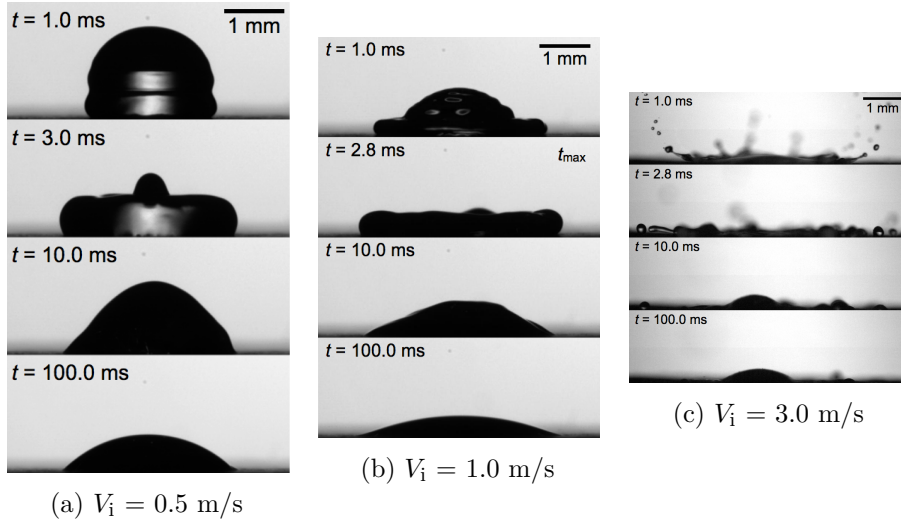(b) $V_i = 1.0$ m/s

(c) $V_i = 3.0$ m/s

Figure 11.1: Drop impact on Savonnières limestone for (a) $V_i = 0.5$ m/s, (b) $V_i = 1.0$ m/s and (c) $V_i = 3.0$ m/s. Deposition (a, b) and splashing (c) can be observed.

porous medium. During the spreading phase, the contact line diameter D_{CL} increases until the droplet reaches its maximum spreading (Figure 11.2a). Spreading ends after 0.003 seconds. Pietra serena attains a slightly higher maximum spreading ratio than Savonnières and Meule. After spreading, the contact line diameter D_{CL} remains constant showing the droplet is pinned. The dynamic contact angle on the different porous stones shows similar behavior (Figure 11.2b): it reaches a maximum during the spreading phase, followed by a decrease of contact angle while staying pinned, followed by some oscillations when reaching its equilibrium value. The dynamic contact angle during spreading shows a dynamic non-wetting or hydrophobic behavior ($\theta_D > 90°$), while after maximum spreading the dynamic contact angle shows a dynamic wetting behavior ($\theta_D \sim 20°$ - $60°$), which is in agreement with the behavior of the porous stones in quasi-static conditions, where they are hydrophilic as indicated by their capillary active behavior. As explained in chapter 10, the hydrophobic behavior during spreading ($\theta_D > 90°$) is attributed to the presence of an air entrapped in the surface pore structure forming a thin air layer between the liquid and the solid material.

Figures 11.3 show the time evolution of the contact line diameter D_{CL} and contact angle θ_{sc} during the capillary absorption phase from 0.1 to

(a) contact line diameter
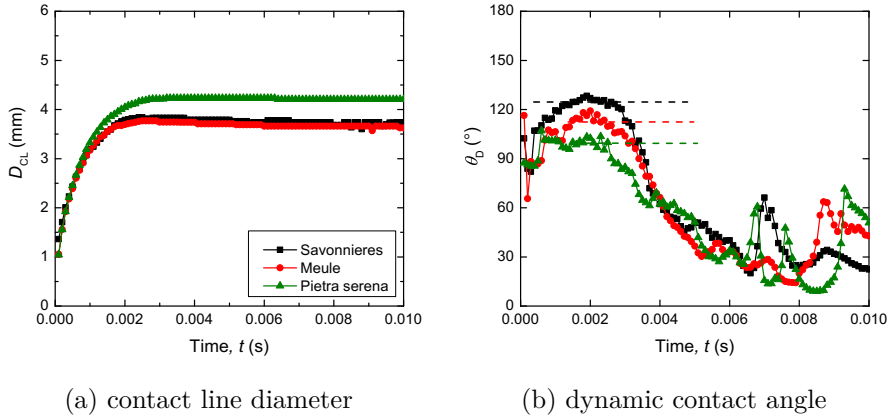
(b) dynamic contact angle

Figure 11.2: Comparison drop impacts for $D_0 = 2.0$ mm and $V_i \sim 1.0$ m/s. on different porous stones, (black) Savonnières, (red) Meule and (green) Pietra serena. (a) Time evolution of spreading diameter at contact line D_{CL}, (b) dynamic contact angle θ_D.

10 seconds for the three porous materials. The spreading diameter at 0.1 seconds, i.e. the start of the absorption process, increases with increasing impact velocity. The contact angle at the start of the absorption process decreases with impact velocity, which leads to a lower contact angle, a logical outcome since a spherical cap with the same mass shows a lower contact angle at higher spreading. The quasi-static contact angles during the absorption phase are remarkably smaller ($\theta_D \sim 20°$ - $80°$) than the dynamic contact angles at maximum spreading.

For Savonnières and Meule, the contact line diameter D_{CL} remains constant during a certain time, while the contact angle decreases from start due to the fact that water is drained from the droplet to the porous stone by capillary absorption. This type of behavior is called the Constant Contact Radius (CCR) mode (Marmur, 1988). The CCR mode is schematically illustrated in Figure 11.4a and captured by snapshots for Meule in Figure 11.4b.

At lower impact velocity ($V_i = 0.5$ and 1 m/s), the CCR mode continues almost until the droplet depletes quickly. For high impact velocity ($V_i = 2$ m/s), the droplet starts to deplete much earlier, since the droplet is spread over a larger area with smaller droplet height, where absorption can more efficiently deplete the droplet. The contact diameter decreases gradually, which is related to water at borders of the droplet becoming totally
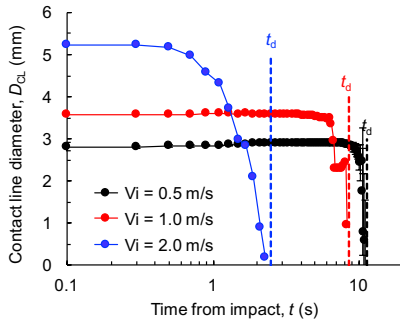
(a) contact line diameter
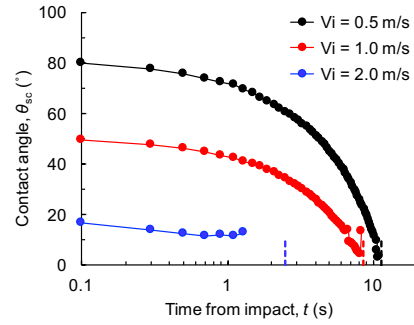
(b) contact angle
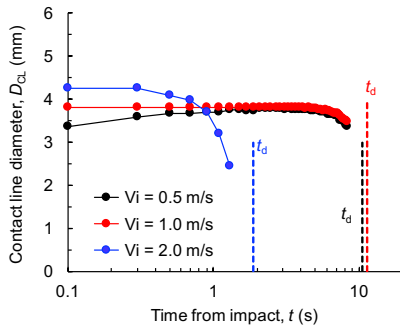
(c) contact line diameter
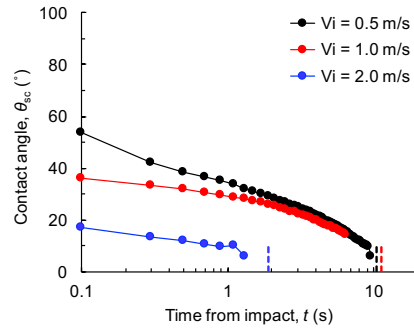
(d) contact angle
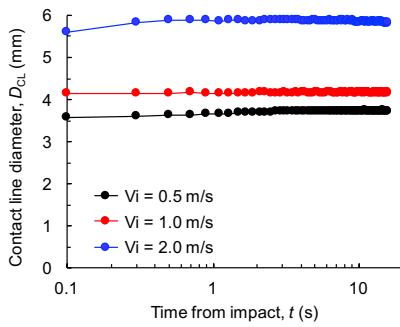
(e) contact line diameter
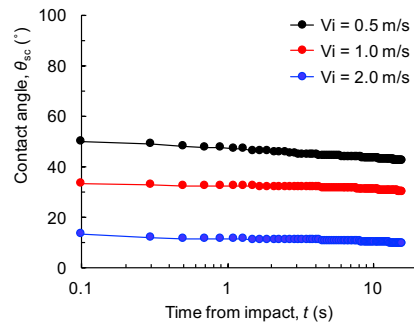
(f) contact angle

Figure 11.3: (a, c, e) Time evolution of contact line diameter D_{CL} and contact angle θ_{sc} in absorption phase (a-b) Savonnières, (c-d) Meule and (e-f) Pietra serena. The dashed vertical lines indicate the depletion time (t_{d}).
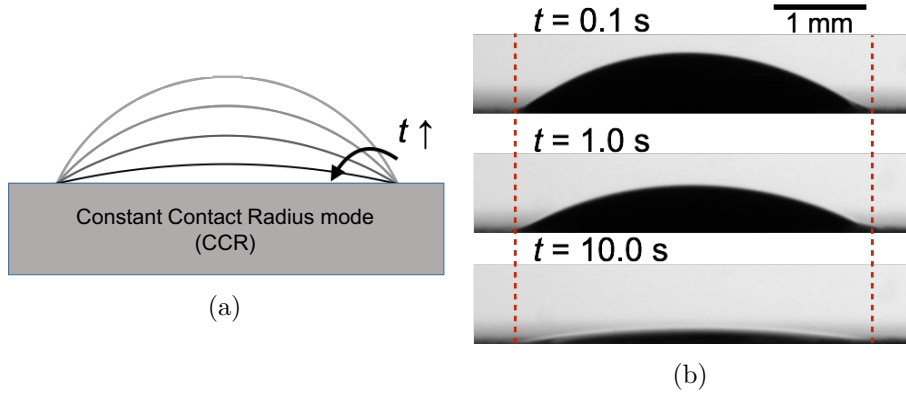
Figure 11.4: (a) Schematic of absorption with Constant Contact Radius (CCR) and (b) snapshots of remaining droplet ($V_{texti} = 1.0$ m/s) on a Meule sandstone during absorption phase.

absorbed and not to a depinning of the contact line. Fast depletion of the droplet starts at a contact angle of almost 10° for all impact velocities, which is close to the equilibrium contact angle.

Figure 11.3e-f shows that, for Pietra serena, the contact line diameter and contact angle remain almost constant, which is explained by the very slow capillary absorption by this material.

11.2.3 *Moisture distribution*

Figure 11.5 shows the moisture distribution in the porous stone as imaged by neutron radiography for different impact velocities and different porous stones. For Savonnières and Meule, the first two images at time $t = 3$ s and $t = 9$ s are during the absorption phase. At impact velocity of 0.5 and 1.0 m/s, the droplet is still visible above the substrate at time $t = 3$ s, while for $V_i = 3.0$ m/s the droplet is already depleted. It indicates that, with increasing impact velocity, the droplet spreads more resulting in an increase of contact area, leading to an increase in mass absorption rate. As a consequence, the time at which the droplet is depleted shortens with increasing impact velocity. At time $t = 18$ s and $t = 30$ s, the droplet is totally depleted and redistribution deeper into the material and evaporation at the surface occurs. While the width of the wetted zone in the porous material in horizontal direction depends on the impact velocity, the depth of the wetted zone seems to be less dependent on

impact speed. Due to the low capillary absorption coefficient of Pietra serena, almost no absorption is observed even at $t = 30$ s. In the following, due to its very slow absorption behavior, Pietra serena is not further discussed in this chapter and this chapter will focus on Savonnières and Meule.

The neutron images are obtained in projection mode, so local moisture contents at a given position are hard to obtain. However, quantitative moisture content profiles can be obtained from the neutron images by averaging the data over a width of 10 pixels at the centerline (Figure 11.6a).
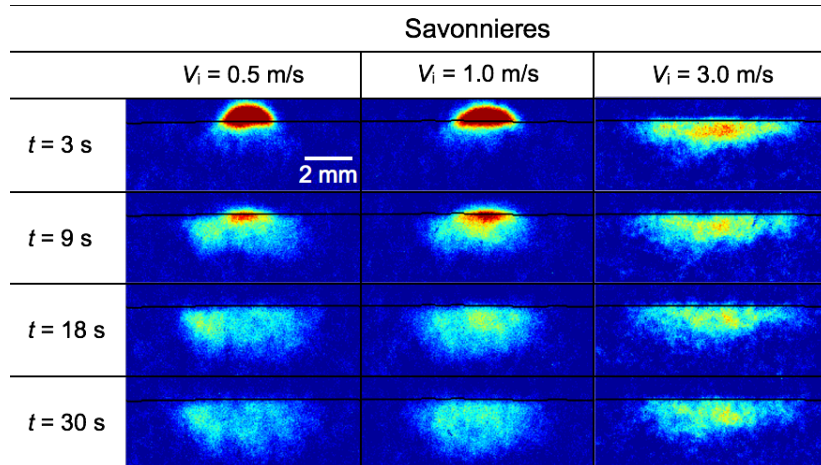
Figure 11.6b shows profiles of moisture mass at the droplet center along the depth of the porous material (Savonnières at impact velocity $V_i = 0.5$ m/s). The moisture mass above the surface of the porous material refers to the droplet sitting on the surface. The moisture mass profiles in the porous material during the absorption phase are quite steep and progress further into the material with time. When the droplet is depleted, the evaporation phase ($t > 18$ s) starts and the moisture mass at the surface decreases. Concurrently moisture is further transported into the porous material, a process referred to as redistribution.

Based on the high-speed camera and neutron radiography data, the cumulative mass of moisture can be determined as function of time. Figures 11.7 give the total mass absorption into the porous material normalized by the initial drop mass in time in semi-log (a-c) and log-log (b-d) plot for Savonnières and Meule. Both high-speed camera, until drop depletion, and neutron radiography measurements are given for different impact velocities. The results show a good agreement between both techniques at $V_i = 0.5$ and 1.0 m/s for both porous materials. The absorption phase with increasing mass and the evaporation phase where the mass decreases again can clearly be distinguished. At the end of the absorption phase, the droplet is depleted. The data show again that the droplet depletion time shortens with impact speed. The data also indicate that penetration of liquid at early time impact is not very likely. By extrapolating the curves to $t \approx 0.003$ s, i.e. the time at maximum spreading, it is concluded that penetration of liquid at early time impact due to inertial effects is not very likely to occur.

It is also plotted the data in a log-log (Figures 11.7b-d) comparing the slope of the data with the slope of 0.5 as predicted by the Washburn equation. While Meule could show a consistency with the Washburn law during the absorption phase, the data of Savonnières clearly devi-

(a) Savonnières

(b) Meule

Moisture mass, $M(t)$ (µg)
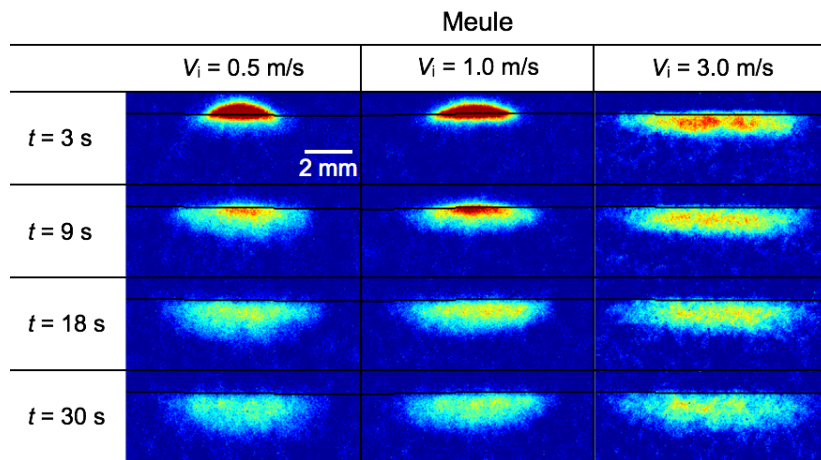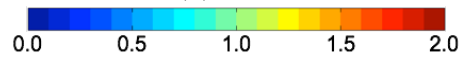
(c) Pietra serena
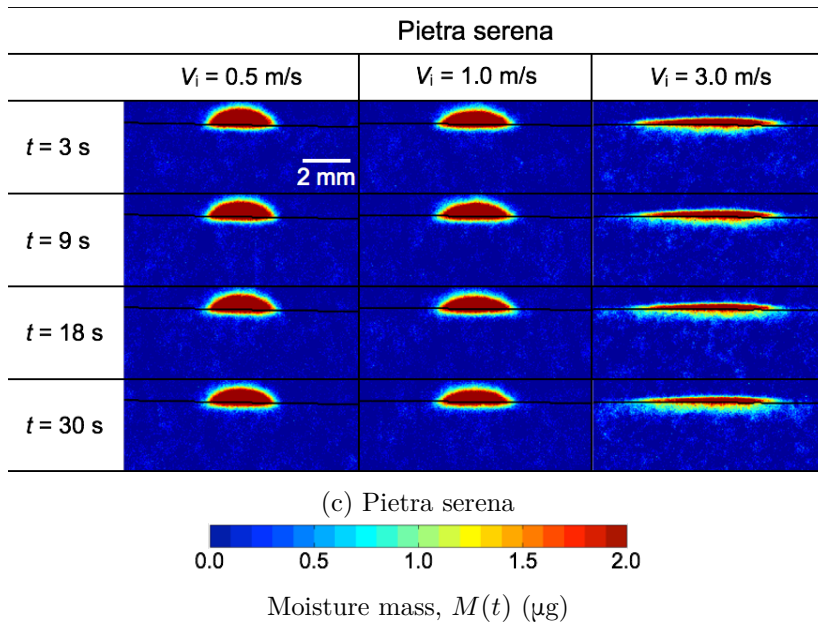
Moisture mass, $M(t)$ (µg)

Figure 11.5: Snapshots of neutron radiography for moisture mass distribution of drop impact with different impact velocities onto porous stones: (a) Savonnières limestone, (b) Meule sandstone and (c) Pietra serena sandstone. The sensitivity of neutron imaging to liquid water is highlighted by the moisture mass legend showing a maximum of 2 µg.

(a)

(b)
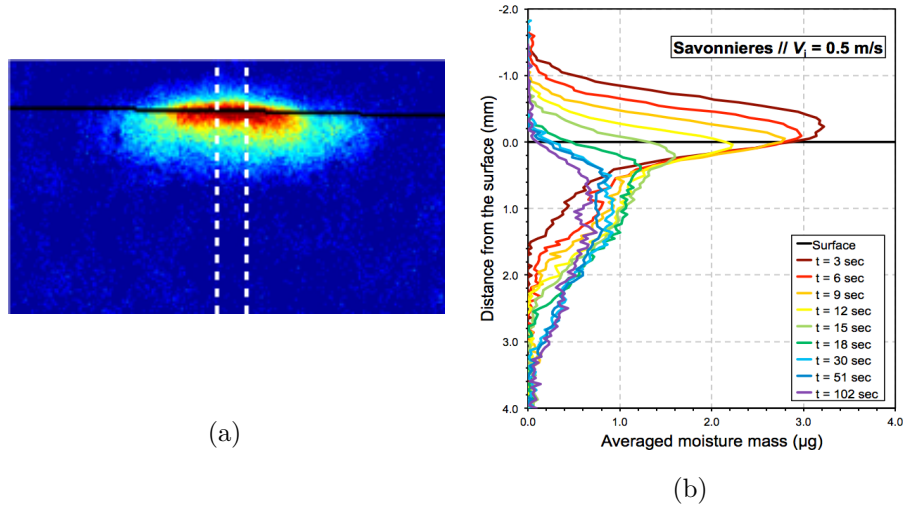
Figure 11.6: (a) Averaging over a width of 10 pixels at the centerline of the moisture content data obtained by neutron imaging in projection mode. (b) Averaged moisture mass profiles at the droplet center along the depth of the porous material, Savonnières, at an impact velocity $V_{\mathrm{i}} = 0.5$ m/s.

ate from Washburn law. Reason is that the absorption process is not unidimensional from an infinite water source, but tridimensional, i.e. a combination of uptake from the wetted zone in horizontal and vertical directions into the porous material.

Figures 11.8 and 11.9 summarize the observations schematically. The life of a droplet after impact on a porous stone covers different time scales (Figure 11.8). At short time after drop impact, the droplet spreads showing a dynamic contact angle higher than 90° indicating a dynamic non-wetting behavior. The dynamic contact angle then decreases sharply after reaching maximum spreading, while the droplet remains pinned. During this dynamic phase, no liquid mass penetrates into the porous substrate. This behavior is explained by the presence of an air layer between the droplet and the porous substrate. During spreading, the presence of this air layer leads to the observed dynamic hydrophobic non-wetting behavior (Figure 11.9a). When the contact line velocity decreases reaching maximum spreading, the air layer between droplet and surface can be broken, leading to capillary contact between droplet and porous substrate (Figure 11.9b). This capillary contact induces capillary
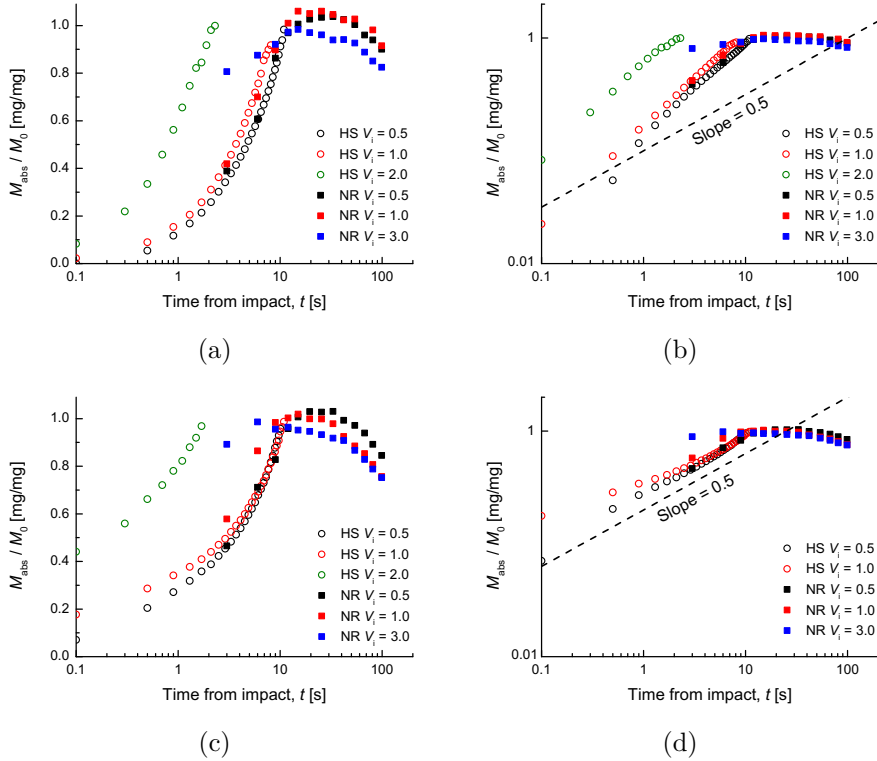
Figure 11.7: Normalized absorption mass versus time for (a-b) Savonnières and (c-d) Meule samples. HS: high-speed camera measurements. NR: NEUTRA measurements. (a) and (c) are in semi-log and (b) and (d) in log-log.
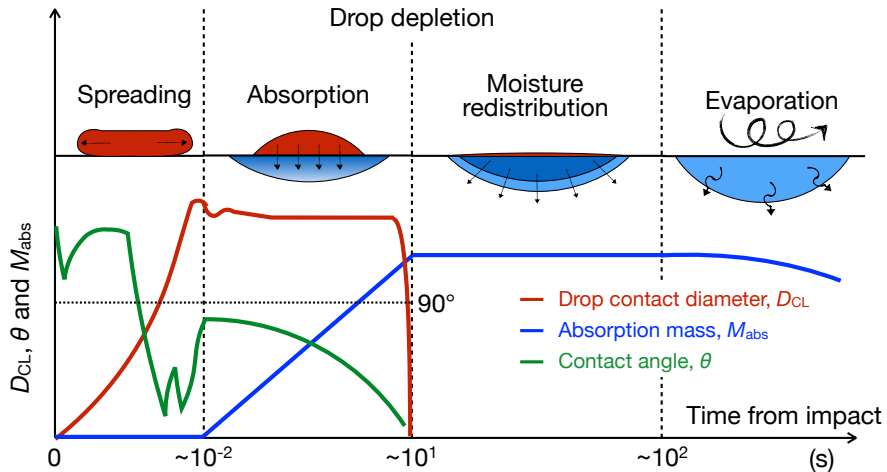
Figure 11.8: Life of a droplet after impact on a porous stone over different time scales: spreading, absorption, drop depletion, moisture redistribution and evaporation and time evolution of droplet contact line diameter, contact angle and absorbed mass in the porous medium.

forces on the droplet by the small pores showing high capillary suction. The droplet remains pinned at the contact line at maximum spreading due to these high capillary forces in the fines pores at the droplet edge leading to a change from non-wetting to wetting behavior and a contact angle $< 90°$. Air remains entrapped under the pinned droplet.

During the absorption phase, the droplet remains pinned and the contact angle decreases in a CCR mode (Figure 11.8). The mass absorbed in the stone increases until the droplet is depleted. At the end of the absorption phase, the droplet radius decreases due to a total suction of the liquid occurring first at the droplet edge. Finally, the droplet is depleted, and moisture is evaporated from the top surface, while moisture redistribution still goes on deeper into the porous material. The absorption phase is now analyzed in more detail by modeling the transport in the porous substrate.

11.3   NUMERICAL MODEL AND RESULTS

In this section, it is presented a simplified model, which focusses on the absorption, evaporation and redistribution process in the porous material.
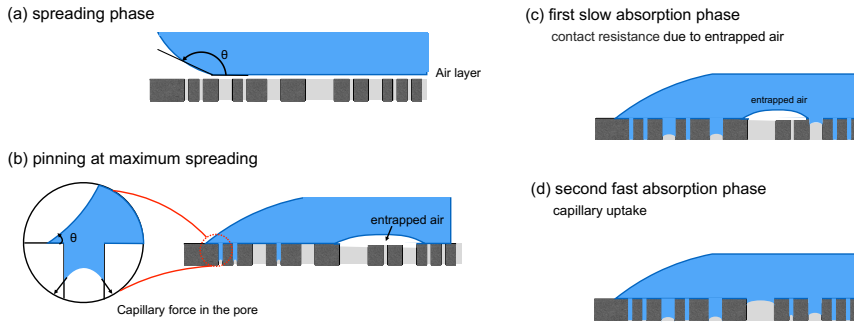
Figure 11.9: Schematic of dynamic spreading (a), pinning at maximum spreading (b), first (c) and second (d) absorption phase. (a) Presence of an air layer between droplet and porous substrate leads to a non-wetting dynamic spreading characterized by a contact angle > 90°. (b) Droplet gets pinned at the contact line at maximum spreading due to capillary forces in fines pores at the droplet edge leading to a wetting behavior and a contact angle < 90°. (c) Slow absorption rate at the beginning of the absorption process due to hydraulic contact resistance caused by the entrapped air under the pinned droplet. (d) When the entrapped air and contact resistance disappeared, the absorption rate increases due to perfect hydraulic contact.

Moisture absorption from a droplet and redistribution in the porous material is modeled using a continuum approach, assuming unsaturated capillary flow in a rigid (non-deformable) porous medium. Assuming a symmetric droplet shape at the surface of the porous material, a two-dimensional geometry with axial symmetry at the droplet center line is considered (Figure 11.10b). Since the droplet remains pinned for an important time during the absorption process, for simplicity the droplet diameter is assumed to be constant during the total depletion process. This assumption is valid for low impact velocities, but becomes less valid for high impact velocities. The droplet depletion is modeled with the droplet considered as a limited uniform reservoir and uniform boundary conditions at the contact area are assumed by imposing a constant capillary pressure at the interface. The droplet volume is monitored during uptake until it is emptied, i.e. until depletion of the droplet. After droplet depletion, boundary conditions are changed to model the evaporation at the surface and the moisture redistribution within the material.

Isothermal moisture transport describes the liquid and vapor transport governed by a gradient in capillary pressure P_c:

$$\frac{\partial w}{\partial t} = \nabla \cdot \left(\left(K_l + \frac{\delta_v \cdot p_{v,sat} \cdot RH}{\rho \cdot R_v \cdot T} \right) \nabla p_c \right) \tag{11.1}$$

with w the volumetric moisture content, K_l the liquid permeability, δ_v the vapor permeability, $p_{v,sat}$ the saturated vapor pressure, RH the relative humidity, the specific gas constant for water vapor, the temperature. In the derivation of Eq. 11.1, local equilibrium between liquid and vapor phases is assumed as expressed by Kelvin's law, which relates the relative humidity to the capillary pressure:

$$RH = \exp \left(-\frac{p_c}{\rho \cdot R_v \cdot T} \right) \tag{11.2}$$

The material modeled is Savonnières. The wetting capillary pressure curve is modeled using a multimodal van Genuchten curve assuming three pore systems (Derluyn, 2012). The liquid permeability of the material is a nonlinear function of capillary pressure, $K_l = K_l(p_c)$ and is determined the methodology described in Refs. (Carmeliet and Roels, 2001; Derluyn, 2012). The method uses as input the capillary absorption coefficient A_{cap} and vapor permeability $\delta_v(RH)$ based on wet cup/dry cup measurements. Figure 11.10 shows the capillary pressure curve and permeability curve for Savonnières.

(a)

(b)

(c)
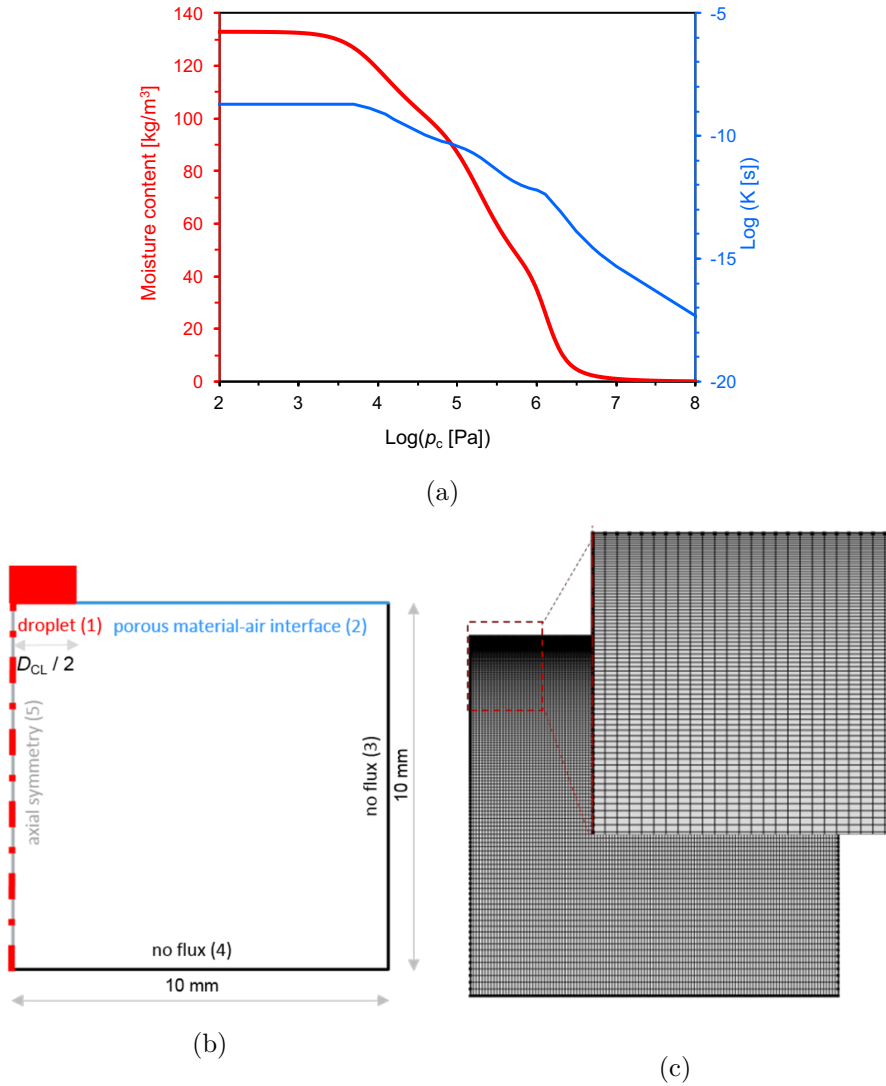
Figure 11.10: (a) Capillary pressure and permeability curves for Savonnières limestone as used in the numerical model; (b) Schematic of model geometry and boundary conditions. (c) Illustration of finite element mesh. The insertion shows a magnified view close to the sample surface, with decreasing element size towards the top surface.

Initially, the entire domain is conditioned at $RH = 10\%$, equal to a capillary $p_{c,t=0} = $ 1E8.5 Pa, which in turn equals according to the capillary pressure curve in Figure 11.10 to a moisture content ≈ 0 kg/m^3. The boundary condition at the top surface of the material being in contact with the droplet, zone 1 in Figure 11.10b, is modeled as a Dirichlet condition, imposing a capillary pressure $p_c = p_{c,\mathrm{drop}}$. The moisture content at the contact droplet-porous material is assumed to be equal to the capillary moisture content as obtained in a capillary uptake experiment from a free water surface ($w \approx 132$ kg/m^3). According to the capillary pressure curve in Figure 11.10a, this equals to a capillary pressure $p_{c,\mathrm{drop}} = $ 1E3 Pa.

The boundary condition at the top surface, zone 2 during absorption phase and zones 1 and 2 during evaporation phase (Figure 11.10b), is of the Neumann type describing the moisture exchange due to evaporation:

$$g_v = \zeta \cdot (p_{v,\mathrm{env}} - p_{v,s}) \tag{11.3}$$

where g_v is the vapor flux, ζ the mass transfer coefficient, $p_{v,\mathrm{env}}$ the vapor pressure of the environment and $p_{v,s}$ the vapor pressure at the porous material surface. The mass transfer coefficient is estimated from the heat transfer coefficient in the experiment using the Chilton-Colburn analogy (Chilton and Colburn, 1934) and equals $\zeta = $ 4E-8 s/m. The temperature and RH of the surrounding air is assumed to be constant, $RH = 10\%$ and $T = 25°$C.

On the lateral and bottom sides (surfaces 3 and 4) and on the symmetry axis (surface 5 in Figure 11.10b) zero flux conditions are imposed, $g_v = 0$. The governing equations are solved using the finite element method in COMSOL Multiphysics (v5.0, Comsol Inc.). The mesh consists of rectangular elements, with a refinement towards the surface of the sample, where steep moisture gradients are expected to occur (Figure 11.10c). The total number of elements is 120 x 150 (18 000 elements), where the smallest element height is 15E-6 m. Adaptive time stepping is used, with an initial time step of 10E-6 s and a maximum time step set to 0.01 s during the absorption.

As an example, Figure 11.11a shows the simulated moisture content distribution during absorption and evaporation for a droplet at an impact velocity $V_i = 1$ m/s. The spherical cap diameter of the droplet equals 3.6 mm. The images at $t = 3$ and $t = 9$ seconds show the moisture distribution during the absorption phase before the droplet is depleted. The images at $t = 18$ and $t = 30$ seconds show the moisture content
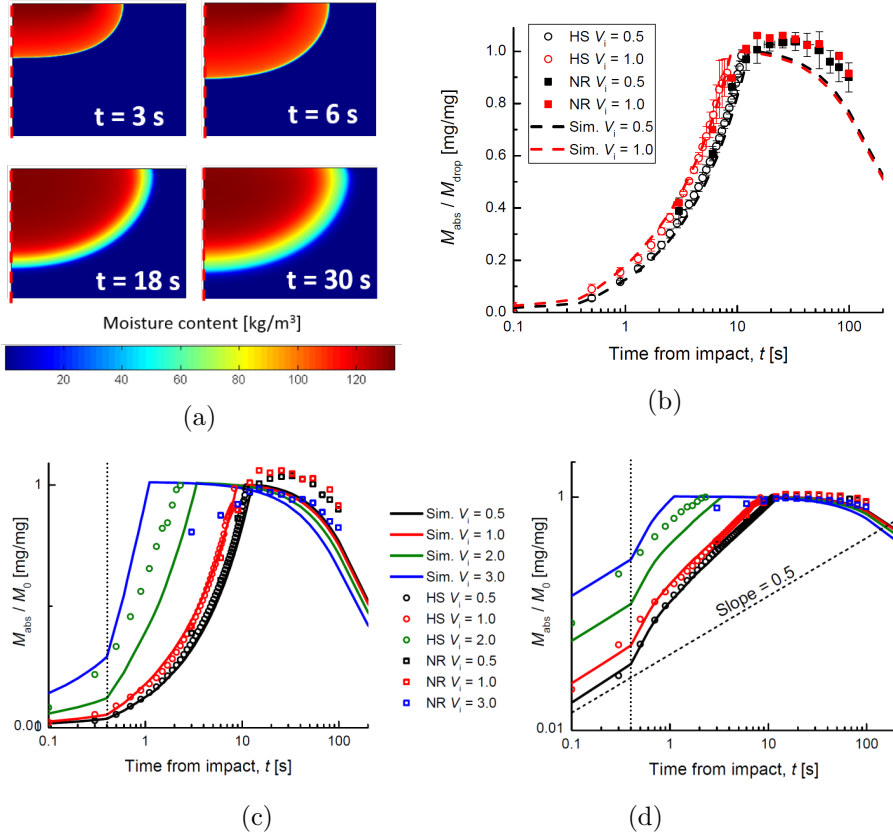
Figure 11.11: (a) Simulated moisture content distribution for impact velocity of 1.0 m/s at different times. The dashed line indicates the symmetry line of the modeled geometry. (b) Comparison of the absorption mass normalized by the initial impinging drop mass in time in semi-log plot for Savonnières for impact velocity of $V_i = 0.5$ and 1 m/s. (c-d) Absorption mass normalized by the initial impinging drop mass for different impact velocities versus time in semi-log plot (c) and in log-log plot (d).

distributions during the evaporation phase. Figure 11.11b compares the absorption mass normalized by the initial impinging drop mass in time in semi-log plot for Savonnières for impact velocity of $V_i = 0.5$ and 1 m/s with a spherical cap diameter of the droplet of 2.8 and 3.6 mm respectively. In first simulations, the absorption process was initiated by imposing a capillary pressure at the droplet contact area equal to the capillary pressure at capillary moisture content ($p_{c,drop} = 10$ Pa). This boundary condition however showed a much too fast uptake by the porous substrate. The overprediction of the initial uptake stems probably from the assumption that a perfect hydraulic contact exists between droplet and porous medium by imposing a too low capillary pressure, while in reality this contact is not perfect due to presence of still entrapped air. This entrapped air leads to a contact resistance for fluid transport from droplet to substrate (Figure 11.9c), which is modeled by imposing a higher capillary pressure ($p_{c,drop} = 1E5$ Pa) at the contact related to a contact moisture content ($w \approx 80$ kg/m^3) lower than the capillary moisture content. This entrapped air will probably disappear with time probably due to air leakage from the contact zone. Therefore, this contact resistance condition is imposed only for the first 0.5 seconds of the absorption process. Figure 11.11b shows that a good agreement between simulation and measurement data is obtained for the absorption phase. During the evaporation phase, the simulations slightly overpredict the drying. Figures 11.11c-d show the simulation results for different impact velocities: 0.5, 1, 2 and 3 m/s, with spherical cap diameter of the droplet of 2.8, 3.6, 5.3 and 8.2 mm, respectively. For the highest impact velocity, splashing is not considered, but a uniform spreading almost equal to the splashing area. All measured data as obtained from high-speed camera and neutron imaging are shown. Figure 11.11c is in semi-log plot, while Figure 11.11d in log-log plot. The first absorption period with contact resistance is clearly visible and follows nearly a 0.5 slope as predicted by the Washburn relation. This means that, during this period, the uptake process is nearly unidimensional. The uptake process during the absorption phase with perfect capillary contact however does not show this 0.5 slope behavior. The simulations also predict the decrease in droplet depletion time with increasing impact velocity.

The simple model allows to predict moisture content profiles over the depth of the porous medium at the center line during the absorption and evaporation stages at different points of time. At low impact velocity

(a) $V_i = 0.5$ m/s (b) $V_i = 3.0$ m/s
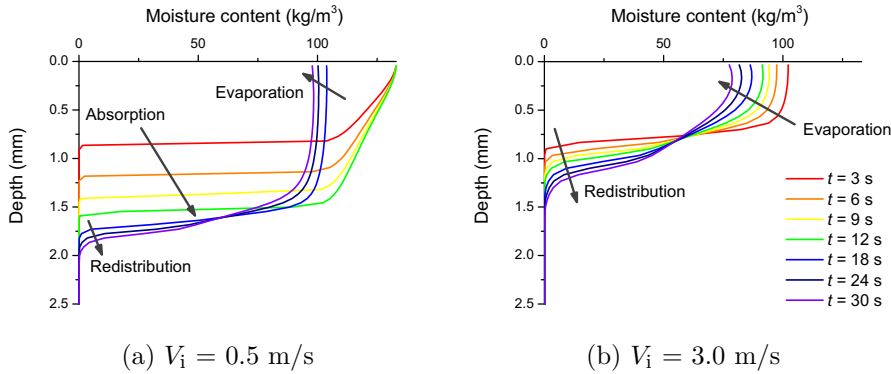
Figure 11.12: Simulated moisture content at centerline of porous medium over depth for different times at impact velocity of 0.5 m/s (a) and 3 m/s (b).

$V_i = 0.5$ m/s (Figure ??), the moisture content increases in time with depth during the absorption phase ($t \approx 12$ s). During the evaporation phase, the moisture content at the surface decreases, while still further penetration of liquid into the porous medium occurs due to redistribution. At high impact velocity $V_i = 3$ m/s (Figure 11.12b) the droplet is already depleted at $t \approx 3$ s. and evaporation has started. This example shows that droplet spreading as well as droplet depletion and evaporation is highly determined by the impact velocity of the droplet.

11.4 CONCLUSION

This chapter presents an experimental investigation and numerical analysis of the absorption of liquid droplets impacting porous stones. High-speed imaging and neutron radiography are used to quantify moisture absorption in three natural stones of varying porosity. Neutron radiography provides high resolution moisture content (re)distribution throughout the different phases of the phenomenon. The life of a droplet after impact on a porous stone continues over different time scales. At short time after drop impact, the droplet spreads showing a non-wetting dynamic behavior. During this dynamic phase, no liquid mass penetrates into the porous substrate due to the presence of an air layer between the droplet and the porous substrate. At maximum spreading, the air layer between droplet and surface is broken at the contact line leading to

capillary contact and pinning of the droplet due to capillary forces in the pores at the droplet edge. As a result, the contact angle changes from a non-wetting to wetting behavior, while air remains entrapped under the pinned droplet. During the absorption phase at larger time scale, the droplet remains pinned and the contact angle decreases in a CCR mode. The mass absorbed in the stone increases until the droplet is depleted. The absorption phase is first hindered by the presence of entrapped air, leading to a contact resistance for fluid transport from droplet to substrate. The entrapped air shortly disappears from the contact zone leading to perfect capillary contact between droplet and porous medium. Droplet absorption and depletion happens faster in highly capillary active stones. Evaporation and further redistribution are observed once the droplet is depleted. Droplet spreading as well as droplet depletion and evaporation is highly determined by the impact velocity of the droplet. A finite-element numerical model for isothermal moisture transport in unsaturated porous media is found to capture properly the mass absorption as observed in the experimental data.

FURTHER EXPLORATIONS OF DROPLET IMPACTS ON POROUS STONES

12.1 INTRODUCTION

In this chapter, a further exploration of droplet spreading and absorption in porous stones takes benefit of neutron radiography. First, a string of droplets is impacting the stone on top of each other at the same position. Second, two series of droplets are dropped side by side. Third, the incident angle of impact is varied. The qualitative description of each experiment highlights the potential of such type of investigation to study complex droplet phenomena.

12.2 EXPERIMENTAL WORK

The impact and absorption process into the porous stone is captured by neutron radiography. The experimental technique and analysis method are explained in chapter 5. The experiments are performed at the NEUtron Transmission RAdiography (NEUTRA) beamline of the Paul Scherrer Institute, Villigen, Switzerland. The porous materials are Savonnières and Meule as described in chapter 4.

Figure 12.1 shows the images of neutron radiography for different drop impact setups including a string of droplets, a string of twin droplets and drop impact at an incident angle. To capture the impinging droplet behavior on the surface and inside material, the NEUTRA beamline is synchronized with the droplet test setup (see chapter 5). The experimental results presented in this chapter are illustrated with images of quantified water mass. Further quantitative analysis and modeling is outside the scope of this thesis, but the results show the potential for further research on these images.

Multiple drops

5 mm

Injector

Sample

Discrete drops

5 mm

7 mm

Injector

Sample

(a) a string of droplets

(b) two string of droplets

Drop onto oblique surface

5 mm

Injector

Sample

Reference target

30°, 60°, 75°

(c) drop impact on a sloped porous stone
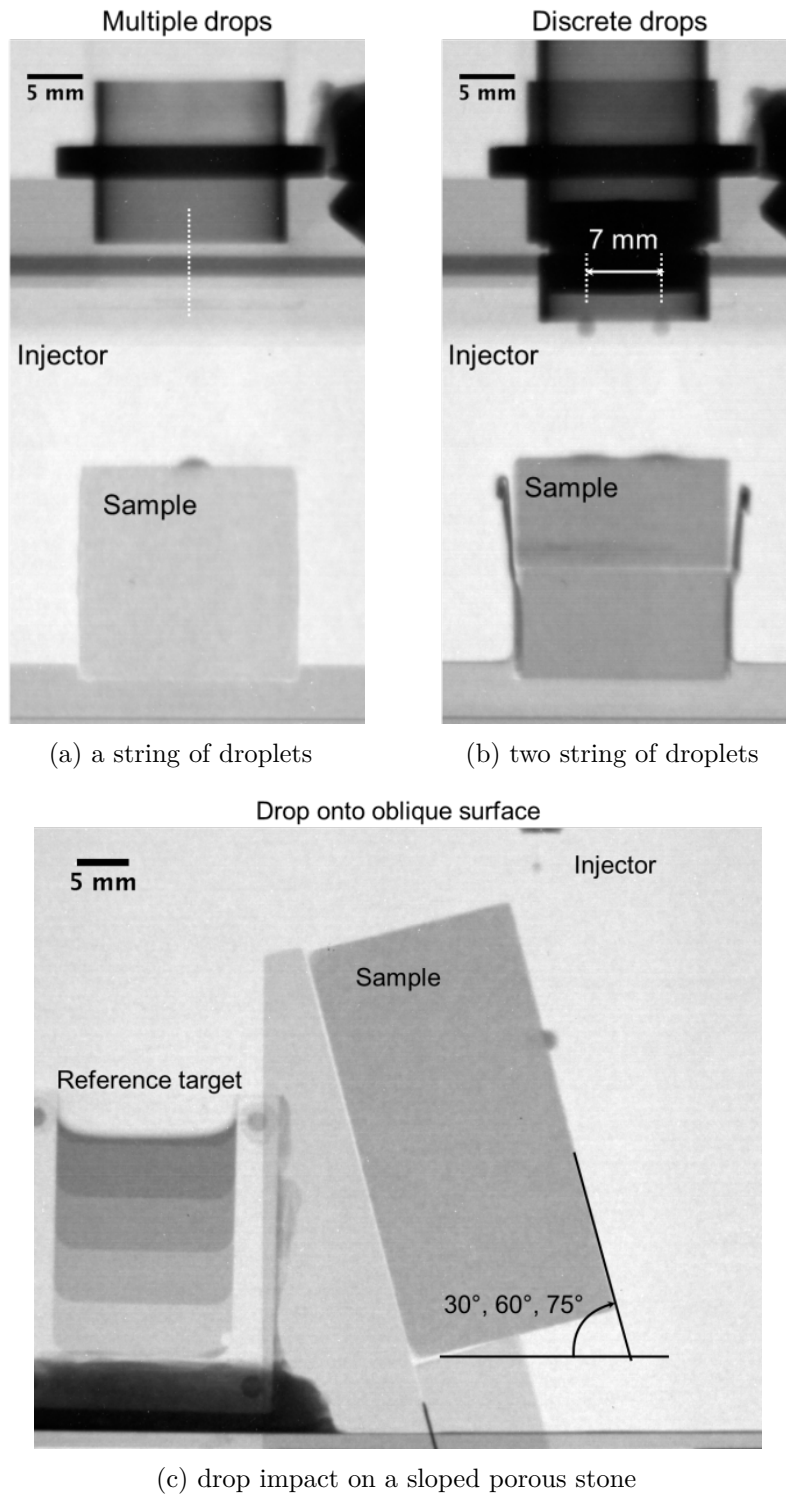
Figure 12.1: Neutron radiography images for different drop impact setup.

12.3 SINGLE TRAIN OF DROPLETS

This section presents the analysis of the impact of a single train of droplets on top of each other at the same location on Savonnières and Meule. Droplets are deposited at three impact velocities $V_i \sim 0.5$, 1.0 and 3.0 m/s, and at two frequencies, 0.1 Hz (at 10 seconds interval) and ~ 0.4 Hz (at 2.5 seconds interval).

Figure 12.2a shows the results on Savonnières for an impact frequency of 0.1 Hz. The images are taken at 3, 30, 60 and 180 seconds, meaning that respectively 1, 4, 7, 19 droplets have been deposited. These images show the shape of the accumulated droplets sitting on the surface and the absorbed water mass distribution within the porous medium. The first image at $V_i \sim 0.5$ m/s (left column) shows that the first droplet is not visible anymore after 3 sec, since it is already depleted due to absorption into the stone. After impact of three more droplets ($t = 30$ s), water is seen to pool on the surface over a larger area increasing the contact area between droplets and surface. Water is absorbed and redistributed within the porous stone, over a width that is in the order of the spreading diameter of the pool. The absorption takes also place along the depth leading to a semi-elliptical wetted zone wider than the drop pool. The semi-elliptical shape of the wetted zone under the pool follows the size of the developing water pool on the surface. The moisture content is the highest directly under the pool and, as water is being transported away from the surface into the material, the moisture content decreases showing the flow to be unsaturated. The picture remains the same after impact of a total of 7 and 19 droplets: the water pool diameter on top of the surface is increasing (from 4 to 7 mm) resulting in a widening semi-elliptical wetting under the pool showing high gradients in moisture content. It is also observed that the height of the droplet increases, leading to an increase in apparent contact angle from 15 to 25. It is remarked that the widening of the water pool includes a de-pinning of the existing water pool due to gravitational forces exceeding the pinning force at the pool edge.

An increase of the impact velocity to $V_i \sim 1$ m/s (middle column) leads to a wider spreading of the droplets and thus a thinner water pool. As a result, the semi-elliptical wetted zone under the pool is larger in the width direction. At an impact velocity of 3 m/s, no water pool is visible on the surface due to the important spreading and faster absorption.
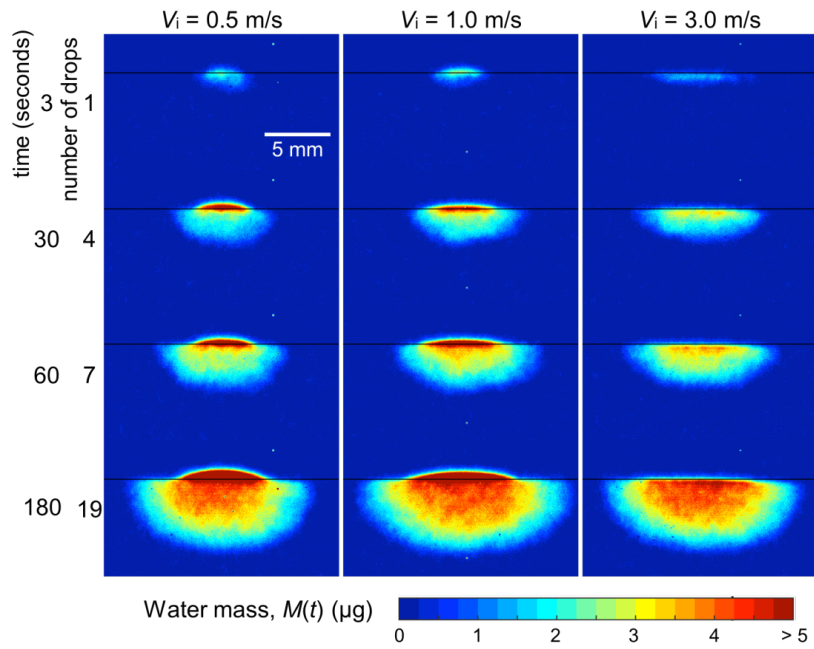
(a) 0.1 Hz (at ∼ 10 seconds interval)
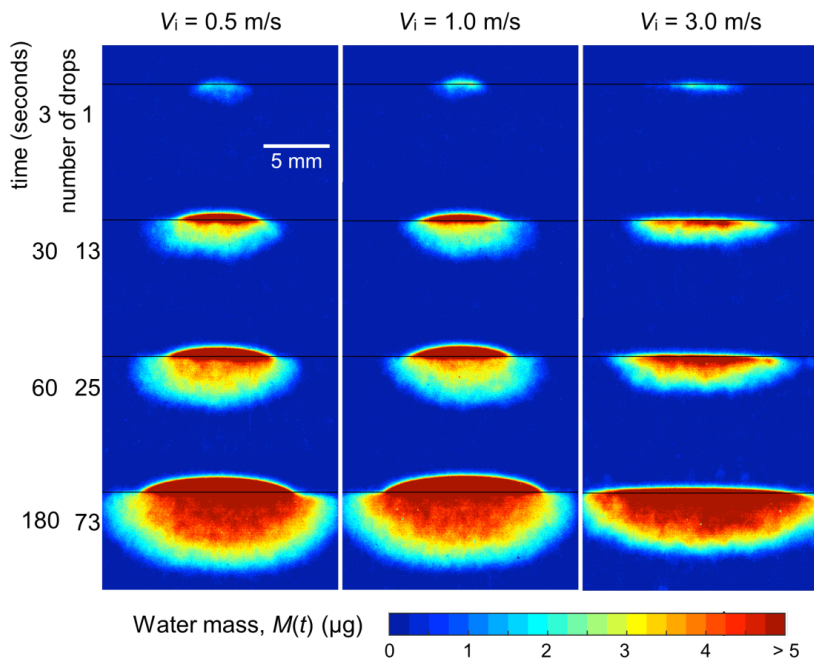
(b) 0.4 Hz (at ∼ 2.5 seconds interval)

Figure 12.2: Water mass distribution for a string of drop impacts on Savonnières limestone with different drop impact frequencies.

Remarkably, the semi-elliptical redistribution of water at longer times (after 19 droplets) converges to the same wetting pattern.

Figure 12.2b shows the results on Savonnières for a higher impact frequency (0.4 Hz). The images are taken at 3, 30, 60 and 180 seconds, meaning that 1, 13, 25, 73 droplets have been impacting the porous medium, respectively. Again the water pool increases in width and height with increasing number of droplets fallen on the substrate, leading to an increase in apparent contact angle. Comparing the wetted zone for the low and high impact velocity at 180 s, it is observed that, at low impact velocity (left column), the wetted zone is deeper compared to the wetted zone at high impact velocity (right column). This is explained by the fact that, at higher impact velocity, the pool spreads more, the height of the droplet sitting on the surface is smaller and thus less water is available at a certain position to be transported inside the porous material, leading to a smaller depth of the wetted zone.

Comparing the images for the two impact frequencies (Figure 12.2a-b), the first obvious effect of higher impact frequency is the increase in size and height of the water pools on the surface. Comparing the state after 19 drops at the low frequency (after 180 s in Figure 12.2a) and 25 drops at the high frequency (after 60 s in Figure 12.2b), the moisture front at low frequency is deeper that the one at high impact frequency, highlighting that water transport takes time and is not accelerated by a higher frequency of impacting droplet.

Figures 12.3(a-b) show the shape of the accumulated droplet sitting on the Meule sandstone surface and presents the water mass distribution under the droplet within Meule. The absorption into Meule and water pool forming on its top surface resemble the ones on Savonnières. However, the length of the water pool on Meule is larger than the water pool on Savonnières. As a result of this larger spreading, the height of the droplet sitting on the surface and the apparent contact angle are smaller compared to the ones for Savonnières. The larger spreading of the water pool on Meule is attributed to the lower pinning forces at the pool boundary for Meule compared to Savonnières. The higher pinning forces for Savonnières may be related to the higher capillary activity of Savonnières, but this explanation needs further in depth analysis. It is observed that the absorption in the depth direction inside Meule is smaller compared to the absorption shape inside Savonnières, while the absorption in lateral direction inside Meule spreads more than the one for Savonnières (see Figure 12.2b and Figure 12.3b at $t = 180$ s).

(a) 0.1 Hz (at ~ 10 seconds interval)
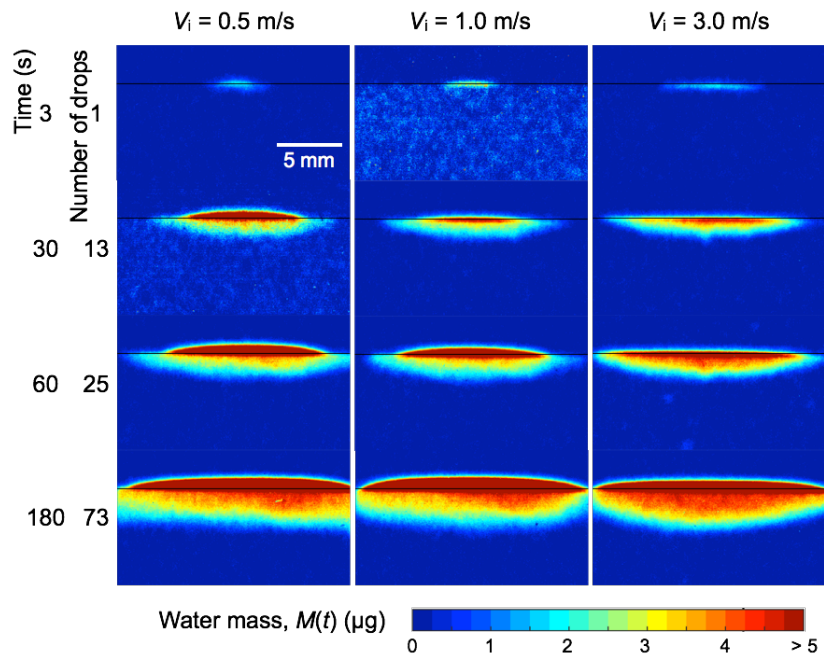
(b) 0.4 Hz (at ~ 2.5 seconds interval)
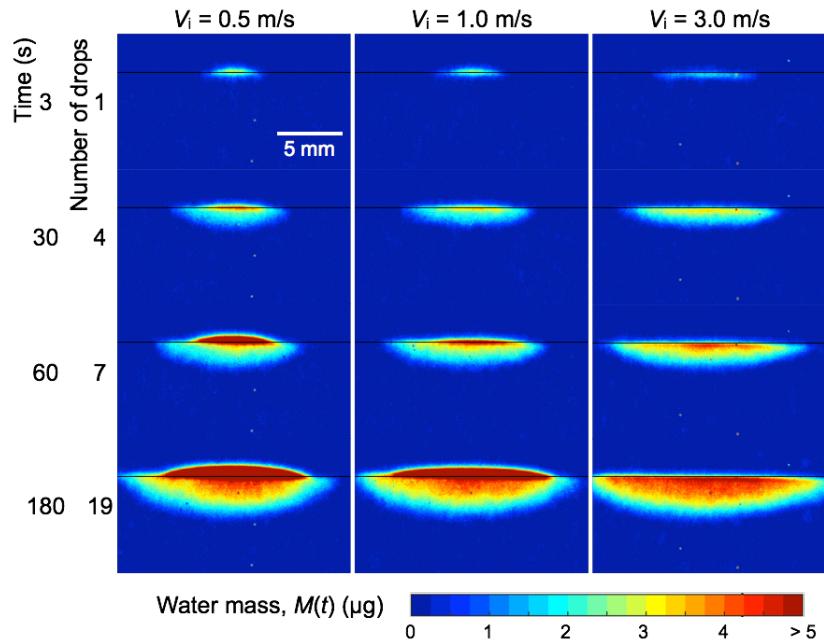
Figure 12.3: Water mass distribution for a string of drop impacts on Meule sandstone with different drop impact frequencies.

Both observations can be attributed to the higher spreading and smaller thickness of the water pools on Meule compared to Savonnières.

It is generally observed that, at low impact frequency, the water pools are smaller and resemble more a spherical cap, while at high impact frequency the larger water pools show more a flattened shape evolving to a pancake. This is especially visible for Meule in Figure 12.3b at $t = 180$ s. For these larger water pools whose radius exceeds the capillary length $\kappa^{-1} = (\gamma_{LV}/\rho g)^{1/2}$, gravitational effects start to play a role. The capillary length for water equals 2.7 mm. The spreading radius of the water pool in Figure 12.3b at 180 s. equals ~ 20 mm, and is thus much higher than the capillary length. The height of water pool h is given by (Gennes et al., 2004):

$$h = 2\kappa^{-1} \sin\left(\frac{\theta_{app}}{2}\right) \tag{12.1}$$

with θ_{app} the apparent contact angle. The relation shows that, with increasing height, the apparent contact angle increases. The droplet height on Meule is smaller than on Savonnières, explaining the lower contact angle on Meule than the one on Savonnières.

12.4 STRING OF TWIN DROPLETS

This section presents the results when droplets coming from two sources next to each other impact a porous medium.

Figure 12.4 shows the water mass distribution on the surface and inside Savonnières at different time steps. The distance between the two sources is 7 mm. Two impact velocities $V_i \sim 0.5$ and 3.0 m/s are considered. Droplets impact every 20 seconds or the impact frequency is 0.05 Hz. The images are taken at 3, 30, 90 and 180 seconds, meaning that respectively 1, 2, 5, 10 droplets have been impacting at each location. At low impact velocity, the impacting droplets accumulate at the two locations forming water pools which do not merge. At high impact velocity, no water pools are observed since the impacting droplets are absorbed totally into the porous medium. The wetted zones under each water pool at low impact velocity are first disconnected, but merge by capillarity after 90 s. At high impact velocity, the spreading of the droplets is larger leading to a merging of the wetted zones already at early stage.

Figure 12.5 shows the water mass distribution on surface and inside Meule at different time steps. The distance between the two sources
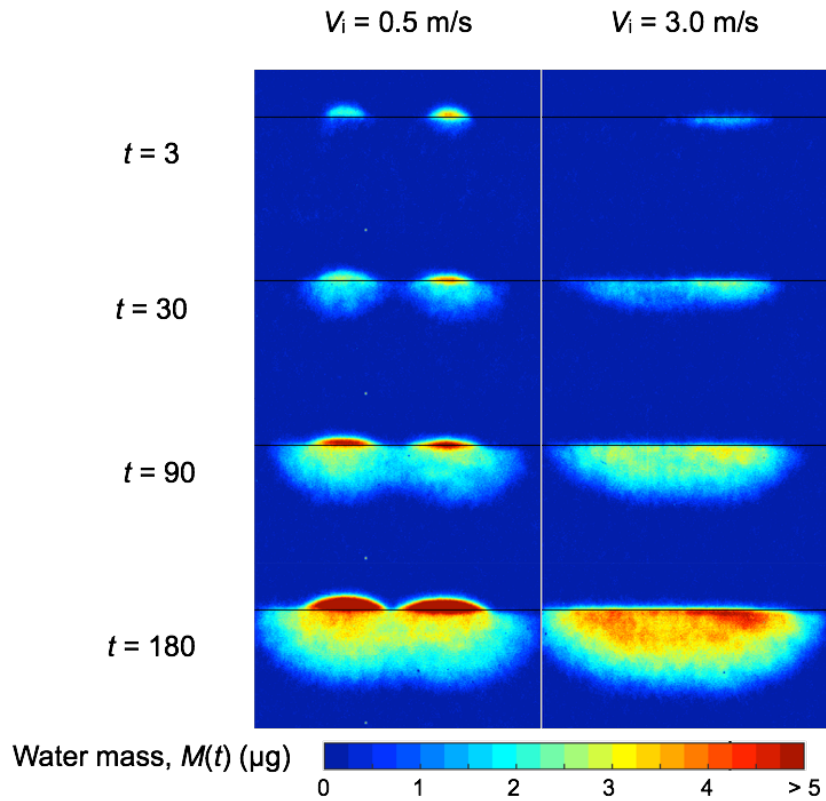
Figure 12.4: Water mass distribution for two strings of drop impacts on Savonnières limestone with different impact velocities.
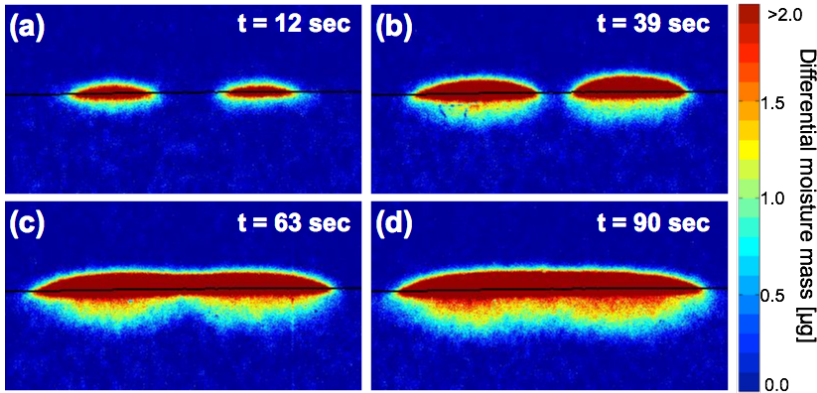
Figure 12.5: Water mass distribution for two strings of drop impacts on Meule (1.0 m/s of impact velocity).

is 7 mm. The impact velocity is $V_i \sim 1.0$ m/s. Droplets impact every 5 seconds or the impact frequency is 0.2 Hz frequency. The images in Figure 12.5 are taken at 12, 39, 63 and 90 seconds, meaning that respectively 3, 8, 13, 19 droplets have been impacting at each location. The impacting droplets first accumulate at the two locations forming separate water pools, which after some time merge. At 63 s, a single water pool is formed, while the wetted zone under the water pool still resembles that the wetting was originally coming from two sources.

12.5 SINGLE DROPLETS ON SLOPED SURFACE

In this section, the droplet impact on a sloped porous surface is studied. The incident angle of the impacting droplet increases from $\theta_{in} = 30°$, $60°$ and $75°$. The substrate is Savonnières and three impact velocities $V_i \sim$ 0.5, 1.0 and 1.5 m/s are considered.

Figure 12.6 shows the shape of the droplet and water mass distribution of droplets impacting at different incident angles and impact velocities, at 3 s after impact. The impact point is indicated by a red arrow. The dashed line denotes the surface. At low velocity ($V_i = 0.5$ m/s) the droplet remains pinned at the impact location for incident angles of θ_{in} = 30° and 60°. For a higher incident contact angle of $\theta_{in} = 75°$, the droplet slips (or rolls) over the surface and remains pinned at a lower location. It is remarkable that the droplet has not penetrated into the porous medium when it slips down or spreads over the surface at $V_i =$
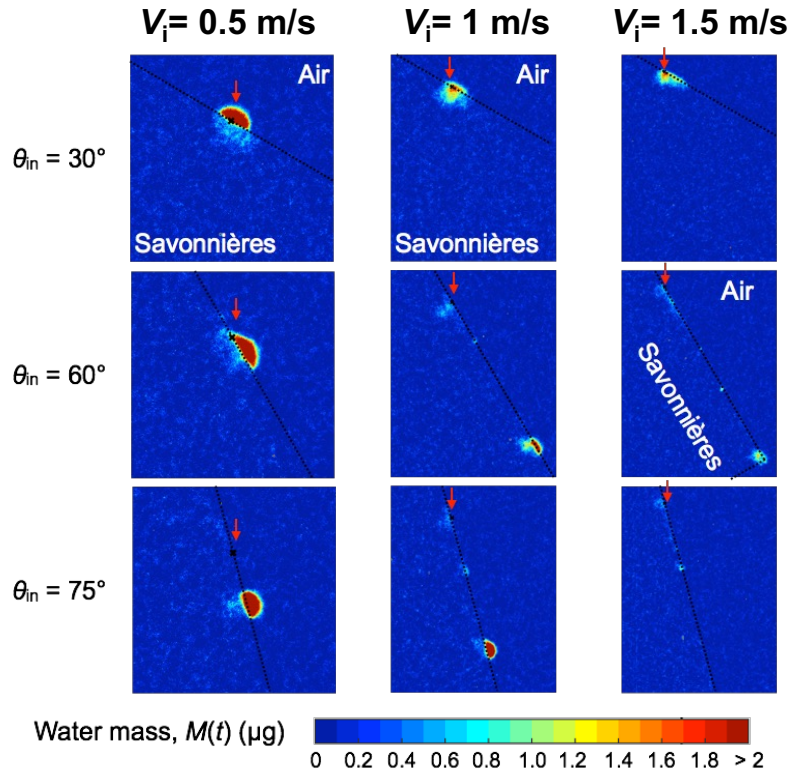
Figure 12.6: Images at $t = 3$ sec after impact of droplets on Savonnières at different incident angles and at different impact velocities after $t = 3$ s.

0.5 m/s, which is in contrast with observations at higher impact velocity. For an impact velocity of Vi=1 m/s and incident angle of $\theta_{in} = 30°$, spreading and uptake of water is observed at the impact location. It is not clear whether all water remained at this position, or that some part of the droplet slipped down. For higher incident angles $\theta_{in} = 60°$ and 75°, some traces of the droplet at impact are left, while the major part of the droplet is found on the lower part of the sample. At high impact velocity (V_i =1.5 m/s), spreading of the droplet is find at low incident angle while, for the higher incident angles, only traces of the droplet are visible along the surface and the droplet itself is not visible.

Figures 12.7 and 12.8 show the lifetime of the droplet for longer times. Once the droplet comes to a halt, the water is absorbed at this location by the substrate and further redistributed. This means that the wetting
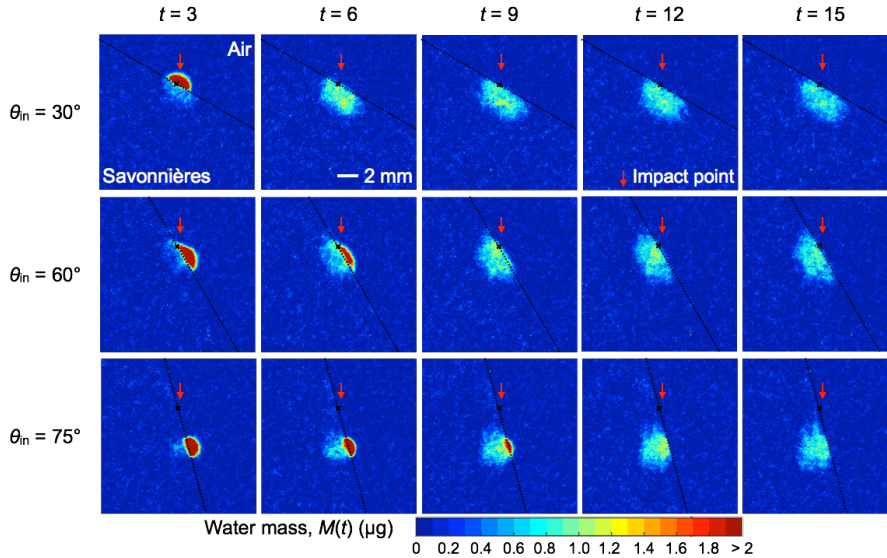
Figure 12.7: Images at different time of water mass on the surface and inside the porous material (Savonnières) at different incident angles and at impact velocity $V_i = 0.5$ m/s.

pattern in the substrate follows closely the droplet behavior on top of the surface.

12.6 CONCLUSION

In this chapter, the study on droplet spreading and absorption in porous stones takes benefit of neutron radiography. A string of droplets dropped on top of the same position, two series of droplets dropped side by side and a drop impact on oblique surface are documented.

When different droplets fall on top of each other at the same location, a water pool is created at the surface which width and height increase with the number of droplets fallen, leading to an increase in apparent contact angle. The widening of the water pool includes a de-pinning of the existing water pool due to gravitational forces exceeding the pinning force at the pool edge. At higher impact velocities, the spreading is higher leading to a thinner water pool and smaller contact angles. The spreading diameter of the water pool depends on the porosity and capillarity of the substrate: a lower porosity and capillarity leads to a higher spreading of the water pool. The wetted zone in the porous medium under the water
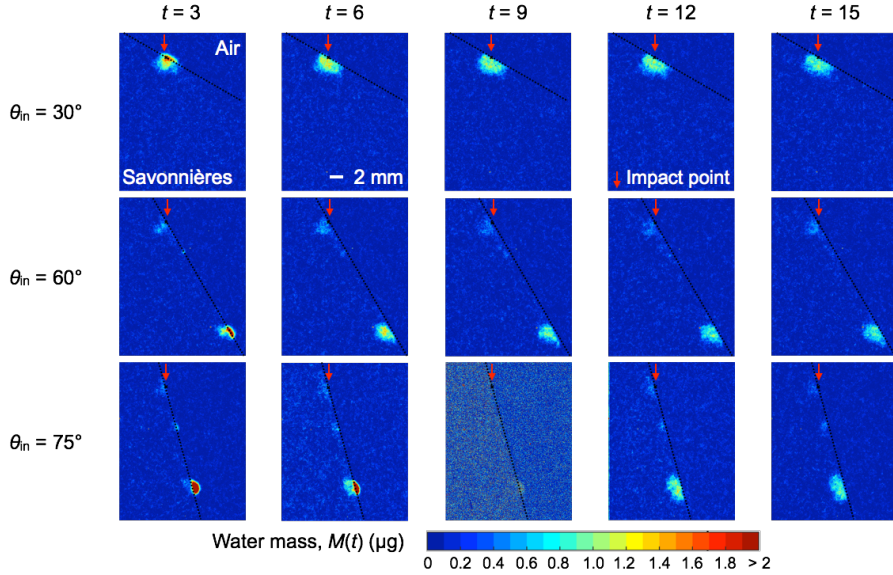
Figure 12.8: Images at different time of water mass on the surface and inside the porous material (Savonnières) at different incident angles and at impact velocity $V_i = 1$ m/s.

pool shows a semi-elliptical unsaturated distribution of water following closely the spreading of the water pool on the surface. At longer times, the wetted zones seem to converge to the same wetting patterns, showing their shape is less dependent on impact velocity and impact frequency.

When droplets fall next to each other, the water pools may merge depending on the impact frequency and impact velocity. The wetted zone under the water pool also merges due to absorption in the width direction.

For droplets impacting at an incident angle, it is found that, at lower incident angle and impact velocity, the droplet remains pinned and spreads on the surface. With increasing impact velocity and incident angle, the droplet slides (rolls) over the surface and pins at lower position, or breaks up leaving some traces on the surface at different locations. The wetting pattern in the substrate follows closely the droplet behavior on top of the surface.

This elaborated quantified neutron radiography dataset should be studied in detail. For further research, it is worth to report this first investigation in this thesis.

13

CONCLUSIONS AND OUTLOOK

13.1 SUMMARY

Understanding the behavior of drop impact on porous media is an essential step for revealing the rain droplet impact and fate onto building façade and for several other applications. The objective of the present research was to characterize the full process of drop physics onto complex rough and porous structured surface and the absorption into natural porous stone. This thesis mainly focused on the description of the spreading behavior of impacting droplet on porous media based on the knowledge on drop physics on impervious surface in terms of the influence of the liquid properties and the surface properties, and the mass transport inside porous media from impacting droplet. The work used experimental, theoretical and numerical approaches. The findings of spreading behavior in this thesis provided understanding of the process, how droplet makes contact on porous media. Moreover, the proposed method for maximum spreading could be extended to predict the maximum spreading for any complex surface. This knowledge provides a predictive tool for many applications including drop deposition problem and is also an inspiration for the design of surfaces where drop dynamics needs to be controlled. The observation on the absorption behavior of impinging droplet into porous media provides understanding of mass transfer from dynamic impinging droplet to anisotropic porous media. These findings allow us to estimate water mass transport accurately from rain droplet to building and any natural porous substrate and water distribution inside porous media. The main conclusions of the present work are summarized in this section.

13.2 CONTRIBUTIONS

Advances in understanding the drop impact:

- Development of a universal scaling to predict maximum spreading ratio for different liquids (surface tension and viscosity) and vari-

173

ous surfaces (wettability and roughness) based on two asymptotic behaviors at low and high impact velocity. In the proposed scaling, the estimated initial spreading ratio is taken into account.

- Investigation of an air layer forming on smooth and rough surfaces and the wetting transition due to the breaking of the droplet balloon hitting a small roughness on surface. This rather random hitting event leads to a touching of the droplet balloon to the substrate, breakage of the surface layer and a change from dynamic non-wetting to dynamic wetting conditions on the hydrophilic porous surface.

- Development of a prediction for maximum spreading ratio based on the energy balance approach. A physically relevant description for boundary layer thickness, the time at maximum spreading and viscous dissipation at maximum spreading is derived theoretically. It is shown that the dynamic wetting process at low impact velocity is dependent on the dynamic contact angle at maximum spreading, and is found to be in general higher than the equilibrium contact angle, showing that statically wetting surfaces can become less wetting or even non-wetting under dynamic droplet impact.

- Development of a CFD-VOF simulations for liquid droplet with different viscosity and surface tension taking into account of the dynamic contact angle at maximum spreading along with Kistler model for the input contact angle. It is shown that at low impact velocity viscous dissipation contributes still for a more substantial part to the energy budget and cannot be neglected in the prediction of maximum spreading, and at high impact velocity, the spreading regime is both dependent on surface energy and viscous dissipation.

Advances in understanding the drop impact on porous media:

- Investigation of the penetration and absorption of an impinging droplet during spreading on natural porous stone. It is found that no liquid penetrated into porous media due to inertial effects at impact and the liquid into the porous substrate is only due to capillary absorption by the porous substrate starting after maximum spreading of the droplet. The presence of an air layer between liquid droplet and porous surface is discussed.

- Investigation of the spreading of an impinging droplet on natural porous stone and identifying the pinning force during receding phase due to capillary uptake. The droplet undergoes pinning when the air layer is broken at the contact line and capillary forces develop in fine pores at the droplet edge pinning the droplet.

- Understanding the maximum spreading of drop impact on porous media. The maximum spreading ratio can be predicted with the proposed model taking the capillary or surface tension energy related to the initial spreading ratio into account.

Advances in understanding the absorption into porous media:

- Investigation of absorption into porous stone using neutron radiography providing high resolution moisture content (re)distribution throughout the different phases of the phenomenon.

- Development of finite-element numerical model for an isothermal moisture transport in unsaturated porous media based on the continuum approach. The absorption of impinging droplet is found to be dependent on the contact area determining the spreading behavior, and is hindered due to the air layer and the entrapped air during spreading.

13.3 FUTURE PERSPECTIVES

Based on this thesis, a number of directions for further research can be formulated. These issues are discussed here:

- There is a need to characterize the effect of the porous structure, i.e., pore size, porosity and wettability of material on the drop evolution. For a better understanding of drop impact on porous media and absorption, the influence of these properties on porous media has further to be considered.

- Investigation the air layer and entrapped air between droplet and porous media. This work provides indirect evidence for the presence of air layer and entrapped air during drop impact. The complex shape of liquid-vapor-solid interfaces can be captured by synchrotron-based X-ray radiography with high spatial and temporal resolution (Lee et al., 2012).

- Development of a boundary condition for moving contact line. For estimating the dynamic contact angle, this study used the analytical solution proposed by Kistler (1993) with measured dynamic contact angle at maximum spreading. However, the question of how to simulate a priori a non-experimentally investigated case, for which contact angle data are not available, still remains to be answered.

- Investigating the deposited volume for different drop impact outcomes, e.g. partial rebound, splash, and for drop impact with different incident impact angle.

- Upscaling presented quantitative and qualitative results on droplet for rain drop impact to building façade incorporating computational WDR CFD simulation.

APPENDIX A

The code presented in this appendix is for drop impact measurement (Impact velocity, initial drop size, height of droplet, spreading diameter, contact angle, volume of droplet). The detail description can be found in chapter 5.

HS_MAX.M

Main structure

```
%% ****************************************
%% Functions:
%% Image analaysis for HS dataset(NXcamera)
%% Variables:
%% Time evolution data (ID.csv / ID.mat)
%% Drop spreading diameter, D(t)
%% Drop contact line diameter, DCL(t)
%% Normalized drop spreading diameter, ND(t)
%% Normalized drop contact line diameter, NDCL(t)
%% Drop height, H(t)
%% Contact line velocity, VCL_L(t), VCL_R(t)
%% Spreading velocity, VR_L(t), VR_R(t)
%% Capillary number, Ca_L(t), CA_R(t) Ca = \mu VCL / sigma
%% Dynamic contact angle(Tangetial method),
%% thetaR(t), thetaL(t) Dynamic contact angle(Area angle
    method)
%% thetaAR(t), thetaAL(t) Volume of drop(reconstructed),
    Vsurf(t)
%% Surface area L-V and S-L, S_LV(t) S_SL(t)
%% Maximum data
%% ID Substrate Liquid rho gamma mu Weber
%% Reynolds
%% D0 / std Vi / std D_max ND_max DCL_max NDCL_max ts
    ts_CL
%% S_LV_ts S_SL_ts S_LV_max t_S_LV_max S_SL_max t_S_SL_max
    SamplePath
%% Programmed by:
```

```matlab
%% Jaebong Lee PhD student at ETH Zurich
%% Revised 23-02-2015
%% ****************************************

%% Initialization
clc;
close all;
clear all;

%% Program specification
mac = 1;
misN = 0;
Title = 'Water';
OutRes = '90_150um';
numS = 200;
GuisliceN = 10;
global SamplePath
SamplePath = '/Users/jaeblee/Downloads/ex';

%% Required value for analysis
pixelsize = 0.012987013; %[mm] 10000 fps
fps = 4700;
Increment = 1; %fps250 50(200ms) %fps10000 1(0.1ms)

NameSL = str2mat(SamplePath);
indsl = find(NameSL=='/');
% Substrate = NameSL(indsl(4)+1:indsl(5)-1);
% Liquid = NameSL(indsl(5)+1:indsl(6)-1);
Substrate = '90_150um';
Liquid = 'Water';

[rho, sigma, mu, theta_eq, theta_adv, theta_rec] = ...
    propertiesS(Substrate, Liquid);

%% Impact slice number
[Flist,anz]=GetFiles(SamplePath,'*.tif',mac);

%% Misnumbered slice corrector
if misN == 1
    FlistT = Flist;
    for it = 1:1:200
        Flist(it) = FlistT(201-it);
    end
    clear FlistT;
else
end

%% Set output folder and directory
```

```matlab
if mac == 1
    ResDir=strcat(SamplePath,'/_ResM');
else
    ResDir=strcat(SamplePath,'\_ResM');
end
mkdirE(ResDir);

%% Preparation for Image analysis
% Get surface line
surfline;

% Time sequence for slice
TiStpm = -(ImN_impact-1)*1/fps:1/fps:(size(Flist,1)*1/fps)
    ;
TiSe = TiStpm';

[ImFlist,TiSeC] = HS_load(SamplePath,Flist,ImN_impact,
    Increment,TiSe,fps,numS);

% Background mean image
[Im_BGM] = backgroud(ResDir,Flist,5);

% Rotation tilted picture
Flag_Ro = 0;

%% Impact velocity and size
BufferIm = 1;
ROI_im = [Surfl(3), 484, 500];
[D0, Vi,Center] = impingingDrop(ImN_impact, Im_BGM, ROI_im
    , Flist, BufferIm, pixelsize,fps);
WeN = (rho*Vi(1)^2*D0(1)/1000)/sigma;
ReN = (rho*Vi(1)*D0(1)/1000)/mu;

% Set ROI
ROI_width = 1382; %10 mm -> 829 (1382 for 10k) (1372 for 5
    k)
ROI_height = 484; %3.5 mm (484 for 10k) (481 for 5k)
ROI = [Center.X-ROI_width/2 Center.Y-ROI_height ROI_width
    ROI_height]; %[left conner x, y, width, height]
Crop_Center.X = Center.X-round(ROI(1));
Crop_Center.Y = Center.Y-round(ROI(2));
xPoL = []; xPoR = []; xDoL = []; xDoR = [];intW = 0;Dt_old
    =0;intEline=0;

%% Image Analysis and Calculation Loop
NumOfSlice = size(ImFlist,1);
for cnt = 1:1:NumOfSlice
    Im_T = imread(ImFlist(cnt).fullname);
```

```matlab
    Im_T = Im_T.*2^6;
    Im_T = im2uint8(Im_T);
    [Im_Crop,Im_BW,By,Bx,B] = imageAnalysis(Im_BGM,Im_T,
        ImFlist,ROI);
    [DCLt,Dt,Ht,VCL,VR,xPoL,xPoR,xDoL,xDoR] = Dmeasure2(By
        ,Bx,pixelsize,fps,xPoL,xPoR,xDoL,xDoR,Crop_Center)
        ;
    [thetaL, thetaR] = tangent_method(B);
    [thetaAL, thetaAR] = AreaAngle_method(B,14);

    if ~isempty(DCLt)
        if ~isempty(B)
            if ~isempty(Dt)
                TimeS(cnt,1) = TiSeC(cnt); %[sec]
                TimsS(cnt,1) = TiSeC(cnt)*1000; %[ms]
                DtS(cnt,1) = Dt; %[mm]
                DCLtS(cnt,1) = DCLt; %[mm]
                NDtS(cnt,1) = Dt/D0(1); %[mm]
                NDCLtS(cnt,1) = DCLt/D0(1); %[mm]
                HtS(cnt,1) = Ht; %[mm]
                VCLS(cnt,:) = VCL; % [m/s]
                VRS(cnt,:) = VR; % [m/s]
                CaS(cnt,1) = mu*VCL(1)/sigma;
                CaS(cnt,2) = mu*VCL(2)/sigma;
                theta(cnt,1) = thetaL; %[degree]
                theta(cnt,2) = thetaR; %[degree]
                thetaA(cnt,1) = thetaAL; %[degree]
                thetaA(cnt,2) = thetaAR; %[degree]

                BPoS{cnt} = B;
            else break; end;
        else break; end;
    else break; end;
end

%% Maximum value
[Dmax, ts] = MaximumVT(DtS,TimsS,5,10);
[DCLmax, ts_CL] = MaximumVT(DCLtS,TimsS,5,1);

NDmax = Dmax/D0(1);
NDCLmax = DCLmax/D0(1);
indT = round(ts*10);

%% theta plateau
ts2sn = round(ts*10);
th_SC = thetaA(ts2sn*0.1:(ts2sn+1)*0.9,1:2);
th_SC = outliers(th_SC);
theta_pla = nanmean(th_SC);
```

```matlab
%% theta max
theta_m = thetaA(ts2sn,:);

%% SLV max
Bmax = BPoS{ts2sn};
[SLVmax] = SLVmaxC(Bmax,ROI,pixelsize); %[m2]

%% Save results
if mac == 1
    ResCodedir = strcat(cd,'/Results/',OutRes);
    Readcsv = strcat(ResCodedir,'/',Title,'.csv');
    mkdirE(ResCodedir);
else
    ResCodedir = strcat(cd,'\Results\',OutRes);
    Readcsv = strcat(ResCodedir,'\',Title,'.csv');
    mkdirE(ResCodedir);
end

if ~exist(Readcsv)
    OutValN = {'ID','Substrate','Liquid','rho','gamma','mu
        ','theta_eq','theta_adv','theta_rec',...
            'theta_m_L','theta_m_R','theta_pla_L','
                theta_pla_R',...
            'We','Re','D0','D0std','Vi','Vistd','Dmax','
                beta','DmaxCL','betaCL','tmax','tmaxCL'
                ,...
            'SLVmaxL','SLVmaxR','SamplePath'};
    cell2csv(Readcsv,OutValN);
else
end

IDs1 = strcat(Substrate(1:2),Liquid(1:1));
VID1 = num2str(floor(Vi(1)));
VID2 = num2str(fix((Vi(1)*10)-(floor(Vi(1))*10)));
IDs2 = strcat(IDs1,'_V',VID1,'d',VID2);

PDATA = readtable(Readcsv);
IDst = PDATA.ID;
IDchar = char(IDst);
NRef = strmatch(IDs2,IDchar);
NCo = numel(NRef);
IDs3 = num2str(NCo);
ID = strcat(IDs2,'_',IDs3);

%% Time variable export
ResValue = [TimeS,TimsS,DtS,DCLtS,NDtS,NDCLtS,HtS,VCLS,VRS
    ,CaS,theta,thetaA];
```

```matlab
ResName = {'time','ms','Dt','DCLt','NDt','NDCLt','Ht','
    VCL_L','VCL_R','VR_L','VR_R','Ca_L','Ca_R',...
    'thetaL','thetaR','thetaAL','thetaAR'};
BSCPoS = [];

%% Maximum variable export
if mac == 1
    ResValue1 = {ID,Substrate,Liquid,rho,sigma,mu,theta_eq
        ,theta_adv,theta_rec...
                    theta_m(1),theta_m(2),theta_pla(1),
                        theta_pla(2),...
                    WeN,ReN,D0(1),D0(2),Vi(1),Vi(2),Dmax,
                        NDmax,DCLmax,NDCLmax,ts,ts_CL,...
                    SLVmax(1),SLVmax(2),SamplePath};
else
    SamplePathW = SamplePath;
    ids = find(SamplePathW=='\');
    SamplePathW(ids) = '/';
    ResValue1 = {ID,Substrate,Liquid,rho,sigma,mu,theta_eq
        ,theta_adv,theta_rec...
                    theta_m(1),theta_m(2),theta_pla(1),
                        theta_pla(2),...
                    WeN,ReN,D0(1),D0(2),Vi(1),Vi(2),Dmax,
                        NDmax,DCLmax,NDCLmax,ts,ts_CL,...
                    SLVmax(1),SLVmax(2),SamplePath};
end

%% Make folder structure
s1 = strcat(ResCodedir,'/tDATA');
s2 = strcat(ResCodedir,'/tDATA/mat');
mkdirE(s1);
mkdirE(s2);

if mac == 0
    FnRes = strcat(ResDir,'\Timevol.csv');
    FnRes2 = strcat(ResDir,'\Maxdata.csv');
    FnRes1 = strcat(ResCodedir,'\tDATA\',ID,'.csv');
    ResMat = strcat(ResCodedir,'\tDATA\mat\',ID,'.mat');
else
    FnRes = strcat(ResDir,'/Timevol.csv');
    FnRes2 = strcat(ResDir,'/Maxdata.csv');
    FnRes1 = strcat(ResCodedir,'/tDATA/',ID,'.csv');
    ResMat = strcat(ResCodedir,'/tDATA/mat/',ID,'.mat');
end

csvwriteh(FnRes,ResValue,ResName);
csvwriteh(FnRes1,ResValue,ResName);
cell2csv(FnRes2,ResValue1);
```

```matlab
cell2csv(Readcsv,ResValue1);
save(ResMat,'Surfl','TimeS','TimsS','theta','thetaA','
    DCLtS','DtS','NDCLtS','NDtS','VCLS','VRS','HtS','DO','
    Vi',...
    'DCLmax','NDCLmax','Dmax','NDmax','ts','ts_CL','WeN','
        ReN','SamplePath','BPoS','ROI','fps');

%% Plotting
plotspread(BPoS,ROI,ts,ts_CL,pixelsize,ResDir,ResCodedir,
    ID,fps);
plotDDCA(TimsS,NDtS,thetaA,DO,Vi,ID,ResCodedir);

background.m (function in MATLAB for generating background
     image)
function [im_BGM] = backgroud(ResDir,Flist,NumOfMean)
    NumEnd = size(Flist,1);

    for i = 1:1:NumOfMean
        fn = Flist(i).fullname;
        im = imread(fn);
        im = im2double(im);
        if i == 1
            imInt = im;
        else
            imSUM = imInt + im;
        end
    end

    imM = imSUM / NumOfMean;
    imM = im2uint8(imM);

    Fn = strcat(ResDir,'/BGM.tif');
    imwrite(imM,Fn);
    im_BGM = imM;
end
```

IMAGEANALYSIS

Function in MATLAB for image treatment

```matlab
function [Im_Crop,Im_BW,By,Bx,B] = imageAnalysis(Im_BGM,
    Im_T,ImFlist,ROI)
    Im_BGM2 = double(Im_BGM);
    Im_T2 = double(Im_T);
    Im_Sub = Im_BGM2./Im_T2;
```

```matlab
    SW = round(size(Im_T,2));
    if ROI(1)+ROI(3) > SW
        Im_Crop = Im_Sub(ROI(2):ROI(2)+ROI(4),ROI(1):SW);
        CSW = size(Im_Crop,2);
        Im_Crop(:,CSW:ROI(3)) = 0;
    elseif ROI(1) < 1
        Im_Crop1 = Im_Sub(ROI(2):ROI(2)+ROI(4),1:ROI(1)+
            ROI(3));
        Im_Crop2(1:ROI(4)+1,1:abs(ROI(1)))=0;
        Im_Crop = [Im_Crop2,Im_Crop1];
    else
        Im_Crop = Im_Sub(ROI(2):ROI(2)+ROI(4),ROI(1):ROI
            (1)+ROI(3));
    end

    H = fspecial('gaussian',50);
    ImgF = imfilter(Im_Crop,H);
    threshR = 0.42; % 0
    Im_Th = ImgF>threshR;

    Im_BW = edge(Im_Th,'canny');
    se = strel('octagon',3); % 30
    Im_BW = imclose(Im_BW,se);

    %% imfill: eliminate light in the middle of droplet
    [h,w] = size(Im_BW);
    mask=ones(h+2,w);
    [mh,mw] = size(mask);
    mask(2:mh-1,1:w)=Im_BW;
    Im_fill = imfill(mask,'holes');
    Im_BW = Im_fill(2:mh-1,1:w);

    %% Boundary segmentation
    %Im_BW = imcomplement(Im_BW);
    [bnd,L,N] = bwboundaries(Im_BW);

    Bx = 0;By = 0;B = [0 0];

    if length(bnd)<1,return;end % no Boundaries
    %find largest boundary
    cm=0;bi=0;
    for i=1:N
      B=bnd{i};
      cnt=size(B,1);
      if cnt>cm
        bi=i;
        cm=cnt;
      end
```

```
      end
      if bi >0
         B=bnd{bi};
      end

      By = B(:,1);
      Bx = B(:,2);

end
```

IMPINGINGDROP.M

Function in MATLAB for impact velocity and initial drop size

```
function [D0, Vi,Center] = impingingDrop(ImN_impact,
    Im_BGM, ROI_im, Flist, BufferIm, pixelsize, fps);

Im_T = imread(Flist(ImN_impact-1-BufferIm).fullname);
Im_T = im2uint8(Im_T);
Im_Sub = Im_T-Im_BGM;
threshR = 60; % 0
Im_Th = Im_Sub<threshR;
se = strel('octagon',3); % 30
Im_BW = imclose(Im_Th,se);
Im_fill = imfill(Im_BW,'holes');
[C,R] = imfindcircles(Im_fill,[40,200]);
if isempty(C)
    [C,R] = imfindcircles(Im_fill,[40,200],'Sensitivity'
        ,0.9);
    display('#####################-----Warning!!!!
        Sensitivity change to 0.9');
end
Center.X = round(C(1));
Center.Y = round(ROI_im(1));

ROI_width = 250;%967%1382;%1105 %10 mm -> 829 (1382 for 10
    k) (1372 for 5k)
ROI_height = 350; %3.5 mm (484 for 10k) (481 for 5k)
ROI = [Center.X-ROI_width/2 Center.Y-ROI_height ROI_width
    ROI_height]; %[left conner x, y, width, height]

NSlice = 4;
    for cns = 1:1:NSlice
        Ns = ImN_impact - cns - BufferIm;

        Im_T = imread(Flist(Ns).fullname);
```

```matlab
        Im_T = im2uint8(Im_T);
        Im_Sub = Im_T-Im_BGM;
        Im_Crop = Im_Sub(ROI(2):ROI(2)+ROI(4),ROI(1):ROI
            (1)+ROI(3));
        threshR = 60; % 0
        Im_Th = Im_Sub<threshR;
        se = strel('octagon',3); % 30
        Im_BW = imclose(Im_Th,se);
        Im_fill = imfill(Im_BW,'holes');
        [C,R] = imfindcircles(Im_fill,[40,200]);
        if isempty(C)
            [C,R] = imfindcircles(Im_fill,[40,200],'
                Sensitivity',0.9);
            display('########################-----Warning
                !!!! Sensitivity change to 0.9');
        end
        DOS(cns) = pixelsize*R*2;
        CS(cns,:) = C;
    end

    for nt = 1:1:NSlice-1
        ds = NSlice + 1 - nt;
        dss = NSlice - nt;

        dX = abs(CS(ds,1)-CS(dss,1));
        dY = abs(CS(ds,2)-CS(dss,2));
        dD = sqrt(dX^2+dY^2);
        dVi = (dD*pixelsize/1000)/(1/fps); %[m/s]
        dViS(nt) = dVi;
    end

DO(1) = mean(DOS);
DO(2) = std(DOS);
Vi(1) = mean(dViS);
Vi(2) = std(dViS);
```

MAXIMUMVT.M

Function in MATLAB for determining maximum spreading

```matlab
function [Valuemax, timemax] = MaximumVT(TD,TimsS,numD,
    stBuf)

stBuf = round(stBuf);

len = length(TD);
```

```matlab
cnt = 0;
if len < numD+stBuf
    Valuemax =0;
    timemax =0;
else
    for csN = stBuf:1:len-1
        psDt = TD(csN+1) - TD(csN);
        if psDt <= 0
            cnt = cnt + 1;
            if cnt > numD
                break;
            else end
        else
            cnt = 0;
        end
    end
    csN = csN - cnt + 1;
    TDcrop = TD(1:csN);
    tsid = find(TDcrop<TD(csN));
    tsind = max(tsid);
    Valuemax = TD(tsind+1);
    timemax = TimsS(tsind+1);
end
```

DMEASURE2.M

Function in MATLAB for measuring geometric shape of droplet

```matlab
function [DCLt,Dt,Ht,VCL,VR,xPoL,xPoR,xDoL,xDoR] =
    Dmeasure2(By,Bx,pixelsize,fps,xPoL_old,xPoR_old,
    xDoL_old,xDoR_old,Crop_Center)

    Baseline = max(By)-1;
    yPnt = find(By==char(Baseline));
    xPo = Bx(yPnt);

    if ~exist('xPoL_old','var') || isempty(xPoL_old)
        xPoL_old = Crop_Center.X;
    end
    if ~exist('xPoR_old','var') || isempty(xPoR_old)
        xPoR_old = Crop_Center.X;
    end
    if ~exist('xDoL_old','var') || isempty(xDoL_old)
        xDoL_old = Crop_Center.X;
    end
    if ~exist('xDoR_old','var') || isempty(xDoR_old)
```

```matlab
        xDoR_old = Crop_Center.X;
    end

    %% D_CL(t)
    Baseline = max(By)-1;
    yPnt = find(By==char(Baseline));
    xPo = Bx(yPnt);
    xPoL = min(xPo);
    xPoR = max(xPo);
    DCLtp = xPoR-xPoL;
    if DCLtp <= 0
        DCLt = 0;
    else
        DCLt = DCLtp*pixelsize; %[mm]
    end

    %% D(t)
    xDoL = min(Bx);
    xDoR = max(Bx);
    Dtp = xDoR-xDoL;
    Dt = Dtp*pixelsize; %[mm]

    %% V_CL(t)
    VCL(:,1) = (xPoL_old - xPoL)*pixelsize/(1/fps)/1000; %
        [m/s]
    VCL(:,2) = (xPoR - xPoR_old)*pixelsize/(1/fps)/1000; %
        [m/s]

    %% V_R(t)
    VR(:,1) = (xDoL_old - xDoL)*pixelsize/(1/fps)/1000; %[
        m/s]
    VR(:,2) = (xDoR - xDoR_old)*pixelsize/(1/fps)/1000; %[
        m/s]

    %% H(t)
    Htp = Crop_Center.Y-min(By);
    Ht = Htp*pixelsize;
end
```

AREAANGLE_METHOD.M

Function in MATLAB for measuring dynamic contact angle

```matlab
function [thetaL, thetaR] = AreaAngle_method(B,R)

y = B(:,1);
```

```matlab
x = B(:,2);

WinL = zeros(R,2*R-1);
WinR = zeros(R,2*R-1);
TriM = zeros(R,2*R-1);
for tri = 1:1:R
    TriM(tri,R-(tri-1):R+(tri-1)) = 1;
end

Ind1 = find(y < max(y)-1);
y1 = B(Ind1,1);
y1 = abs(y1-max(y1));
x1 = B(Ind1,2);
%% left
ind2 = find(y1 == 0);
xol = min(x1(ind2));
xl = x1-xol;

WinL(R,R:2*R-1) = 1;
for lines = 1:1:R-1
    tmp1 = find(y1 ==lines);
    tmp2 = min(xl(tmp1));
    if abs(tmp2) > R-1
        if tmp2 > 0
            WinL(R-lines,1:2*R-1)=0;
        else
            WinL(R-lines,1:2*R-1)=1;
        end
    else
        WinL(R-lines,R+tmp2:2*R-1)=1;
    end
end

Ind2 = find(y < max(y)-1);
y2 = B(Ind2,1);
y2 = abs(y2-max(y2));
x2 = B(Ind2,2);
%% Right
xor = max(x2(ind2));
xr = x2-xor;

WinR(R,1:R) = 1;
for lines = 1:1:R-1
    tmp1 = find(y2 ==lines);
    tmp2 = max(xr(tmp1));
    if abs(tmp2) > R-1
        if tmp2 > 0
            WinR(R-lines,1:2*R-1)=1;
```

```matlab
            else
                WinR(R-lines,1:2*R-1)=0;
            end
        else
            WinR(R-lines,1:R+tmp2)=1;
        end
end

%% lamda
TriSM = zeros(R,2*R-1);
for lam = 1:1:R
      TriSM(lam,R-(lam-1))=1;
      TriSM(lam,R+(lam-1))=1;
end

det1 = sum(sum(TriSM.*WinL));
if det1 < R
    lamdaL = 1;
elseif det1 == R
    lamdaL = 0;
else
    lamdaL = -1;
end

det1 = sum(sum(TriSM.*WinR));
if det1 < R
    lamdaR = 1;
elseif det1 == R
    lamdaR = 0;
else
    lamdaR = -1;
end

AL = sum(sum(WinL.*TriM));
AR = sum(sum(WinR.*TriM));

alphaL = (pi/2)*(1-lamdaL)+atan(lamdaL*((R^2*(1-lamdaL)-2*
    AL)/(2*AL-R^2)));
alphaR = (pi/2)*(1-lamdaR)+atan(lamdaR*((R^2*(1-lamdaR)-2*
    AR)/(2*AR-R^2)));

thetaL = abs(alphaL*180/pi);
thetaR = abs(alphaR*180/pi);
end
```

SPHERECAP_METHOD.M

Function in MATLAB for measuring volume of droplet on surface

```matlab
function [thetaSC,xPnt,yPnt,VolSC,DCLtSC,HtSC,PL] =
    spherecap_method(B,pixelsize)
    thetaSC = 0; xPnt=0; yPnt=0; VolSC=0; DCLtSC=0;HtSC=0;
        PL=0;
    if length(B)<40,return;end % no Boundaries
    BaseOff = 8;
    Bline = max(B(:,1))-BaseOff;
    LV = find(B(:,1)<Bline);
    LVx = B(LV,2);
    LVy = B(LV,1);
    Hdrop = min(LVy);
    [xc,yc,R,a,xPnt,yPnt] = circfit(LVx,LVy);

    Bottomline = max(B(:,1));
    dyc = yc - Bottomline;   % h
    yRpt = round(yPnt);
    ind = find(yRpt == Bottomline);
    xCPnt = xPnt(ind);
    dxc = max(xCPnt) - xc; % a
        thetaT = arccos(dxc/(R-dyc));
    thetaSC = abs(thetaT)*180/pi;
    if isempty(thetaSC)
        thetaSC = 0;
    end

    hSC = (R-dyc)*pixelsize; %[mm]
    aSC = dxc*pixelsize;
    RSC = R*pixelsize; % [mm]

    VolSC = pi*hSC/6*(3*aSC.^2+hSC.^2); % [mm3]spherical
        cap volume Ref. wiki
    AreaSC = 2*pi*RSC*hSC; % [mm2]surface area of
        spherical cap
    DtSC = aSC*2; % [mm] contact line diameter based on
        spherical cap
    HtSC = hSC; % Spherical cap height [mm]
    PL = (2*0.072)/(RSC/1000); % Pa
end
```

APPENDIX B

The code presented in this appendix is for quantification of neutron radiography and moisture content calculation. The detail description can be found in chapter 5.

CORRNEUTRA.M

Main structure

```matlab
%% Properties
mu = 362; %[1/m] effective water attenuation coeffficient
rho = 998; %[kg/m3] density of water
pxsize = 45.5e-6; %[m] pixelsize
Mdrop = 4.4e-6; %[kg] initial drop mass

thHV = 3e-10; %thresholding Value [kg]

%% Loading images
Path = '/Users/jaeblee/Desktop/Projects/NEUTRA/
    Single_drop_RH10/Savo/V30/4';
ImPath = strcat(Path,'/Res');

bbPath = strcat(ImPath,'/bb.tif');
bb = imread(bbPath);

ffPath = strcat(ImPath,'/ff.tif');
ff = imread(ffPath);

refPath = strcat(ImPath,'/ref.tif');
ref = imread(refPath);

dropPath = strcat(ImPath,'/drop');
[Flist,anz]=GetFiles(dropPath,'*.tif',1);

%% ROI for dose and surface horizontal line
ROIdoseR;

Tdry = dose(ref,bb,ff,ROIdose);
CoI = imread(Flist(1).fullname);
```

```matlab
CoIm = dose(CoI,bb,ff,ROIdose);

SetCoord;
Center.X = round(ycorl(1));
Center.Y = round(xcorl(3));

width = 264;
AirH = 66;
DepthZ = 154;
ROIT = [Center.X-width/2 Center.Y-AirH width AirH+DepthZ];

TdryC = Tdry(ROIT(2):ROIT(2)+ROIT(4),ROIT(1):ROIT(1)+ROIT
    (3));



scanW = 10;
scanD = 20;
sliceN = 36;
Ti = [3:3:sliceN*3]'; %[s]
ZMF = zeros(0);DMF = zeros(0);
DDth = 0.1;

for cnt = 1:36
    ImdT = imread(Flist(cnt).fullname);
    Tt = dose(ImdT,bb,ff,ROIdose);
    Tt = Tt(ROIT(2):ROIT(2)+ROIT(4),ROIT(1):ROIT(1)+ROIT
        (3));
    Tcorr{cnt} = Tt;
    Mt = (rho*pxsize^2/mu).*log(TdryC./Tt); %[ug]
    M{cnt} = Mt;
    MFt = Thesholding(Mt,thHV);
    MF{cnt} = MFt;
    Zcrop = MFt(AirH:DepthZ,132-scanW:132+scanW);
    rezt = zeros(0);
    for col = 1:scanW*2+1
        ztt = Zcrop(:,col);
        zt = max(find(ztt == 1))*pxsize*1000; %[mm]
        rezt = [rezt;zt];
    end
    ZMFt = mean(rezt);
    ZMF = [ZMF;ZMFt];

    Dcrop = MFt(AirH+2:AirH+scanD,1:width);
    redt = zeros(0);
    for row = 1:scanD-1
        dtt = Dcrop(row,:);
```

```
        dt = (max(find(dtt == 1))-min(find(dtt == 1)))*
            pxsize*1000; %[mm]
        redt = [redt;dt];
    end
    DMFt = max(redt);
    DMF = [DMF;DMFt];

end
```

MC__PROFILE.M

Calculation of MC profile

```
samplePath = '/Users/jaeblee/Documents/Library/Experiment/
    QNI_mat/Savo/RH10/V0d5/1'
sampleName = '/Qni.mat';

Path = strcat(samplePath,sampleName);
load(Path);


pixelsize = 45.5e-6; %[um]

width = 110; %10mm
depth = 110; %5mm

MCPS = zeros(0);

cutlinew = 0.5; %[mm]
for i = 1:10
    Im = WaterMass{i+10};
    ImC = Im(Center.Y:Center.Y+depth,Center.X-width:Center
        .X+width);
    ImBW = Thesholding(Im,2e-7);
    ImBWC = ImBW(Center.Y:Center.Y+depth,Center.X-width:
        Center.X+width);
    MCP = MCprofile(ImC, ImBWC, pixelsize, cutlinew);
    MCPS = [MCPS,MCP];
end


MCprofile.m (function in MATLAB for drop volume estimation
    )
function MCP = MCprofile(ImC, ImBWC, pixelsize, cutlinew)
cntP = round(cutlinew/1000/pixelsize/2);
```

```matlab
[lt,rt] = size(ImBWC);
MCMD = zeros(0);

for ix = 1:lt
    TL = ImBWC(ix,:);
    TLL = TL(1:rt/2);
    TLR = TL(rt/2:rt);
    LP = rt/2-max(find(TLL==0));
    RP = min(find(TLR==0));
    LM = (LP+RP)*pixelsize; %[m]
    IL = ImC(ix,:);
    MCL = (IL/1000)/(LM*pixelsize*pixelsize); %kg/m3
    MCM = mean(MCL(rt/2-cntP:rt/2+cntP));
    MCMD = [MCMD;MCM];
end

MCP = MCMD;
```

THRESHOLDING.M

Function in MATLAB for segmentation moisture mass

```matlab
function [seg] = Thesholding(Img,Th)
    H = fspecial('gaussian',10);
    ImgF = imfilter(Img,H);
    ImgTh = ImgF > Th;
    se = strel('disk',10);
    Imclose = imclose(ImgTh,se);

    seg = imfilter(Imclose,H);
    %seg = Imclose;
end
```

BIBLIOGRAPHY

Alam, Parvez, Martti Toivakka, Kaj Backfolk, and Petri Sirviö (2007). "Impact spreading and absorption of Newtonian droplets on topographically irregular porous materials." In: *Chemical Engineering Science* 62.12, pp. 3142–3158.

Alleborn, N and H Raszillier (2004). "Spreading and sorption of droplets on layered porous substrates." In: *Journal of Colloid And Interface Science* 280.2, pp. 449–464.

Antonini, C, A Amirfazli, and M Marengo (2012). "Drop impact and wettability: From hydrophilic to superhydrophobic surfaces." In: *Physics of Fluids* 24.10.

Ardebrant, H . and R . J . Pugh (1991). "Wetting studies on silicate minerals and rocks used in bituminous highways." In: *Colloids and Surfaces* 58.1-2, pp. 111–130.

Attané, P, F Girard, and V Morin (2007). "An energy balance approach of the dynamics of drop impact on a solid surface." In: *Physics of Fluids (1994-present)* 19.1, p. 012101.

Aytouna, Mounir, Denis Bartolo, Gerard Wegdam, Daniel Bonn, and Salima Rafaï (2009). "Impact dynamics of surfactant laden drops: dynamic surface tension effects." In: *Experiments in Fluids* 48.1, pp. 49–57.

Bartolo, Denis, Christophe Josserand, and Daniel Bonn (2005). "Retraction dynamics of aqueous drops upon impact on non-wetting surfaces." In: *Journal of Fluid Mechanics* 545.-1, p. 329.

Bartolo, Denis, Arezki Boudaoud, Grégoire Narcy, and Daniel Bonn (2007). "Dynamics of Non-Newtonian Droplets." In: *Physical review letters* 99.17.

Bayer, IS and CM Megaridis (2006). "Contact angle dynamics in droplets impacting on flat surfaces with different wetting characteristics." In: *Journal of Fluid Mechanics* 558, pp. 415–449.

Bechtel, S E, D B Bogy, and F E Talke (1993). "Impact of a Liquid Drop Against a Flat Surface." In: *IBM Journal of Research and Development* 25.6, pp. 963–971.

Ben Jazia, Dorra, Laurent Vonna, Gautier Schrodj, Hugues Bonnet, Yves Holl, and Hamidou Haidara (2011). "Imbibing drops of ethanol/water

mixtures in model nanoporous networks with tunable pore structure: Deviation from square root to linear time regime imbibition kinetics." In: *Colloids and Surfaces A: Physicochemical and Engineering Aspects* 384.1-3, pp. 643–652.

Bennett, T and D Poulikakos (1993). "Splat-quench solidification: estimating the maximum spreading of a droplet impacting a solid surface." In: *Journal of Materials Science* 28.4, pp. 963–970.

Berthier, Erwin and David J . Beebe (2007). "Flow rate analysis of a surface tension driven passive micropump." In: *Lab on a Chip* 7.11, pp. 1475–1478.

Biolè, D and V Bertola (2015). "A goniometric mask to measure contact angles from digital images of liquid drops." In: *Colloids and Surfaces A: Physicochemical and Engineering Aspects* 467, pp. 149–156.

Blocken, B and J Carmeliet (2015). "Impact, runoff and drying of wind-driven rain on a window glass surface: Numerical modelling based on experimental validation." In: *Building and Environment* 84, pp. 170–180.

Bussmann, M, J Mostaghimi, and S Chandra (1999). "On a three-dimensional volume tracking model of droplet impact." In: *Physics of Fluids* 11, p. 1406.

Bussmann, M, S Chandra, and J Mostaghimi (2000). "Modeling the splash of a droplet impacting a solid surface." In: *Physics of Fluids* 12, p. 3121.

Carmeliet, Jan and Staf Roels (2001). "Determination of the Isothermal Moisture Transport Properties of Porous Building Materials." In: *Journal of Building Physics* 24.3, pp. 183–210.

Caviezel, D ., C . Narayanan, and D . Lakehal (2008). "Adherence and bouncing of liquid droplets impacting on dry surfaces." In: *Microfluidics and Nanofluidics* 5.4, pp. 469–478.

Chandra, S and C T Avedisian (1991). "On the collision of a droplet with a solid surface." In: *Proc. R. Soc. Lond. A* 432, pp. 13–41.

Chandra, S and CT Avedisian (1992). "Observations of droplet impingement on a ceramic porous surface." In: *International Journal of Heat and Mass Transfer* 35.10, pp. 2377–2388.

Cheng, Nian-Sheng (2008). *Formula for the Viscosity of a Glycerol-Water Mixture.* Vol. 47. American Chemical Society.

Chilton, T . H . and A . P . Colburn (1934). "Mass Transfer (Absorption) Coefficients Prediction from Data on Heat Transfer and Fluid Fric-

tion." In: *INDUSTRIAL AND ENGINEERING CHEMISTRY* 26.11, pp. 1183–1187.

Clanet, Christophe, Cédric Béguin, Denis Richard, and David Quéré (2004). "Maximal deformation of an impacting drop." In: *Journal of Fluid Mechanics* 517, pp. 199–208.

Clarke, A, T D Blake, K Carruthers, and A Woodward (2002). "Spreading and Imbibition of Liquid Droplets on Porous Surfaces." In: *Langmuir* 18.8, pp. 2980–2984.

Collings, E W, A J Markworth, J K McCoy, and J H Saunders (1990). "Splat-quench solidification of freely falling liquid-metal drops by impact on a planar substrate." In: *Journal of Materials Science* 25.8, pp. 3677–3682.

Crooks, Regan, Justin Cooper-White, and David V Boger (2001). "The role of dynamic surface tension and elasticity on the dynamics of drop impact." In: *Chemical Engineering Science* 56.19, pp. 5575–5592.

Davis, S H and L M Hocking (1999). "Spreading and imbibition of viscous liquid on a porous base." In: *Physics of Fluids* 11.1, p. 48.

– (2000). "Spreading and imbibition of viscous liquid on a porous base. II." In: *Physics of Fluids* 12.7, pp. 1646–1655.

Delon, G ., D . Terwagne, S . Dorbolo, N . Vandewalle, and H . Caps (2011). "Impact of liquid droplets on granular media." In: *Physical Review E* 84.4, p. 046320.

Denesuk, M., GL Smith, BJJ Zelinski, NJ Kreidl, and DR Uhlmann (1993). "Capillary penetration of liquid droplets into porous materials." In: *Journal of Colloid And Interface Science* 158.1, pp. 114–120.

Derluyn, Hannelore (2012). "Salt Transport and Crystallization in Porous Limestone." PhD thesis. ETH Zurich.

D'Onofrio, Terrence G, Homayun K Navaz, Bojan Markicevic, Brent A Mantooth, and Kenneth B Sumpter (2010). "Experimental and Numerical Study of Spread and Sorption of VX Sessile Droplets into Medium Grain-Size Sand." In: *Langmuir* 26.5, pp. 3317–3322.

Dreesen, Roland and Michiel Dusar (2004). "Historical building stones in the province of Limburg (NE Belgium): role of petrography in provenance and durability assessment." In: *Materials Characterization* 53.2-4, pp. 273–287.

Dullien, F (2012). *Porous Media Fluid Transport and Pore Structure.* Elsevier.

Eggers, Jens, Marco A Fontelos, Christophe Josserand, and Stéphane Zaleski (2010). "Drop dynamics after impact on a solid wall: Theory and simulations." In: *Physics of Fluids* 22.6, p. 062101.

Engel, Olive G (1955). "Waterdrop collisions with solid surfaces." In: *J. Res. NBS* 5, pp. 281–298.

Erkal, Aykut, Dina D'Ayala, and Lourenço Sequeira (2012). "Assessment of wind-driven rain impact, related surface erosion and surface strength reduction of historic building materials." In: *Building and Environment* 57, pp. 336–348.

Farhangi, M. M., P. J. Graham, N. R. Choudhury, and A. Dolatabadi (2012). "Induced Detachment of Coalescing Droplets on Superhydrophobic Surfaces." In: *Langmuir.*

Fronteau, Gilles (2000). "Comportements télogénétiques des principaux calcaires de Champagne-Ardenne." PhD thesis.

Fukai, J, Y Shiiba, T Yamamoto, O Miyatake, C M Megaridis, and Z Zhao (1995). "Wetting effects on the spreading of a liquid droplet colliding with a flat surface: Experiment and modeling." In: *Physics of Fluids (1994-present)* 7.2, pp. 236–247.

Gambaryan-Roisman, Tatiana (2014). "Liquids on porous layers: wetting, imbibition and transport processes." In: *Current Opinion in Colloid & Interface Science* 19.4, pp. 320–335.

Gennes, P G de, F Brochard-Wyart, and D Quéré (2004). *Capillarity and wetting phenomena: drops, bubbles, pearls, waves.* Springer.

George W Wagner, Richard J O'Connor, Jennifer L Edwards, and Carol A S Brevett (2004). *Effect of Drop Size on the Degradation of VX in Concrete.* Vol. 20. American Chemical Society.

German, G and V Bertola (2009). "Impact of shear-thinning and yield-stress drops on solid substrates." In: *JOURNAL OF PHYSICS CONDENSED MATTER* 21.37, p. 375111.

Griebel, Michael and Margrit Klitz (2014). "Simulation of Droplet Impact with Dynamic Contact Angle Boundary Conditions." In: *Singular Phenomena and Scaling in Mathematical Models.* Cham: Springer International Publishing, pp. 297–325.

Hapgood, Karen P, James D Litster, Simon R Biggs, and Tony Howes (2002). "Drop Penetration into Porous Powder Beds." In: *Journal of Colloid And Interface Science* 253.2, pp. 353–366.

Huh, Chun and L . E Scriven (1971). "Hydrodynamic model of steady movement of a solid/liquid/fluid contact line." In: *Journal of Colloid And Interface Science.*

Jung, Sung Yong, Seungmin Lim, and Sang Joon Lee (2012). "Investigation of water seepage through porous media using X-ray imaging technique." In: *Journal of Hydrology* 452-453, pp. 83–89.

Kannan, R and D Sivakumar (2008). "Impact of liquid drops on a rough surface comprising microgrooves." In: *Experiments in Fluids* 44.6, pp. 927–938.

Katsuragi, Hiroaki (2010). "Morphology Scaling of Drop Impact onto a Granular Layer." In: *Physical review letters* 104.21, p. 218001.

Kim, H and J Chun (2001). "The recoiling of liquid droplets upon collision with solid surfaces." In: *Physics of Fluids* 13.3, pp. 643–659.

Kistler, S F (1993). *Hydrodynamics of wetting.* Wettability.

Laan, N, K G de Bruin, D Bartolo, C Josserand, and D Bonn (2014). "Maximum Diameter of Impacting Liquid Droplets." In: *Physical Review Applied* 2, p. 044018.

Lee, J S, B M Weon, J H Je, and K Fezzaa (2012). "How does an air film evolve into a bubble during drop impact?" In: *Physical review letters* 109.20.

Lee, Jae Bong and Seong Hyuk Lee (2011). "Dynamic wetting and spreading characteristics of a liquid droplet impinging on hydrophobic textured surfaces." In: *Langmuir* 27.11, pp. 6565–6573.

Lee, Jae Bong, Dominique Derome, Ali Dolatabadi, and Jan Carmeliet (2016a). "Energy Budget of Liquid Drop Impact at Maximum Spreading: Numerical Simulations and Experiments." In: *Langmuir* 32.5, pp. 1279–1288.

Lee, Jae Bong, Dominique Derome, Robert Guyer, and Jan Carmeliet (2016b). "Modeling the Maximum Spreading of Liquid Droplets Impacting Wetting and Nonwetting Surfaces." In: *Langmuir* 32.5, pp. 1299–1308.

Lee, Jae Bong, N Laan, K G de Bruin, G Skantzaris, N Shahidzadeh, D Derome, J carmeliet, and D Bonn (2016c). "Universal rescaling of drop impact on smooth and rough surfaces." In: *Journal of Fluid Mechanics* 786, R4.

Lehmann, E. H. (2008). "Recent improvements in the methodology of neutron imaging." In: *Pramana* 71.4, pp. 653–661.

Madejski, J (1976). "Solidification of droplets on a cold surface." In: *International Journal of Heat and Mass Transfer* 19.9, pp. 1009–1013.

Malgarinos, Ilias, Nikolaos Nikolopoulos, Marco Marengo, Carlo Antonini, and Manolis Gavaises (2014). "VOF simulations of the contact angle dynamics during the drop spreading: Standard models and a new

wetting force model." In: *Advances in Colloid and Interface Science* 212, pp. 1–20.

Mani, Madhav, Shreyas Mandre, and Michael P Brenner (2010). "Events before droplet splashing on a solid surface." In: *Journal of Fluid Mechanics* 647, pp. 163–185.

Mao, T, DCS Kuhn, and H Tran (1997). "Spread and rebound of liquid droplets upon impact on flat surfaces." In: *AIChE Journal* 43.9, pp. 2169–2179.

Marengo, Marco, Carlo Antonini, Ilia V Roisman, and Cameron Tropea (2011). "Drop collisions with simple and complex surfaces." In: *Current Opinion in Colloid & Interface Science* 16.4, pp. 292–302.

Markicevic, B and H K Navaz (2010). "Primary and Secondary Infiltration of Wetting Liquid Sessile Droplet into Porous Medium." In: *Transport in Porous Media* 85.3, pp. 953–974.

Markicevic, B, H Li, Y Sikorski, A R Zand, M Sanders, and H K Navaz (2009). "Infiltration time and imprint shape of a sessile droplet imbibing porous medium." In: *Journal of Colloid And Interface Science* 336.2, pp. 698–706.

Marmur, A (1988). "Drop penetration into a thin porous medium." In: *Journal of Colloid And Interface Science* 123.1, pp. 161–169.

Marston, J O, S T Thoroddsen, W K Ng, and R B H Tan (2010). "Experimental study of liquid drop impact onto a powder surface." In: *Powder Technology* 203.2, pp. 223–236.

Moonen, P . (2009). "Contiuous-discontinuous modelling of hygrothermal damage processes in porous media." PhD thesis. TU Delft, Delft University of Technology.

Mundo, CHR, M Sommerfeld, and C Tropea (1995). "Droplet-wall collisions: experimental studies of the deformation and breakup process." In: *International Journal of Multiphase Flow* 21.2, pp. 151–173.

Navaz, Homayun K, Bojan Markicevic, Ali R Zand, Yuri Sikorski, Ewen Chan, Matthew Sanders, and Terrence G D'Onofrio (2008). "Sessile droplet spread into porous substrates—Determination of capillary pressure using a continuum approach." In: *Journal of Colloid And Interface Science* 325.2, pp. 440–446.

Nefzaoui, E and O Skurtys (2012). "Impact of a liquid drop on a granular medium: Inertia, viscosity and surface tension effects on the drop deformation." In: *EXPERIMENTAL THERMAL AND FLUID SCIENCE* 41, pp. 43–50.

Nikolopoulos, N, A Theodorakakos, and G Bergeles (2007). "A numerical investigation of the evaporation process of a liquid droplet impinging onto a hot substrate." In: *International Journal of Heat and Mass Transfer* 50.1-2, pp. 303–319.

Okayama, T, D S Keller, and P Luner (1997). "The wetting of calcite surfaces." In: *The Journal of Adhesion* 63.1-3, pp. 231–252.

Pasandideh-Fard, M, Y M Qiao, S Chandra, and J Mostaghimi (1996). "Capillary effects during droplet impact on a solid surface." In: *Physics of Fluids* 8.3, p. 650.

Pasandideh-Fard, M, R Bhola, and S Chandra (1998). "Deposition of tin droplets on a steel plate: simulations and experiments." In: *International Journal of Heat and Mass Transfer* 41.19, pp. 2929–2945.

Pasandideh-Fard, M, S D Aziz, S Chandra, and J Mostaghimi (2001). "Cooling effectiveness of a water drop impinging on a hot surface." In: *International Journal of Heat and Fluid Flow* 22.2, pp. 201–210.

Qian, Tiezheng, XIAO-PING WANG, and PING SHENG (2006). "A variational approach to moving contact line hydrodynamics." In: *Journal of Fluid Mechanics* 564, pp. 333–360.

Reis, N C, R F Griffiths, M D Mantle, and L F Gladden (2003). "Investigation of the evaporation of embedded liquid droplets from porous surfaces using magnetic resonance imaging." In: *International Journal of Heat and Mass Transfer* 46.7, pp. 1279–1292.

Reis Jr., N C, R F Griffiths, M D Mantle, L F Gladden, and J M Santos (2006). "MRI investigation of the evaporation of embedded liquid droplets from porous surfaces under different drying regimes." In: *International Journal of Heat and Mass Transfer* 49.5-6, pp. 951–961.

Reis Jr., Neyval C, Richard F Griffiths, and Jane M Santos (2004). "Numerical simulation of the impact of liquid droplets on porous surfaces." In: *Journal of Computational Physics* 198.2, pp. 747–770.

Reis Jr., Neyval C, Richard F Griffiths, and Jane Méri Santos (2008). "Parametric study of liquid droplets impinging on porous surfaces." In: *Applied Mathematical Modelling* 32.3, pp. 341–361.

Rioboo, R, C Tropea, and M Marengo (2001). "Outcomes from a drop impact on solid surfaces." In: *Atomization and Sprays* 11, pp. 155–165.

Rioboo, R, M Marengo, and C Tropea (2002). "Time evolution of liquid drop impact onto solid, dry surfaces." In: *Experiments in Fluids* 33.1, pp. 112–124.

Rodriguez-Valverde, MA, MA Cabrerizo-Vilchez, P. Rosales-Lopez, A. Paez-Duenas, and R. Hidalgo-Alvarez (2002). "Contact angle measure-

ments on two (wood and stone) non-ideal surfaces." In: *Colloids and Surfaces A: Physicochemical and Engineering Aspects* 206.1-3, pp. 485–495.

Roels, Staf (2000). "Modelling unsaturated moisture transport." PhD thesis. KU LEUVEN.

Roisman, I V (2009). "Inertia dominated drop collisions. II. An analytical solution of the Navier-Stokes equations for a spreading viscous film." In: *Physics of Fluids* 21.5, p. 052104.

Roisman, I V, L Opfer, C Tropea, M Raessi, J Mostaghimi, and S Chandra (2008). "Drop impact onto a dry surface: Role of the dynamic contact angle." In: *Colloids and Surfaces A: Physicochemical and Engineering Aspects* 322.1-3, pp. 183–191.

Roisman, I V, E Berberović, and C Tropea (2009). "Inertia dominated drop collisions. I. On the universal flow in the lamella." In: *Physics of Fluids* 21.5, p. 052103.

Roisman, Ilia V ., Romain Rioboo, and Cameron Tropea (2002). "Normal impact of a liquid drop on a dry surface: model for spreading and receding." In: *Proceedings of the Royal Society of London A: Mathematical, Physical and Engineering Sciences* 458.2022, pp. 1411–1430.

Ruiter, Jolet de, Rudy Lagraauw, Dirk van den Ende, and Frieder Mugele (2015). "Wettability-independent bouncing on flat surfaces mediated by thin air films." In: *Nature Physics* 11.1, pp. 48–53.

Scheller, Brian L and Douglas W Bousfield (1995). "Newtonian drop impact with a solid surface." In: *AIChE Journal* 41.6, pp. 1357–1367.

Šikalo, Š, M Marengo, C Tropea, and E N Ganić (2002). "Analysis of impact of droplets on horizontal surfaces." In: *Experimental Thermal and Fluid Science* 25, pp. 503–510.

Šikalo, Š, H D Wilhelm, I V Roisman, S Jakirlić, and C Tropea (2005). "Dynamic contact angle of spreading droplets: Experiments and simulations." In: *Physics of Fluids* 17.6, pp. 1–13.

Sikalo, S, C Tropea, and EN Ganic (2005). "Dynamic wetting angle of a spreading droplet." In: *EXPERIMENTAL THERMAL AND FLUID SCIENCE* 29.7, pp. 795–802.

Stalder, AF, G Kulik, D Sage, L Barbieri, and P Hoffmann (2006). "A snake-based approach to accurate determination of both contact points and contact angles." In: *Colloids and Surfaces A: Physicochemical and Engineering Aspects* 286.1-3, pp. 92–103.

Stow, C D and M G Hadfield (1981). "An Experimental Investigation of Fluid Flow Resulting from the Impact of a Water Drop with an Unyield-

ing Dry Surface." In: *Proceedings of the Royal Society A: Mathematical, Physical and Engineering Sciences* 373.1755, pp. 419–441.

Strotos, G, G Aleksis, M Gavaises, K S Nikas, N Nikolopoulos, and A Theodorakakos (2011). "Non-dimensionalisation parameters for predicting the cooling effectiveness of droplets impinging on moderate temperature solid surfaces." In: *International Journal of Thermal Sciences* 50.5, pp. 698–711.

Thoroddsen, S T, T G Etoh, and K Takehara (2008). "High-speed imaging of drops and bubbles." In: *Annual Review of Fluid Mechanics* 40, pp. 257–285.

Ukiwe, Chijioke and Daniel Y Kwok (2004). "On the Maximum Spreading Diameter of Impacting Droplets on Well-Prepared Solid Surfaces." In: *Langmuir* 21.2, pp. 666–673.

Vadillo, D C, A Soucemarianadin, C Delattre, and D C D Roux (2009). "Dynamic contact angle effects onto the maximum drop impact spreading on solid surfaces." In: *Physics of Fluids* 21.12, pp. 1–8.

Vaikuntanathan, V, R Kannan, and D Sivakumar (2010). "Impact of water drops onto the junction of a hydrophobic texture and a hydrophilic smooth surface." In: *Colloids and Surfaces A: Physicochemical and Engineering Aspects.*

Villermaux, E and B Bossa (2009). "Single-drop fragmentation determines size distribution of raindrops." In: *Nature Physics* 5.9, pp. 697–702.

Visser, C W, P E Frommhold, S Wildeman, R Mettin, Detlef Lohse, and Chao Sun (2015). "Dynamics of high-speed micro-drop impact: numerical simulations and experiments at frame-to-frame times below 100 ns." In: *Soft Matter* 11.9, pp. 1708–1722.

Visser, Claas Willem, Yoshiyuki Tagawa, Chao Sun, and Detlef Lohse (2012). "Microdroplet impact at very high velocity." In: *Soft Matter* 8.41, pp. 10732–10737.

Wallace, K and K Yoshida (1978). "Determination of dynamic spread factor of water droplets impacting on water-sensitive paper surfaces." In: *Journal of Colloid And Interface Science* 63.1, pp. 164–165.

Willis, Matthew P ., Brent A . Mantooth, and Teri A . Lalain (2011). "Novel Methodology for the Estimation of Chemical Warfare Agent Mass Transport Dynamics, Part I: Evaporation." In: *The Journal of Physical Chemistry C* 116.1, pp. 538–545.

Worthington, A M (1876). "On the forms assumed by drops of liquids falling vertically on a horizontal plate." In: *Proceeding of the royal society of London.*

Yarin, A L (2006). "Drop impact dynamics: splashing, spreading, receding, bouncing..." In: *Annual Review of Fluid Mechanics* 38, pp. 159–192.

Yokoi, K, D Vadillo, J Hinch, and I Hutchings (2009). "Numerical studies of the influence of the dynamic contact angle on a droplet impacting on a dry surface." In: *Physics of Fluids* 21, p. 072102.

Yu, Zhao, Fei Wang, and L S Fan (2008). "Experimental and numerical studies of water droplet impact on a porous surface in the film-boiling regime." In: *Industrial and Engineering Chemistry Research* 47.23, pp. 9174–9182.

Zhang, X and O A Basaran (1997). "Dynamic surface tension effects in impact of a drop with a solid surface." In: *Journal of Colloid And Interface Science* 187.1, pp. 166–178.

Zhao, Runchen, Qianyun Zhang, Hendro Tjugito, and Xiang Cheng (2015a). "Granular impact cratering by liquid drops: Understanding raindrop imprints through an analogy to asteroid strikes." In: *Proceedings of the National Academy of Sciences* 112.2, pp. 342–347.

Zhao, Song-Chuan, Rianne de Jong, and Devaraj van der Meer (2015b). "Raindrop impact on sand: a dynamic explanation of crater morphologies." In: *Soft Matter* 11.33, pp. 6562–6568.

NOMENCLATURE

This list of symbols is not exhaustive. Symbols that only appear locally in the text, or are self-explanatory, are not included.

ROMAN SYMBOLS

SYMBOL	MEANING	UNIT
D	spreading diameter	m
D_0	initial drop diameter	m
Ca	Capillary number	-
Co	Courant number	-
d	total thickness of the object along beam direction	m
$D_{\max}$	maximum spreading diameter	m
D_μ	transverse momentum diffusion constant	-
E_k	kinetic energy	J
E_γ	capillary energy	J
E_μ	viscous energy	J
f	indicator function for phase fraction	-
f_{H}	Hoffman's function	-
g_v	vapor flux	m/s
h	height of droplet at maximum spreading	m
H	distance between drop generator and surface	m
I	intensity of transmitted beam	number of neutrons/s
I_0	intensity of incident neutron beam	number of neutrons/s
KE	kinetic energy	J
K_l	liquid permeability	s
M_0	initial droplet mass	kg
M_{abs}	absorption mass	kg
m_{dry}	dry stone mass	kg
m_{sat}	saturated stone mass	kg
Oh	Ohnesorge number	-

SYMBOL	MEANING	UNIT
p_{c}	capillary pressure	Pa
p_v	vapor pressure at porous material surface	Pa
$p_{v,\mathrm{env}}$	vapor pressure of environment	Pa
$p_{v,\mathrm{sat}}$	saturated vapor pressure	Pa
R_a	roughness	μm
Re	Reynolds number	-
RH	relative humidity	-
R_v	specific gas constant	-
SE	surface energy	J
S_{LV}	liquid-vapor interfacial surface area	m^2
S_{SL}	solid-liquid interfacial surface area	m^2
T	change of transmission	-
T_{corr}	corrected transmission value	-
t_{max}	time at maximum spreading	s
$\mathbf{U}$	fluid velocity vector	m/s
V_{i}	impact velocity of droplet	m/s
V_{CL}	contact line fluid velocity	m/s
V_{drop}	volume of droplet in spherical cap shape	m^3
W	viscous dissipation energy	J
w	moisture content	$\mathrm{kg/m}^3$
w_{cap}	capillary moisture content	$\mathrm{kg/m}^3$
w_{sat}	saturated moisture content	$\mathrm{kg/m}^3$
We	Weber number	-

GREEK SYMBOLS

SYMBOL	MEANING	UNIT
β	spreading ratio	-
β_{max}	maximum spreading ratio	-
Γ	effective surface energy	-
γ_{LV}	liquid-vapor surface tension	N/m
γ_{SL}	solid-liquid surface tension	N/m
γ_{SV}	solid-vapor surface tension	N/m
Δ	non-dimensional boundary thickness	-
δ	boundary layer thickness	m
$\bar{\delta}$	spatially averaged boundary layer thickness	m
δ_v	vapor permeability	s
ζ	mass transfer coefficient	-
θ_{adv}	advancing contact angle	°
θ_{app}	apparent contact angle	°
θ_{D}	dynamic contact angle	°
$\theta_{\mathrm{D,sim}}$	dynamic contact angle from simulation	°
$\theta_{\mathrm{D}}(t_{\mathrm{max}})$	dynamic contact angle at maximum spreading	°
θ_{eq}	equilibrium contact angle	°
θ_{in}	incident angle of impacting droplet	°
θ_{rec}	receding contact angle	°
κ^{-1}	capillary length	m
μ	viscosity of liquid	Pa·s
ρ	density of liquid	kg/m^3
ρ_{bulk}	density of bulk stone	kg/m^3
Σ	macroscopic linear attenuation coefficient	1/m
σ	microscopic attenuation coefficient	1/m
Φ	porosity	-
ϕ	dissipation function	-
Ω	volume of viscous dissipation occurs	m^3

SUBSCRIPTS

SYMBOL	MEANING
air	air
drop	droplet
max	maximum spreading
stone	porous stone
water	water

ACRONYMS

ACA   Advancing Contact Angle

CA   Contact Angle

CCA   Constant Contact Angle

CCR   Constant Contact Radius

CFD   Computational Fluid Dynamics

CSF   Continuum Surface Force

DCA   Dynamic Contact Angle

ECA   Equilibrium Contact Angle

EBA   Energy Balance Approach

MRI   Magnetic Resonance Imaging

NMR   Nuclear Magnetic Resonance

RCA   Receding Contact Angle

VOF   Volume-of-Fluid

WDR   Wind-Driven Rain

CURRICULUM VITAE

JAEBONG LEE

Date of birth	May 26th, 1981
Place of birth	Gumi, Republic of Korea
Nationality	Korean
E-mail address	jaebong2lee@gmail.com

EDUCATION

04.2012 – 11.2015	Doctor of Sciences Chair of Building Physics Swiss Federal University of Technology, ETH Zurich Thesis: Droplet dynamics on non-porous and porous media: impact, spreading and absorption.
03.2009 – 02.2011	Master of Science Mechanical Engineering Chung-Ang University Graduate School (Seoul, Ref. of Korea) Thesis: Dynamic wetting and spreading of a liquid droplet impinging on microtextured hydrophobic surfaces.
03.2002 – 02.2009	Bachelor of Science Mechanical Engineering Chung-Ang University (Seoul, Ref. of Korea)

ACADEMIC EXPERIENCE

04.2012 – 11.2015	Scientific guest at Swiss Federal Laboratories for Materials Science and Technology, EMPA (Switzerland).
09.2011 – 12.2011	Research member, Next Generation Energy Safety Research Institute (Korea).
12.2010 – 01.2011	Visiting Scholar at Michigan Technological University (MI, USA).
03.2009 – 02.2010	Teaching Assistantship at Chung-Ang University (Korea).
06.2008 – 02.2011	Research Assistant, Multi-scale Thermal Engineering Lab. at Chung-Ang University (Korea).

JOURNAL PUBLICATIONS

Jae Bong Lee, , A. Radu, P. Vontobel, D. Derome, J. Carmeliet, (2016). Absorption of impinging droplet on porous stones, *Journal of Colloid and Interface Science*, submitted.

Jae Bong Lee, D. Derome, J. Carmeliet, (2016). Drop impact on natural porous stones, *Journal of Colloid and Interface Science*, accepted for publication.

Jae Bong Lee, D. Derome, A. Dolatabadi, J. Carmeliet, (2016). Energy budget of liquid drop impact at maximum spreading: numerical simulations and experiments, *Langmuir*, 32 (5), pp 1279–1288.

Jae Bong Lee, D. Derome, R. Guyer, J. Carmeliet, (2016). Modelling the maximum spreading of impacting on dynamic wetting and non-wetting surfaces, *Langmuir*, 32 (5), pp 1299–1308.

Jae Bong Lee, N. Laan, N. Shahidzadeh, D. Derome, J. Carmeliet, D. Bonn, (2016). Universal rescaling of drop impact on smooth an rough surfaces, *Journal of Fluid Mechanics*, Vol. 786 R4.

Jae Bong Lee, C. Antonini, T. Maitra, S. Irvine, D. Derome, M.K. Tiwari, J. Carmeliet, D. Poulikakos, (2014). Unraveling wetting transition through surface textures with X-rays: Liquid meniscus penetration phenomena, *Scientific Reports*, Vol. 4, 4055.

Joo Hyun Moon, **Jae Bong Lee**, Seong Hyuk Lee, (2013). Dynamic Behavior of non-Newtonian Droplets Impinging on Solid Surfaces, *Material Transactions*, Vol. 54, No. 2, pp. 260-265.

Jae Bong Lee, Seong Hyuk Lee, Chang Kyoung Choi, (2011). Dynamic Spreading of a Droplet Impinging on Micro-Textured Surfaces, *Journal of Heat Transfer*, Vol. 133, 080905-1.

Jae Bong Lee, Seong Hyuk Lee, (2011). Dynamic Wetting and Spreading Characteristics of a Liquid Droplet Impinging on Hydrophobic Textured Surfaces, *Langmuir*, Vol. 27, pp. 6565 – 6573.

Jae Bong Lee, Hyuk Rok Gown, Seong Hyuk Lee, Minhaeng Cho, (2010). Wetting Transition Characteristics on Microstructured Hydrophobic Surfaces, *Material Transactions*, Vol. 51, No. 9, pp. 1709 – 1711.

DOMESTIC JOURNAL PUBLICATIONS

Jae Bong Lee, Joo Hyun Moon, Seong Hyuk Lee, (2012). Spreading and Deposition Characteristics of a Water Droplet Impacting on Hydrophobic Textured Surfaces, *Journal of ILASS-Korea*, Vol. 17, No. 1, pp. 14-19.

Jae Bong Lee, Minhaeng Cho, (2009). The Effect of Surface Micro Texturing on Friction and Wear of Polyoxymethylene, *Journal of the KSTLE*, Vol. 25, No. 3, pp. 141-149.

ACCEPTED RESEARCH PROPOSALS

Jae Bong Lee(Principal Investigator), D. Derome, J. Carmeliet, Neutron imaging of impinging droplet and transport in porous material, NEUTRA, The Swiss Spallation Neutron Source (SINQ), Paul Scherrer Institute, Villigen, Switzerland (2012).

M.K. Tiwari, D. Derome, D. Poulikakos, **Jae Bong Lee**, T. Maitra, J. Carmeliet, Droplet impact on textured surfaces: Penetration of water meniscus into surface microtexture, TOMCAT, Swiss Light Source, Paul Scherrer Institute, Villigen, Switzerland (2013).

Jae Bong Lee(Principal Investigator), D. Derome, J. Carmeliet, Neutron imaging of impinging droplets, film forming and transport in porous materials, NEUTRA, The Swiss Spallation Neutron Source (SINQ), Paul Scherrer Institute, Villigen, Switzerland (2013).

Jae Bong Lee(Principal Investigator), D. Derome, J. Carmeliet, Oblique impact: fate of water drops on porous media, NEUTRA, The Swiss Spallation Neutron Source (SINQ), Paul Scherrer Institute, Villigen, Switzerland (2015).

INTERNATIONAL CONFERENCES

Jae Bong Lee, Dominique Derome, Jan Carmeliet, Spreading and absorption of impinging droplet into porous stones, Twente, Netherlands, Oct. 6 - 8, 2015.

Jae Bong Lee, Dominique Derome, Robert Guyer, Jan Carmeliet, Maximum spreading of impinging droplet on partial wetting surfaces: surface energy versus viscous dissipation energy, Twente, Netherlands, Oct. 6 - 8, 2015.

Jae Bong Lee, D. Derome, J. Carmeliet, Fate of water drops on porous building stones, 7th International Conference on Porous Media and Annual Meeting, Padova, Italy, May 18 - 21, 2015.

Jae Bong Lee, D. Derome, S. Carl, P. Vontobel, J. Carmeliet, Spreading and absorption of impinging droplet on porous stones, 10th World Conference on Neutron Radiography, Grindelwald, Switzerland, Oct. 5 - 10, 2014.

Jae Bong Lee, D. Derome, S. Carl, J. Carmeliet, Impingement and absorption of droplets on porous stones using neutron imaging technique, PSI user meeting, Viligen, Switzerland, Sep. 18 - 20, 2013.

Jae Bong Lee, Seong Hyuk Lee, Chang Kyoung Choi, Dynamic Spreading of a Droplet Impinging on Micro-Textured Surfaces, American Society of Mechanical Engineering (ASME)-International Mechanical Engineering Congress and Exhibition (IMECE), Vancouver, Canada, Nov. 12 - 18, 2010.

Jae Bong Lee, Seong Hyuk Lee, Spreading Characteristics of a Single Water Droplet Impinging on Hydrophobic Micro-Textured Metal Surfaces, 14th Annual Conference on Liquid Atomization and Spray Systems – Asia, Jeju, Korea, Oct. 21 - 22, 2010.